University of Sussex

Space Debris Mitigation in Low Earth Orbit (LEO) Using High Power Pulsed Lasers

by

Alaa Adnan Hussein BSc, MSc

Department of Engineering and Design

School of Engineering and Informatics

University of Sussex

Brighton, England, United Kingdom

Submitted in Fulfilment of the Requirements for the Degree of Doctor of Philosophy in Engineering at the University of Sussex

Alaa Adnan Hussein, *Space Debris Mitigation in Low Earth Orbit (LEO) Using High Power Pulsed Lasers*, Doctor of Philosophy, Department of Engineering and Design, School of Engineering and Informatics, University of Sussex, Brighton, England, United Kingdom, © 2017

Supervisors:

Prof Chris Chatwin, Professor in Engineering, Chair of Engineering, Research Director of the Industrial Informatics and Signal Processing (iisp) Research Group and the Laser and Photonics Systems Engineering Group, Department of Engineering and Design, School of Engineering and Informatics, University of Sussex, Brighton, England, United Kingdom

Dr Rupert Young, Reader in Engineering, Department of Engineering and Design, School of Engineering and Informatics, University of Sussex, Brighton, England, United Kingdom

Examiners:

Dr Ian Watson, Reader in Systems Power and Energy, School of Engineering, University of Glasgow, Glasgow, Scotland, United Kingdom

Convener:

Dr Tai Yang, Reader in Computer and Control Engineering, Department of Engineering and Design, School of Engineering and Informatics, University of Sussex, Brighton, England, United Kingdom

Location:

Department of Engineering and Design, School of Engineering and Informatics, University of Sussex, Brighton, England, United Kingdom

Exam Date:

2nd August 2018

Abstract

Mitigating space debris with lasers is investigated as a possible mechanism for contactless space debris deflection in Low Earth Orbit (LEO). This deflection mechanism can be carried out by irradiating the space debris surface with a high-power laser beam. The energy absorbed by the surface of the debris, from the laser beam, sublimates the irradiated surface, transforming it to gas from solid. The ablated material is formed into a plume of ejecta, which acts against the orbital debris if the laser is beamed in the right direction; it produces a small push or thrust that deflects the debris by reducing its orbital velocity, altitude and eventually its lifetime in orbit. This approach could also be used to push space debris away from operational satellites paths.

Laser ablation depends mainly on understanding the physical properties of both, the laser beam and the space debris. The interaction process for three different commonly used spacecraft materials are illuminated by a laser beam and investigated both experimentally and by using theoretical models. Experimental results and theoretical verifications are employed to evaluate the feasibility of the ablation model and to understand its performance in producing an effective deflection of space debris. This was investigated using Nd^{3+} Glass laser pulses with three metals: nickel (Ni), aluminium (Al) and copper (Cu). The Nd^{3+} Glass laser operated at a wavelength of 1.06 μm that provided intensities just below the threshold for plasma formation. This interaction produces surface power intensities ranging between one GW/m^2 to one TW/m^2, which produces high order temperature gradients that cause non-equilibrium energy transport phenomenon. This phenomenon cannot be explained by classical theories. The results have been used for the enhancement of the ablation model. Additional enhancements included the temperature penetration in the target surface. The surface temperature transients of metals due to laser interaction have also been investigated, and heat transfer is simulated by utilising a kinetic particle model, which captures the dominant energy transport processes. This model of energy transport permits determination of the significant decline in temperature gradients and the non-equilibrium conditions that occur between the Fermi surface conduction electrons and lattice phonons. This results in an accurate temperature distribution calculation within the space debris. The laser pulse specification and the properties of the space debris material were specified for simulation. The kinetic model has been used to simulate the

spatial temperature distribution growth in the space debris when illuminated with a 1.06 μm wavelength Nd^{3+} Glass laser. The evaporation physics are also incorporated into the kinetic model. The average mass flow rate has been evaluated. A critical difference has been discovered between the experimental results and the predicted results using the classical Fourier Theory. The experimental data of the target surface temperatures are compared with Fourier and electron Kinetic theories. The experimental results validate the theoretical results and model improvements. It also illustrated the inaccuracy of Fourier theory regarding its solution of steep energy gradients and its failure to illustrate the non-equilibrium energy transport state, which grows between electrons and lattice phonons. It was noticed that the electron Kinetic theory results provide sufficient agreement with the experimental results below the boiling point and give a much better model than Fourier theory above the boiling temperature. The enhancements have permitted the laser specifications and the performance of the ablation treatment to be characterised.

The performance of orbital debris mitigation with pulsed lasers outperformed alternative techniques that can produce a small contactless push on space junk. This method avoids sending complicated spacecraft into orbits to take space debris away from Earth orbits. The laser power that is required to reduce the altitude and the orbital velocity of space debris were predicted and calculated theoretically. The performance has been assessed by its capability to move small debris, centimetre size, by at least a couple of m/s. The results confirmed the possible benefits of using lasers to mitigate space debris in LEO. Employing current technologies together with a high Technology Readiness Level (TRL), an affordable and compact laser system could be successfully constructed and attached to traditional artificial satellites as a space-based laser system. Such a system could demonstrate the method, synergies and techniques of laser ablation. Mission complexity and the extra mass are saved by the direct debris ablation process, which can operate at a relatively small distance compared to a ground-based laser system. The analysis thus confirms the feasibility of utilising space-based laser systems and the applicability of the model's experimental validation.

Table of Contents

Page Number

ABSTRACT ..... **I**

TABLE OF CONTENTS ..... **III**

LIST OF FIGURES ..... **VI**

LIST OF TABLES ..... **XI**

NOMENCLATURE ..... **XII**

ACKNOWLEDGEMENTS ..... **XX**

DEDICATION ..... **XXI**

DECLARATION ..... **XXII**

PUBLICATIONS ..... **XXIII**

CHAPTER 1 ..... **1**

BACKGROUND AND INTRODUCTION 1

1.1 Summary *2*

1.1 The Space Environment *2*

1.2 Space Surveillance Network (SSN) *4*

1.3 Space Situational Awareness (SSA) *7*

1.4 Satellite Orbits *12*

1.5 Space Debris Population *15*

1.6 Orbital Debris in LEO *20*

1.7 Thesis Structure and Outline *22*

CHAPTER 2 ..... **23**

LASERS AS DEFLECTION TOOLS 23

2.1 Summary *24*

2.2 Lasers as Engineering Tools *24*

2.2.1 Laser beam output characteristics 25

2.2.2 Space debris physical characteristics 29

2.2.3 Interaction environments 32

2.3 Laser Pulse *32*

2.4 Laser Ablation *32*

2.5 Space Debris Mitigation and Deflection Techniques *35*

2.6 Laser-Space Debris Interaction *37*

CHAPTER 3 ..... **39**

LASER POWER, BEAM SIZE AND REPETITION RATE 39

3.1 Summary *40*

3.2 Mitigation Techniques based on Space Debris Size *40*

3.3 Impacts of Laser Energy and Beam Radius on Laser Treatment *41*

3.3.1 General Assumptions 43

3.3.2 Melting and Boiling Debris in Space with Lasers 44

3.4 Laser Power Density Distribution (PDD) *49*

3.4.1 Laser Gaussian PDD 49
3.4.2 Laser Top-Hat PDD....50
3.5 Impact of Laser Repetition Rate on Laser Treatment 51

CHAPTER 4 55

IRRADIATION OF SPACE DEBRIS WITH LASER PULSES: KINETIC THEORY.... 55
4.1 Summary 56
4.2 Employment of Experimental Temperature Data.... 56
4.3 Simulation of Spatial Temperature Distribution Evolution in Space Debris Beamed with Laser Pulses 58
4.4 Fourier theory and Kinetic theory.... 59
4.5 Kinetic Theory of Energy Transport 59
4.5.1 Kinetic Theory Model: Below Boiling Point (BBP) 60
A. Energy of Electron 62
B. Equations of Energy Transport 64
C. Thermal Characteristics 66
D. Temperatures of electron and lattice (phonon) 67
E. Discussion of Theoretical Results....70
4.5.2 Kinetic Theory Model: Above Boiling Point (ABP)....82
4.6 Results and Discussion.... 86

CHAPTER 5 100

IRRADIATION OF SPACE DEBRIS WITH LASER PULSES: FOURIER CONDUCTION THEORY 100
5.1 Summary 101
5.2 Fourier Conduction Theory 101
5.3 Spatial Lattice Temperature 104
5.4 Input Power Profile with Lattice Surface Temperature of Space Debris 113
5.5 Fourier Conduction Theory versus Electron Kinetic Theory.... 116
5.6 Discussion 119

CHAPTER 6 120

THEORETICAL ANALYSIS OF SPACE DEBRIS PROPULSION USING LASERS.... 120
6.1 Summary 121
6.2 Characterisation of Space Junk.... 121
6.3 Laser Ablation Propulsion.... 122
6.4 How Lasers Can Transfer Momentum to Space Debris.... 122
6.5 General Concerns about the Laser Technique 124
6.6 Design Choices and Challenges.... 124
6.7 Dragging and Deorbiting Space Debris 126
6.8 Required Delta-V $\Delta \boldsymbol{v}$ for Different Operational Conditions 127
6.9 Theoretical Analysis of the Laser Ablation Propulsion.... 129
6.10 Discussion of Results and Conclusion 137

CHAPTER 7 139

EXPERIMENTAL RESULTS ANALYSIS 139
7.1 Summary 140
7.2 Optical Mechanism.... 140
7.3 Measurements of the Laser Output Power.... 141
7.4 Laser Beam Assumptions.... 143
7.5 Determination and Measurement of Emissive Power Ratios and Temporal Change of the Space Debris Surface Temperature.... 144

7.6 Implementation of Blackbody Irradiation for the Determination of Space Debris Surface Temperature *145*
7.7 Discussion and conclusions *149*
7.8 Analysis of Experimental Results *150*
7.8.1 Results for Nickel Space Debris 150
I. At central wavelength of 662.4 nm 150
II. At central wavelength of 750.0 nm 152
III. At central wavelength of 950.0 nm 153
7.8.2 Results for Aluminium Space Debris 155
I. At central wavelength of 662.4 nm 155
II. At central wavelength of 750.0 nm 155
III. At a central wavelength of 950.0 nm 156
7.8.3 Results for Copper Space Debris 159
I. At central wavelength of 662.4 nm 159
II. At central wavelength of 750.0 nm 159
III. At central wavelength of 950.0 nm 160
7.8.4 Discussion 162
I. Classical Fourier Theory 162
II. Kinetic Theory 162
7.9 Limitations and Inadequacies *163*
7.9.1 Mathematical Model Limitations 163
7.9.2 Measurement Inadequacies 164
7.10 Spatial Temperature Distribution *165*
7.11 Heating Rate of the Space Debris Surface *165*
7.12 Space Debris Material Characteristics Determination *166*
7.12.1 $\boldsymbol{f}$-parameter: The energy loss rate of electrons in elastic collisions with phonons 166
7.12.2 $\boldsymbol{v1}$: Electron Speed at Fermi Surface 167
7.12.3 $\boldsymbol{l}$: Average free path of electron 168
7.12.4 $\boldsymbol{D}$: Thermal Diffusivity 168
7.12.5 $\boldsymbol{Z}$: Temperature penetration depth 169
7.13 Ablation of Space Debris Material *169*
7.14 Outcomes *170*

CHAPTER 8 172

GENERAL SUMMARY, RECOMMENDATIONS FOR FUTURE WORK AND CONCLUSIONS 172
8.1 General Summary *173*
8.2 Recommendations for Future Work *175*
8.3 Conclusions *176*

BIBLIOGRAPHY AND KEY REFERENCES 178

List of Figures

Page Number

FIGURE 1: SPACE DEBRIS AT DIFFERENT ALTITUDES IN EARTH ORBITS 4
FIGURE 2: CHILBOLTON 25 M RADAR 7
FIGURE 3: NUMBER OF SATELLITES PLACED IN GEO PER ANNUM (26 SATELLITE ON AVERAGE) 9
FIGURE 4: THE COMPLEXITY OF GEO ORBITS FOR OPERATIONAL SATELLITE DRAMATICALLY INCREASED OVER JUST 12 YEARS WINDOW (1999-2011) 10
FIGURE 5: ORBIT ALTITUDES FOR SATELLITE CONSTELLATIONS BY LLOYD WOOD 12
FIGURE 6: SATELLITE NAVIGATION ORBITS 13
FIGURE 7: POST COLLISION DEBRIS CLOUD OVER THREE YEARS 16
FIGURE 8: CHRONOLOGICAL TIMELINE OF THE US SSN OFFICIALLY CATALOGUED NUMBER BY US SSN OF OBJECTS IN EARTH ORBIT BETWEEN 1957 AND 2017 17
FIGURE 9: CHRONOLOGICAL TIMELINE OF THE US SSN OFFICIALLY CATALOGUED MASS OF OBJECTS IN EARTH ORBIT BETWEEN 1956 AND 2016 18
FIGURE 10: TIMELINE OF EARTH ORBITS WITH SPACE OBJECTS 18
FIGURE 11: LOCATIONS OF SPACE JUNK AFTER RE-ENTRY (IMAGE CREDIT: ESA) 19
FIGURE 12: EXAMPLES OF RE-ENTRY SPACE DEBRIS IN FIVE DIFFERENT CONTINENTS AND COUNTRIES 20
FIGURE 13: EXPERIMENTAL HYPERVELOCITY IMPACT STUDY BY ESA 21
FIGURE 14: OVERVIEW OF THE COMMERCIALLY AVAILABLE LASERS TYPES AND WAVELENGTHS []. LINE HEIGHT GIVES MAXIMAL POWER AND PULSES ENERGY INDICATION. FULL LINES AND AREAS MEAN CW EMISSION AND DOTTED MEAN PULSED EMISSION 26
FIGURE 15: LAGUERRE-GAUSSIAN TEM PATTERN 27
FIGURE 16: GAUSSIAN BEAM AND ITS WAIST PARAMETERS 28
FIGURE 17: TWENTY MOST COMMONLY USED MATERIALS IN MANUFACTURING SPACE SYSTEMS (BACKGROUND IMAGE CREDITS NASA) 30
FIGURE 18: LASER ORBITAL DEBRIS REMOVAL (LODR) SYSTEM USING GROUND-BASED LASER SYSTEM 34
FIGURE 19: INTERACTION BETWEEN THE LASER PULSES AND A SPACE DEBRIS 37
FIGURE 20: SPACE SYSTEMS SHIELDING 40
FIGURE 21: 3D GEOMETRY OF AN IDEAL ABLATED CONE 42
FIGURE 22: 2D GEOMETRY OF AN IDEAL ABLATED CONE 43
FIGURE 23: THERMAL PROFILE OF ALUMINIUM DEBRIS IRRADIATED BY 50 KW LASER POWER WITH 30 CM LASER BEAM RADIUS 45
FIGURE 24: THERMAL PROFILE OF ALUMINIUM DEBRIS IRRADIATED BY 100 KW LASER POWER WITH 10 CM LASER BEAM RADIUS 45
FIGURE 25: THERMAL PROFILE OF ALUMINIUM DEBRIS IRRADIATED BY 75 KW LASER POWER WITH 5 CM LASER BEAM RADIUS 46
FIGURE 26: THERMAL PROFILE OF ALUMINIUM DEBRIS IRRADIATED BY 100 KW LASER POWER WITH 5 CM LASER BEAM RADIUS 47
FIGURE 27: REQUIRED HEAT AND TIME TO MELT 10 CM DIAMETER SOLID ALUMINIUM DEBRIS BY 100 KW LASER POWER WITH 5 CM LASER BEAM RADIUS 48
FIGURE 28: REQUIRED HEAT AND TIME TO BOIL 10 CM DIAMETER MELTED ALUMINIUM DEBRIS WITH 100 KW LASER POWER WITH 5 CM LASER BEAM RADIUS 48
FIGURE 29: RADIATED POWER BY IRRADIATED ALUMINIUM SPACE DEBRIS WITH 100 KW LASER POWER WITH 5 CM LASER BEAM RADIUS 49
FIGURE 30: LASER POWER INTENSITY PROFILE OF GAUSSIAN LASER BEAM (GAUSSIAN PDD) 50
FIGURE 31: LASER TOP-HAT POWER DENSITY PROFILE (TOP-HAT PDD) 51

FIGURE 32: OVERLAP IN LASER PULSES AT 0.5 KHZ 52
FIGURE 33: OVERLAP IN LASER PULSES AT 1 KHZ 53
FIGURE 34: OVERLAP IN LASER PULSES AT 0.75 KHZ 53
FIGURE 35: BLACK BODY CURVES OF PLANCK AT DIFFERENT TEMPERATURES 57
FIGURE 36: HEAT TRANSFER PHENOMENA BY CONDUCTION (CREDIT BBC.CO.UK) 59
FIGURE 37: MOVEMENT OF AN ELECTRON INSIDE METAL SPACE DEBRIS FOR THE TOP HALF OF THE CONE. ELECTRONS TRANSPORT ENERGY FROM ALL THE DEBRIS AREAS AND PART OF THIS ENERGY IS MOVED TO THE LATTICE THROUGH COLLISIONS WITH PHONONS. THE LEFT-HAND SIDE OF THE FREE SURFACE ILLUSTRATES THE MIRROR IMAGE METHOD AND $\boldsymbol{x} = \boldsymbol{0}$ REPRESENTS THE FREE SURFACE. 61
FIGURE 38: PHOTON ABSORPTION PROCESS FROM $\boldsymbol{\epsilon}$ TO $\boldsymbol{x}$ 63
FIGURE 39: TOP HAT CIRC FUNCTION AND GAUSSIAN BEAM PROFILE ASSUMPTIONS WITH RESPECTS TO THE ACTUAL LASER BEAM INTENSITY DISTRIBUTION 70
FIGURE 40: BELOW BOILING POINT: ELECTRON TEMPERATURE PROFILE AT 0.2 μS TIME INTERVALS IN NI SPACE DEBRIS USING KINETIC THEORY WHEN GAUSSIAN BEAM IS ASSUMED (BBP, NI, KINETIC, GAUSSIAN, ELECTRON) 72
FIGURE 41: BELOW BOILING POINT: ELECTRON TEMPERATURE PROFILE AT 0.2 μS TIME INTERVALS IN NI SPACE DEBRIS USING KINETIC THEORY WHEN CIRC FUNCTION BEAM IRRADIANCE PROFILE IS ASSUMED (BBP, NI, KINETIC, CIRC, ELECTRON) 72
FIGURE 42: BELOW BOILING POINT: ELECTRON TEMPERATURE PROFILE AT 0.2 μS TIME INTERVALS IN AL SPACE DEBRIS USING KINETIC THEORY WHEN GAUSSIAN BEAM IS ASSUMED (BBP, AL, KINETIC, GAUSSIAN, ELECTRON) 73
FIGURE 43: BELOW BOILING POINT: ELECTRON TEMPERATURE PROFILE AT 0.2 μS TIME INTERVALS IN AL SPACE DEBRIS USING KINETIC THEORY WHEN CIRC FUNCTION BEAM IRRADIANCE PROFILE IS ASSUMED (BBP, AL, KINETIC, CIRC, ELECTRON) 73
FIGURE 44: BELOW BOILING POINT: ELECTRON TEMPERATURE PROFILE AT 0.2 μS TIME INTERVALS IN CU SPACE DEBRIS USING KINETIC THEORY WHEN GAUSSIAN BEAM IS ASSUMED (BBP, CU, KINETIC, GAUSSIAN, ELECTRON) 74
FIGURE 45: BELOW BOILING POINT: ELECTRON TEMPERATURE PROFILE AT 0.2 μS TIME INTERVALS IN CU SPACE DEBRIS USING KINETIC THEORY WHEN CIRC FUNCTION BEAM IRRADIANCE PROFILE IS ASSUMED (BBP, CU, KINETIC, CIRC, ELECTRON) 74
FIGURE 46: BELOW BOILING POINT: LATTICE TEMPERATURE PROFILE AT 0.2 μS TIME INTERVALS IN NI TARGET USING KINETIC THEORY WHEN GAUSSIAN BEAM IS ASSUMED (BBP, NI, KINETIC, GAUSSIAN, LATTICE) 76
FIGURE 47: BELOW BOILING POINT: LATTICE TEMPERATURE PROFILE AT 0.2 μS TIME INTERVALS IN NI TARGET USING KINETIC THEORY WHEN TOP HAT OR CIRC FUNCTION BEAM IRRADIANCE PROFILE IS ASSUMED (BBP, NI, KINETIC, CIRC, LATTICE) 76
FIGURE 48: BELOW BOILING POINT: LATTICE TEMPERATURE PROFILE AT 0.2 μS TIME INTERVALS IN AL TARGET USING KINETIC THEORY WHEN GAUSSIAN BEAM IS ASSUMED (BBP, AL, KINETIC, GAUSSIAN, LATTICE) 77
FIGURE 49: BELOW BOILING POINT: LATTICE TEMPERATURE PROFILE AT 0.2 μS TIME INTERVALS IN AL TARGET USING KINETIC THEORY WHEN TOP HAT OR CIRC FUNCTION BEAM IRRADIANCE PROFILE IS ASSUMED (BBP, AL, KINETIC, CIRC, LATTICE) 77
FIGURE 50: BELOW BOILING POINT: LATTICE TEMPERATURE PROFILE AT 0.2 μS TIME INTERVALS IN CU TARGET USING KINETIC THEORY WHEN GAUSSIAN BEAM IS ASSUMED (BBP, CU, KINETIC, GAUSSIAN, LATTICE) 78
FIGURE 51: BELOW BOILING POINT: LATTICE TEMPERATURE PROFILE AT 0.2 μS TIME INTERVALS IN CU TARGET USING KINETIC THEORY WHEN TOP HAT OR CIRC FUNCTION BEAM IRRADIANCE PROFILE IS ASSUMED (BBP, CU, KINETIC, CIRC, LATTICE) 78
FIGURE 52: NICKEL ELECTRON AND LATTICE SURFACE TEMPERATURES (CONTINUOUS LINES) BELOW BOILING POINT USING KINETIC THEORY. HIDDEN LINES ARE THE LASER BEAM INPUT POWER AS A FUNCTION OF TIME. 80
FIGURE 53: ALUMINIUM ELECTRON AND LATTICE SURFACE TEMPERATURES (CONTINUOUS LINES) BELOW BOILING POINT USING KINETIC THEORY. HIDDEN LINES ARE THE LASER BEAM INPUT POWER AS A FUNCTION OF TIME. 80
FIGURE 54: COPPER ELECTRON AND LATTICE SURFACE TEMPERATURES (CONTINUOUS LINES) BELOW BOILING POINT USING KINETIC THEORY. HIDDEN LINES ARE THE LASER BEAM INPUT POWER AS A FUNCTION OF TIME. 81
FIGURE 55: MOVEMENT OF AN ELECTRON INSIDE THE SPACE DEBRIS METAL FOR THE TOP HALF OF THE CONE: ELECTRONS TRANSPORT ENERGY FROM ALL METAL AREAS OF THE WRECKAGE AND PART OF THIS ENERGY IS MOVED TO THE LATTICE THROUGH COLLISIONS WITH PHONONS. THE DEBRIS MATERIAL IS MOVING TOWARDS THE ORIGIN WITH VELOCITY $\boldsymbol{vs}$ AND $\boldsymbol{x} = \boldsymbol{0}$ REPRESENTS THE FREE SURFACE 83

FIGURE 56: ABOVE BOILING POINT: ELECTRON TEMPERATURE PROFILE AT 0.2 μS TIME INTERVALS IN NI SPACE DEBRIS USING KINETIC THEORY WHEN GAUSSIAN BEAM IS ASSUMED (ABP, NI, KINETIC, GAUSSIAN, ELECTRON) 87
FIGURE 57: ABOVE BOILING POINT: ELECTRON TEMPERATURE PROFILE AT 0.2 μS TIME INTERVALS IN NI SPACE DEBRIS USING KINETIC THEORY WHEN TOP HAT OR CIRC FUNCTION BEAM IRRADIANCE PROFILE IS ASSUMED (ABP, NI, KINETIC, CIRC, ELECTRON) 87
FIGURE 58: ABOVE BOILING POINT: ELECTRON TEMPERATURE PROFILE AT 0.2 μS TIME INTERVALS IN AL SPACE DEBRIS USING KINETIC THEORY WHEN GAUSSIAN BEAM IS ASSUMED (ABP, AL, KINETIC, GAUSSIAN, ELECTRON) 88
FIGURE 59: ABOVE BOILING POINT: ELECTRON TEMPERATURE PROFILE AT 0.2 μS TIME INTERVALS IN AL SPACE DEBRIS USING KINETIC THEORY WHEN TOP HAT OR CIRC FUNCTION BEAM IRRADIANCE PROFILE IS ASSUMED (ABP, AL, KINETIC, CIRC, ELECTRON) 88
FIGURE 60: ABOVE BOILING POINT: ELECTRON TEMPERATURE PROFILE AT 0.2 μS TIME INTERVALS IN CU SPACE DEBRIS USING KINETIC THEORY WHEN GAUSSIAN BEAM IS ASSUMED (ABP, CU, KINETIC, GAUSSIAN, ELECTRON) 89
FIGURE 61: ABOVE BOILING POINT: ELECTRON TEMPERATURE PROFILE AT 0.2 μS TIME INTERVALS IN CU SPACE DEBRIS USING KINETIC THEORY WHEN TOP HAT OR CIRC FUNCTION BEAM IRRADIANCE PROFILE IS ASSUMED (ABP, CU, KINETIC, CIRC, ELECTRON) 89
FIGURE 62: ABOVE BOILING POINT: LATTICE TEMPERATURE PROFILE AT 0.2 μS TIME INTERVALS IN NI SPACE DEBRIS USING KINETIC THEORY WHEN GAUSSIAN BEAM IS ASSUMED (ABP, NI, KINETIC, GAUSSIAN, LATTICE) 90
FIGURE 63: ABOVE BOILING POINT: LATTICE TEMPERATURE PROFILE AT 0.2 μS TIME INTERVALS IN NI SPACE DEBRIS USING KINETIC THEORY WHEN TOP HAT OR CIRC FUNCTION BEAM IRRADIANCE PROFILE IS ASSUMED (ABP, NI, KINETIC, CIRC, LATTICE) 90
FIGURE 64: ABOVE BOILING POINT: ZOOMED LATTICE TEMPERATURE PROFILE AT 0.2 μS TIME INTERVALS IN NI SPACE DEBRIS USING KINETIC THEORY WHEN THE GAUSSIAN BEAM IS ASSUMED (ABP, NI, KINETIC, GAUSSIAN, LATTICE) 91
FIGURE 65: ABOVE BOILING POINT: ZOOMED LATTICE TEMPERATURE PROFILE NEAR SURFACE AT 0.2 μS TIME INTERVALS IN NI SPACE DEBRIS USING KINETIC THEORY WHEN TOP HAT OR CIRC FUNCTION BEAM IRRADIANCE PROFILE IS ASSUMED (ABP, NI, KINETIC, CIRC, LATTICE) 91
FIGURE 66: ABOVE BOILING POINT: LATTICE TEMPERATURE PROFILE AT 0.2 μS TIME INTERVALS IN AL SPACE DEBRIS USING KINETIC THEORY WHEN GAUSSIAN BEAM IS ASSUMED (ABP, AL, KINETIC, GAUSSIAN, LATTICE) 92
FIGURE 67: ABOVE BOILING POINT: LATTICE TEMPERATURE PROFILE AT 0.2 μS TIME INTERVALS IN AL SPACE DEBRIS USING KINETIC THEORY WHEN TOP HAT OR CIRC FUNCTION BEAM IRRADIANCE PROFILE IS ASSUMED (ABP, AL, KINETIC, CIRC, LATTICE) 92
FIGURE 68: ABOVE BOILING POINT: ZOOMED LATTICE TEMPERATURE PROFILE AT 0.2 μS TIME INTERVALS IN AL SPACE DEBRIS USING KINETIC THEORY WHEN GAUSSIAN BEAM IS ASSUMED (ABP, AL, KINETIC, GAUSSIAN, LATTICE) 93
FIGURE 69: ABOVE BOILING POINT: ZOOMED LATTICE TEMPERATURE PROFILE AT 0.2 μS TIME INTERVALS IN AL SPACE DEBRIS USING KINETIC THEORY WHEN TOP HAT OR CIRC FUNCTION BEAM IRRADIANCE PROFILE IS ASSUMED (ABP, AL, KINETIC, CIRC, LATTICE) 93
FIGURE 70: ABOVE BOILING POINT: LATTICE TEMPERATURE PROFILE AT 0.2 μS TIME INTERVALS IN CU SPACE DEBRIS USING KINETIC THEORY WHEN GAUSSIAN BEAM IS ASSUMED (ABP, CU, KINETIC, GAUSSIAN, LATTICE) 94
FIGURE 71: ABOVE BOILING POINT: LATTICE TEMPERATURE PROFILE AT 0.2 μS TIME INTERVALS IN CU SPACE DEBRIS USING KINETIC THEORY WHEN TOP HAT OR CIRC FUNCTION BEAM IRRADIANCE PROFILE IS ASSUMED (ABP, CU, KINETIC, CIRC, LATTICE) 94
FIGURE 72: ABOVE BOILING POINT: ZOOMED LATTICE TEMPERATURE PROFILE AT 0.2 μS TIME INTERVALS IN CU SPACE DEBRIS USING KINETIC THEORY WHEN GAUSSIAN BEAM IS ASSUMED (ABP, CU, KINETIC, GAUSSIAN, LATTICE) 95
FIGURE 73: ABOVE BOILING POINT: ZOOMED LATTICE TEMPERATURE PROFILE AT 0.2 μS TIME INTERVALS IN CU SPACE DEBRIS USING KINETIC THEORY WHEN TOP HAT OR CIRC FUNCTION BEAM IRRADIANCE PROFILE IS ASSUMED (ABP, CU, KINETIC, CIRC, LATTICE) 95
FIGURE 74: NICKEL ELECTRON AND LATTICE SURFACE TEMPERATURES (CONTINUOUS LINES) BELOW AND ABOVE BOILING POINT USING KINETIC THEORY. HIDDEN LINES ARE THE LASER BEAM INPUT POWER AS A FUNCTION OF TIME. 96
FIGURE 75: ALUMINIUM ELECTRON AND LATTICE SURFACE TEMPERATURES (CONTINUOUS LINES) BELOW AND ABOVE BOILING POINT USING KINETIC THEORY. HIDDEN LINES ARE THE LASER BEAM INPUT POWER AS A FUNCTION OF TIME. 96

FIGURE 76: COPPER ELECTRON AND LATTICE SURFACE TEMPERATURES (CONTINUOUS LINES) BELOW AND ABOVE BOILING POINT USING KINETIC THEORY. HIDDEN LINES ARE THE LASER BEAM INPUT POWER AS A FUNCTION OF TIME. 97
FIGURE 77: MOVING BORDER ISSUE (ONE-DIMENSIONAL)..... 103
FIGURE 78: ZOOMED LATTICE TEMPERATURE PROFILE AT 0.2 μS TIME INTERVALS IN NI SPACE DEBRIS USING FOURIER CONDUCTION THEORY WHEN GAUSSIAN BEAM IS ASSUMED (NI, FOURIER, GAUSSIAN, LATTICE)..... 105
FIGURE 79: ZOOMED LATTICE TEMPERATURE PROFILE AT 0.2 μS TIME INTERVALS IN AL SPACE DEBRIS USING FOURIER CONDUCTION THEORY WHEN GAUSSIAN BEAM IS ASSUMED (AL, FOURIER, GAUSSIAN, LATTICE) 106
FIGURE 80: ZOOMED LATTICE TEMPERATURE PROFILE AT 0.2 μS TIME INTERVALS IN CU SPACE DEBRIS USING FOURIER CONDUCTION THEORY WHEN GAUSSIAN BEAM IS ASSUMED (CU, FOURIER, GAUSSIAN, LATTICE)..... 106
FIGURE 81: ZOOMED LATTICE TEMPERATURE PROFILE AT 0.2 μS TIME INTERVALS IN NI SPACE DEBRIS USING FOURIER CONDUCTION THEORY WHEN TOP HAT OR CIRC FUNCTION BEAM IRRADIANCE PROFILE IS ASSUMED (NI, FOURIER, CIRC, LATTICE) 107
FIGURE 82: ZOOMED LATTICE TEMPERATURE PROFILE AT 0.2 μS TIME INTERVALS IN AL SPACE DEBRIS USING FOURIER CONDUCTION THEORY WHEN TOP HAT OR CIRC FUNCTION BEAM IRRADIANCE PROFILE IS ASSUMED (AL, FOURIER, CIRC, LATTICE) 107
FIGURE 83: ZOOMED LATTICE TEMPERATURE PROFILE AT 0.2 μS TIME INTERVALS IN CU SPACE DEBRIS USING FOURIER CONDUCTION THEORY WHEN TOP HAT OR CIRC FUNCTION BEAM IRRADIANCE PROFILE IS ASSUMED (CU, FOURIER, CIRC, LATTICE) 108
FIGURE 84: LATTICE TEMPERATURE PROFILE AT 0.2 μS TIME INTERVALS IN NI SPACE DEBRIS USING FOURIER CONDUCTION THEORY WHEN GAUSSIAN BEAM IS ASSUMED (NI, FOURIER, GAUSSIAN, LATTICE) 109
FIGURE 85: LATTICE TEMPERATURE PROFILE AT 0.2 μS TIME INTERVALS IN AL SPACE DEBRIS USING FOURIER CONDUCTION THEORY WHEN GAUSSIAN BEAM IS ASSUMED (AL, FOURIER, GAUSSIAN, LATTICE) 109
FIGURE 86: LATTICE TEMPERATURE PROFILE AT 0.2 μS TIME INTERVALS IN CU SPACE DEBRIS USING FOURIER CONDUCTION THEORY WHEN GAUSSIAN BEAM IS ASSUMED (CU, FOURIER, GAUSSIAN, LATTICE)..... 110
FIGURE 87: LATTICE TEMPERATURE PROFILE AT 0.2 μS TIME INTERVALS IN NI SPACE DEBRIS USING FOURIER CONDUCTION THEORY WHEN TOP HAT OR CIRC FUNCTION BEAM IRRADIANCE PROFILE IS ASSUMED (NI, FOURIER, CIRC, LATTICE).. 110
FIGURE 88: LATTICE TEMPERATURE PROFILE AT 0.2 μS TIME INTERVALS IN AL SPACE DEBRIS USING FOURIER CONDUCTION THEORY WHEN TOP HAT OR CIRC FUNCTION BEAM IRRADIANCE PROFILE IS ASSUMED (AL, FOURIER, CIRC, LATTICE).. 111
FIGURE 89: LATTICE TEMPERATURE PROFILE AT 0.2 μS TIME INTERVALS IN CU SPACE DEBRIS USING FOURIER CONDUCTION THEORY WHEN TOP HAT OR CIRC FUNCTION BEAM IRRADIANCE PROFILE IS ASSUMED (CU, FOURIER, CIRC, LATTICE) . 111
FIGURE 90: LATTICE TEMPERATURE PROFILE AT 0.2 μS TIME INTERVALS IN NI, AL AND CU SPACE DEBRIS USING FOURIER CONDUCTION THEORY WHEN GAUSSIAN BEAM IS ASSUMED (FOURIER, GAUSSIAN, LATTICE)..... 112
FIGURE 91: LATTICE TEMPERATURE PROFILE AT 0.2 μS TIME INTERVALS IN NI, AL AND CU SPACE DEBRIS USING FOURIER CONDUCTION THEORY WHEN TOP HAT OR CIRC FUNCTION BEAM IRRADIANCE PROFILE IS ASSUMED (FOURIER, CIRC, LATTICE) 112
FIGURE 92: CHANGE OF NI, AL AND CU SPACE DEBRIS SURFACE TEMPERATURES (CONTINUOUS LINES) USING FOURIER THEORY. POINTS LINES ARE THE LASER BEAM INPUT POWER AS A FUNCTION OF TIME. 114
FIGURE 93: NI, AL AND CU SPACE DEBRIS LATTICE TEMPERATURE PROFILES 117
FIGURE 94: PLUME OF EJECTA PRODUCED DUE TO THE INTERACTION BETWEEN LASER PULSES AND AN OBJECT 123
FIGURE 95: GROUND-BASED LASER FACILITY FOR DEBRIS REMOVAL..... 125
FIGURE 96: HOHMANN TRANSFER ORBIT FOR LAUNCHING A SATELLITE..... 127
FIGURE 97: ORBIT TRANSFER IN LEO (400 KM TO 1,000 KM INITIAL ALTITUDE), STEP SIZE IS 100 KM..... 128
FIGURE 98: ORBIT TRANSFER IN LEO (1,100 KM TO 1,700 KM INITIAL ALTITUDE), STEP SIZE IS 100 KM..... 128
FIGURE 99: ABLATION OF 0.5 KG ALUMINIUM SPACE DEBRIS VIA LASER BEAM WITH DIFFERENT ENERGY: FROM 1,000 J TO 4,000 J WITH STEP SIZE OF 500 J 132
FIGURE 100: ABLATION OF 0.5 KG CARBON SPACE DEBRIS VIA LASER BEAM WITH DIFFERENT ENERGY: FROM 1,000 J TO 4,000 J WITH STEP SIZE OF 500 J 133
FIGURE 101: ABLATION OF 0.5 KG ALUMINIUM SPACE DEBRIS VIA LASER BEAM WITH DIFFERENT ENERGY: FROM 1,000 J TO 7,000 J WITH A STEP SIZE OF 1,000 J. OVER THE PERIOD OF 7,000 LASER PULSES. 134

FIGURE 102: ABLATION OF 0.5 KG CARBON SPACE DEBRIS VIA LASER BEAM WITH DIFFERENT ENERGY: FROM 1,000 J TO 7,000 J WITH A STEP SIZE OF 1,000 J. OVER THE PERIOD OF 7,000 LASER PULSES. 135
FIGURE 103: GRAPH SHOWING THE CHANGING ALTITUDE OF THE ISS OVER THE PERIOD OF 10 YEARS, FROM NOVEMBER 1998 UNTIL JANUARY 2009, THE DISCONTINUITIES ARE WHERE THE ISS DID A RE-BOOST TO RAISE ITS ALTITUDE. 135
FIGURE 104: ABLATION OF 1 KG ALUMINIUM SPACE DEBRIS VIA LASER BEAM WITH DIFFERENT ENERGY: FROM 1,000 J TO 7,000 J WITH A STEP SIZE OF 1,000 J. OVER THE PERIOD OF 7,000 LASER PULSES. 136
FIGURE 105: ABLATION OF 1 KG CARBON SPACE DEBRIS VIA LASER BEAM WITH DIFFERENT ENERGY: FROM 1,000 J TO 7,000 J WITH A STEP SIZE OF 1,000 J. OVER THE PERIOD OF 7,000 LASER PULSES. 137
FIGURE 106: LASER INPUT VOLTAGE AGAINST THE LASER OUTPUT ENERGY. 142
FIGURE 107: CORRECTED EMISSIVE POWER RATIOS AGAINST TIME FOR NICKEL, ALUMINIUM AND COPPER SPACE DEBRIS AT 662.4 NM, 750.0 NM AND 950.0 NM CENTRAL WAVELENGTHS. 145
FIGURE 108: SUMMARISES THE NICKEL (NI) SPACE DEBRIS SURFACE TEMPERATURE PROFILE WITH RESPECT TO TIME, USING DIFFERENT METHODS AT A CENTRAL WAVELENGTH OF 662.4 NM. IT ALSO PRESENTS THE OUTPUT POWER OF THE LASER WITH RESPECT TO TIME. 151
FIGURE 109: SUMMARISES THE NICKEL (NI) SPACE DEBRIS SURFACE TEMPERATURE PROFILE WITH RESPECT TO TIME, USING DIFFERENT METHODS AT A CENTRAL WAVELENGTH OF 750.0 NM. IT ALSO PRESENTS THE OUTPUT POWER OF THE LASER WITH RESPECT TO TIME. 153
FIGURE 110: SUMMARISES THE NICKEL (NI) SPACE DEBRIS SURFACE TEMPERATURE PROFILE WITH RESPECT TO TIME, USING DIFFERENT METHODS AT A CENTRAL WAVELENGTH OF 950.0 NM. IT ALSO PRESENTS THE OUTPUT POWER OF THE LASER WITH RESPECT TO TIME. 154
FIGURE 111: SUMMARISES THE ALUMINIUM (AL) SPACE DEBRIS SURFACE TEMPERATURE PROFILE WITH RESPECT TO TIME, USING DIFFERENT METHODS AT A CENTRAL WAVELENGTH OF 662.4 NM. IT ALSO PRESENTS THE OUTPUT POWER OF THE LASER WITH RESPECT TO TIME. 155
FIGURE 112: SUMMARISES THE ALUMINIUM (AL) SPACE DEBRIS SURFACE TEMPERATURE PROFILE WITH RESPECT TO TIME, USING DIFFERENT METHODS AT A CENTRAL WAVELENGTH OF 750.0 NM. IT ALSO PRESENTS THE OUTPUT POWER OF THE LASER WITH RESPECT TO TIME. 156
FIGURE 113: SUMMARISES THE ALUMINIUM (AL) SPACE DEBRIS SURFACE TEMPERATURE PROFILE WITH RESPECT TO TIME, USING DIFFERENT METHODS AT A CENTRAL WAVELENGTH OF 950 NM. IT ALSO PRESENTS THE OUTPUT POWER OF THE LASER WITH RESPECT TO TIME. 157
FIGURE 114: SUMMARISES THE COPPER (CU) SPACE DEBRIS SURFACE TEMPERATURE PROFILE WITH RESPECT TO TIME, USING DIFFERENT METHODS AT A CENTRAL WAVELENGTH OF 662.4 NM. IT ALSO PRESENTS THE OUTPUT POWER OF THE LASER WITH RESPECT TO TIME. 159
FIGURE 115: SUMMARISES THE COPPER (CU) SPACE DEBRIS SURFACE TEMPERATURE PROFILE WITH RESPECT TO TIME, USING DIFFERENT METHODS AT A CENTRAL WAVELENGTH OF 750.0 NM. IT ALSO PRESENTS THE OUTPUT POWER OF THE LASER WITH RESPECT TO TIME. 160
FIGURE 116: SUMMARISES THE COPPER (CU) SPACE DEBRIS SURFACE TEMPERATURE PROFILE WITH RESPECT TO TIME, USING DIFFERENT METHODS AT A CENTRAL WAVELENGTH OF 950 NM. IT ALSO PRESENTS THE OUTPUT POWER OF THE LASER WITH RESPECT TO TIME. 161

List of Tables

Page Number

TABLE 1: EXAMPLE OF CURRENT AND PROPOSED SATELLITE CONSTELLATIONS 14
TABLE 2: REFLECTIVITY OF METALS AT AMBIENT TEMPERATURE 31
TABLE 3: DATA TABLE FOR NICKEL, ALUMINIUM AND COPPER SPACE DEBRIS 71
TABLE 4: PENETRATION DISTANCE COMPARISON FOR NICKEL, ALUMINIUM AND COPPER SPACE DEBRIS WHEN KINETIC THEORY OF ENERGY TRANSPORT IS USED, BELOW BOILING POINT 79
TABLE 5: TIME TO REACH BOILING POINT AND THE TEMPERATURE VARIATION OF ELECTRON AND LATTICE AT THE BOILING POINT. 82
TABLE 6: THE BOILING POINT FOR THE SELECTED THREE SPACE DEBRIS TARGETS. 97
TABLE 7: PERIODIC TABLE AND ITS $\boldsymbol{s}-$, $\boldsymbol{f}-$, $\boldsymbol{d}-$, $\boldsymbol{p}-$BLOCK 98
TABLE 8: ELECTRONIC CONFIGURATION OF NI, AL AND CU ATOMS 98
TABLE 9: PHYSICAL PROPERTIES OF THE TARGETED DEBRIS MATERIALS 105
TABLE 10: PENETRATION DISTANCE COMPARISON FOR NICKEL, ALUMINIUM AND COPPER SPACE DEBRIS WHEN FOURIER CONDUCTION THEORY IS USED 113
TABLE 11: VARIATION BETWEEN ELECTRON TEMPERATURE AND PHONON (LATTICE) TEMPERATURE AT AN ELECTRON TEMPERATURE OF 6,000 K USING KINETIC THEORY 115
TABLE 12: NI, AL AND CU SPACE DEBRIS LATTICE TEMPERATURES USING FOURIER THEORY 116
TABLE 13: SPACE DEBRIS PHYSICAL PROPERTIES 116
TABLE 14: MATERIAL PURITY OF THE SPACE DEBRIS 164
TABLE 15: TIME TAKEN FOR THE SPACE DEBRIS MATERIALS TO ACHIEVE 5,500 K 166

Nomenclature

Acronyms:

2D	Two-Dimensional
3D	Three-Dimensional
AGI	Analytical Graphics, Inc.
ABP	Above Boiling Point
BBP	Below Boiling Point
BGAN	Broadband Global Area Network
C	Carbon
CW	Continuous Wave
DMC	Disaster Monitoring Constellation
EOL	End-Of-Life
ESA	European Space Agency
GEO	Geostationary Earth Orbit
GPS	Global Positioning System
GUI	Graphical User Interface
HEO	High Earth Orbit
HPPL	High Power Pulsed Laser
ISS	International Space Station
LASER	Light Amplification by Stimulated Emission of Radiation
LEO	Low Earth Orbit
LIFE	Laser Inertial Fusion Energy
LLNL	Lawrence Livermore National Laboratory
LODR	Laser Orbital Debris Removal
MEO	Medium Earth Orbit
MHR	Millstone Hill Radar

NASA	National Aeronautics and Space Administration
NEO	Near Earth Object
NIF	National Ignition Facility
ODTK	Orbit Determination Tool Kit
PPD	Power Density Distribution
PRF	Pulse Repetition Frequency
SDIRAT	Space Debris Impact Risk Assessment Tool
SSA	Space Situational Awareness
SSN	Space Surveillance Network
STK	Systems Tool Kit
TDRSS	Tracking and Data Relay Satellite System
US	United States
USA	United States of America

Abbreviations:

Al	Aluminium
A-Train	Afternoon Train
Cu	Copper
GLONASS	GLObal NAvigation Satellite System
Nd^{3+} Glass	Neodymium in Glass
Nd^{3+} YAG	Neodymium in Yttrium Aluminium Garnet
Ni	Nickel
SaVi	Satellite Visualization
SBIRS	Space Based InfraRed Systems
S2ANSat	SSA Nano Satellite
TEM	Transverse ElectroMagnetic Modes
TNT	TriNitroToluene

Constants:

$k_B = Boltzmann\ constant = 1.38064852 \times 10^{-23}\ \left[\frac{J}{K}\right]$

$\sigma = Stefan\ Boltzmann\ constant = 5.670367 \times 10^{-8}\ \left[\frac{W}{m^2K^4}\right]$

$h = Planck\ constant = 6.626070040 \times 10^{-34}\ [J.s]$

$c_0 = Speed\ of\ light\ in\ the\ medium = 299792458\ \left[\frac{m}{s}\right]$

$m = Mass\ of\ electrons = 9.10938356 \times 10^{-31}\ [kg]$

$N_0 = Avogadro's\ number = 6.022140857 \times 10^{26}\ \left[\frac{kg}{mole}\right]$

e = Electronic charge =Eementary electric charge = Electric charge carried by a single proton = Magnitude of the electric charge carried by a single electron= $1.6021766208 \times 10^{-19}$ [C]

Mathematical Terms:

Chapter 2

z	Axial distance from the laser beam waist or focus (narrowest point of the beam) = Distance along the beam from the beam waist
$w(z)$	Gaussian beam width or spot (focus) size at z = Variation of the spot size for the beam of wavelength λ at distance z along the beam from the beam waist = Radius at which field amplitude fall to $1/e$ of its axial value, at the plane z along the laser beam = Radius at which field intensity decreases from its centric value by a factor of e^2 or drops to $1/e^2$ of its axial value
$w_0 = w(0)$	Laser beam waist size (radius)
$z_R = z_0$	Rayleigh range (length)
λ	Wavelength
$b = 2z_R$	Confocal parameter or depth of focus of the beam
Θ	Total angular spread of the beam far from the waist ($z \gg z_R$). To keep the laser beam very well collimated, it must have a large

	diameter because a Gaussian beam that is focused to a small spot spreads out rapidly as it propagates away from the spot and thus Θ is inversely proportional to the spot size at the waist w_0
θ	Divergence of the beam = Angle between the straight line when $(r = w(z)\ for\ z \gg z_R)$ and the central axis of the beam when $(r = 0)$
$r = w(z)\ at\ z \gg z_R$	Radial distance from the laser beam centre axis
$I_0 = I_{(0,0)} = I_{max}$	Intensity at the laser beam centre at its waist
k	Thermal conductivity $\left[\frac{W}{m.K}\right]$
ρ	Density of the space debris $\left[\frac{kg}{m^3}\right]$
c_p	Specific heat capacity $\left[\frac{J}{kg.K}\right]$
ρc_p	Considered as volumetric heat capacity $\left[\frac{J}{m^3.K}\right]$

Chapter 3

P	Power of the laser [W]
d	Diameter of the PDD [m]
x and y	Coordinates on the x, y plane

Chapter 4

N'	Participating electrons number density, those at Fermi surface $\left[\frac{1}{m^3}\right]$
z	Electron collision frequency in dV $[Hz]$
v_1	Fermi electron velocity $\left[\frac{m}{s}\right]$
l	Electron mean free path for collisions with phonons $[m]$
$I(x,t)$	Power intensity at position x and time t $\left[\frac{W}{m^2}\right]$

$I_0(t)$	Radiation intensity at the target surface when x is zero (i.e. power intensity incident on the target surface) $\left[\frac{W}{m^2}\right]$
$R(t)$	Reflection coefficient (i.e. reflectivity at the metal free surface)
δ	Absorption coefficient $\left[\frac{1}{m}\right]$
Δt	Average time interval an electron stays in dp element
$E(x, t+dt)$	Energy of electron $[J]$
$E_p(x,t)$	Average energy of phonon (lattice) in dV at x $[J]$
f	Fraction of the excess electron energy that is moved to a phonon due to the collision with that electron
N	Number density of valence electrons $\left[\frac{1}{m^3}\right]$
T_e	Temperature of Kinetic electron $[K]$
T_F	Temperature of Fermi electron $[K]$
ρ	Density of the space debris material (assumed to be temperature independent)
C_p	Specific heat of target material $\left[\frac{J}{kg.K}\right]$ (assumed to be temperature independent)
n	Phonon (atoms) number density $\left[\frac{1}{m^3}\right] \rightarrow \rho C_p$
$E_p(x,t) \rightarrow T(x,t)$	Temperature of phonon
$E(\epsilon, t) \rightarrow T_e(\epsilon, t)$	Temperature of Kinetic electron $[K]$
$E_p(x,t) \rightarrow T(x,t)$	Temperature of phonon (lattice) $[K]$
$T_e(0,x) = T(0,x)$	Room temperature, which is the initial temperature of photons (lattice) and electrons $= T_0$ $[K]$
$T_e(t,\infty) = T(t,\infty)$	Room temperature $= T_0$ $[K]$

T_{ej}	The x-axis
w_j	The weights along with these points
n	Number of atoms per unit volume at the surface = Density of atoms (phonon) number $\left[\frac{1}{m^3}\right]$
U_0	The energy needed to fully remove 1-atom from the target material = The vaporisation latent heat per atom $[J]$
T	Temperature of phonon (lattice) $[K]$
m	Atom mass $[kg]$
T_s	Lattice temperature of the surface $[K]$
$v_s = G$	Evaporation velocity of space debris surface $\left[\frac{m}{s}\right]$
L_0	Vaporisation normal specific latent heat
T_c	Critical temperature of the metal $[K]$

Chapter 5

x	Depth of light penetration
l	Electron-phonon mean free path
I_0	Incident intensity
$T(\infty, t) = T_0$	Normal specific latent heat of vaporisation
$T(0, s) = T_0$	Normal specific latent heat of vaporisation
L	Specific latent heat of vaporisation
c_m	Coupling coefficient
E_d	Delivered energy

Chapter 7

P	Instantaneous laser output power

$P(t)$	Output power of the laser beam
$I(t)$	Intensity of the laser beam
ω	Radius of the laser dot
$R_{Detected}$	Detected emissive power ratio
T	Termperature of the surface [K]
W_{B_1}	Blackbody emissive power ratios across bandwidth $a_1 b_1$
W_{B_2}	Blackbody emissive power ratios across bandwidth $a_2 b_2$
$W_{B\lambda}$	Monochromatic emissive power at wavelength λ
λ	Wavelength of radiation [m]
a	Defined by the $1/e$ points
x	Beam radius
x_0	Radius of fibre optic
λ_c	Central wavelength = Wavelength of emitted light detected at the monochromator exit slit centre
M	Mass of molecule (lattice atom) = Mass of atom
Ω	Average kinetic energy of molecules (lattice atoms)
W	Average kinetic energy of electrons
$\mathrm{T}(x,t)$	Temperature of lattice atoms at distance x and time t
$\mathrm{T}_e(x,t)$	Temperature of electron at distance x and time t
$E_F(0)$	Maximum electron kinetic energy at absolute temperature ($T = 0\ K$) = E_F = Fermi Energy
M_W	Molecular weight of metal
ρ	Density of metal

τ	Time of mean collision
γ	Electrical conductivity
K	Material thermal conductivity
C_p	Material specific heat
ρ	Material density

Acknowledgements

Firstly and foremost, I wish to thank my supervisors. Thank you to Professor Chris Chatwin and Dr Rupert Young for being my main advisors. They have been supportive all the time ever since I joined the department and started working on this project as a researcher. They have assisted me not only by giving an educational research assistant but also emotionally over the tough time to conclude this thesis. Prof Chris supported me to come up with the research subject and guided me through all these years. Chris and Rupert gave me the good assistance and the freedom I required to progress over the tough periods of my project and when I was writing up this thesis.

This thesis reflects not only my work on the keyboard, but it also reflects a great milestone for about half-decade of research and works in the Department of Engineering and Design at the University of Sussex. The whole experience at Sussex has been nothing short of wonderful. I have felt at home at Sussex since my earliest days, and over these years, I have acquired skills in cutting-edge research.

I participated in numerous activities outside the University of Sussex where I met and worked with wonderful professional people from around the world. I have been granted distinct opportunities in participating in outstanding programs such as the Space Studies Program (SSP) and taken unique and lifetime experiences from them as well as learned through hands-on workshops in how to do new things and most importantly the professionalism needed in creating them. I especially have to thank everyone I met at the International Space University (ISU), NASA (in particular NASA Glenn Research Center) and the Space Generation Advisory Council (SGAC) who have worked with me or educated me on how to complete things perfectly and inspired me in many ways. I am also very thankful for the opportunities to talk with Dr Claude R. Phipps (from Photonic Associates, LLC), Professor Philip Lubin (from University of California, Santa Barbara) and James D. Burke (The Planetary Society). Talks to these people pushed my thought limits and boosted my research topic value.

I finish with my family and friends, where the origins of my life energy reside. I have a wonderful family and friends, unique in numerous ways. Special thanks go to them as an amazing source of help. The assistance from my family has been unconditional and necessary in each step all these years. I wish to express my thanks to all of them.

Dedication

This thesis is dedicated to the ever-loving memory of my father, Adnan Alhadad (deceased) who did not live to see the fruit of his work. He was a great professional and a great person. He taught me the value of good administration and how to write and do math before my teachers did. This thesis is not complete as it lacks the benefit of his comments, insights and criticisms. It is dedicated to my mother Firdows who highly values the importance of education for the success of a person. She taught me the value of hard work. To my brother Baraa who took the fatherly role perfectly after my father's death and provided me with education and knowledge, and to my lovely sisters, Suhair and Nora.

I also dedicate this thesis and give special thanks to my wife Ragad for being there for me throughout my entire PhD program and to my marvellous children: Mustafa, Sarah and Sama. They have given up many things for me to complete this thesis and supported me whenever I needed.

Declaration

I hereby declare that this thesis has not been and will not be, submitted in whole or in part to another University for the award of any other degree.

Signature: .....

Publications

Papers:

Hussein, Alaa, Silva-Martinez, Jackelynne and Wilson, Thomas (2018). "*From Project Management to Planetary Defense: Implementation of a Systems Engineering Approach Using Integrated Product and Process Development (IPPD)*," in *IEEE Aerospace & Electronics Systems Magazine*, ISSN: 0018-9251. https://doi.org/10.1109/MAES.2018.160212

Al-Mayyahi, Auday, Wang, Weiji, Birch, Philip, **Hussein, Alaa** (2018). *Obstacle Detection System Based on Colour Segmentation Using Monocular Vision for an Unmanned Ground Vehicle*. International Journal of Computational Vision and Robotics, ISSN: 1752-9131. http://dx.doi.org/10.1504/IJCVR.2018.093072

Al-Mayyahi, Auday, Wang, Weiji, **Hussien, Alaa**, Birch, Philip (2017). *Motion Control Design for Unmanned Ground Vehicle in Dynamic Environment Using Intelligent Controller*. International Journal of Intelligent Computing and Cybernetics, ISSN: 1756-378X. https://doi.org/10.1108/IJICC-11-2016-0044

Jackelynne P. Silva-Martinez, **Alaa Hussein**, and Thomas Wilson (2016). "*Modelling IPPD for an Interdisciplinary Planetary Defense Project*", AIAA SPACE 2016, AIAA SPACE Forum, (AIAA 2016-5560). eISBN: 978-1-62410-427-5. https://doi.org/10.2514/6.2016-5560

Alaa Hussein, Oshri Rozenheck, Carlos Manuel Entrena Utrilla (2016), *From detection to deflection: Mitigation techniques for hidden global threats of natural space objects with short warning time*, Acta Astronautica, Volume 126, September–October 2016, Pages 488-496, ISSN 0094-5765. https://doi.org/10.1016/j.actaastro.2016.06.013

Silva-Martinez, J., **Hussein, A**. and Wilson, T. (2016), *Implementation of a Systems Engineering Approach to the Management of a Planetary Defense Team Project in an Intensive Space Studies Program Using IPPD*. INCOSE International Symposium, John Wiley & Sons, Ltd, Volume 26, July 2016, Pages 614–629, ISSN 2334-5837. https://doi.org/10.1002/j.2334-5837.2016.00182.x

P. Nambiar, Shrrirup, **Hussein, Alaa**, Silva-Martinez, Jackelynne, Reinert, Jessica and Gonzalez, Fernando (2016) *Architecture for Mitigating Short-Term Warning Cosmic Threats: READI Project*, IEEE, ISBN: 978-1-4673-7676-1. https://doi.org/10.1109/AERO.2016.7500925

Rozenheck, Oshri, Entrena Utrilla, Carlos M. and **Hussein, Alaa** (2016) *Detection and Deflection Techniques for Short-Time Warning PHOs: ISU Planetary Defense Project*. In: 56th Annual Conference on Aerospace Sciences (ACAS), 9-10 March 2016.

Gourdon, Remi, **Hussein, Alaa**, Soni, Anushree, Aliaj, Bora, Manuel Entrena Utrilla, Carlos, Sisaid, Idriss, Reinert, Jessica, Faull, Jonathan, Bettiol, Laura, Schmidt, Nikola, Nambiar, Shrrirup, Dimitrov, Tihomir and Thangavelu, Madhu (2015) *The International Space University Space Studies Program 2015 Planetary Defense Project*. In: 66th International Astronautical Congress 2015 (IAC 2015) "Space - The Gateway for Mankind's Future", 12-16 Oct 2015.

Conference Posters:

Burke, Jim, **Hussein, Alaa**, Soni, Anushree, Thangavelu, Madhu, Schmidt, Nikola and Wilson, Thomas (2015) *Planetary Defence: A Duty for World Defenders*. In: American Geophysical Union (AGU) Fall Meeting, 14-18 Dec 2015, San Francisco, USA.

Emanuele Chiuri, Daniele, Turconi, Andrea, **Hussein, Alaa**, Nader, Nourhane, Raval, Siddharth, Emanuelli, Matteo and Nasseri, Seyed Ali (2015) *Active Debris Removal: Overview and Figures of Merit of Debris Grabbing Strategies*. In: 66th International Astronautical Congress 2015 (IAC 2015) "Space - The Gateway for Mankind's Future", 12-16 Oct 2015.

Hussein, Alaa, Chatwin, Chris, Young, Rupert and Birch, Philip (2014) *LEO Space Debris Mitigation Using Laser Ablation*. In: 65th International Astronautical Congress 2014 (IAC 2014) "Our World Needs Space", 29 Sep - 03 Oct 2014, Toronto, Canada.

Hussein, Alaa, Chatwin, Chris, Young, Rupert and Birch, Philip (2014) *Mitigating Orbital Debris in LEO with High Power Pulsed Laser*. In: 65th International Astronautical Congress 2014 (IAC 2014) "Our World Needs Space", 29 Sep - 03 Oct 2014, Toronto, Canada.

Nasseri, S. Ali, Borriello, Ciro, **Hussein, Alaa** and Kebe, Fatoumata (2014) *Active Debris Removal Mapping Project*. In: 65th International Astronautical Congress 2014 (IAC 2014) "Our World Needs Space", 29 Sep - 03 Oct 2014, Toronto, Canada.

Hussein, Alaa, Chatwin, Chris and Young, Rupert (2013) *Mitigating Space Debris in Low Earth Orbit Using High Power Pulsed Lasers*. In: Postgraduate Poster Presentation Event, 26 Jun 2013, University of Sussex, Brighton, United Kingdom.

Technical Reports:

Hussein, Alaa, Soni, Anushree, Aliaj, Bora, Entrena, Carlos, Lee, Chanwoo, Shterman, Doron, Gonzalez, Fernando, Byrne, Hugh, Sisaid, Idriss, Silva, Jackelynne, McCreight, James, Reinert, Jessica, Faull, Jonathan, Hoving, Lars, Bettiol, Laura, Neophytou, Louis, Girard, Marianne, Glauber, Naama, Strzalkowski, Nicholas, Schmidt, Nikola, Rozenheck, Oshri, Stratton, Parker, Gourdon, Remi, Meeran, Shajiha, Ouyang, Shangrong, Ji, Shitao, Call, Toby, Peters, Susanne, Dimitrov, Tihomir, Nambiar, Shrrirup, Parikh, Umang, Yang, Yunjun, Jia, Yuxian and Fang, Zheng (2015) *Planetary Defense Team Project: READI (Roadmap for EArth Defense Initiatives)*. Project Report. International Space University (ISU), Ohio, USA.

Hacker, Jacob, Losekamm, Martin, Sardesai, Nikita, Johnson, Christopher, Bell, Robert, Rey, Daniel, Vigneron, Adam, Bettiol, Laura, Brack, Daniel, Braegen, Emma, Calder-Potts, George, Chatterjee, Joyeeta, Coderre, Kathleen, Côtè Bigras, Roxanne, Driedger, Matthew, Egen, Caitlin, Froeliger, Emilie, Gorur, Eren, Hankins, Weston, **Hussein, Alaa**, Jang, Ilji, Noyes, Matthew, Roberts, Lyle, Sarli, Bruno, Sinn, Thomas, Wen, Anne and Wille, Eric (2014) *On-Orbit Servicing Commercial Opportunities with Security Implications*. Project Report. Space Generation Advisory Council (SGAC), Toronto, Canada.

Chapter 1

Background and Introduction

1 Background and Introduction

1.1 Summary

This chapter provides a literature review of the space environment, space situational awareness and focuses on space debris and their population in popular Earth orbits. The chapter also studies the properties of orbital debris in low Earth orbit and identifies the research gap. References to some previous work on detection and tracking of artificial objects in the Earth orbits are also presented.

1.1 The Space Environment

Human-made satellites have evolved significantly since the launch of the first satellite. They are used in a vast range of interesting applications from satellite navigation and weather forecasting to commercial civil telecommunications services and remote sensing. Some satellite services, like navigation, require a group of satellites that are launched, synchronised and coordinated to accomplish a common purpose or service because a single satellite can only cover a small part of the Earth's surface. Such a group is called a satellite constellation. The term satellite constellation can be described as a group of similar artificial satellites that are synchronised to orbit the Earth in some optimal way and work together in concert under shared control and are synchronised so that the satellites overlap well in coverage and complement rather than interfere with other satellites' important coverage. Satellite constellations have also evolved significantly because they are the only way to achieve coordinated global coverage; they have been used mostly for navigation and telecommunication services. Popular examples of satellite constellations include the global positioning system (GPS), Glonass and Iridium. A good design example is the Walker Constellation [1] with reference to the author of this method, which is one of the popular types or method to achieve global coverage using satellites. It is imperative to design the constellation accurately before launching any of its satellites into orbit, around the Earth, to avoid any collisions. Nowadays, satellite constellations enable key technologies such as disaster monitoring, global positioning, telecommunications, remote sensing, voice networking and satellite radio. A correctly designed satellite constellation system can provide continuous global coverage, allowing any part of the Earth to be seen by at least one satellite at any given time. Satellite constellation services and applications are always in high demand, so there is no doubt that avoiding any collision or impact with non-

operational space systems or even space debris is of keen interest to all satellite operators for present and future generations. Such events can disable or perhaps destroy an operational system and interrupt its services. Obviously launching a satellite is no small matter, it is a big field in itself. It can cost multi-millions to billions of pounds to develop a satellite, construct it and place it into orbit. Avoiding collision events can be achieved by applying appropriate methods and techniques in addition to a holistic assessment of the space environment including a complete catalogue of all objects in orbit: operational, non-operational and debris. New space systems differ from those of their predecessors of several decades ago. Analysis of an optimum design strategy must also be performed, which of course adds challenges to the design of space systems. However, with the development and introduction of new key technologies in the design of space systems, it is possible to protect the main systems from sub-centimetre size debris. Other development includes reducing the fuel usage and hence increasing the lifetime of satellites in space. However, some fuel usage due to manoeuvring tasks is unavoidable. For instance, missions that include reconfiguration of satellite constellations. Such a reconfiguration mission is defined as a deliberate change of the relative arrangements of satellites in a constellation by orbital manoeuvring and adding or removing satellites to achieve the desired changes [2,3]. The reconfiguration of the satellite constellation is necessary to either increase the performance, capacity or coverage of the constellation or to transfer the constellation, after its initial deployment, with low capacity into a new constellation with higher capacity. Those instances require launching one or more additional satellite, which means completing prelaunch testing to make sure it is ready for launch and then launching the satellite [4]. When satellites need to be added in stages, the on-orbit satellites are then reconfigured to form a new satellite constellation with the additional satellites incorporated. In other words, the on-orbit satellites are transferred from their initial orbit into a new trajectory, usually lower in altitude. The deployment of the Iridium constellation that consists of 72 LEO satellites is a good example of satellite constellation deployment. It was deployed in a staged manner within just one year between May 1997 and May 1998 by three countries, which are the USA, China and Russia. The US Delta II launcher with a length of 8.5 m and a diameter of 2.9 m has a payload accommodation of 56 m^3 carried five satellites per launch [5], the Chinese Long March carried only two satellites per launch whereas the Russian Proton has accommodation of 206 m^3. It had a length of 15.6 m and diameter of 4.1 m and carried seven satellites per launch. However, due to the high cost

of satellite manufacturing, it is hazardous to launch too many satellites in one launch vehicle due to the risk of collision with space debris. This risk of collision developed due to the fact that after just a few decades of space exploration, there are now millions of pieces of human-made space debris in Earth orbit, which need to be limited to protect operational space systems. The fragmentation in Earth orbits and the major collision events between large spacecraft systems in addition to the poor housekeeping in space for more than five decades has generated millions of pieces of orbital debris above the Earth, Figure 1.

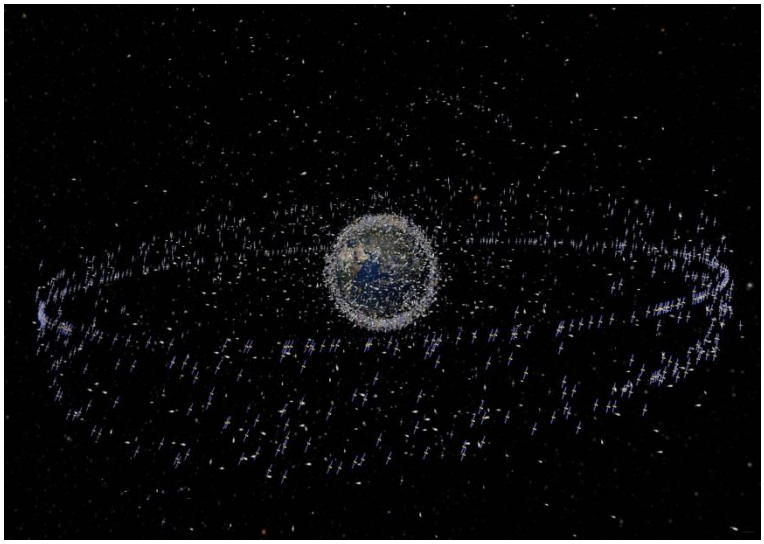

Figure 1: Space debris at different altitudes in Earth orbits

This massive space wreckage was produced mainly by collisions between hypervelocity objects in space. As the problem of spacecraft flights safety is rather urgent, the growing space debris problem has now become one of the most important space situational issues. That is mainly due to the massive number of junk items in space. Therefore, a detailed study of the short-term as well as the long-term evolution of the space debris cloud is required. In fact, due to the hypervelocity and the massive number of debris in space, the problem of space debris requires significant mitigating measures to protect our assets in space.

1.2 Space Surveillance Network (SSN)

Since the first spacecraft was put into space, scientists and engineers have been pondering ways in which they can remove satellites, after their end-of-life (EOL), from Earth orbits. Many people believe that the space surveillance is not really important, but in fact, the space situational awareness (SSA) in relation to space surveillance is an

important area of study, especially for the detection and monitoring of space objects. Others believe that the mitigation of orbital debris is a vital area of research that needs more attention for a better and sustainable use of Earth orbits in particular and space in general. The literature on space debris mitigation has described and discussed the difficulty and complexity of providing free access to space. Space is becoming increasingly congested with artificial space objects especially in low Earth orbit (LEO) and geostationary Earth orbit (GEO). In fact, space becomes an economic centre, and the space environment becomes one of the most dynamic areas in the space industry. Perhaps it is time to think more seriously about the space environment, and therefore, the goal of this project is to study in detail one of the proposed techniques to mitigate orbital debris in LEO and to increase the space situational awareness.

Investigating the effects of objects in the Earth orbits on the operational space systems including collision avoidance and debris mitigation measures is crucial for most space agencies. Currently, the research community focuses on issues related to SSA. Many of these problems arise due to the high number of satellites launched in orbits around the Earth, which eventually increases the number of space debris and space junk in the Earth orbits. That is why a major consideration in designing any satellite constellation is to provide the specified coverage area with the fewest number of satellites.

In order to perform a space objects observation, some obvious obstacles need to overcome such as the orbiting object must be in sunlight and the minimum elevation angle needs to be met. Therefore, more research needs to be conducted into looking at designing and describing concepts and ideas of an observation and tracking system to be used for the detection of faint objects and small space debris.

Orbital debris detection and tracking have been extensively studied over the past few decades as satellites operators principally demand these studies. There are a couple of software tools that have been used in industry to build trajectory prediction models of objects in space and provide a comprehensive analysis and simulation for early warning of potential collisions. Good examples of such software tools include systems tool kit (STK) and orbit determination tool kit (ODTK), which are both developed by Analytical Graphics, Inc. (AGI). MATLAB & Simulink software platforms, which are developed by The MathWorks, Inc. can also be used for orbital modelling. These computer software programmes are useful tools to create, design and display the

trajectory of space objects easily from user input parameters through a graphical user interface (GUI). These software tools are very useful in modelling the interaction of satellites with the space environment and small debris. Space debris impact risk assessment tool (SDIRAT) is a software code that is specifically developed for orbital debris density, relative velocity and directional flux estimation on a target satellite. This software has been used by Pardini [6] to obtain snapshots of the evolving object distribution during the considered time span, together with an estimation of the changing collision probability with a satellite of the operational navigation systems in medium Earth orbit (MEO). Traditional satellite constellation design has focused on achieving global or zonal coverage while minimising the necessary number of satellites in the constellation, which is the main goal for most satellite constellation designers. The satellite visualization (SaVi) tool, which was developed by Worfolk at the Geometry Center at the University of Minnesota and maintained by Wood at the University of Surrey is an another straightforward and useful software tool for designing the trajectory of a satellite constellation [7].

The space surveillance network (SSN) can be implemented by using satellites with capable radars and a network of electro-optical sensors that help to build up a catalogue containing the space objects. The large angular velocity of objects in space is one of the biggest challenges in optical observations of objects in Earth orbits, especially in LEO. Thus, the exposure times must be very short, and the telescope aperture needs to be large enough to detect objects. In fact, large telescopes are required for observation and tracking since small objects also need to be observed [8]. The Haystack 37 m radar is a good example of the space surveillance mechanical tracker. It is capable of imaging near-Earth and deep space objects [9]. It conducts measurements of orbital debris to sizes of 1 cm. Another example is the Millstone Hill Radar (MHR), which is a high power sensitive radar that routinely tracks debris, rocket bodies and satellites in the geostationary belt. It produces highly accurate orbital data, due to its high precision. Chilbolton Observatory has a high-power fully steerable radar with 25 m diameter dish antenna, see Figure 2, that has been used to carry out radar observations on intact satellites under the ESA's SSA Preparatory Programme [10]. Future satellite constellation could be used to observe and monitor space junk in LEO to deliver space surveillance capability and protect operational space missions. We believe that a cohesive methodology for developing a capacity for detection and tracking of space

objects in the upper part of the LEOs region and the near-GEO regime is needed if we are looking for a sustainable free access to space. This is demanding especially with an ability to detect a substantial number of small debris as small as 1 cm up to 100 cm, to build-up and maintain satellite catalogues.

Figure 2: Chilbolton 25 m radar

The next generation of radars and telescopes will allow us to track moving targets in uncrowded areas from space-based radar satellites. This can be achieved by using a constellation of satellites in LEO. One of the major considerations in such a system is the number and the size of individual satellites in the constellation because it determines the overall constellation capacity. In general, coordinating smaller satellites has some benefits over a single satellite, including simpler designs, cheaper to launch, faster build times, cheaper replacement in addition to the constellation ability to search targets at multiple times or from multiple angles. Kayal [11] proposed a satellite constellation for the detection of orbital objects in space. He has briefly described his proposal and focused on using lightweight and low-cost nanosatellites for the detection of space objects in orbit. However, large satellites have other benefits such as generating more onboard power from its solar panels, higher bandwidth, higher bit rate, longer lifetime (15 years in average), carry large telescopes with high viewing resolution. Having said that, the bigger the satellite dry mass, the more the onboard fuel mass is needed to perform manoeuvres.

1.3 Space Situational Awareness (SSA)

Space situational awareness is a comprehensive knowledge of the population of space objects and the existing threats and risks in the space environment. Space situational

awareness contains many different aspects including observation from Earth and space, data archiving, processing, data policy, dissemination, control centre, et cetera. SSA is a big field of research although very little is known publicly about it. There is significant ongoing research concentrating on SSA at some universities and space agencies, like the national aeronautics and space administration (NASA) and the European space agency (ESA). To understand the status of the space environment and analyse its current situation in relation to space debris, some important matters and questions need to be addressed here. These questions include first what is space debris? How much is out there? Where does it come from? How common are collisions in orbit? What has been the effect of the crash? In this section, we have attempted to answer these questions based on the current literature review. NASA defined space debris "duh BREE" as junk that is orbiting the Earth [12]. It emanates from space systems that humans have been launching into space over the last 60 years. Many of these objects have returned to the Earth, but the returning rate is low, about an object per day. The returning objects either burn up in the atmosphere or land on Earth with impact, usually in water as water makes up 70% of the surface of the Earth. The current observation shows that a significant number of the objects sent into space are still in orbit around Earth. There are millions of debris orbiting the Earth at speeds up to 25,000 mph. That is a huge number even though most new space missions are now designed to eliminate the release of launch vehicles, rocket bodies and stages, apogee kick motors, propulsion units, sensor covers, and so forth. Tens of thousands of them are at least 10 cm in size, hundreds of thousands are between 1-10 cm, and tens of millions are smaller than that. In fact, there are no fixed rules for space debris to establish whether an object can be numbered. There are many different types of debris in the space such as derelict propulsion stages or smaller debris, abandoned spacecraft, mission-related debris, intact spacecraft, non-functional satellites or defunct satellites, fragmentation debris, catastrophic fragmentation, bolts and nuts and even flecks of paint, to name only some of them. These kinds of debris are human-made. In 2007, the International Space Station (ISS) crew jettisoned a tank of fridge-size [13]. It was part of the spacecraft cooling system and contained ammonia.

So far, there have been few observed collisions between objects in space; some were considered minor collisions because they involved parts of spent rockets or small satellites. Space junk is considered as one of the biggest threats to satellites and space

shuttles because the high density of derelict objects in space might give rise to future collisions; which would rain debris in some orbits of the Earth. That is expected as the number of objects in space is always increasing especially in LEO and even in high-altitude orbits like GEO. Figure 3 and Figure 4 show that the number of GEO satellites continues to grow at the rate of 12 satellites, on average, per year [14].

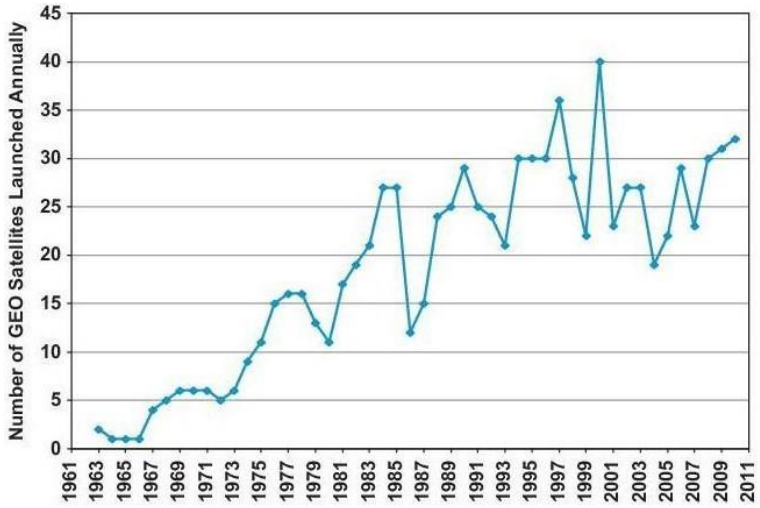

Figure 3: Number of satellites placed in GEO per annum (26 satellite on average)

Usually, operational spacecraft can perform avoidance manoeuvres if the projectile is large enough to be tracked from the ground. However, if a fragmentation would ever happen in the orbits of the navigation satellite constellation, for example, the resulting cloud of debris would be very difficult to track by the ground sensors due to the considerable distance and would, therefore, represent a serious hazard for all the satellites in the region. Also, a potential problem, which is even more dangerous can arise from the accumulation of non-operational spent satellites unable to perform avoidance manoeuvres or to move to the graveyard zones, away from operational satellites. Cloud-based computing architecture can be used for SSA and planetary defence, Steven Johnston and his team demonstrated this as a case study at the University of Southampton by showing how utility computer and Microsoft Windows Azure can facilitate both a financially economical and highly scalable solution for space debris and near-earth object impact analysis [15].

Another question that needs to be answered is: can this significant amount of space objects including satellites pose a risk of collision? Earl [16] responded to this question, and he pointed out that before Tuesday 10 February 2009 the answer was “Yes, but an

extremely slim chance". However, the answer has been changed since then to "Yes, and unfortunately a major collision has already happened".

That is because the problem became more evident and severe after 10 February 2009 when a major first-ever accidental collision occurred between the intact Iridium-33 commercial satellite and the Russian Cosmos-2251 satellite, which was launched in 1993 and believed to be non-functioning. This incident was the first high-speed impact between two intact satellites. However, NASA expects more such events [17]. This event created more than 2204 tracked fragments, which increased the trackable space debris population by 16%. The US SSN has detected the resulting two massive debris clouds after the satellites collided nearly 500 miles over Siberia. Even worse, the major contribution to the orbital debris population came from a Chinese anti-satellite test targeting the Feng Yun-1C weather satellite on 11 January 2007 [18]. This event created more than 3383 tracked fragments, which increased the trackable space object population by 25%.

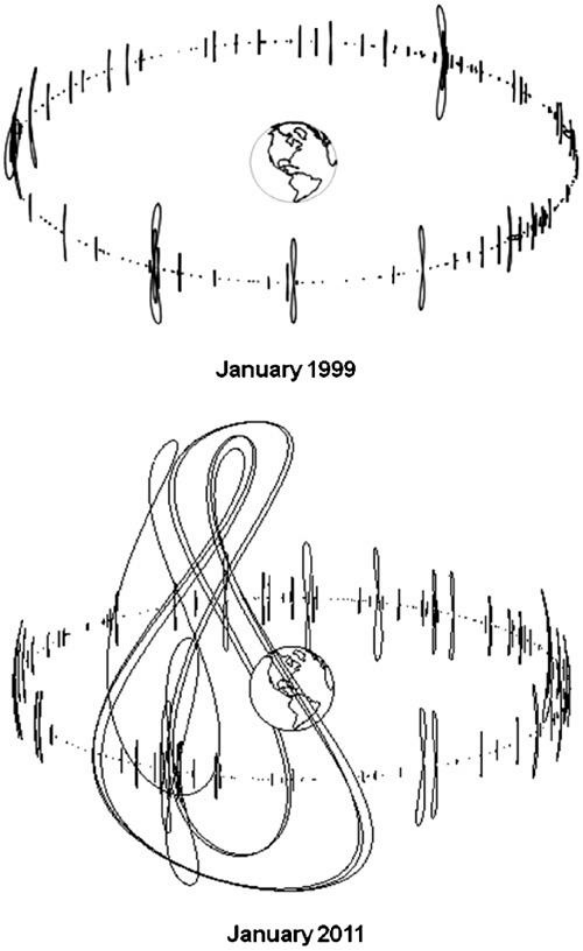

Figure 4: The complexity of GEO orbits for operational satellite dramatically increased over just 12 years window (1999-2011)

Early warning radar measurements have detected hundreds of objects of space debris. Such debris in space, in addition to any other non-operational items, are recognised internationally as a hazard to current and future space activities. Currently assumed that the maximum number of the space debris that can be generated coincides with the most significant collision events between large satellites. Just over a decade ago, the probability of an impact event between an operational spacecraft and a space debris was almost neglected but after few significant collision events, the situation has changed. Aside from the numerous minor collision events, each major collision event has added many swarms of orbital debris in different directions. These orbital junk are actually considered as a threat against all operational space systems. Mainly, that is because the space surrounding the Earth is densely populated by an increasing number of human-made space debris most of which has been generated from the break-up of operational satellites or abandoned spacecraft systems. As of May 2013, all human-made space objects are generated from the 4935 successful launches that have been made since the start of the space age in 1957. That led to 3690 satellites, 1908 orbital stages, 1155 mission-related objects and 10160 breakups and released debris (larger than 10 cm in size) in the US SSN Catalogue. The total current mass in orbit is on the order of 7 thousand tonnes, some of it in controlled missions and most of it in uncontrolled missions. Pardini [19] pointed out that the first step in the responsible and long-term sustainable use of space is the adoption of measures aimed at reducing the generation of orbital debris through the combined actions associated with the design, manufacture, operation and disposal phases of a mission. In the same field, Johnson [20] studied the new look of the GEO and near-GEO regimes; he pointed out that more than 300 satellites have been manoeuvred into disposal orbits at mission termination to reduce the collision risk and relieve unnecessary congestion in the limited GEO region.

On the other hand, studies in this field proved that more than a thousand spacecraft and launch vehicle upper stages have entered into the vicinity of the geosynchronous regime during the past half-century. Therefore, the stability issue is important in the definition of possible disposal strategies for any space mission, after their EOL. In general, there are two possible disposal strategies, which involve either stable or unstable orbits. The security of space assets from in-orbit collisions and space protection must evolve from a routine space program to a very robust and dynamic SSA architecture with protection measures. Therefore, the purpose of this research project is to describe the use of a

novel possible solution to mitigate the problem of space debris using a contactless deflection tool.

A methodology for mitigating space debris is thus presented in this thesis, it will be useful as a foundation for future works in this field, and it will help to move from the space research community into the industry, which is a demanding requirement. Regardless of the hardware techniques required to achieve this, the gains would be invaluable. Such a subject might be fascinating to consider after completing and designing a powerful laser system to aid the mitigation process.

1.4 Satellite Orbits

When a satellite is in orbit, there is only one major force acting on it, this force is the gravitational force exerted by the Earth on the satellite, and this force is constantly pulling the satellite to the centre of the Earth. However, the satellite does not fall straight down to the Earth because of its high velocity. Throughout the orbit of a satellite, there is a perfect balance between the Earth gravitational force, and the centrifugal force necessary to maintain the satellite orbit [21]. The orbit altitudes for current and some proposed satellite constellations are shown in Figure 5.

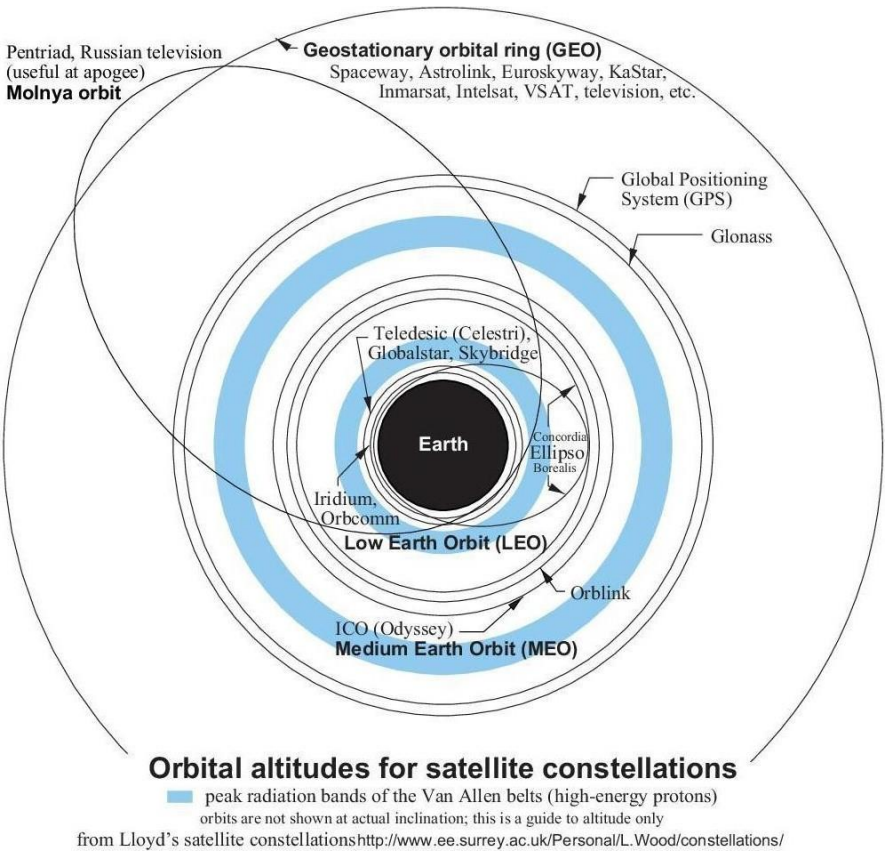

Figure 5: Orbit altitudes for satellite constellations by Lloyd Wood

The classifications for geocentric orbits are:

- Low Earth orbit (LEO) which has an altitude up to 2,000 km
- Medium Earth orbit (MEO) which has an altitude region between 2,000 km and just below the GEO orbit at 35,786 km. It is the home of the navigation constellations, and it is populated by large number of space debris [22]
- Geostationary Earth orbit (GEO) which has an altitude of 35,786 above the equator
- High Earth orbit (HEO) which has an altitude above the GEO altitude

At present, there are many operational satellite constellations, which utilise specific orbits and provide a large variety of services. Table 1 has been produced to give detailed information about the existing and some proposed satellite constellation systems.

The table shows how necessary it is to protect Earth orbits as these constellation systems provide unique services that we rely on every day. The first American navigation satellite constellation was the global positioning system (GPS) launched in February 1978, followed by the first Russian (GLONASS) navigation satellite constellation launched in October 1982. The first European navigation satellite constellation (Galileo) was launched in December 2005 and the first Chinese (Beidou) navigation satellite constellation launched in April 2007. Figure 6 summarises and illustrates some of these systems.

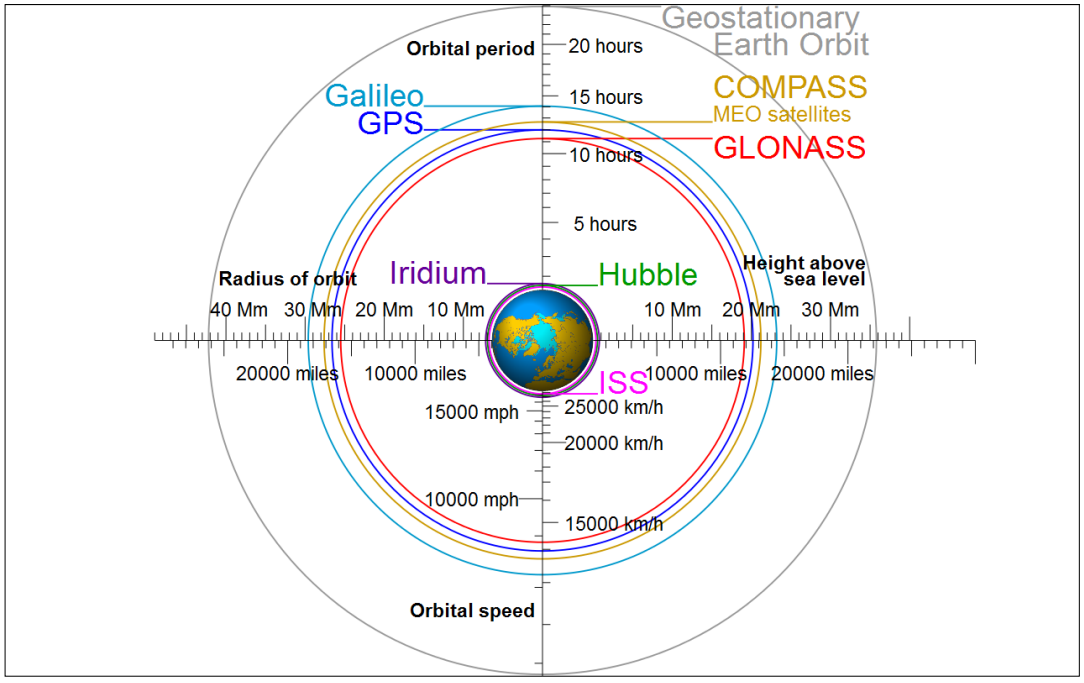

Figure 6: Satellite navigation orbits

Table 1: Example of current and proposed satellite constellations

Satellite Constellation Name	Number of Satellites or Total Satellites (Excluding on-orbit spares)	Orbit	Orbital Altitude (km)	Inclination or Plane Inclined at (degrees)	Number of Planes
Iridium constellation	66+6+9	LEO	780	86.4	6
Globalstar	48+12	LEO	1414	52	8
NASA's A-Train (Afternoon Train)	5 active	Sun-synchronous orbits	690	98.14	
US Global Positioning System (GPS) system	24-32 operational	MEO	20200	55	6
ORBCOMM Constellation	32	LEO	802	45	4
Galileo Navigation system	27+3	MEO	23,222	56 to the equator	3
COMMStellation	78+6 micro	LEO	1000		6
Disaster Monitoring Constellation (DMC)		Sun-Synchronous Orbits			
RapidEye	5	Sun-synchronous orbit	630	97.8	
Molniya constellation		Elliptic orbit			
GLONASS (Global Navigation Satellite System)	24	Medium Circular Orbit	20000	64.8	3
Broadband Global Area Network (BGAN)	3	GEO			
Beidou Navigation System or BeiDou (Compass) Navigation Satellite System	35	27 MEO+ 5 GEO+3 Inclined GEO	21150 at MEO and 36000 at HEO	55.5	
Tracking and Data Relay Satellite System (TDRSS)	3				
XM Satellite Radio	2	GEO			
Sirius Satellite Radio	3	GEO		85.2	
LEO infrared observation satellites	2	LEO	1350		
Space Based Infrared Systems (SBIRS)	4 GEO+2 HEO	GEO			
NOAA satellites	7	Sun-synchronous orbits	836 above the equator		7
WEST	12 GEO+9 MEO	GEO and MEO	For MEO: 13890		
SkyBridge Broadband	40 active	LEO	1400		10
DMSP satellites	7	Sun-synchronous orbits			7
SSA Nano Satellite (S2ANSat)	at least 2	Sun-synchronous LEO orbit	660		
GIPSE	24 equally distributed	MEO	10350	45 to the equatorial plane	6 circular orbit planes
SPECTRAL RADIANCE SHELL CONSTELLATION	1st proposal: 8 2nd proposal: 7	Sun-synchronous orbits	1st proposal: 1676 2nd proposal: 850	1st proposal: 85.2 2nd proposal: 98.7	1st proposal: 4 2nd proposal: 7
Teledesic Boeing	In 1994: 840 active In 1997 Redesign: 288 larger active	LEO	In 1994: 700 In 1997: 1350	84.7	In 1994: 21 sun-sync near-polar orbital planes In 1997 Redesign: 12 near-polar planes

The exponential growth of civil, commercial, scientific and military applications will render the world more and more dependent on satellite services. Any collision between a satellite in a constellation with a non-operational object or space debris can endanger the proper functioning of the satellite and disable its subsystems, and that could affect the function of the whole system. Therefore, research to reduce the vulnerability of space assets needs to be addressed.

1.5 Space Debris Population

Space debris is defined as all inactive, non-operational human-made objects that are orbiting the Earth. These objects no longer serve any useful purpose; they are also known as orbital debris, space junk and space waste. These objects are generated from breakups, projectiles, derelict objects, release events, non-functional satellites, launch vehicles, used rocket bodies, mission-related debris and propulsion units. There is an awful lot of space debris that we humans have put into space since the first satellite was launched in 1957, and most are still orbiting the Earth. It is estimated that there are over one hundred million space debris objects - most of which are small particles. In general, objects in space, whatever their size, are still potentially hazardous. Historically, an average of three large pieces of debris are produced from each successful mission. However, space vehicles are likely to release significant amounts of non-trackable materials into space. Therefore, with today's annual launch rate of 70-90 and with future break-ups continuing at mean historical rates of 4-5 per year [23], the number of space objects will increase and, as a result, the probability of catastrophic collisions will grow progressively.

Most debris in space are small in size, less than 1 cm, and not trackable but they have the potential to impact and disable any operational space system. It may be extremely difficult, or impossible, to mitigate non-trackable debris due to the uncertainty, which is caused by their non predictable orbital motions. The main source of information especially for large space debris comes from the US SSN. As of September 2012, SSN tracked, correlated and catalogued about 23 thousand space objects between 5 and 10 cm in Earth orbit, about 17000 of which were published. 60% of this published space objects came from explosion and collision fragments, which originate from more than 250 break-ups events in orbit mainly caused by explosions and about ten known collisions. 16% are retired satellites, 11% are spent orbital stages, 7% are mission-related objects during mission deployment and only 6%, which is about one thousand

are operational satellites. These figures are about five years old because access to exact and recent figures is not easy however even these old data give useful percentages and provide an indication of how significant is the number of human-made space objects and this number is always increasing without any doubt. Debris environment models, such as the ESA MASTER Model, has been used to estimate the total number of space debris population, resulting in:

- Thirty thousand larger than 10 cm in diameter, each could cause catastrophic spacecraft breakups – the destruction of the spacecraft and produce a cloud of wreckage, see Figure 7. Large debris objects such as satellites, rocket bodies and large fragments that re-enter the atmosphere in an uncontrolled way, which can reach the ground and pose a risk to the population on Earth.
- Seven hundred and fifty thousand greater than 1 cm in diameter, each could disable an operational satellite or break-up a satellite or a rocket body. As an example, a 100 g fragment of size 6-10 cm possesses the kinetic energy equivalent to 1 kg of TNT and can produce extensive damage on any satellite and would destroy any small satellite
- More than 170 million space debris larger than 1 mm in diameter [24]. Impacts by millimetre-sized objects could cause local damage or disable a subsystem of operating satellites. As an example, a 1.6 mm debris has the same kinetic energy as a 9 mm pistol slug

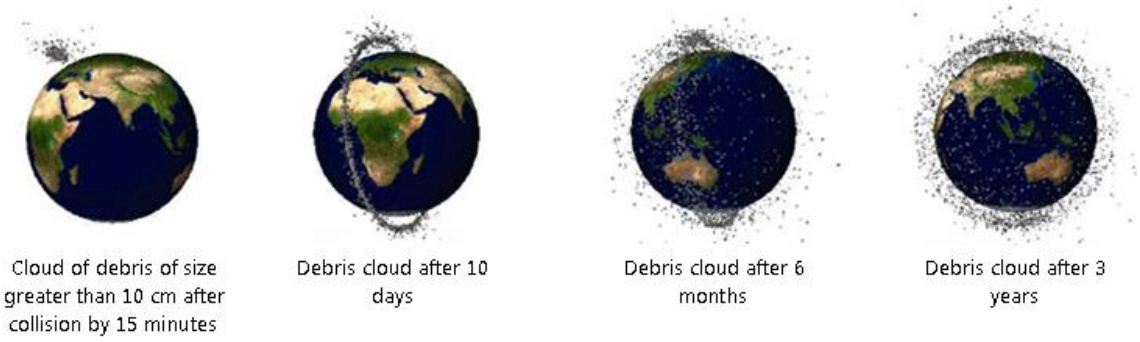

Figure 7: Post collision debris cloud over three years

The frequency of collision events between human-made objects in LEO is generating a significant number of space debris travelling at very high orbital velocities, in different directions and altitudes. This instability of the space environment was predicted by Kessler and Cour-Palais back in 1978 [25]. Major collision events like the Kosmos collision with Iridium in 2009 and the Feng Yun 1C anti-satellite test have almost

doubled the amount of debris in LEO. Another example is the spontaneous explosion of the Russian rocket 'Breeze M' on 16th October 2012. Figure 8 shows the growth of the catalogued population of space objects, operational and non-operational, in Earth orbits over the past 60 years [26]. It also demonstrates the growth of fragmentation debris due to the major collision events.

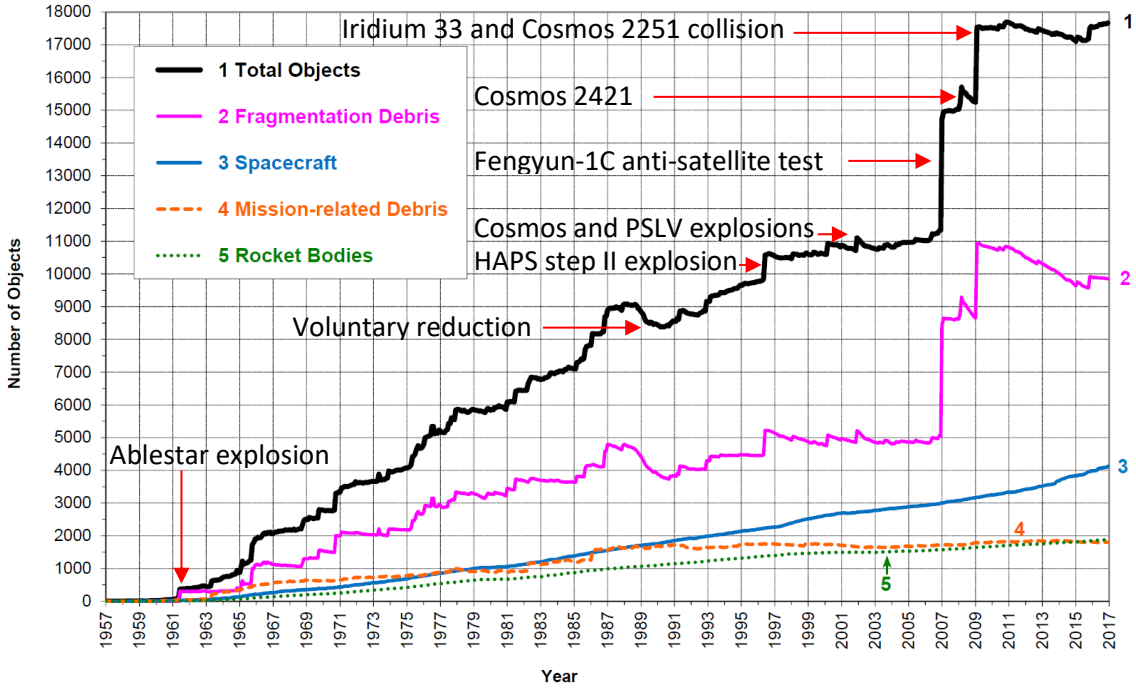

Figure 8: Chronological timeline of the US SSN officially catalogued number by US SSN of objects in Earth orbit between 1957 and 2017

Therefore, stabilising the space debris environment is extremely important to maintain the free access to space and protect operational satellites. In order to respond to the massive growth rate in the mass of objects ~ 150-200 metric tons a year in LEO [27], as shown in Figure 9.

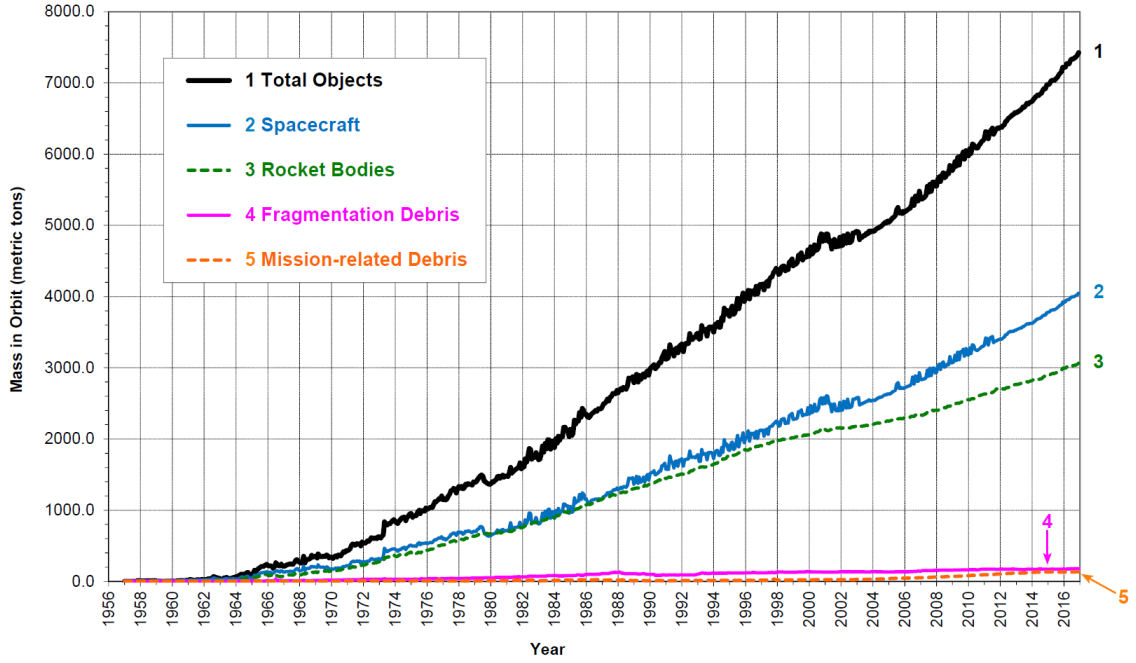

Figure 9: Chronological timeline of the US SSN officially catalogued mass of objects in Earth orbit between 1956 and 2016

Figure 9 and Figure 10 are self-explanatory. However, it should be noted that the number of objects in Earth orbits is always increasing with every space mission or collision event. Figure 10 illustrates this increase of objects in about five years intervals.

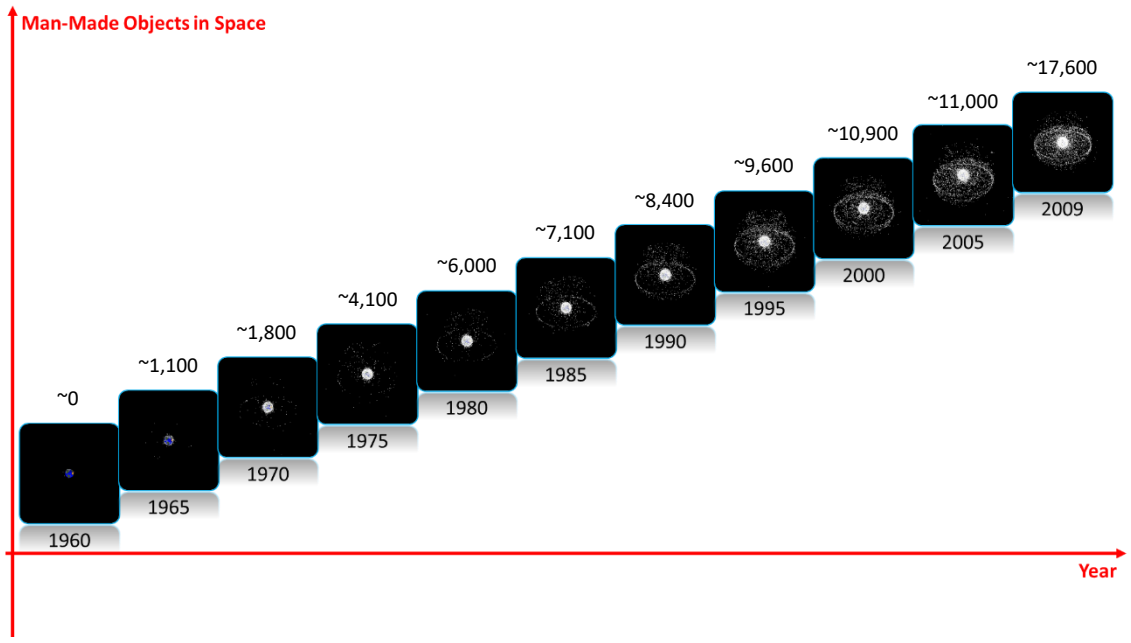

Figure 10: Timeline of Earth orbits with space objects

The re-entry of orbital debris is another challenge especially for large non-operational objects because there is no way to control the re-entry missions for such objects. Figure

11 shows only the recorded location of space objects that have been retrieved and impacted the Earth.

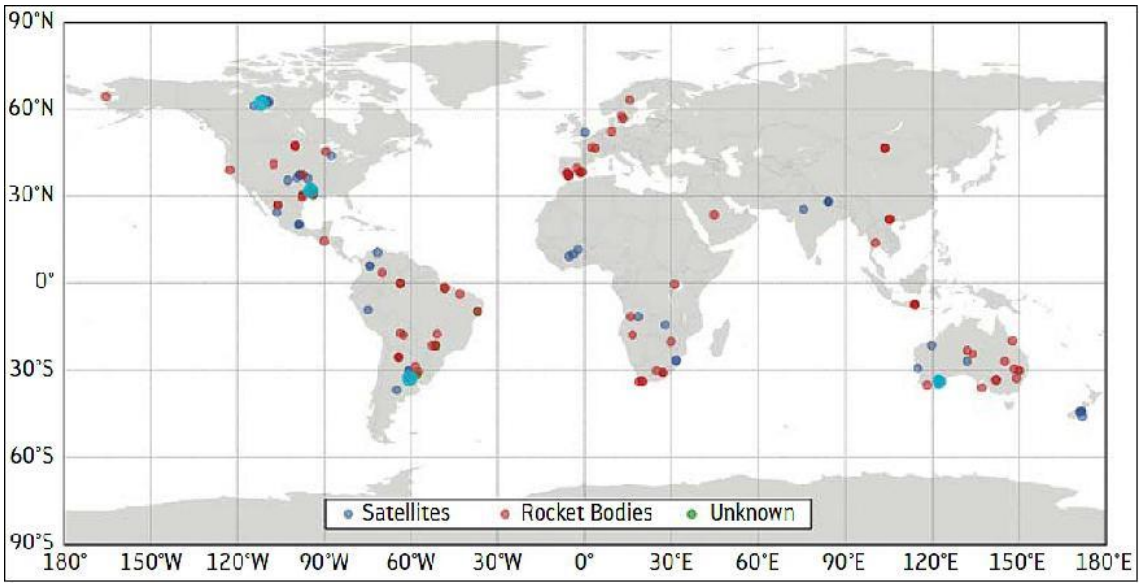

Figure 11: Locations of space junk after re-entry (image credit: ESA)

Space debris is a significant environmental issue; it poses two types of serious threats of the alarming growth of space debris. These threats are space-to-space threats and space to Earth threats. The following major space collision events summarised the threats of debris in space:

- 11 Aug 1993: Something hit the British Olympus-1 Sat and left it adrift
- 24 Jul 1996: French Cerise MilSat was hit by fragments of an Ariane-1 launcher
- 29 Mar 2006: A debris hit Russian Express-AM11 SatCom
- 11 Jan 2007: Chinese AntiSat test targeting Feng Yun-1C weather Sat and created more than 3,300 tracked fragments
- 10 Feb 2009: Iridium-33 Commercial Sat collided with Kosmos-2251 Russian MilSat and created more than 2,200 tracked fragments
- 28 Oct 2010: Eutelsat W3B (5.37 ton) suffered a leak, then was declared a total loss
- 28 Jun 2011: A significant debris discovered at the last minute and flew less than 250 m from ISS
- 18 Aug 2011: Express AM-4 misplaced, now considered risk to GPS and GEO Sats
- 16 Oct 2012: Spontaneous explosion of the Russian rocket ‘BreezeM’

As space debris forms threats to astronauts living in space and space assets, the re-entry of large space debris is a threat to life on Earth (nevertheless it is a small threat statistically). Figure 12 shows a few of examples of some large space debris that returned to the Earth with impact on five different countries and continents.

Figure 12: Examples of re-entry space debris in five different continents and countries

Scientific figures indicate that 15 large non-operational objects must be removed and re-enter the atmosphere to keep the LEO environment useable [28]. To achieve the objective of performing an in-orbit removal of debris, scientists and space agencies have proposed ideas, and some of them have even developed systems to deflect, remove or mitigate space debris threats. Proposed removal ideas include mechanical capture techniques like tethers, grasping, nets, expanding foam, harpoons, et cetera. Non-mechanical techniques like ionic beams can, however, provide contactless removal techniques. Each idea or method has some advantages and disadvantages, but it is important to note that many of these proposals complement each other rather than give alternatives.

1.6 Orbital Debris in LEO

Near-Earth orbits like LEO are sufficiently dense with space debris because of the large masses of human-made space materials that have been placed in the LEO band. The relative velocities of orbiting objects in this band are very high, ranging between 9 and 10 km/s with a maximum value of 14 km/s. To illustrate the problem, a 1 cm aluminium sphere at an orbital velocity of 10 km/s possesses the kinetic energy equivalent to a midsize car of 1.5 tonnes moving at 50 km/h or the explosion of a hand grenade. Also at this velocity, a piece of debris has ten times the energy density of dynamite; LEO debris are common at such high speed and can cause considerable damage to the impacted system, with and numerous secondary fragments as a result. The effects of 6.8 km/s hypervelocity impact by a spherical aluminium projectile on a solid aluminium block have been studied by ESA, the result is shown in Figure 13.

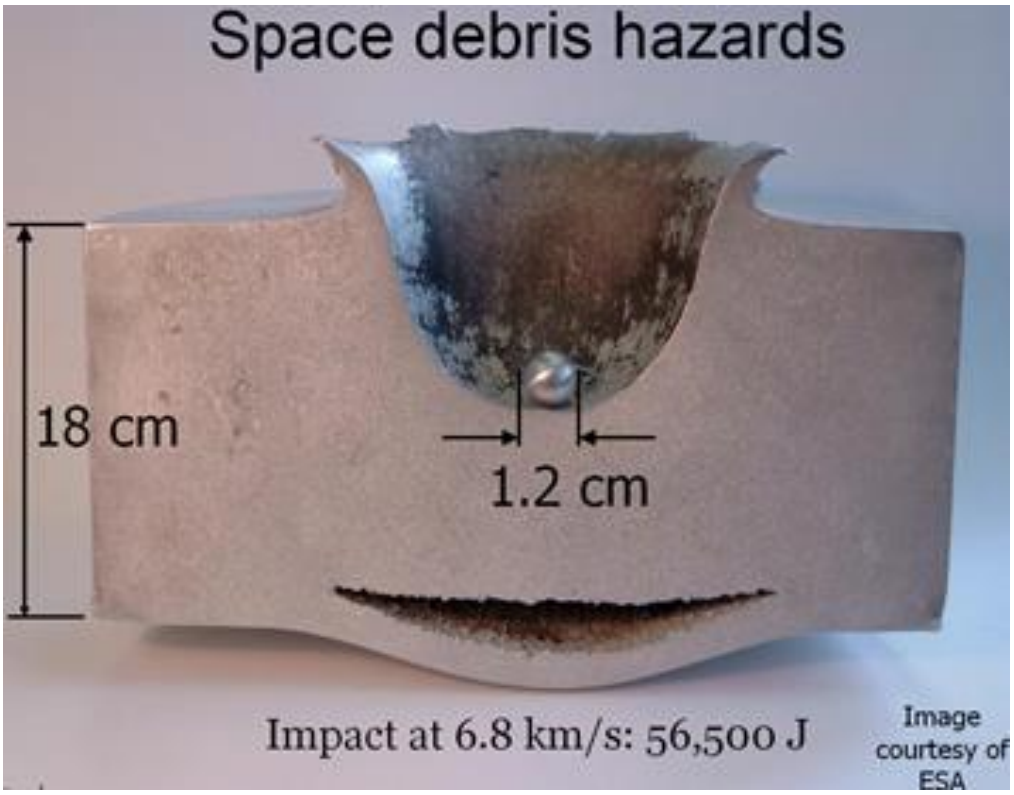

Figure 13: Experimental hypervelocity impact study by ESA

Also, a gram of aluminium at a velocity of 2 km/s has the same kinetic energy as a gram of trinitrotoluene (TNT). Therefore, the use of space in LEO is threatened by collision cascading processes [29], the Kessler syndrome, in which each collision between objects generates more space debris, which increases the likelihood of further collisions [30]. Collisions among existing LEO debris are now the largest source of new debris, threatening future use of LEO space. The relative catastrophic collision flux in LEO to GEO is about 1000 to 1. Based on this, mitigating orbital debris in LEO demands serious attention, and it is an important area of study, which requires more research. The research question of this thesis is 'how we can effectively mitigate space debris practically and cost-effectively without adding more to the space debris problem?'. A variety of mitigation techniques has been proposed by scientists, to mention some: attaching de-orbiting tools, deploying nets to capture objects, chasing and grappling the debris. Many of such proposed solutions are costly because they require launching satellites to perform mechanical activities in space, which will also produce additional debris.

1.7 Thesis Structure and Outline

This section outlines the entire scope of this thesis. The thesis research was divided into seven main phases, which can be summarised as below:

- A detailed and comprehensive literature review of the space environment, focusing on artificial objects and space debris in Earth orbits, has been conducted in this chapter, Chapter 1. That also includes an investigation of the existing space environmental issues and the proposed solutions and remediation. It also studies the population and distribution of space debris in Earth orbits.
- Laser options and the process of laser ablation when it is operated as a deflection tool are described in Chapter 2. The chapter also conducted a study to understand lasers fundamentals including laser properties. This chapter also includes some background and literature review on the laser as a deflection tool to mitigate orbital debris.
- The impacts of laser energy, beam size and pulse frequency have been simulated using MATLAB codes in Chapter 3.
- Space debris irradiation with laser pulses will be investigated in Chapter 4 and Chapter 5. The interaction investigation of the laser beam with three selected targets performs the main part in the enhancement of the laser ablation mechanism of the concentrated Nd^{3+} Glass laser radiation of metals, and this is presented in Chapter 4 and Chapter 5.
- Simulation of the required laser energy to change the orbital velocity of different space debris have been investigated and discussed in Chapter 6. This includes the simulation of the total laser output energy.
- The employed experimental results validated the Kinetic theory theoretical model. Comparison between the measurements of surface temperatures and both the classical Fourier conduction theory and the Kinetic theory are described in Chapter 7.
- Conclusions and recommendations for further work are given in Chapter 8.

Chapter 2

Lasers as Deflection Tools

2 Lasers as Deflection Tools

2.1 Summary

Based on the introduction and discussion conducted in Chapter 1, there is a pressing need for an effective means for space debris removal to overcome the considerable current risk that space debris poses to operational satellites and other space probes. Space debris mitigation using laser ablation is one of the proposed techniques to mitigate the growth of orbital debris. This chapter discusses the lasers option and how it can be used as deflection tools to act on objects in space including space debris, asteroids and meteoroids. It shows how such a contactless deflection tool can be used to push orbital debris and change their altitude in orbit for collision avoidance, especially with large objects. It studies the geometry and behaviour of a Gaussian beam field. This chapter also details the proposal for this research project. References to some previous work on lasers and space debris mitigation solutions are also presented.

2.2 Lasers as Engineering Tools

Light amplification by stimulated emission of radiation (LASER) can be considered as feasible, economical and practical engineering tools due to its unique properties namely: coherence, directionality and high monochromaticity [31]. It has been used actively in manufacturing and industry for many processes such as fusion, cutting, drilling and ablation. We believe that space debris mitigation can be achieved by using a high power pulsed laser to move and cause the debris to deorbit. This action will lower the velocity of the orbital debris and hence its perigee, which will cause the debris to re-enter the atmosphere and burn up. However, for a ground-based laser system, this technique only works if the laser beam has enough power to penetrate through the atmosphere with enough remaining power to reduce the velocity of the space junk by a small amount ~ 100 m/s which will suffice to reduce its perigee. Also, the laser must operate in a pulsed mode to generate high power. So this research project proposes to employ a laser beam as a deflection tool to remove space debris from LEO, by ablating some of the object material.

A power intensity of one GW/m^2 (10^9 W/m^2) or more is essential for a laser to produce high fusion or melting under situations where vaporisation does not happen during the interaction. In general, one GW/m^2 to one TW/m^2 laser power intensities are necessary to produce non-conduction finite heating that is essential for these laser processes.

Lasers, as a source of energy, can be focused by lenses to attain these relatively high power intensities at the focus point. This is due to the laser intensity and spatial coherence properties.

The concentrated beam of a laser is a key technology that has been advanced over the last five decades, and its main potential benefits as a machine tool are well-defined by many authors in the literature [32] especially for solid-state or gas laser systems. Lasers are available in either continuous wave (CW) emission or as a pulsed emission. Pulsed emission solid-state laser systems can produce heat transfer mechanisms favourable for interaction with a variety of materials due to its 1.06 µm wavelength see Figure 14. These laser systems use elements of neodymium in yttrium aluminium garnet (Nd^{3+} YAG) or elements of neodymium in glass (Nd^{3+} Glass).

Solid-state lasers such as Nd^{3+} Glass, Nd^{3+} YAG (which has high pulse repletion rate) or ruby lasers are very beneficial where high-energy pulses are required. In 1960, the solid-state ruby laser was used as a first practical laser drilling application by Maiman to make holes in diamond dies [33]. CO_2 laser systems can work in the multi kW output power ranges. The CO_2 laser is widely utilised for heavy-duty cutting applications due to the high average power necessary. The CO_2 laser was the first laser to be effectively used for continuous emission and operation, but it has a limited peak power ability, and for efficient processing, it relies on gas jet enhancement.

Laser interaction results and performance in any of the applications mentioned before are influenced and controlled by many factors. The main three factors are the laser beam output characteristics, the target physical characteristics and the interaction environment. These three main factors are discussed below:

2.2.1 Laser beam output characteristics

The electron distribution as a result of laser pulses interacting with metals relies on many parameters in addition to the metal material properties that will be discussed later. These parameters include laser wavelength, beam concentration conditions and laser pulse data (pulse energy and shape). Some of these parameters are explained in more details after the next figure:

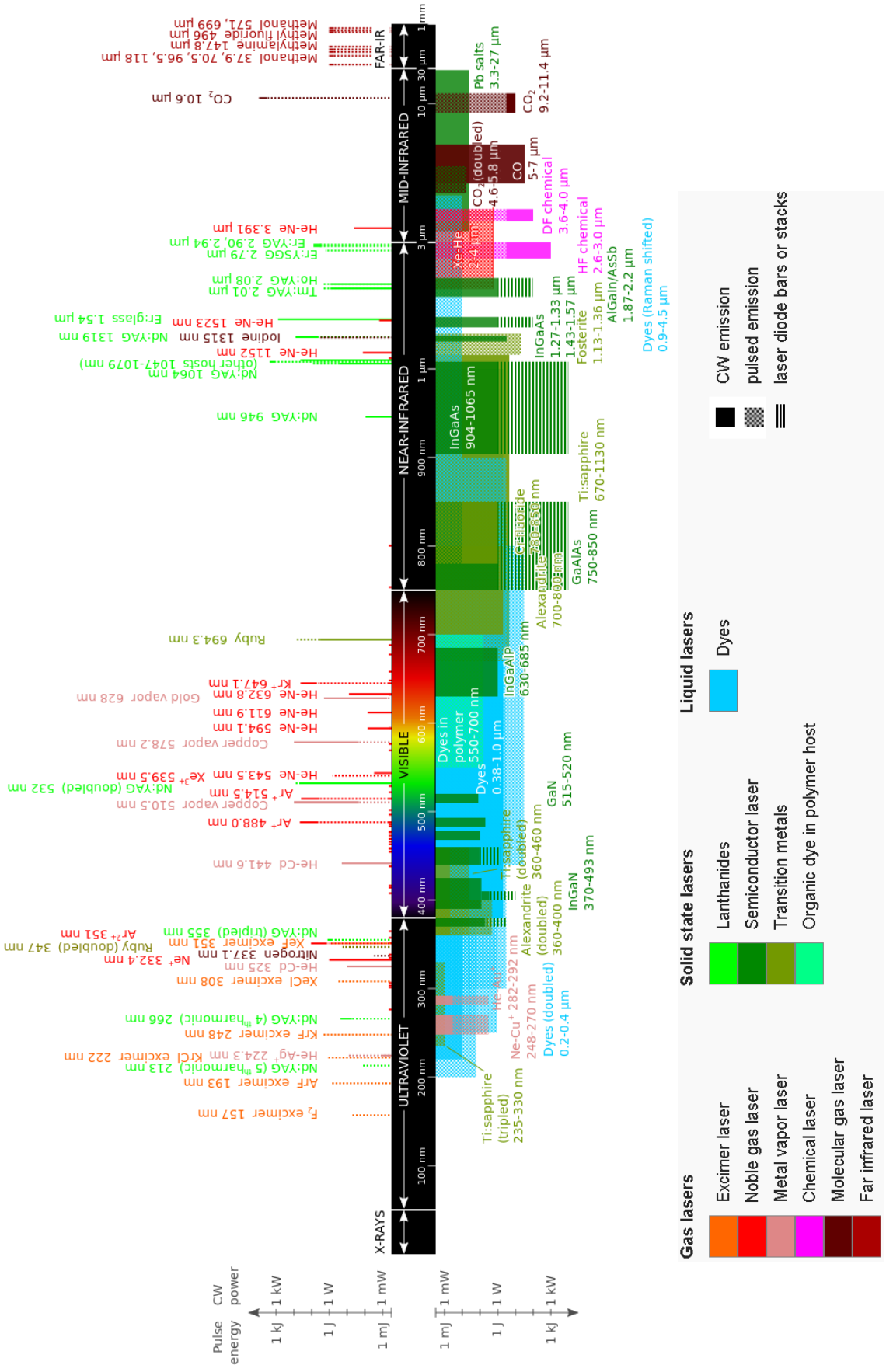

Figure 14: Overview of the commercially available lasers types and wavelengths [34]. Line height gives maximal power and pulses energy indication. Full lines and areas mean CW emission and dotted mean pulsed emission

- Laser beam transverse spatial profile: Laser beam may work in one of numerous cylindrical transverse electromagnetic (TEM) modes [35] as shown in Figure 15. However, the Gaussian profile TEM_{00} is essential for laser interaction with materials. That is because of the Gaussian profile shape is maintained as the laser beam propagates, and because of the symmetry of the TEM_{00}. Also, the diffraction angle of the TEM_{00} beam is small comparing to the higher-order TEMs, and thus TEM_{00} can be focused more effectively and can deliver larger irradiance on the target than for other transverse modes.

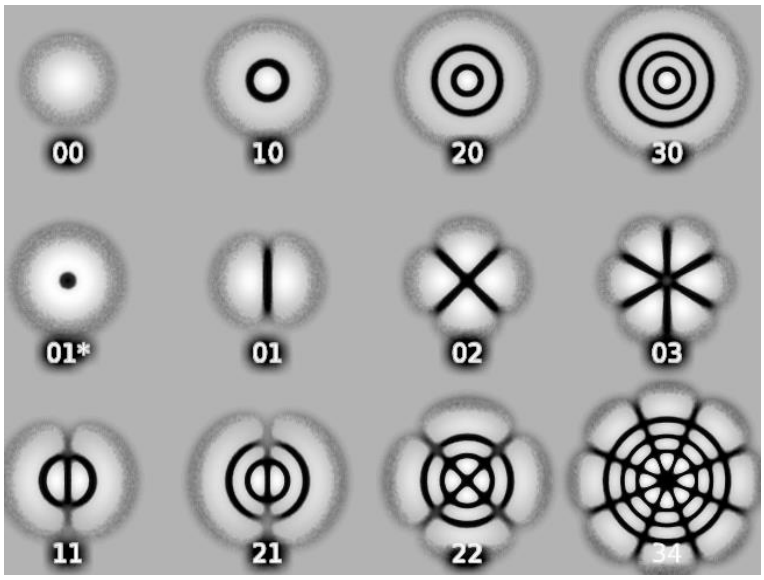

Figure 15: Laguerre-Gaussian TEM pattern

Figure 16 shows that the behaviour and geometry of a Gaussian beam is governed by a set of beam parameters that can be expressed by the following equation:

$$w(z) = w_0\sqrt{1 + \left(\frac{z}{z_R}\right)^2} \qquad \text{Equation 2.1}$$

Where:

z = Axial distance from the laser beam waist or focus (narrowest point of the beam) = Distance along the beam from the beam waist

$w(z)$ = Gaussian beam width or spot (focus) size at z = Variation of the spot size for the beam of wavelength λ at distance z along the beam from the beam waist = Radius at which field amplitude fall to $1/e$ of its axial

value, at the plane z along the laser beam = Radius at which field intensity decreases from its centric value by a factor of e^2 or drops to $1/e^2$ of its axial value

$w_0 = w(0)$ = Laser beam waist size (radius)

$z_R = z_0$ = Rayleigh range (length)

$$z_R = \frac{\pi w_0^2}{\lambda} = z_0 \qquad \text{Equation 2.2}$$

Where:

λ = Wavelength

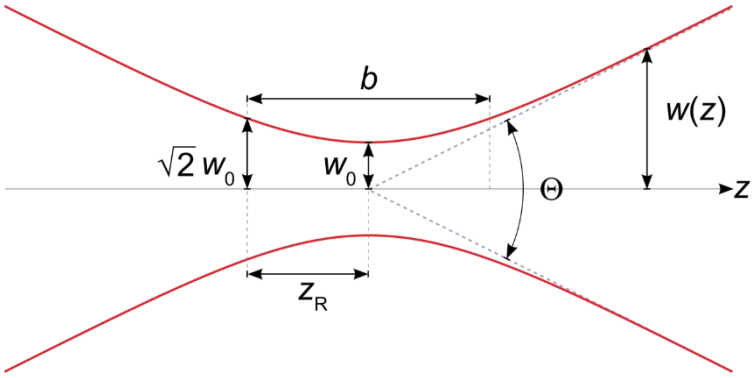

Figure 16: Gaussian beam and its waist parameters

$b = 2z_R$ = Confocal parameter or depth of focus of the beam

Θ = Total angular spread of the beam far from the waist ($z \gg z_R$). To keep the laser beam very well collimated, it must have a large diameter because a Gaussian beam that is focused to a small spot spreads out rapidly as it propagates away from the spot and thus Θ is inversely proportional to the spot size at the waist w_0 as expressed in the following equation:

$$\Theta = 2\theta = \frac{\lambda}{\pi w_0} \qquad \text{Equation 2.3}$$

Where:

θ = Divergence of the beam = Angle between the straight line when ($r = w(z)\ for\ z \gg z_R$) and the central axis of the beam when ($r = 0$)

- Laser beam concentration: Beam concentration is crucial for laser ablation, for controlling and delivering the irradiance at the target, which is in this project is space debris. Lenses with appropriate focal lengths are used to

manage beam intensity, depth of field and focusing the beam to high power intensities on the surface of the target. Multiple lenses can be arranged and sorted in a way to produce the required effective focal lengths. At the focal point, the centre of the beam at its waist, the intensity of the laser beam is maximum, but its value decreases with the distance from the focal point. The irradiance $I_{(r,z)}$ or the time-averaged intensity at any location of the laser beam in the TEM_{00} transverse mode is represented by this equation [36].

$$I_{(r,z)} = I_0 \left(\frac{w_0}{w_{(z)}}\right)^2 e^{\left(\frac{-2r^2}{(w(z))^2}\right)} \quad \text{Equation 2.4}$$

Where:

$r = w(z)\ when\ z \gg z_R$ = Radial distance from the laser beam centre axis

$I_0 = I_{(0,0)} = I_{max}$ = Intensity at the laser beam centre at its waist

The spatial intensity distribution in TEM_{00} laser beam is when $z = 0$; it is a function of the beam radius as shown in the following equation:

$$I_{(r,0)} = I_{(r)} = I_0 e^{(-2r^2/w_0^2)} \quad \text{Equation 2.5}$$

And, when $r = w_0$

$$I_{(w_0,0)} = I_{(w_0)} = I_0 e^{-2} = I_0/e^2 \quad \text{Equation 2.6}$$

- Laser wavelength: In a limited diffraction situation, the concentrated spot size of the laser beam is proportional to its wavelength λ and the laser irradiance is proportional to $1/\lambda^2$.
- Laser beam energy: Higher laser energy produces greater vaporisation and raises the amount of laser energy coupled into the materials of the target, which is in this project space debris.
- Laser beam transient fluctuation: For ablation of space debris, initial spikes or relaxation oscillations in the laser pulse substructure are substantial.

2.2.2 Space debris physical characteristics

The main physical properties that influence the laser-material interaction efficiency are reflectivity, thermal diffusivity and vaporisation latent heat. The following bullet points explain each of these properties in more details:

- Space debris materials: None of the satellites are built of a single material [37]; it is usually a combination of a vast variety of materials, and thus it is important to break down the geometry of space systems to find out the most common materials in them. It is important to study the engagement between the laser beam and the debris. In this project, a material study has been conducted to summarise the twenty most commonly used materials in designing and manufacturing space systems [38], which are also the materials that make up most orbital debris as shown in Figure 17. Application wise, the copper material has been utilised in almost every electrical motors and generator. This is a fact because copper as a metal is a good electricity conductor and that is why it has also been used for electrical cabling and wiring. The copper material also conducts heat and thus is utilised in system radiators, air-conditioning and heating systems that are heavily used in space systems. Therefore, even though it might not be listed as one of the most commonly used materials in space systems, in the literature, we believe that it is a necessary material to be considered when we talk about centimetre size space objects.

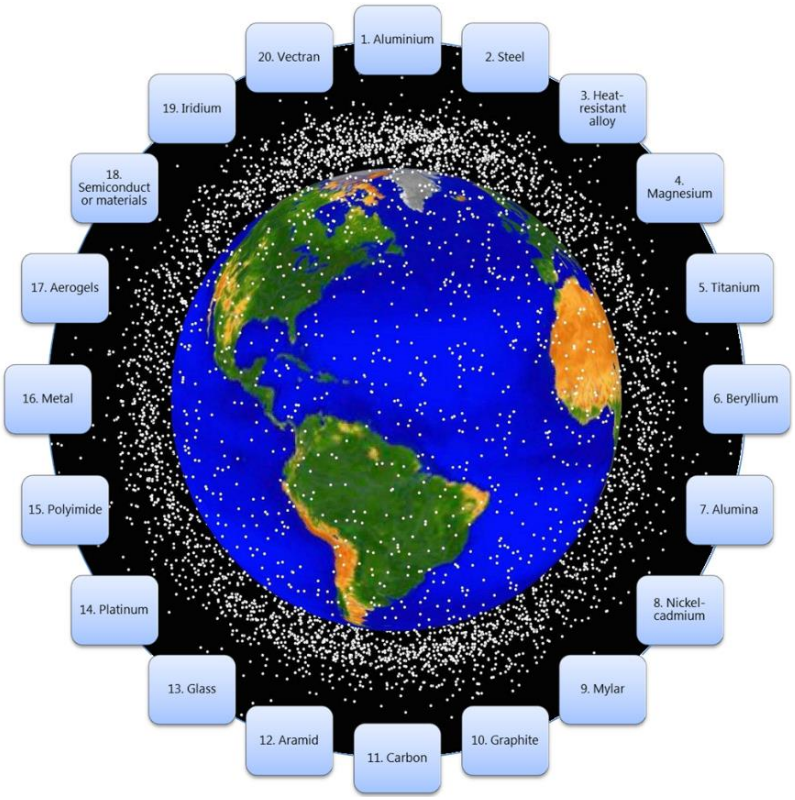

Figure 17: Twenty most commonly used materials in manufacturing space systems (background image credits NASA)

- Space debris optical characteristics: The physical reflectivity of the wreckage is one of the main factors that determines the proportion of the laser radiation to penetrate into the wreckage. When a concentrated laser beam hits the surface of the debris, a portion of the laser irradiation will be reflected, but the rest of flux will be absorbed into the wreckage material bulk by the electrons above the Fermi surface. The proportion of the absorbed and reflected radiant energy rely mainly on the reflectivity of the debris surface material. The reflectivity of the wreckage material is a function of the surface temperature, laser wavelength, surface finish and its oxidation status.

  Surface reflectivity of an object is proportional to the laser wavelength, for cold material, and inversely proportional to the temperature of the surface; these relationships have been investigated experimentally by Chun and Rose [39]. For many metals, reflectivity at 10.6 μm wavelength is much bigger than at 1.06 μm wavelength, see Table 2. It is important to note that the low reflectivity of metals at 1.06 μm wavelength is preferable for laser ablation of space debris. Even though these reflectivity values reduce over the laser pulse as a result of heating, since reflectivity is a function of temperature, lasers with high wavelength values are inappropriate due to the large reflectivity values of the metals.

Table 2: Reflectivity of metals at ambient temperature

Metal	Reflectivity at Laser Wavelength 1.06 μm	Reflectivity at Laser Wavelength 10.6 μm
Nickel (Ni)	66%	94%
Aluminium (Al)	70%	96%
Copper (Cu)	88%	98%

- Space debris thermal characteristics: Debris thermal properties vary from material to material, and they are a function of temperature. Laser beams focused onto space junk generates a heating rate, which relies on the junk thermal diffusivity α and is influenced by the non-equilibrium energy transfer mechanisms that are happening during the process of energy

transport. Thermal diffusivity largely influences the melting area depth. It is proportional to the thermal conductivity k and inversely proportion to the specific heat capacity c_p and the density ρ of the space debris material as shown in following equation [40]:

$$Thermal\ diffusivity = \alpha = \frac{k}{\rho c_p} \qquad \text{Equation 2.7}$$

Where:

k = Thermal conductivity $\left[\frac{W}{m.K}\right]$

ρ = Density of the space debris $\left[\frac{kg}{m^3}\right]$

c_p = Specific heat capacity $\left[\frac{J}{kg.K}\right]$

ρc_p = Considered as volumetric heat capacity $\left[\frac{J}{m^3.K}\right]$

- Vaporisation latent heat

2.2.3 *Interaction environments*

The laser-space debris interaction performance is affected by the space environment. However, in this thesis, it has been assumed that the impacts of the space environment on the interaction performance are negligible when compared to the standard environment at room temperature.

2.3 Laser Pulse

For accurate simulation and modelling, laser output pulses are desired to be similar from pulse to pulse. It is necessary to measure the energy that is produced per pulse from the laser beam, which is in our case from the Nd^{3+} Glass laser beam and it was measured at the same time with the irradiance emitted from the target-impacted zone. In this thesis, the laser output pulses were sampled every 200 ns and interpolated to provide power intensities with every 50 ns for simulation.

2.4 Laser Ablation

The laser ablation process includes vaporisation and removal of some of the material, the same as in industrial cutting and drilling applications. Once the molten material reaches its temperature of vaporisation and the laser beam continues to transfer additional energy into the molten material, the vaporisation process starts to vaporise the molten material. This is because this extra energy provides the vaporisation latent heat. The goal in laser ablation is to vaporise the material as rapidly as possible

especially for deflection of orbital debris as the timeframe for such interaction is very limited. Also, doing this results in a small heat impacted area with minimum distortion of the wreckage.

Laser ablation nowadays is a very well used material removal mechanism that has been used widely in many industries on Earth particularly when it is necessary for a contactless mechanism and when there is a need to minimise the heat impacted area zone. However, the challenge is that during the ablation process the laser-debris interaction will initiate a complex process in a highly nonlinear style. The ablated material leaves surface debris, leaving irregular conical to a cylindrical shape in the impacted area. The poor precision of this irregular shape, of conical-cylindrical geometry, is mostly because of the uncontrollable redistribution of molten material at the walls and the bottom of the impacted area, at the end of the laser pulse. This behaviour also happens in laser drilling applications [41]. The impacted area deepness proportionally increases with the laser beam energy that is delivered to the target surface [42].

High power laser pulses with high pulse repetition rate are needed for ablation especially for space debris deflection, as non-operational objects in space tend to tumble. Low laser beam intensities, below the threshold of ablation, have been proposed to deliver light pressure on space debris and slightly deflect it [43]. A pulsed laser is preferable for deflecting space debris as thermal conduction in a continuous laser spreads too much heat into a larger zone of the debris material. A pulsed laser is inefficient for the heating of a significant volume of material, but it can quickly increase the debris surface temperature. The high-power laser beam can provide extreme heat increase in a thin layer of the debris surface at the focus point of the laser beam. Due to the relatively low-temperature of the bulk material below the debris surface, it will cool very quickly once the laser radiation is removed.

A concept validation studied at NASA summarised that the proposal of deflecting 1-10 cm size space junk in 400-1,100 km altitude in 2 years by utilising laser pulses was feasible compared to the cost of replacing, fixing or even shielding high-value satellites [44]. Due to the high cost of putting systems into space, even in LEO with the current cost of $10,000 per kg, any alternative solutions that involve launching satellites for mechanical interactions may not be feasible.

Schall suggested in 1991 to use pulsed laser space-based systems to remove orbital debris [45]. Phipps [46] proposed a laser-optical system to remove and clear space debris in LEO and called it laser orbital debris removal (LODR) system by focusing 1.06 μm wavelength 5 ns high repetitively power pulsed laser beam and large mirrors on Earth to make plasma jets on LEO space debris from the ground. He illustrated a schematic diagram of a ground-based pulsed laser system for spinning space debris removal as shown in Figure 18. He proposed to use a high power (multi-kJ) pulsed laser-based system and focus it on debris in LEO with high intensity, after the wreckage is detected and tracked, to slow its orbital velocity slightly by the small amount needed to re-enter and burn up in the atmosphere. He explained how and why LODR is a versatile and cost-effective way to solve the space debris problem. His proposed LODR system addresses both small debris, less than 0.75 kg in mass, and large debris with 1000 kg mass. The effective mirror diameter is 13-25 m to overcome diffractive spreading of the light at a range of 1,000 km altitude [47]. International collaboration and cooperation, however, will be crucial for operating and implementing such laser system [48].

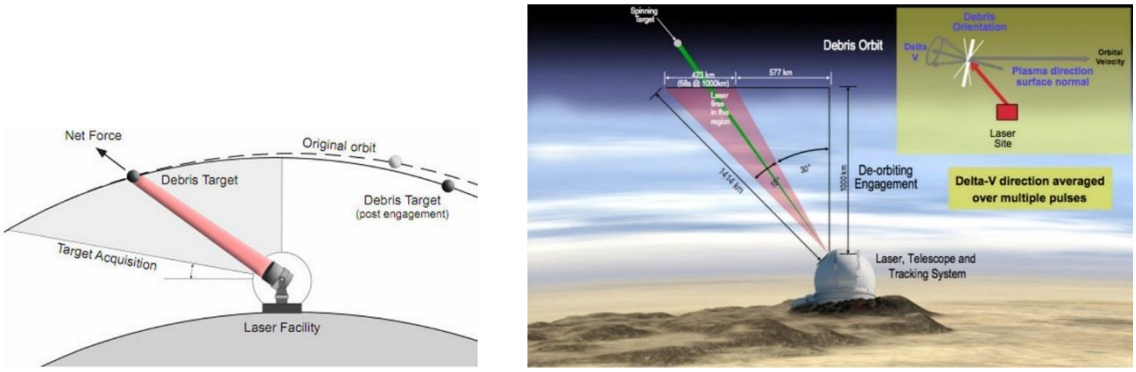

Figure 18: Laser orbital debris removal (LODR) system using ground-based laser system

Rubenchik [49] suggested the possibility of merging two laser beams to produce very high-energy value per pulse ~ 20 kJ, by combining two laser beams from the proposed laser inertial fusion energy (LIFE) system. LIFE project, which was an attempt run by Lawrence Livermore national laboratory (LLNL), has been cancelled due to the failure of national ignition facility (NIF) from achieving ignition in 2012.

Propulsion using a ground-based laser system eliminates the need for launching satellites to interact with space debris in Earth orbit physically. That reduces the overall complexity, the warning time and the risk of this technique comparing to other removal

techniques. However, for the technique to be sufficiently useful, the laser beam positioning would need to be successfully deployed on the targeted debris. As a result of a long path distance between any ground or space-based laser system and orbital debris, tracking objects in space is crucial for dynamic alignment to guide any power beam; an autocollimator can be used to achieve a very high level of alignment between the laser beam and the debris. This eliminates any alignment inaccuracy, which is strongly unwanted especially in busy Earth orbits. It is common to utilise a laser and autocollimator to fulfil accurate alignment between devices, maximise the interaction process and improve the use of the output power of the laser. Ablation with the laser beam has also been proposed by some scientists to deflect bigger objects including natural space objects, like meteoroids, asteroids [50] and comets [51,52].

Laser stability is an important factor, which is influenced by the laser rod temperature after each shot. However, this issue can be overcome by letting the laser rod cool down between laser shots; this can be done by utilising a cooling system after each shot.

2.5 Space Debris Mitigation and Deflection Techniques

To address the orbital debris impact risk, numerous methods of space debris mitigation and deflection techniques have been considered by various space agencies, universities, establishments, researchers and authors. However, to date, no single research group, establishment or organisation has selected a definitive solution to the problem of debris in Earth orbits. That is why it is still considered to be an ongoing and open problem as almost all of the proposed solutions are at the design and development stages. The laser ablation propulsion method is one of the proposed solutions; it can be divided into two main techniques, which are:

- Mitigation for deorbiting: The common objective of this technique is to decrease the orbit altitude of the space debris. Doing this will reduce the lifetime of the space debris in orbit and eventually deorbit the debris by re-entering the dense atmosphere.
- Deflection for collision avoidance: The common objective of this technique is to increase the minimum distance between the space debris and any operational spacecraft in orbit. This distance between a space debris and an operational spacecraft, like the ISS, can be maximised by applying a deflection action on the space debris at a specific time before impact. Deflecting objects in space is

heavily dependent on the size of the target. This technique could also be used to deflect asteroids, comets and NEOs in general [53,54]. However, deflecting such objects require international collaboration [55,56].

The success of the above techniques is dependent on understanding many factors such as the warning time of the space debris, the orbital elements of the debris, its mass, shape, size and material. An efficient way to deflect or mitigate space debris, or in general any non-operational object in space, is to apply an impulse or a controllable low thrust on the surface of the object to change its orbital velocity by Δv along the orbital path of the object, aligned with its velocity vector.

The potential of mitigating space debris by laser ablation propulsion, which is the subject of this thesis, is dependent on the ablation process and the chemical and physical properties of the target including its surface thermo-optical properties such as absorptivity, reflectivity and emissivity. The success is also dependent on the engagement between the surface of the space debris and the laser beam radiation, which depends on the diameter, intensity, attenuation and wavelength of the laser beam in addition to the orbital elements of the debris, its structural composition, geometry and relative mass.

As the laser ablation model is based on the energy balance of sublimation, the intensities of the laser beam are one of the leading properties of these techniques. The Nd^{3+} Glass laser, solid-state laser, has been recommended for laser ablation as it provides acceptable intensities, which are below the threshold of plasma formation. This type of laser operates at a wavelength of 1.06 μm.

The ideal conditions of these techniques are very hard to be achieved due to the dispersion of the space debris orbital elements and the uncertainty of the shape and size of the orbital debris. Therefore, adequate margin must be considered in the design of any general laser ablation propulsion strategy since errors could be generated. For the deflection technique, it is critical to apply at the earliest possible time as a more considerable deflection distance can be generated with a more extended warning time, where less Δv is required to change the trajectory of the space debris.

2.6 Laser-Space Debris Interaction

Understanding the interaction process between a laser beam and debris is crucial for knowing the strengths and limitations, especially for laser activities in space. The interaction process fundamentally relies on the beam power intensity, laser pulse length, laser wavelength and also relies on the physical characteristics of the space debris, see Figure 19.

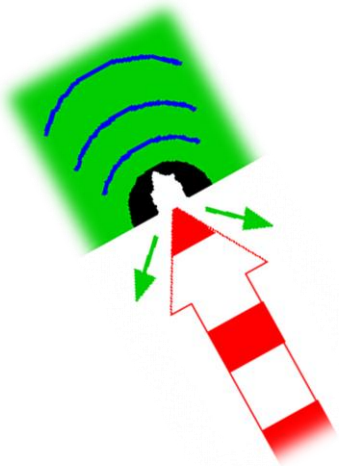

Figure 19: Interaction between the laser pulses and a space debris

The interaction mechanism starts once the laser radiation hits the orbital debris. Part of the laser radiation will be absorbed by the debris surface, whereas the other part will be reflected. The absorbed portion of the radiation is a result of interacting with conduction electrons; it appears as temperature spreads on a larger area of the debris material by thermal diffusion that relies on the beam energy involved. The absorption of radiant energy by the wreckage material is achieved at a depth estimated by the conduction electrons mean free path [57]. At low power intensities, less than or equal to one GW/m^2, the radiation is absorbed in a very thin layer ~ 0.01 µm thick of the debris surface. Thus, no transformation in the material status will happen. For higher power intensities, more than one GW/m^2, the impacted zone reaches the melting point. So, a liquid interface propagates into the debris, and the delivered energy from the laser beam will be absorbed in a deeper layer. Any further rise in power intensity will lead to increase the hot pool surface temperature to the boiling point; and when the boiling point is reached, the melt phase becomes less significant and thus the vaporisation becomes the dominant physical process. Some material would leave the space debris if more laser energy arrived at the impacted zone. In the vaporisation phase, the

interaction process is very complex. That is because of some complex physical events that occur in this phase, like the sub-surface nucleation phenomena leading to the expulsion of material in the molten phase. Most of the ejected material will leave the debris surface as a vapour, and that is the core idea of laser ablation. However, some will stay in the molten phase and thus will leave the surface as liquid droplets.

The description of the interaction process has been studied in some detail by many scholars. For example, Chun [58] analysed the interaction mechanism by utilising Fourier conduction theory at levels where no phase variation is produced. They considered the radiation energy as having been changed immediately to heat on the metal surface where the radiation energy is absorbed. They also assumed the energy absorbed by electrons during the interaction process was transferred to the lattice.

As discussed in Chapter 1, orbital debris in LEO is now sufficiently dense that the use of LEO is threatened by runaway collision cascading. The threat from junk larger than one cm demands serious attention. Therefore, we must add solutions for quick, efficient and high-quality execution. Removal methods of orbital debris using laser ablation have evolved quite slowly. System risks are low, if it is run correctly, and this type of operation on space junk will not generate additional orbital debris. However, this removal technique is still immature, and thus more research is essential to evaluate this approach for debris removal. In this thesis, we employed experimental results for the simulation and the validation of the model. We describe the application of laser ablation in deflecting orbital debris in LEO using Nd^{3+} Glass pulsed laser. The experimental results were implemented by utilising a 600-watt Nd^{3+} Glass laser. This thesis shows that the method of deflecting small space debris with a pulsed laser performs well especially with specific kinds of debris materials.

Chapter 3

Laser Power, Beam Size and Repetition Rate

3 Laser Power, Beam Size and Repetition Rate

3.1 Summary

This chapter will evaluate and simulate the potential melting and boiling process of space debris due to the high-energy pulse delivered from the laser beam to the surface material of the space debris. The chapter will also determine the required energy, laser beam size and repetition rate (pulse frequency) for melting and vaporising space debris to reduce its size from 10 cm to less than 1 cm in diameter. It also simulates the time to vaporise and transform the irradiated junk particle from solid status to a gaseous status. Gaussian and top hat laser beams are also discussed in this chapter.

3.2 Mitigation Techniques based on Space Debris Size

Space debris mitigation techniques are usually classified to target three different space debris groups. They are based on the size of the wreckage. Manoeuvring techniques are used to avoid collisions with large objects or debris, greater than 10 cm in diameters. However, non-operational space objects including space debris and satellites without propulsion are always in danger; they simply collide with each other. Satellites with propulsion can avoid collisions by performing manoeuvres to reduce the collision probability; ISS is an excellent example.

A shielding technique is used to protect space systems from small sub centimetre size debris particles, which are difficult to mitigate its impact if they cross paths and a collision is going to happen because such debris particles are very hard to detect and track in orbit. NASA, for example, used space systems lightweight shielding for collision protection on the ISS. It is called multishock [59] and forms as a bumper, which is made of several layers of ceramic fabric, as shown in Figure 20.

Figure 20: Space systems shielding

The third mitigation technique type is to mitigate mid-size space debris, between 1 and 10 cm in diameter. Debris in this size range is quite large to be shielded against, and it is not feasible to manoeuvre an operational space system to avoid collision with them, as there are hundreds of thousands of them orbiting the Earth.

Geostationary satellites are usually transferred to the disposal orbit when they reach their EOL. However, this is not the case in LEO, as satellites in LEO tend to be left in orbit for natural decay. Most space debris orbit the Earth in LEO at very high orbital velocities, around 7 km/s, with great inclination, so they will stay in orbit for about ten thousand years before they decay and re-enter the atmosphere. A collision between two objects in LEO could occur at very high relative velocity, which could reach to 14 km/s and as discussed in Chapter 1 that at this hypervelocity the kinetic energy is enormous and any impact, even with small sized debris, could disable a subsystem or destroy a small satellite. Space debris will always pose a high threat to astronauts and objects in space, especially to the operational ones. This issue becomes even worse as the number of space debris in orbit is increasing with every breakup or collision in space and with every launch event. On average, there are 80 launch events per year, and usually, each event leaves at least one to three rocket bodies in space. Therefore, this dilemma will not solve itself, at least in the near future, and thus mitigation strategies are now essential to sustain the space environment and provide free access to space.

3.3 Impacts of Laser Energy and Beam Radius on Laser Treatment

In Chapter 2, we explained the usability of the laser as an engineering tool. It has so many applications in industry, and that is true even in the space industry including SSA as lasers could affect space debris from detection and tracking to deflection, ablation and removal. It is a handy engineering tool to detect objects in space that are not detectable or trackable using radar, especially for non-metallic space objects. Lasers have the potential energy that can be used to melt, boil, ablate and deflect objects in space remotely without sending a spacecraft to fly by the object in orbit and remove it. This is in most cases a perilous mission to perform because orbital debris tends to tumble and fly in formation and thus sending a satellite to do a mechanical removal will leave the mission satellite in a position where there is at least one debris somewhere behind or ahead of the removal satellite. Whereas, debris illumination by high power laser provides a contactless near-term mitigation technique from a very great distance.

Melting and boiling some of the debris material can reduce its size and so reduce its kinetic energy if it collides with another object in space. As a result, this can reduce the potential risk of orbital debris to any operational space system. Having said that, melting some of the surface material of the debris without boiling or evaporating it will make the problem of space debris even worse. The reason why is because although it will reduce the kinetic energy of the parent debris; at the same time it will produce more little debris, which will contribute to the space debris catalogue, even more, so more new debris to detect, track and deflect and more debris to manoeuvre and avoid a collision with.

On the other hand, laser ablation is the technique that we propose to use to ablate some of the wreckage material in LEO and create impulsive delta-v that can act as a small thrust on the wreckage. Figure 21 and Figure 22 have been produced using AutoCAD software application to show the three-dimensional (3D) geometry and the two-dimensional (2D) geometry, respectively, of an ideal conical ablated material between two subsequent laser pulses.

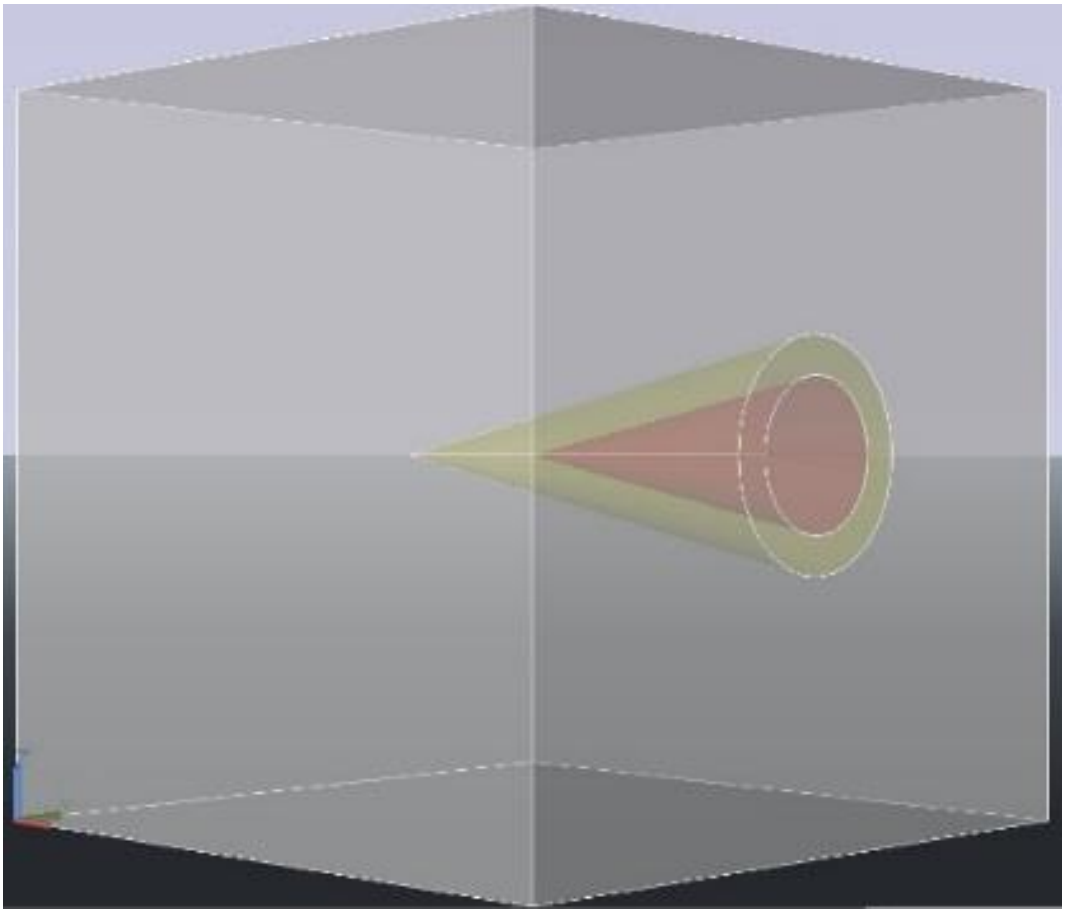

Figure 21: 3D geometry of an ideal ablated cone

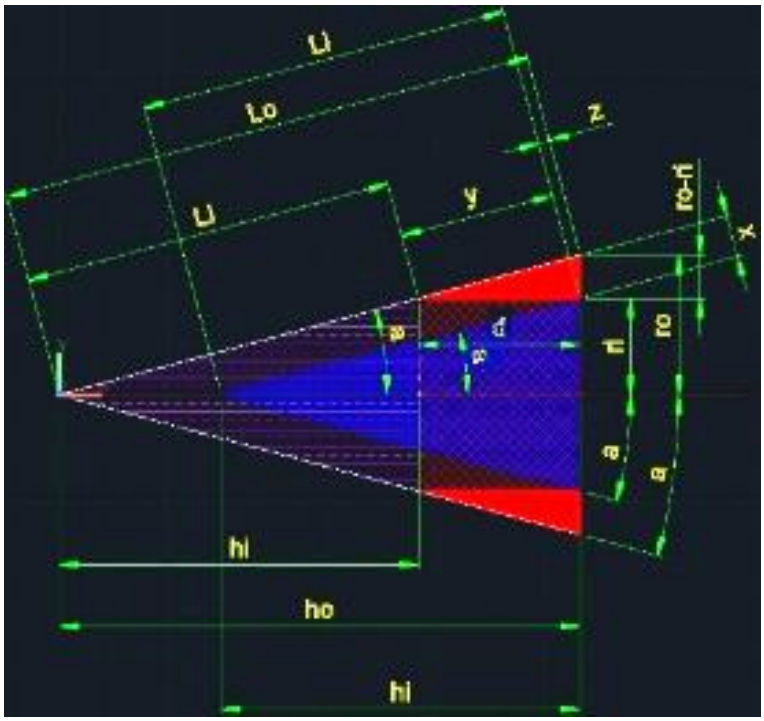

Figure 22: 2D geometry of an ideal ablated cone

Objects in Earth orbits have unique orbital velocity at each moment; any technique resulting in reducing its speed will lead to reducing its altitude and thus its lifetime in orbit. Therefore, the small thrust that can be generated by laser ablation will be able to change the orbital velocity of the space debris and lower its perigee. Varying the orbital velocity of space junk, at any given time, will result in leaving the junk in a new orbit. When the object is at its perigee, the orbit eccentricity tends to circularise the orbit over time at the same altitude as its perigee due to the atmospheric drag. The change in orbital velocity depends on many factors such as the debris mass, its material, size and altitude. Of course, it also depends on the spot size, power and pulse duration of the laser beam. If sufficient laser energy is delivered to space junk, it will ablate some of its surface material and the more the laser energy, the more the ablated materials from the junk.

3.3.1 General Assumptions

In this chapter, we made a couple of general assumptions in order to perform our simulations and calculations. Those assumptions include the use of a high-power pulsed laser beam with 50 percent atmospheric transmission for the Nd^{3+} Glass laser system on the ground, operating at 1.06 µm wavelength. That means only half of the laser power will pass through the atmosphere. We also assumed that precise detection and reliable tracking capabilities are available in addition to the very accurate targeting techniques to

keep the laser illumination focused on the space debris. The thermal and turbulence effects are ignored and the simulation in this chapter assumed that the targeted object is a homogeneous and pure spherical aluminium debris with 10 cm diameter that orbits the Earth at 800 km altitude. For debris removal, aluminium is a quite a challenging object to be removed as it has a quite high melting temperature of 933 K and also a high boiling temperature of 2,743 K comparing to other metals. The reason why we picked aluminium to run the simulation is that aluminium is one of the most commonly used materials in manufacturing and constructing space systems, as illustrated in Chapter 2.

3.3.2 Melting and Boiling Debris in Space with Lasers

This section simulates the thermal properties of an aluminium space debris that has ten cm diameter of an equivalent sphere. In this simulation we assumed that the space debris is heated directly by the laser beam through the interaction process and also by the direct daylight solar flux which is about 1.366 kW/m^2 as shown in the following power balance equation:

$$Power\ Received\ by\ Debris = (Laser\ Power\ Density + Daylight\ Solar\ Flux) \times Debris\ Cross\ Sectional\ Area \quad \text{Equation 3.1}$$

Laser density is assumed to be constant during the interaction time of the laser with the object in space. The space debris initial temperature is assumed to be about 270 K for the simulation. Access to the space debris from laser system was assumed to be limited to 600 seconds, that is the line of sight access which is 10 minutes. So, any change in the material phase of the debris particle can only be considered if the total duration of interaction between the laser beam and the material is less than 600 seconds. MATLAB codes were created to simulate the thermal profile and the temperature increase of the debris surface due to a laser firing at the wreckage material at different laser powers and spot size. Figure 23 shows the thermal profile of aluminium debris when it is irradiated by a laser beam of 50 kW power and 30 cm beam radius on the target.

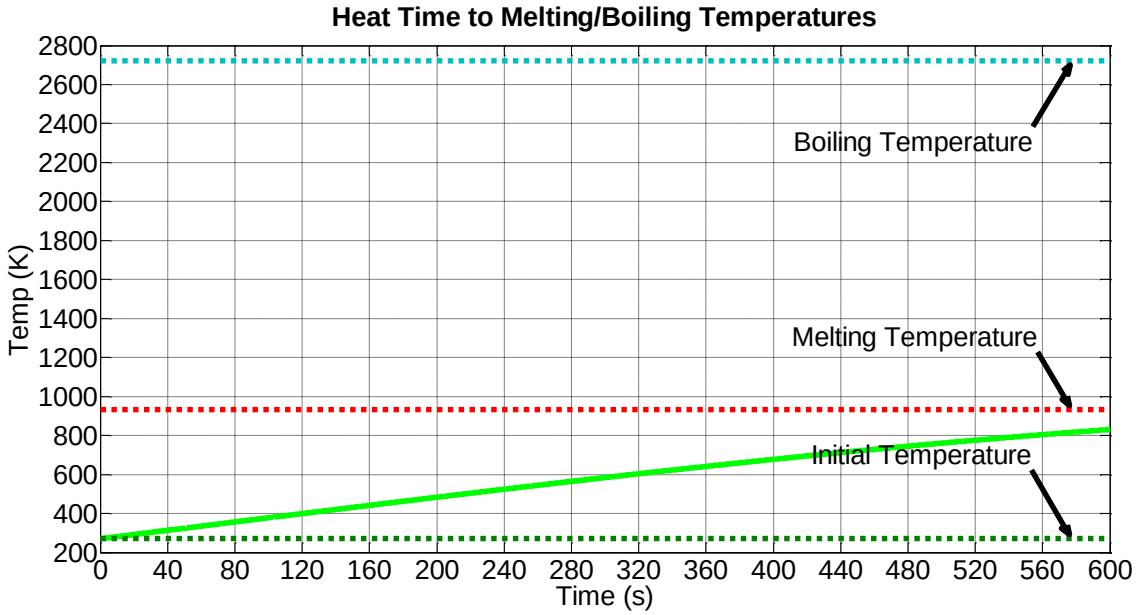

Figure 23: Thermal profile of aluminium debris irradiated by 50 kW laser power with 30 cm laser beam radius

It is important to note that during 600 seconds of access, the green curve of the material temperature increased gradually but never reached the melting temperature of the aluminium, which is 933 K, meaning all the power was wasted and left no effect on the debris. Changing the delivered laser power and the spot size of the laser beam on the target will dramatically change the thermal profile of the wreckage. Figure 24 shows the thermal profile of the wreckage after we doubled the delivered laser power (i.e. 100 kW) and decreased the laser beam radius on the target to 10 cm to make the laser beam more focused on the space debris.

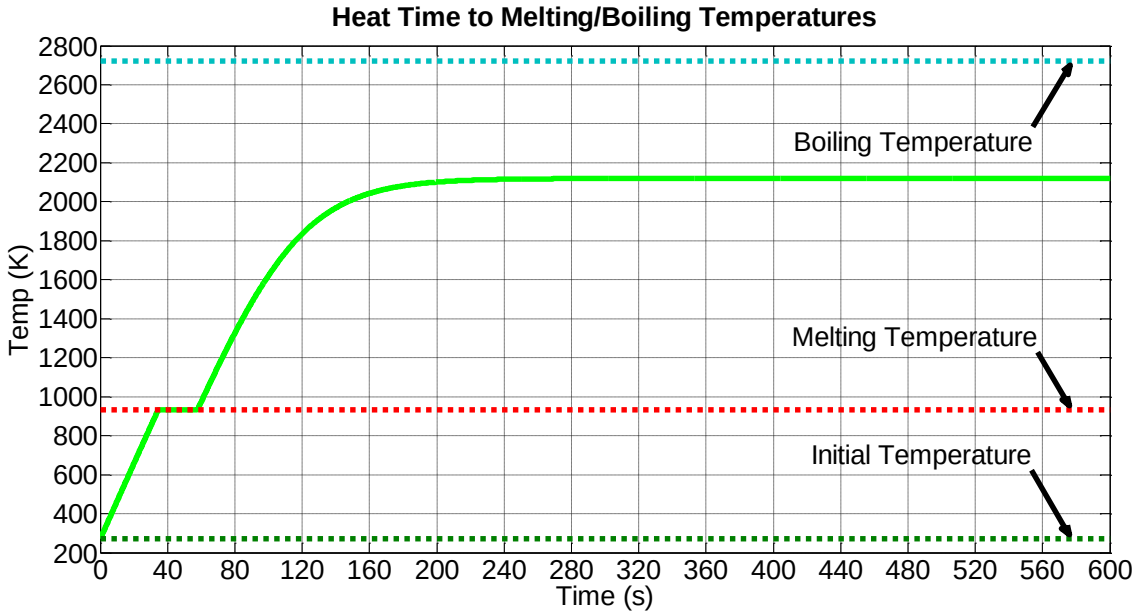

Figure 24: Thermal profile of aluminium debris irradiated by 100 kW laser power with 10 cm laser beam radius

The figure shows that the aluminium temperature climbed quickly (within 40 seconds) to its melting temperature and as the laser beam delivered more heat energy, the temperature of the debris surface increased even more but never reached the boiling temperature. Therefore, there was only one phase change from solid to liquid but not from liquid to gas. That is because the final temperature is quite far from the aluminium boiling temperature, which is 2,743 K. Also as mentioned earlier in this chapter, melting some of the debris material without boiling or evaporating them will make the problem of space debris even worse because that will produce new tiny debris, which will build the space debris catalogue.

Decreasing the laser spot radius even more or to the half (i.e. 5 cm) was also investigated. This change shows a better thermal profile for the debris material even with less laser power like 75 kW. The results are illustrated in Figure 25. The temperature of the aluminium debris in this scenario climbed to the melting temperature rapidly, and due to the focused laser beam, the temperature jumped again to the boiling temperature. These temperature changes happened in just under 80 seconds.

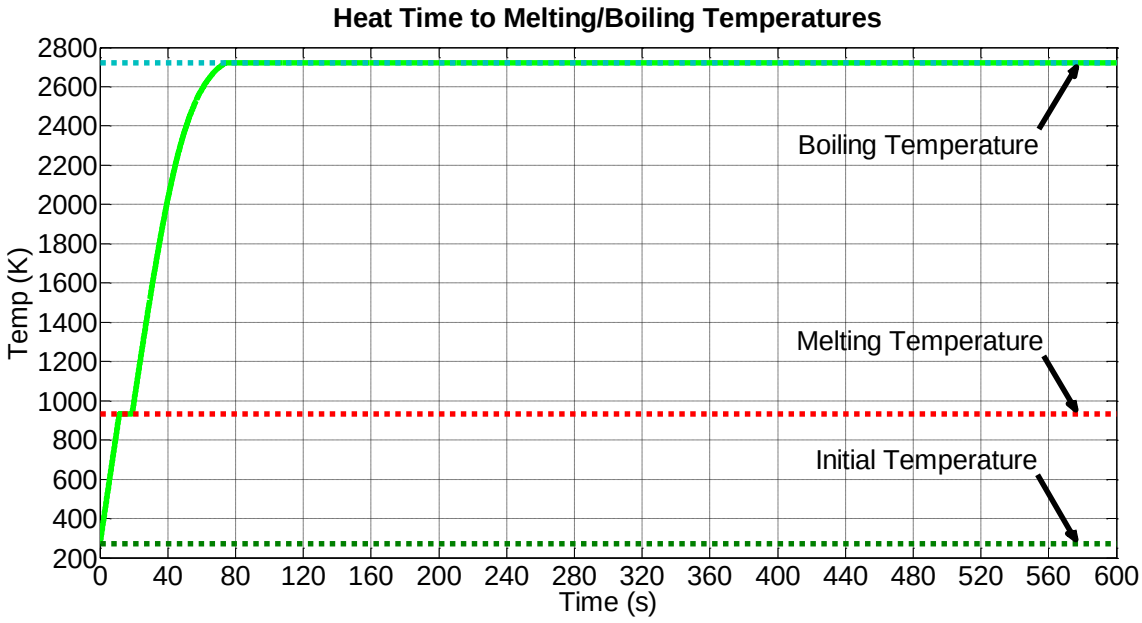

Figure 25: Thermal profile of aluminium debris irradiated by 75 kW laser power with 5 cm laser beam radius

It can be noticed that some of the wreckage material boiled, but due to the limited access time of 600 seconds, the debris did not reach the desired size, which is about 1 cm or less in diameter. However, putting back the laser power to 100 kW and fixing the laser spot radius to 5 cm shows perfect results within the limited 600 seconds access window. With this setup, the aluminium surface temperature jumped from its initial

temperature of 270 K to its melting temperature of 933 K in just under 10 seconds and then jumped again to the boiling temperature of 2,743 K within the next 30 seconds, as represented in Figure 26. The results show that the laser power and access time were sufficient to boil most of the debris material and reduce its diameter to less than 1 cm within 555 seconds only.

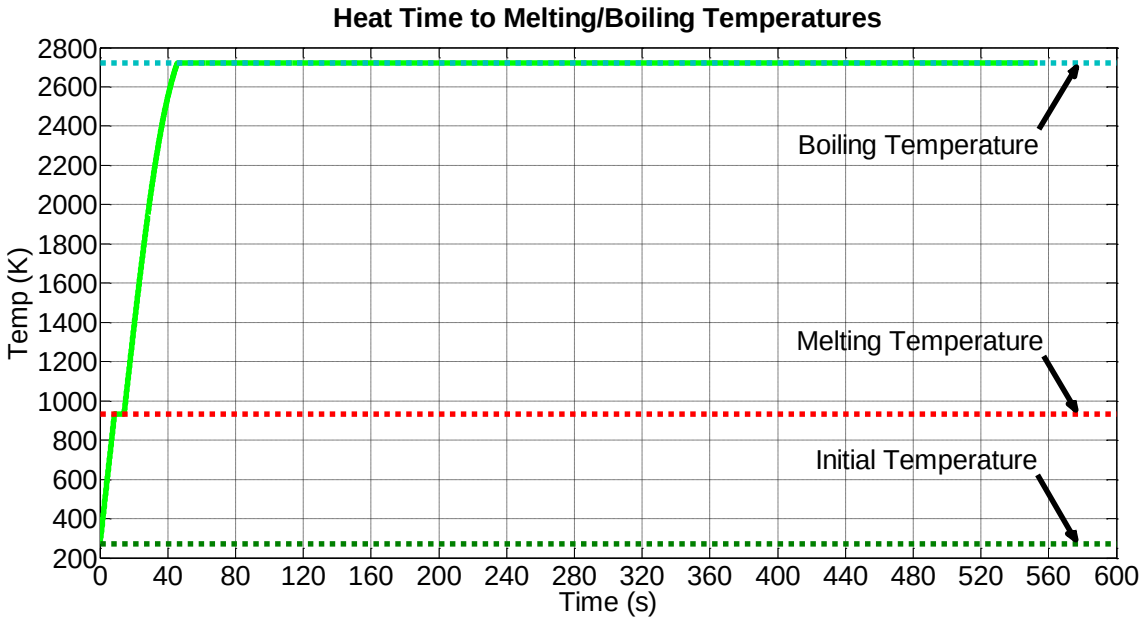

Figure 26: Thermal profile of aluminium debris irradiated by 100 kW laser power with 5 cm laser beam radius

The figure also shows the two phases of transition of the wreckage material, from solid to liquid during the melting phase and then from liquid to gas during the boiling phase. The melting transition phase starts after 8.5 seconds when some of the debris material temperatures reach 933 K, which is the aluminium melting temperature. This melting transition phase stays for about 6 seconds before the temperature of the wreckage become higher than the melting temperature, and most of the wreckage is transformed from solid to liquid. Figure 27 shows that it requires about 560 kJ of heat energy over the period of about 6 seconds to complete the melting transition phase.

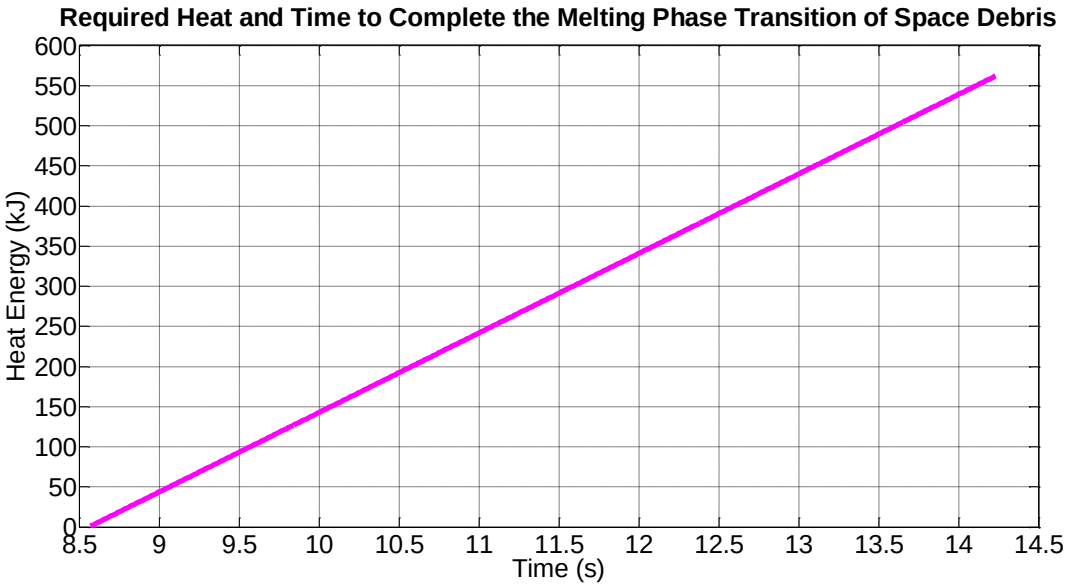

Figure 27: Required heat and time to melt 10 cm diameter solid aluminium debris by 100 kW laser power with 5 cm laser beam radius

The boiling transition phase starts at 45 seconds when some of the wreckage material temperatures reach 2,743 K, which is the aluminium boiling temperature. This boiling transition phase stays for about 510 seconds before most of the debris is transformed from liquid to gas as shown in Figure 28. This figure also demonstrates that it requires about 16.5 MJ of heat energy over the period of about 510 seconds to complete this boiling transition phase. The slope of the required heat line for the boiling phase is about a third of the slope of the required heat line for the melting phase, and that is why the boiling phase takes much longer.

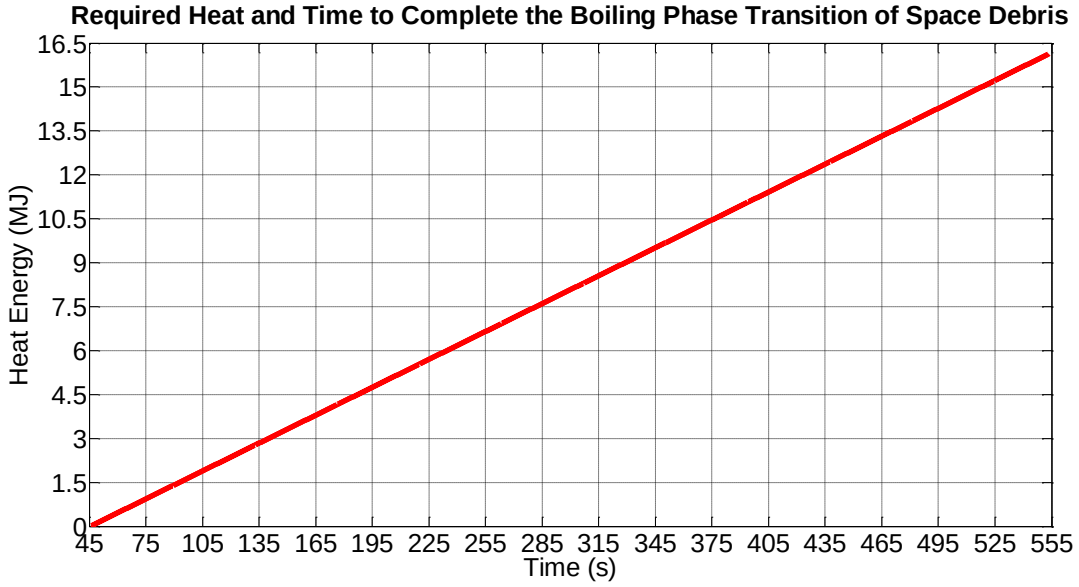

Figure 28: Required heat and time to boil 10 cm diameter melted aluminium debris with 100 kW laser power with 5 cm laser beam radius

The radiated power from the space debris was also simulated using MATLAB codes and the results are represented in Figure 29. During the boiling transition phase, the aluminium space debris radiated 68.25 kW of power, which is huge compared to the radiated power of only 932.70 W during the melting transition phase (i.e. ratio of 1:73).

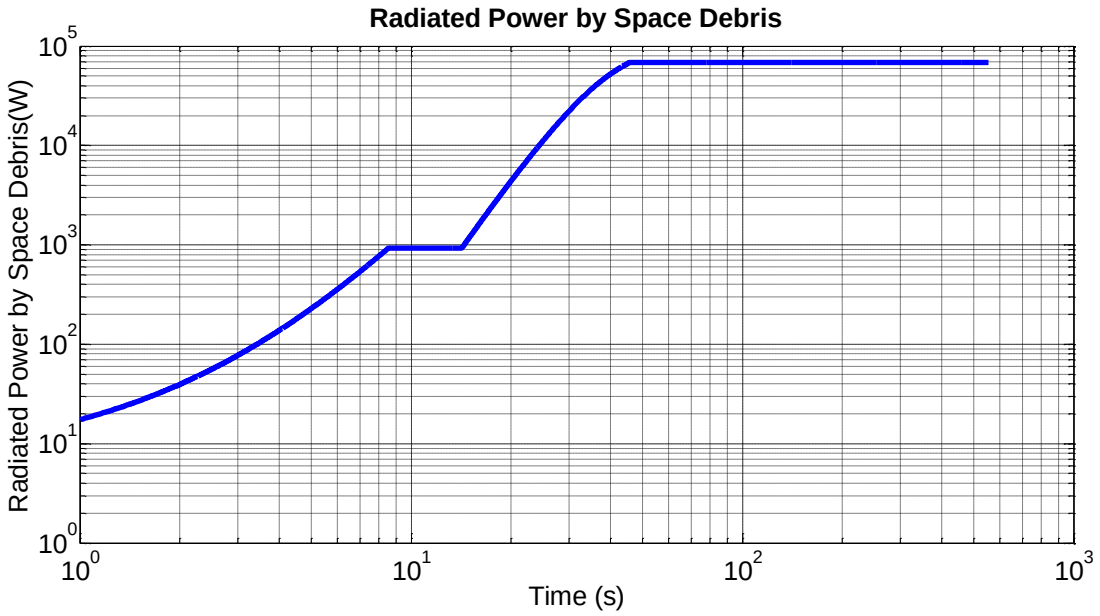

Figure 29: Radiated power by irradiated aluminium space debris with 100 kW laser power with 5 cm laser beam radius

3.4 Laser Power Density Distribution (PDD)

The following two sections will investigate the laser Gaussian power density distribution (PDD) and the laser top-hat PDD for the laser beam that we discussed in the last case of the previous section.

3.4.1 Laser Gaussian PDD

Simulating the normal or Gaussian distribution of laser beam power density is essential to determine the power density (intensity) at different radii of the laser beam. The following equation defines the Gaussian PDD:

$$I(x,y) = \frac{8P}{\pi d^2} e^{\left[-\left(\frac{2\sqrt{2}}{d}\right)^2 \cdot (x^2+y^2)\right]} \qquad \text{Equation 3.2}$$

Where:

P = Power of the laser [W]

d = Diameter of the PDD [m]

x and y are the coordinates on the x, y plane

Figure 30 shows the power intensity profile of the Gaussian laser beam or the Gaussian PDD of the 5 cm laser beam radius with 100 kW power that we discussed in the previous section to boil space debris of 10 cm in diameter and reduce its size to 1 cm or less in diameter. The first plot on the top-left hand corner shows the 2D density profile of the Gaussian beam that is propagating out of the paper. The centre of the beam has the highest density. That is the peak density, which is about 25.5 MW/m^2. The other three plots show the intensity field amplitude curves for the same Gaussian laser beam.

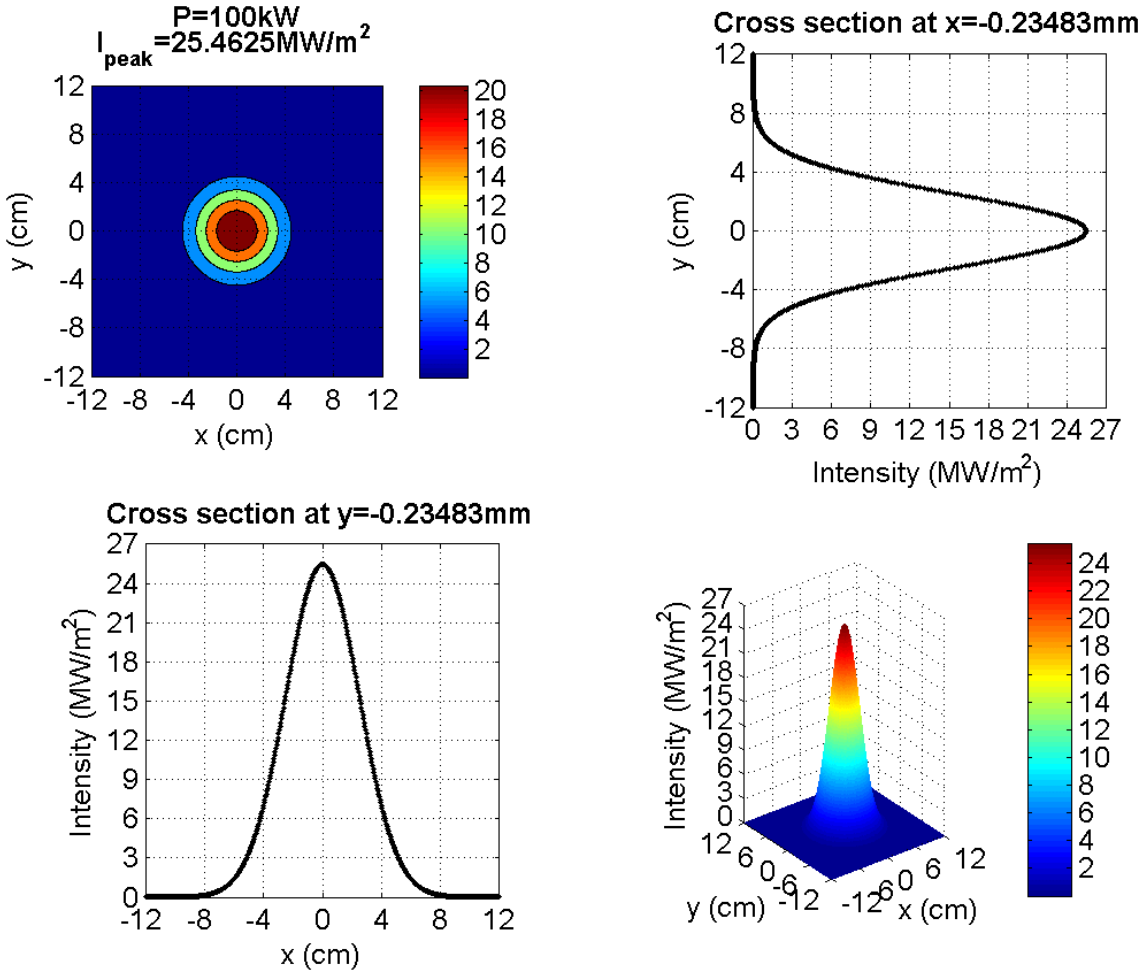

Figure 30: Laser power intensity profile of Gaussian laser beam (Gaussian PDD)

3.4.2 Laser Top-Hat PDD

The laser beam has a near-uniform energy density or fluence within a circular disk that is shaped by diffractive optical elements from the Gaussian laser beam. The circular disk shape is similar to the form of a top-hat. The top-hat beams based on the circ function are used in very high-energy laser systems, and the following equation defines its PDD:

$$I(x,y) = \begin{cases} P \Big/ \left(\pi \frac{d^2}{4}\right) & , \sqrt{x^2+y^2} \le \frac{d}{2} \\ 0, & \sqrt{x^2+y^2} > \frac{d}{2} \end{cases}$$

Equation 3.3

The top-hat power density profile or the top-hat PDD of the same 5 cm radius Gaussian laser beam with 100 kW has been simulated, and the results are shown in Figure 31. The first plot on the top-left hand corner shows the 2D top-hat profile of the Gaussian laser beam that is propagating out of the paper plane. It is clear that the peak intensity at the top-hat PDD is almost half the peak intensity at the Gaussian PDD. This can be considered as a disadvantage of the laser top-hat PDD. The other plots show the intensity field amplitude for the same Gaussian laser beam.

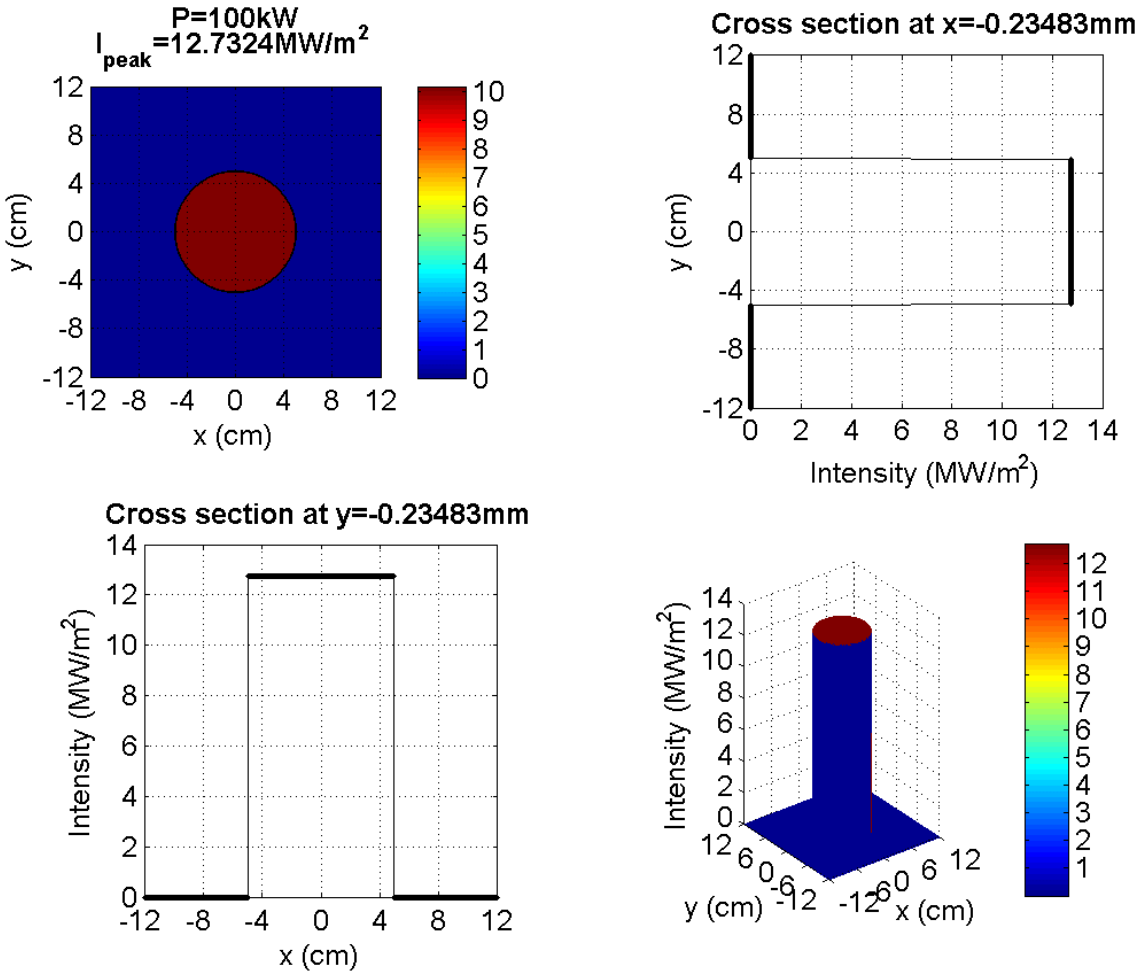

Figure 31: Laser top-hat power density profile (top-hat PDD)

3.5 Impact of Laser Repetition Rate on Laser Treatment

This project is proposing to use high power pulsed lasers and not continuous wave lasers to mitigate space debris in LEO. Thus, the repetition rate of the laser pulses needs

to be very precise. In general, the overlap between each consecutive laser pulse mainly depends on three factors. These factors are the size of the laser beam at the target, the pulse frequency (i.e. repetition rate) and the relative velocity between the laser beam and the space debris. Obviously, low laser pulse frequency leaves a gap between each consecutive laser pulse and that leads to the material to cool down before the next laser pulse arrives. Leaving the material to cool down will reduce the amount of the ablated material from the space debris. This has been simulated for a 10 cm diameter circular laser pulse with 500 Hz pulse repetition frequency (PRF). The relative velocity was assumed to be 80 m/s. The results in this scenario show that there is no overlap between any laser pulses, however; there is a 6 cm gap between each consecutive laser pulse, as shown in Figure 32.

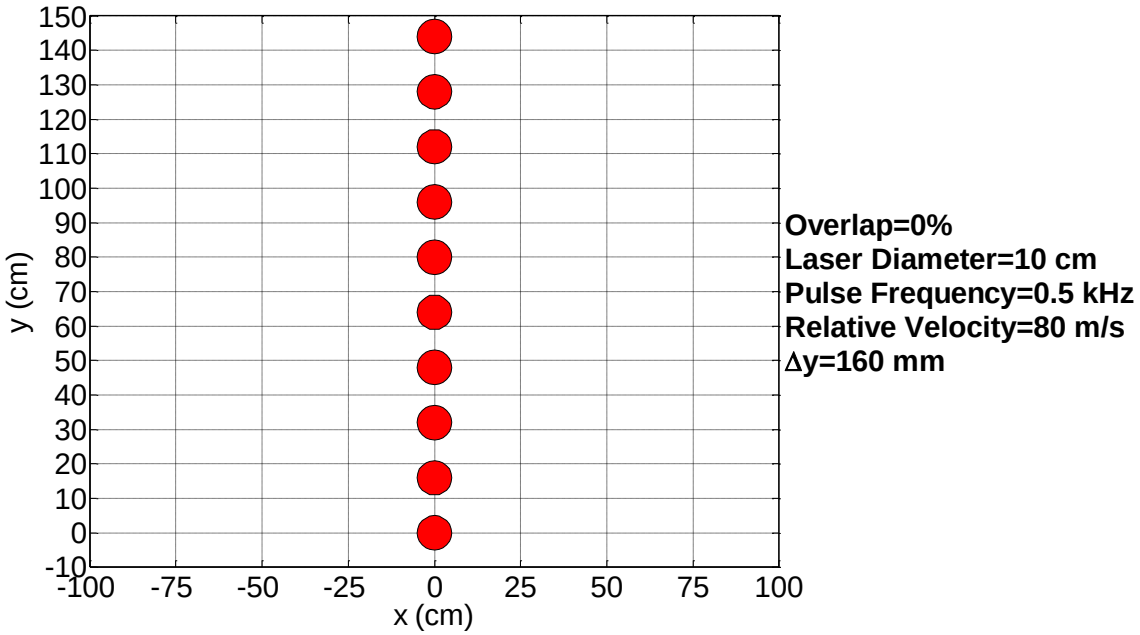

Figure 32: Overlap in laser pulses at 0.5 kHz

Another scenario has been simulated after only increasing the laser PRF to the double (1 kHz), but this increase seems to be too much because it leads to creating an overlap of 20% between each consecutive laser pulse. This overlap is quite large and leads to waste the generated power for each laser pulse by 20% as well, see Figure 33.

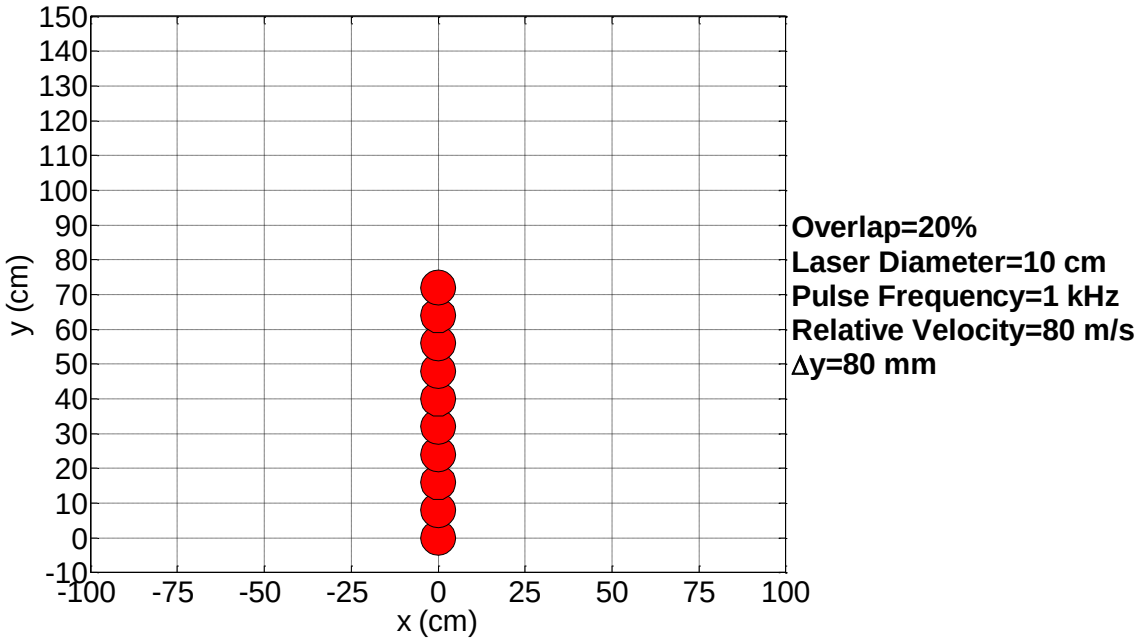

Figure 33: Overlap in laser pulses at 1 kHz

The best scenario would be the one that has no gaps or at least a minimal gap between the consecutive pulses. Therefore, a third simulation has been done by changing only the repetition rate or the laser frequency from 1 kHz to 750 Hz. The results were very close to the best scenario. The gap was only 6.67 mm between each consecutive pulses, as shown in Figure 34.

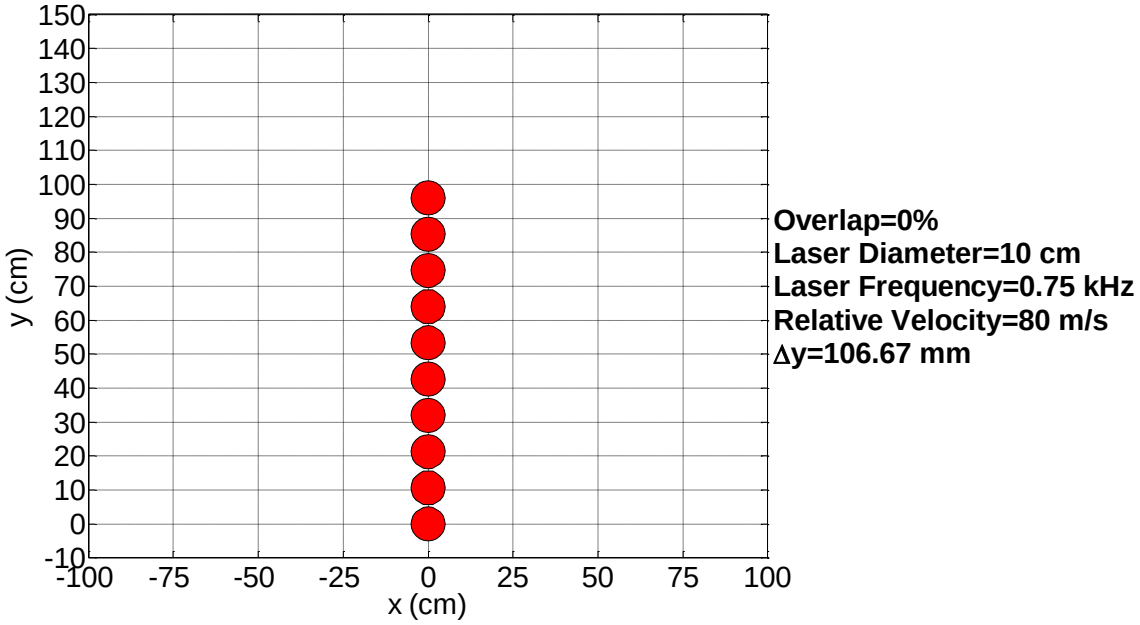

Figure 34: Overlap in laser pulses at 0.75 kHz

This scenario provides the debris material with a minimal time for cooling down before the next laser pulse arrives at the surface of the wreckage. It boosts the temperature

climb of the debris surface material and enhances the ablation process. This also improves the interaction model between the laser pulses and the orbital debris with minimum power and a short time. Irradiation of three different space debris materials with laser pulses will be investigated in the next chapter, Chapter 4.

Chapter 4

Irradiation of Space Debris with Laser Pulses: Kinetic Theory

4 Irradiation of Space Debris with Laser Pulses: Kinetic Theory

4.1 Summary

This chapter will focus on the irradiation of orbital debris with laser pulses. Experimental data from targets temperatures have been used for the development of the ablation model. The evolution of spatial temperature distribution has been simulated in this chapter for three different surface materials of space debris illuminated with laser pulses. Kinetic theory is used in this chapter to simulate the phenomena of heat conduction and discuss the results on three different space debris materials.

4.2 Employment of Experimental Temperature Data

Impacts on metal targets by concentrated laser pulse heating has been examined by utilising several methods in the literature. Some work has been done for target surface radiant temperature measurement under vacuum environment and utilising spectral methods [60]. The authors utilised a one-dimensional, Fourier conduction classical model to determine the metal surface temperature temporal evolution. However, they found that when the vaporisation regime was considered, the equations became very complex to analyse and simulate. Another method of measuring the target temperature has been used by directly measuring the thermoelectric signals from a thermocouple junction that is located at the target rear [61]. The idea of this technique is to try to measure the spatial and temporal evolution of the material temperature when the target is exposed to a high power laser pulse. However, this technique has insufficient spatial and temporal resolution, but some others succeeded in calculating the velocity of the interaction process, like drilling, by recording the drilling time for a known metal thickness. This has been accomplished by utilising two detectors to trigger a timer, one at the front and another one at the rear of the target. This drilling velocity appeared to be high compared to the estimated velocity by using the Kinetic theory model when evaporation is occurring. This technique presents big errors mostly because:

1. The technique is inappropriate to include the entire domain of the fusion operation, as it is impossible to enhance the temporal resolution. Also, due to the fact that the evaporated plasma absorbs the incident laser radiation.
2. The thermoelectric signal corresponding to the temperature has the highest value at the metal fusion temperature and therefore has a limited domain and

thus any further extrapolation to approximate the evaporation temperature will be imprecise.

The spectroscopic method has been used to estimate the target surface temperature that is irradiated with Nd^{3+} Glass laser pulses. The target material surface evaporation needed 50 µs. The data that has been employed in this thesis were experimentally measured for the target material surface irradiation (i.e. collected the target interaction zone radiation levels). The spectrum was sampled between 662.4nm and 950.0nm, and the ambient temperature in the laboratory during the calibration was 24°C with ± 2°C [62]. In these experimental data, two-colour temperature measurement was used and it was assumed that the emissive power intensity ratio at two spectral frequencies could be correlated with the fitted radiation curve of the black body see Figure 35. This helped in estimating the temperature. The emissive power ratio temporal evolution was used to estimate the correlated time-dependent target surface temperature history. The time needed for material surface evaporation was of the order of 3µs, and so it was sufficient for the emissive power ratios to be sampled at 200ns. The results were obtained by focusing Nd^{3+} Glass laser pulses down to a 750µm diameter spot at e^{-2} intensity points. The laser pulse length was 1.48ms and pulse energy was constantly varying between 6.08J and 19.78J.

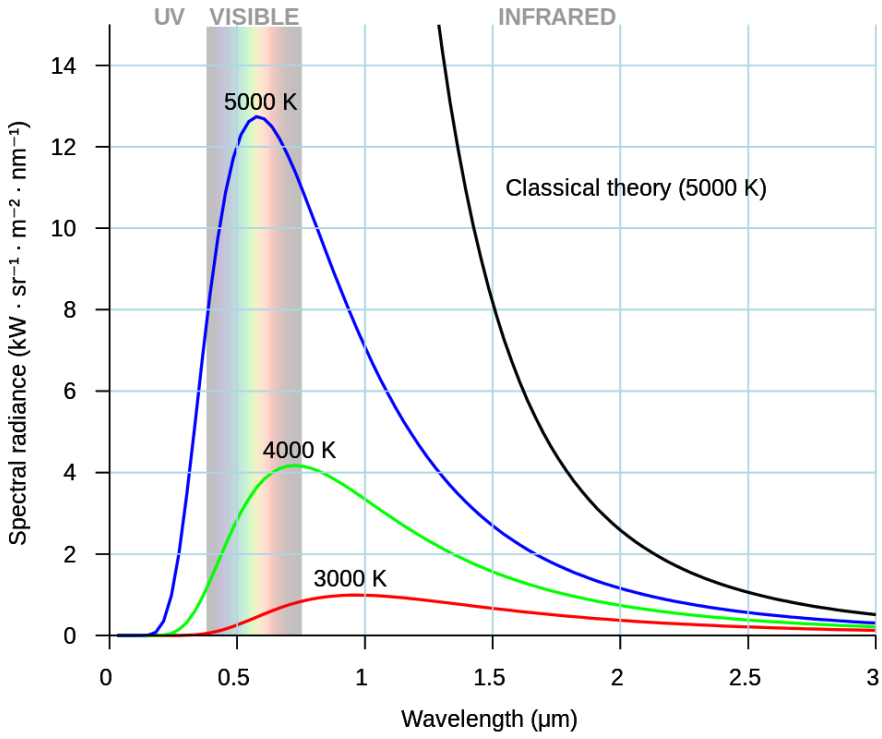

Figure 35: Black body curves of Planck at different temperatures

4.3 Simulation of Spatial Temperature Distribution Evolution in Space Debris Beamed with Laser Pulses

To understand any laser-space debris interaction process, it is necessary to study the temperature distribution in the orbital debris due to this interaction. This section provides physical characterisations of the dominant energy transport mechanisms when a laser irradiation pulse is interacting with the surface of space debris. Radiant energy is absorbed by the interaction between photons and electrons above the Fermi surface. This interaction increases the electrons' kinetic energies in the conduction band. Excited electrons are giving up some of their kinetic energy when colliding with lattice phonons. Electrons can collide with themselves too or give back their irradiation by spontaneous emission. Laser energy absorption occurs during photon interactions with free and bound electrons in the material structure of the debris where these electrons are raised to higher energy levels [63]. If that photon energy is big enough, the photons can be absorbed by the valence electrons too, which are then excited to the conduction band. Immediate energy transfer to lattice phonons from photons is possible too, however, because of the relatively small collision cross-section the portion of the energy transferred in this way is not considerable [64]. Therefore, in general, the energy of a photon is transferred to the electrons initially and after that to the lattice phonons. Colliding electrons, on the other hand, have equal overall kinetic energy before and after they collide with each other, i.e. electron-to-electron collision is elastic [65].

Due to the relatively large mass of lattice molecules compared to the electron mass, just a small portion of the excited electron energy is transferred through a collision with the lattice. Hence, the electrons begin to be very hot compared to the lattice phonons, and so lattice phonons and electrons are at different temperatures. The rate of change of electron temperature is larger than the rate of change of the phonon temperature change, although in the beginning, the phonon temperature is slightly smaller than electron temperature. As time evolves, the difference begins to be larger. Therefore, the new kinetic model contains the non-equilibrium condition between phonons and electrons. At high irradiation intensities, the variation is evident due to the fact that the energy transfer rate from electrons to phonons is small. The variation value relies on the incident power and the energy transfer rate between electrons and phonons. The electron-to-electron collisions mean free path is a few orders of magnitude bigger in comparison of an electron to phonon collisions, and thus the electron-phonon collisions can be excluded [66].

4.4 Fourier theory and Kinetic theory

In this thesis, Fourier theory and Kinetic theory are employed to simulate the phenomena of heat conduction in three different orbital debris materials. The computational results provide a theoretical prediction of the temporal and spatial temperature distribution based on two assumptions of the power intensity distribution, which are circ function assumption and Gaussian assumption, which represent the worst- and best-case scenario. As the real intensity distribution of laser radiation approaches Gaussian distribution, this thesis focused on the computations that are based on Gaussian assumption. The Gaussian profile provides the top end of the simulation, whereas, the circ function profile provides the bottom end of the simulation and thus it will also be discussed. The main focus of this chapter is the Kinetic theory; Fourier theory will be discussed in detail in the next chapter.

4.5 Kinetic Theory of Energy Transport

Depending on the space debris physical properties, the energy transported to the wreckage material from the laser radiation differs. Through the absorption period, the energy of the incident beam is transformed to a temperature rise in the space junk material. This temperature rise relies on the magnitude of the laser energy that is associated with this process. The temperature of the space debris material at its surface and the lower layers can be increased to achieve one or more of the material transformations, which are heating, melting and vaporisation. This is similar to the phenomena that occur in heat transfer, which is shown in Figure 36.

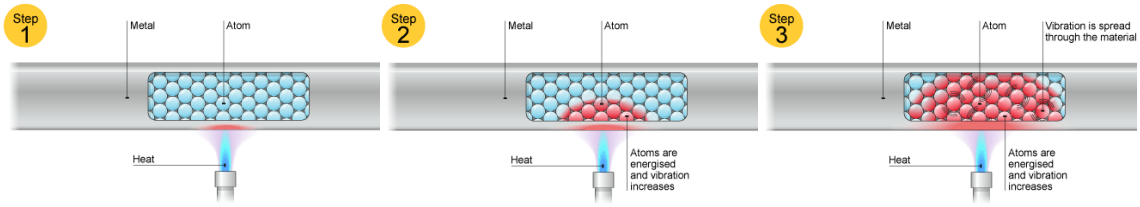

Figure 36: Heat transfer phenomena by conduction (Credit BBC.co.uk)

The Kinetic electron theory is employed in this thesis to estimate the targeted space debris temperature profile. An electron Kinetic theory version supposed that electron movement as one-dimensional and that electrons and phonons are in equilibrium; it also assumed that the spatial temperature distribution follows an exponential curve [67,68]. A few corrections have been applied to this version of the Kinetic electron theory. Also, similar supposition has been put with regarding the equilibrium between phonons and electrons, but then it has been developed by proposing that for each electron-phonon

collision, just a little electron energy portion moved to the phonons, which creates non-equilibrium situations between the phonon and electron populations [69]. To link the transfer process of the energy between electrons and phonons, a macroscopic technique was utilised and the two-temperature system, as supposed in the targeted object, but this model is correct only for illumination by ultrashort laser pulses (picoseconds) [70]. An energy transport model has been built on the Kinetic electron theory to compute temperature profiles in metals. This model has been utilised to simulate the interaction process of a high pulse repetition frequency CO_2 laser beam at 10.6 µm wavelength with different target materials. The model integrated the non-equilibrium potential between phonons and electrons and in this thesis, this model has been utilised to simulate the spatial temperature distribution evolution in three different space debris materials when illuminated by Nd^{3+} Glass laser pulses. The three materials are aluminium, copper and nickel. These materials have been used as samples from the most commonly used materials to manufacture space systems, and thus they potentially are the most common space debris materials. The electron temperature and the lattice temperature profiles are discussed, in the following subsections for both: below and above the boiling temperature of each of the three space debris materials.

4.5.1 Kinetic Theory Model: Below Boiling Point (BBP)

The three different space debris materials temporal and spatial lattice and electron temperature distribution, below the boiling point (BBP), are computed at 50 ns time intervals by utilising the Kinetic theory model that is developed and described by Byabagambi [71]. This model is also used in the electron transport phenomena description. It relies on the supposition that the transport of electron energy is from all areas of the space debris areas and that a part of this energy is moved to the lattice through collisions with phonons, see Figure 37. The same supposition is reported by Lee [72]. The energy transport mathematical expressions derivation and assumptions for this Kinetic theory model are presented later in this subsection.

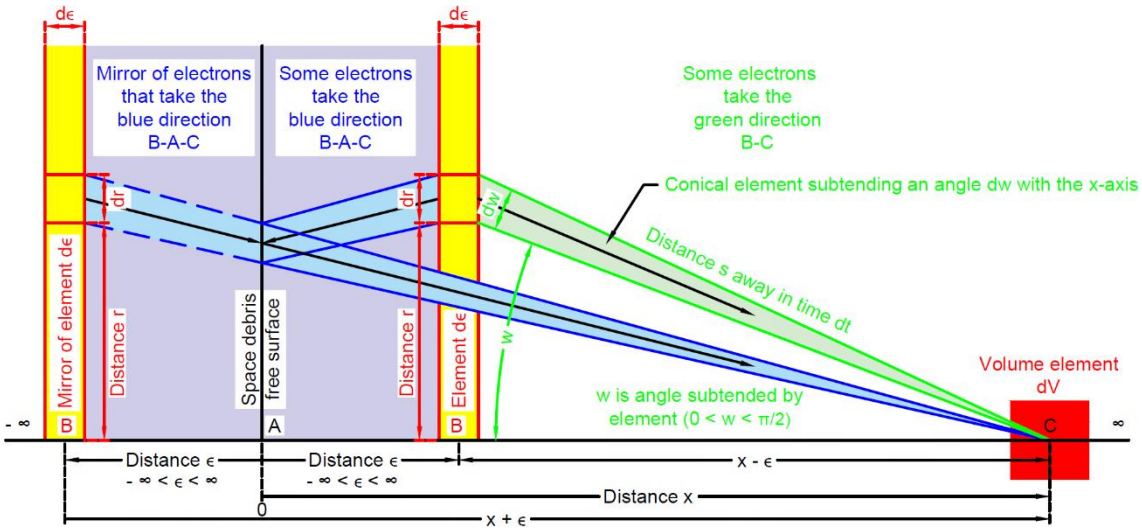

Figure 37: Movement of an electron inside metal space debris for the top half of the cone. Electrons transport energy from all the debris areas and part of this energy is moved to the lattice through collisions with phonons. The left-hand side of the free surface illustrates the mirror image method and $x = 0$ represents the free surface.

The challenge is in calculating the number of electrons that leave an element $d\epsilon$ after colliding there and then experience their next collision in a volume element dV a distance s in time dt in a conical element meeting an angle dw with the x-axis. To start the theoretical simulation, we firstly identified the solid angle as shown below:

$$Solid\ angle\ met\ at\ dV, by\ the\ region, at\ (r, \varepsilon) = {\pi 2r(sdw)}/{s^2} = {\pi 2rdw}/{s}$$

Equation 4.1

$$\therefore Total\ solid\ angle = {\pi 2rdw}/{4\pi s} = {rdw}/{2s}$$

Equation 4.2

$$\therefore Number\ of\ electrons\ resulting\ in\ d\epsilon\ that\ have\ their\ first\ collision\ in\ dV = \frac{rdw}{2s} N' z \frac{d\epsilon dV}{l \cos w} e^{-s/l}$$

Equation 4.3

Where:

N' = Participating electrons number density, those at Fermi surface $\left[{1}/{m^3}\right]$

$z = {v_1}/{l}$ = Electron collision frequency in dV $[Hz]$

v_1 = Fermi electron velocity $[{m}/{s}]$

l = Electron mean free path for collisions with phonons $[m]$

It is necessary to take into account the:

- Electrons that are arriving from the right of dV when $\epsilon > x$
- Electrons in $d\epsilon$ that travel through the free surface wall when $x = 0$ and follow the path from B to A to C, which is the volume element dV

Although several electrons may escape to the surroundings, a steady state charge is supposed so that the number of escaping electrons at a given temperature is always equal to those coming back from the space charge in the interaction surrounding areas at that temperature. So a mirror image method was used to overcome the challenge of electrons reflected from the surface, this is also illustrated in Figure 37. Hence, the challenge is minimised to that of calculating the energy transported from all electrons in $d\epsilon$ at ϵ to dV. That means integrating for all w and ϵ to give contributions from all samples, in another words for $0 < w < {}^{\pi}/_{2}$ and for -∞ < ϵ < ∞. Some electrons collide in dV after they arrive straight away from $d\epsilon$, following the path B to C. So, in this case the:

$$Number\ of\ electrons\ leaving\ d\epsilon\ and\ arriving\ in\ dV = \sin w \frac{dw}{2} N' \frac{v_1}{l} \frac{d\epsilon dV}{l \cos w} e^{\frac{-|x-\epsilon|}{l \cos w}}$$

Equation 4.4

A. Energy of Electron

Electrons from $d\epsilon$ at ϵ transfer energy E to dV in time dt. This can be expressed mathematically as shown in the following equation:

$$E = E(\epsilon, \mathrm{t}) + \frac{1}{2}\left(dt - 2\frac{|s|}{v_1}\right)\frac{\partial E(\epsilon,\mathrm{t})}{\partial t} \qquad \text{Equation 4.5}$$

For the photon absorption process, which relies on the temporal rate of the photon flux change and on the electrons flight time, the same result is needed. Electrons are assumed to absorb the photons that arrive from laser radiation. In fact, photons can be absorbed by free and bound electrons. Quantum mechanics has shown this possibility. However, this process can happen only with the discrete quanta transfer of energy. For model simplification, these quantum impacts will be disregarded, and free electrons assumed to get the laser energy by only crossing the incident radiation electromagnetic field that can be modelled from Beer-Lambert Law [73] that is:

$$I = I_0 e^{-\delta x}$$ Equation 4.6

From this law, the beam intensity is exponentially reduced with deepness in the material. After taking into account the material reflectivity, this field or radiation intensity (after propagating x distance inside the material at t time) can be rewritten as the following:

$$Power\ intensity\ at\ position\ x\ and\ time\ t = I(x,t) = I_0(t)[1 - R(t)]e^{-\delta x}\ \left[{}^{W}/_{m^2}\right]$$ Equation 4.7

Where:

$I_0(t) =$ Radiation intensity at the target surface when x is zero (i.e. power intensity incident on the target surface) $\left[{}^{W}/_{m^2}\right]$

$R(t) =$ Reflection coefficient (i.e. reflectivity at the metal free surface)

$\delta =$ Absorption coefficient $\left[{}^{1}/_{m}\right]$

For a small dp element that is located in between ϵ and x, see Figure 38.

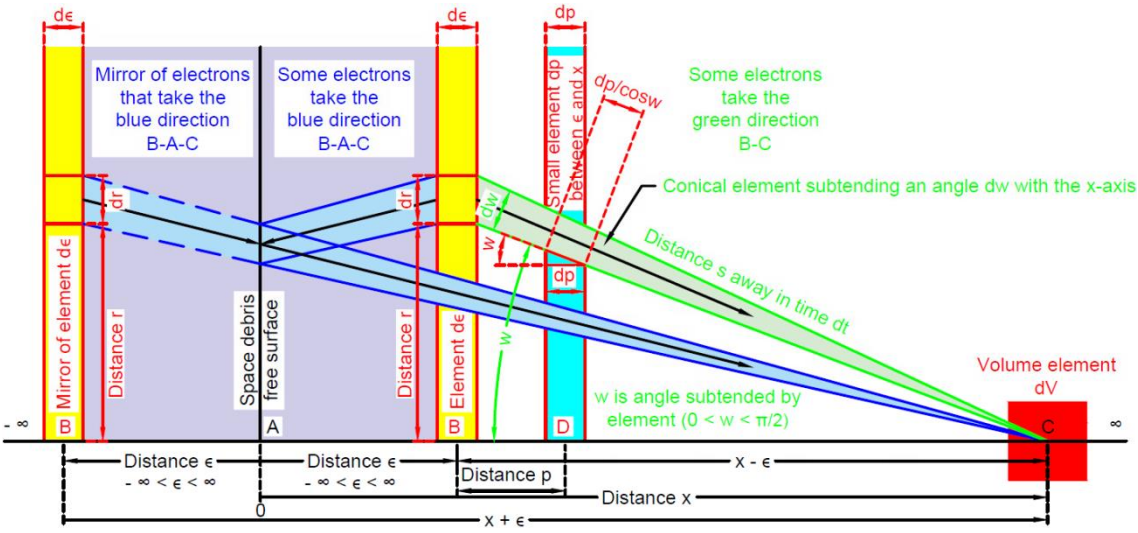

Figure 38: Photon absorption process from ϵ to x

The power absorbed by electrons per unit area at time t can be expressed mathematically as following:

$$I_0(t)[1 - R(t)]e^{-\delta p}\delta dp \qquad \text{Equation 4.8}$$

For equilibrium, this absorbed power should be equal to the electrons energy rise ΔE in the dp element.

$$\Delta E.\,dp = \Delta t\big(I_0(t)[1 - R(t)]e^{-\delta p}\delta dp\big) \qquad \text{Equation 4.9}$$

Where:

$\Delta t =$ Average time interval an electron stays in dp element

Thus the energy absorbed per electron is:

$$\frac{\Delta E.dp}{N'} = \Delta t\,\frac{I_0(t)[1-R(t)]e^{-\delta p}\delta dp}{N'} \qquad \text{Equation 4.10}$$

In fact, the time interval Δt can be calculated from Figure 38.

$$\Delta t = \frac{dp/_{\cos w}}{v_1} = \frac{dp}{v_1 \cos w} \Leftrightarrow \frac{\Delta t}{dp} = \frac{1}{v_1 \cos w} \qquad \text{Equation 4.11}$$

So that the energy absorbed per electron is equal to:

$$\frac{\Delta E}{N'} = \frac{I_0(t)[1-R(t)]e^{-\delta p}\delta dp}{N' v_1 \cos w} \qquad \text{Equation 4.12}$$

From the above equation, as the time evolves, and electrons move from ϵ to x, $I_0(t)$ and $R(t)$ values are changing simultaneously – they are functions of time and, that is why it is extremely hard to calculate the energy absorbed by electrons. However, we know the speed of the electron is extremely high and thus we can assume that $I_0(t)$ and $R(t)$ values are fixed and do not change during the period of time that electrons move from ϵ to x. Thus, by integrating the previous equation, above, the energy absorbed by electron that is moving from ϵ to x will be equal to this:

$$\frac{I_0[1-R]\delta}{N' v_1 \cos w}\left|\int_\epsilon^x e^{-\delta p}dp\right| \qquad \text{Equation 4.13}$$

B. Equations of Energy Transport

The average electron energy that is coming from ϵ and entering the elemental volume dV at x after dt can be determined from the previous subsection, Equation 4.5 and Equation 4.13, as following:

$$E(x,t+dt) = E(\epsilon,\mathrm{t}) + \frac{1}{2}\left(dt - 2\frac{|s|}{v_1}\right)\frac{\partial E(\epsilon,\mathrm{t})}{\partial t} + \frac{I_0[1-R]\delta}{N' v_1 \cos w}\left|\int_{\epsilon}^{x} e^{-\delta p} dp\right| \qquad \text{Equation 4.14}$$

On collision between electrons and phonons, electrons give up some energy, which can be described by this expression:

$$f\left[E(x,t+dt) - E_p(x,t)\right] \qquad \text{Equation 4.15}$$

Where:

$E(x,t+dt) =$ Energy of electron $[J]$

$E_p(x,t) =$ Average energy of phonon (lattice) in dV at x $[J]$

$f =$ Fraction of the excess electron energy that is moved to a phonon due to the collision with that electron (detailed discussion about this parameter in Chapter 7)

From Equation 4.4, Equation 4.14 and Equation 4.15, the overall energy that moved from all electrons to the phonon (lattice) after colliding in dV at x during the period dt can be determined as:

$$\int_{-\infty}^{\infty}\int_{0}^{\pi/2} \sin w \frac{dw}{2} N' \frac{v_1}{l} \frac{d\epsilon dV}{l\cos w} e^{\frac{-|x-\epsilon|}{l\cos w}} \times$$
$$f\left[E(\epsilon,\mathrm{t}) + \frac{1}{2}\left(dt - 2\frac{|s|}{v_1}\right)\frac{\partial E(\epsilon,\mathrm{t})}{\partial t} + \frac{I_0[1-R]\delta}{N' v_1 \cos w}\left|\int_{\epsilon}^{x} e^{-\delta p} dp\right| - E_p(x,t)\right] \qquad \text{Equation 4.16}$$

To simplify writing the above expression, we assumed that:

$$\alpha = \int_{-\infty}^{\infty}\int_{0}^{\pi/2} \frac{\sin w}{\cos w} e^{\frac{-|x-\epsilon|}{l\cos w}} dw d\epsilon = \int_{-\infty}^{\infty}\int_{0}^{\pi/2} \tan w \, e^{\frac{-|x-\epsilon|}{l\cos w}} dw d\epsilon \qquad \text{Equation 4.17}$$

$$\beta = \left|\int_{\epsilon}^{x} e^{-\delta p} dp\right| \qquad \text{Equation 4.18}$$

Thus, Equation 4.16 can be re-written as:

$$N' \frac{v_1}{2l^2} dV\alpha \times f\left[E(\epsilon,\mathrm{t}) + \frac{1}{2}\left(dt - 2\frac{|s|}{v_1}\right)\frac{\partial E(\epsilon,\mathrm{t})}{\partial t} + \frac{I_0[1-R]\delta}{N' v_1 \cos w}\beta - E_p(x,t)\right] \qquad \text{Equation 4.19}$$

Given that $n(x,t)$ is the number of atoms density, the above equation represents the rise of the lattice (phonon) energy. Therefore, the equation above is equal to:

$$\frac{\partial nE_p(x,t)}{\partial t}dV = N'\frac{v_1}{2l^2}dV\alpha \times f\left[E(\epsilon,\mathrm{t}) + \frac{1}{2}\left(dt - 2\frac{|s|}{v_1}\right)\frac{\partial E(\epsilon,\mathrm{t})}{\partial t} + \frac{I_0[1-R]\delta}{N'v_1\cos w}\beta - E_p(x,t)\right]$$

Equation 4.20

The average change in electrons energy at x is equal to the retained energy in the electrons after collision minus the energy that transferred away when electrons are leaving dV, over the period dt, as shown in this expression:

$$\frac{\partial N'E(x,t)}{\partial t}dV = N'\frac{v_1}{2l^2}dV\alpha \times \left[E(\epsilon,\mathrm{t}) + \frac{1}{2}\left(dt - 2\frac{|s|}{v_1}\right)\frac{\partial E(\epsilon,\mathrm{t})}{\partial t} + \frac{I_0[1-R]\delta}{N'v_1\cos w}\beta\right] - \frac{\partial nE_p(x,t)}{\partial t}dV - \frac{N'v_1}{l}E(x,t)dV$$

Equation 4.21

By substituting Equation 4.20 into Equation 4.21, the above equation becomes:

$$\frac{\partial N'E(x,t)}{\partial t}dV = N'\frac{v_1}{2l^2}dV\alpha \times \left[E(\epsilon,\mathrm{t}) + \frac{1}{2}\left(dt - 2\frac{|s|}{v_1}\right)\frac{\partial E(\epsilon,\mathrm{t})}{\partial t} + \frac{I_0[1-R]\delta}{N'v_1\cos w}\beta\right] - N'\frac{v_1}{2l^2}dV\alpha \times f\left[E(\epsilon,\mathrm{t}) + \frac{1}{2}\left(dt - 2\frac{|s|}{v_1}\right)\frac{\partial E(\epsilon,\mathrm{t})}{\partial t} + \frac{I_0[1-R]\delta}{N'v_1\cos w}\beta - E_p(x,t)\right] - \frac{N'v_1}{l}E(x,t)dV$$

Equation 4.22

Moreover, by applying further simplification, it becomes:

$$\frac{\partial N'E(x,t)}{\partial t} = (1-f)\times N'\frac{v_1}{2l^2}\alpha \times \left[E(\epsilon,\mathrm{t}) + \frac{1}{2}\left(dt - 2\frac{|s|}{v_1}\right)\frac{\partial E(\epsilon,\mathrm{t})}{\partial t} + \frac{I_0[1-R]\delta}{N'v_1\cos w}\beta\right] + N'\frac{v_1}{2l^2}\alpha \times fE_p(x,t) - \frac{N'v_1}{l}E(x,t)$$

Equation 4.23

The electrons continuity expression should be satisfied so:

$$\frac{\partial N'(x,t)}{\partial t} = \frac{N'v_1}{2l^2}\alpha - \frac{N'v_1}{l}$$

Equation 4.24

C. Thermal Characteristics

To find a solution for the electron and lattice (phonon) energy expressions, the number of electrons that is participating is needed. This figure can be calculated from the standard expression for the Fermi distribution, considering that the electron gas is in a balanced state [74].

$$N' = N\pi^2\frac{T_e}{2T_F}$$

Equation 4.25

Where:

$N =$ Number density of valence electrons $\left[{}^{1}/_{m^3}\right]$

$T_e =$ Temperature of Kinetic electron $[K]$

$T_F =$ Temperature of Fermi electron $[K]$

The above expression is also considered that $T_F > T_e$. The material thermal conductivity can be described by statistical consideration [75]:

$$K = K(x,t) = {}^{N' v_1 lk}/_{3} \quad \left[{}^{W}/_{m^2.K}\right] \qquad \text{Equation 4.26}$$

Where:

$k = 1.38064852 \times 10^{-23} =$ Boltzmann constant $\left[{}^{J}/_{K}\right]$

The heat capacity is:

$$\rho C_p = 3nk \qquad \text{Equation 4.27}$$

Where:

$\rho =$ Density of the space debris material (assumed to be temperature independent)

$C_p =$ Specific heat of target material $\left[{}^{J}/_{kg.K}\right]$ (assumed to be temperature independent)

D. Temperatures of electron and lattice (phonon)

The variation in the phonons (lattice) and electrons kinetic energies define the rate of energy transfer, although the absorbed energy by phonons (lattice) raises the translational energy as well as raising their kinetic energy. By using Equation 4.26 and Equation 4.27, Equation 4.20, Equation 4.23 and Equation 4.24 can be rewritten as the following:

$$\frac{\partial}{\partial t}\left[\rho C_p T\right] = \frac{9K}{4l^3}\alpha \times f\left[T_e(\epsilon,\mathrm{t}) + \frac{1}{2}\left(dt - 2\frac{|s|}{v_1}\right)\frac{\partial T_e(\epsilon,\mathrm{t})}{\partial t} - T(x,t)\right] + f\frac{I_0[1-R]\delta}{2l^2\cos w}\alpha\beta$$

Equation 4.28

In fact, this is Equation 4.20 after changing:

$n =$ Phonon (atoms) number density $\left[{}^{1}/_{m^3}\right] \rightarrow \rho C_p$

$E_p(x,t) \rightarrow T(x,t) =$ Temperature of phonon

$N' \rightarrow K$

$v_1 \rightarrow \dfrac{9}{2l}$

$E \rightarrow T_e$

$$\frac{\partial}{\partial t}\left[\frac{9KT_e}{2lv_1}\right] = (1-f)\times\frac{9K}{4l^3}\alpha \times \left[T_e(\epsilon,\mathrm{t}) + \frac{1}{2}\left(dt - 2\frac{|s|}{v_1}\right)\frac{\partial T_e(\epsilon,\mathrm{t})}{\partial t}\right] + (1-f)\times \frac{I_0[1-R]\delta}{2l^2\cos w}\alpha\beta + \frac{9K}{4l^3}\alpha \times fT(x,t) - \frac{9K}{2l^2}T_e(x,t)$$

Equation 4.29

This is Equation 4.23 after changing:

$N' \rightarrow K$

$v_1 \rightarrow {}^{9}/_{2l}$

$E(\epsilon,t) \rightarrow T_e(\epsilon,t) =$ Temperature of Kinetic electron $[K]$

$E_p(x,t) \rightarrow T(x,t) =$ Temperature of phonon (lattice) $[K]$

$$\frac{\partial K}{\partial t} = \frac{Kv_1}{2l^2}\alpha - \frac{Kv_1}{l}$$

Equation 4.30

This is Equation 4.24 after changing:

$N' \rightarrow K$

Numerical methods were used to solve Equation 4.28, Equation 4.29 and Equation 4.30 as these equations give a nonlinear system of partial integro-differential equations that are difficult to simulate using analytical procedures. Solutions for these equations are described in detail by Byabagambi [76]. However, to provide a numerical solution of these equations, mathematical expressions were obtained by manipulating, reforming

and solving these equations using some initial conditions. Thus, the following initial conditions were utilised to solve Equation 4.28, Equation 4.29 and Equation 4.30:

At time: $t = 0 \Rightarrow T_e(0,x) = T(0,x) = T_0 =$ Room temperature $[K]$, which is the initial temperature of photons (lattice) and electrons

At: $x = \infty \Rightarrow T_e(t,\infty) = T(t,\infty) = T_0 =$ Room temperature $[K]$

The following quadrature rule was employed to replace the transport equations integrals:

$$\int_{-\infty}^{\infty} T(\epsilon)d\epsilon \cong \sum_{j=1}^{n} w_j T_e(\epsilon_j)\left[\epsilon_j(-\infty,\infty)\right] \quad \text{Equation 4.31}$$

For:

$j = 1$ to n

$T_{ej} =$ The x-axis

$w_j =$ The weights along with these points

Also:

$$\rho C_p \frac{dT}{dt} = A_1 f\left[\sum_{j=1}^{n} w_j h(x-\epsilon_j)\left[KT(t,\epsilon_j) - KT_e(t,x)\right]\right] - A_1 f\left[\sum_{j=1}^{n} w_j h(x-\epsilon_j)\left[K(t,\epsilon_j) - K(t,x)\right]\right] - A_1 f 2l[KT_e(t,x) - KT(t,x)] + Bfg(x)I_0 \quad \text{Equation 4.32}$$

Where:

$$A_1 = {}^{9}/_{4l^3} \quad \text{Equation 4.33}$$

$$h(x-\epsilon_j) = \int_0^1 \frac{1}{u} e^{\frac{-|x-\epsilon|}{ul}} du \quad \text{Equation 4.34}$$

$$u = l\delta \quad \text{Equation 4.35}$$

$$B = \frac{1-R(t)}{2l} \quad \text{Equation 4.36}$$

$$g(x) = \frac{l}{\delta} e^{-\delta x} \ln\left|\frac{1+l\delta}{1-l\delta}\right| - 2l^2\delta^2 \int_1^{\infty} \frac{1}{u(u^2-l^2\delta^2)} e^{\frac{-xu}{l}} du \quad \text{Equation 4.37}$$

$$\frac{d}{dt}(KT_e) = C_3(1-f)\left[\sum_{j=1}^{n} w_j h(x-\epsilon_j)\left[KT_e(t,\epsilon_j) - KT_e(t,x)\right]\right] + C_3(1-f)H(x)KT_e(t,x) - \sigma_1 kT_e(t,x) + C_3 fT\left[\sum_{j=1}^{n} w_j h(x-\epsilon_j)\left[k(t,\epsilon_j) - k(t,x)\right]\right] + C_3 fTkH(x) + D_1(1-f)g(x)I_0 \quad \text{Equation 4.38}$$

Where:

$$C_3 = {v_1}/{2l^2} \quad \text{Equation 4.39}$$

$$H(x) = \int_{-\infty}^{\infty} h(x-\epsilon)d\epsilon \quad \text{Equation 4.40}$$

$$\sigma_1 = lC_3 \quad \text{Equation 4.41}$$

$$D_1 = v_1 \frac{1-R(t)}{9} \quad \text{Equation 4.42}$$

E. Discussion of Theoretical Results

As mentioned in Chapter 3, circ function (top hat) beam profile and Gaussian beam profile assumptions, represent the worst case and best-case ends of the intensity distribution of the laser beam as illustrated in Figure 39. The intensity distribution of an actual laser beam is considerably closer to the assumption of the Gaussian beam profile, and thus this thesis focused more on the results of using the Gaussian beam profile assumption. At the centre of the laser beam, the circ function intensity gives half the intensity of a Gaussian beam. This was simulated and investigated in Chapter 3. It gives a prediction of the low surface temperature of the debris material.

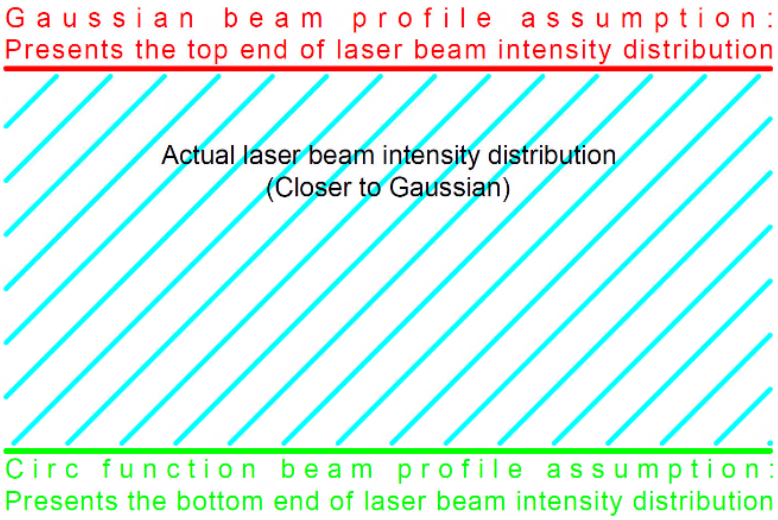

Figure 39: Top hat circ function and Gaussian beam profile assumptions with respects to the actual laser beam intensity distribution

Based on the information that is given in Table 3, the interaction simulations between the laser beam and the three different space debris materials are displayed in Figure 40 to Figure 51. These figures present the measured temperature increase as a function of distance from the surface of the space debris material, i.e. the penetration depth. The reduced temperature is the ratio of the space debris material temperature to the critical temperature of that material.

Table 3: Data table for nickel, aluminium and copper space debris

Space Debris Material Type	Critical Temperature of the Space Debris Material (T_c) [K]	Absorption Coefficient (δ) [$1/m$]	Electron-Phonon Mean Free Path (l) [nm]	Diffusivity [m^2/sec]
Nickel (Ni) Space Debris	10,800	68×10^{6}	5.8	27.2×10^{-6}
Aluminium (Al) Space Debris	7,400	84×10^{6}	14.9	90.9×10^{-6}
Copper (Cu) Space Debris	8,500	75×10^{6}	40.0	96.1×10^{-6}

Figure 40 to Figure 45 present the spatial temperature profile of electrons in each of the above three different space debris metals, which are made of nickel (Ni), aluminium (Al) and copper (Cu). Each curve in these figures presents the temperature profile at a given moment at 0.2 μs time intervals. So as the laser beam illuminated the target material, the time evolves and climbs in a vertical direction, and each curve is a snapshot at every 0.2 μs. Figure 40 and Figure 41 are for nickel space debris, Figure 42 and Figure 43 are for aluminium space debris, and Figure 44 and Figure 45 are for copper space debris.

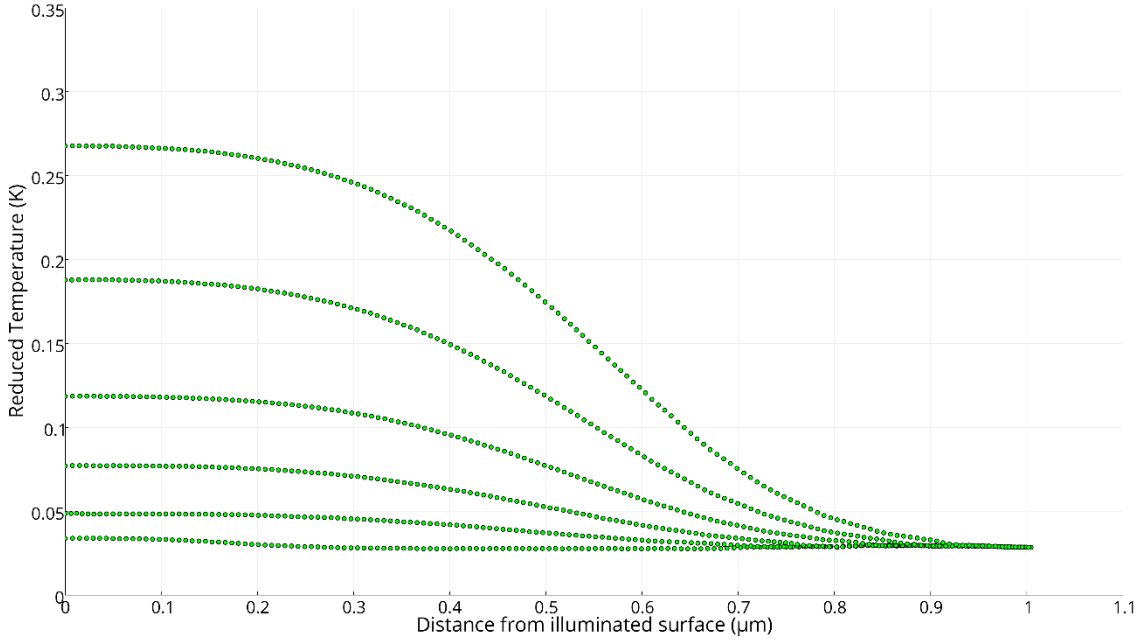

Figure 40: Below boiling point: Electron temperature profile at 0.2 μs time intervals in Ni space debris using Kinetic theory when Gaussian beam is assumed (BBP, Ni, Kinetic, Gaussian, Electron)

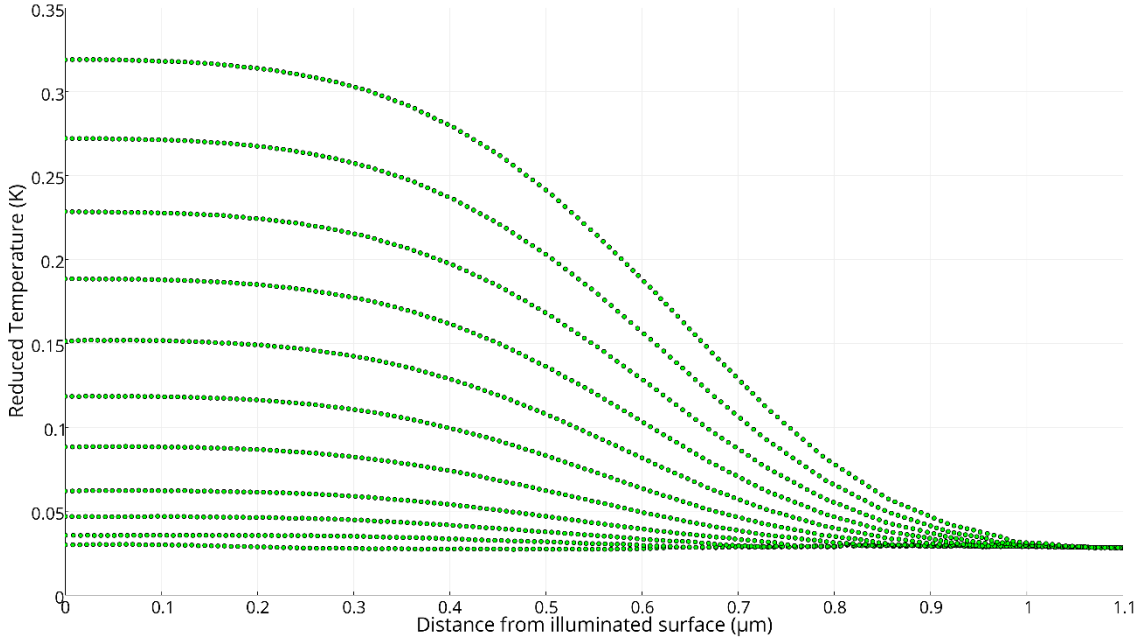

Figure 41: Below boiling point: Electron temperature profile at 0.2 μs time intervals in Ni space debris using Kinetic theory when circ function beam irradiance profile is assumed (BBP, Ni, Kinetic, Circ, Electron)

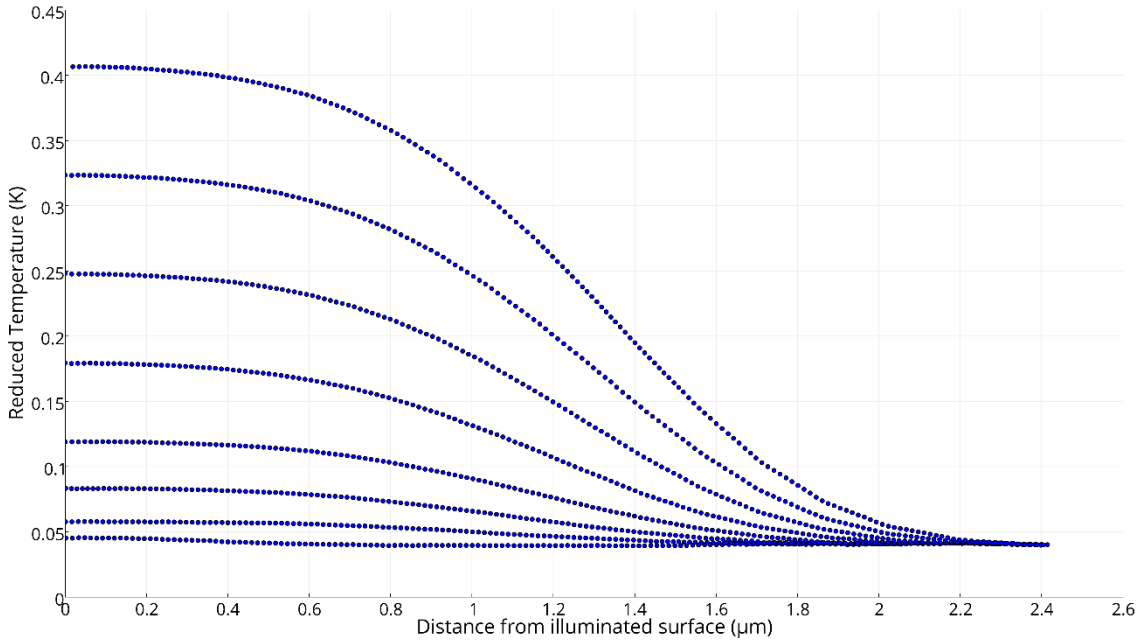

Figure 42: Below boiling point: Electron temperature profile at 0.2 μs time intervals in Al space debris using Kinetic theory when Gaussian beam is assumed (BBP, Al, Kinetic, Gaussian, Electron)

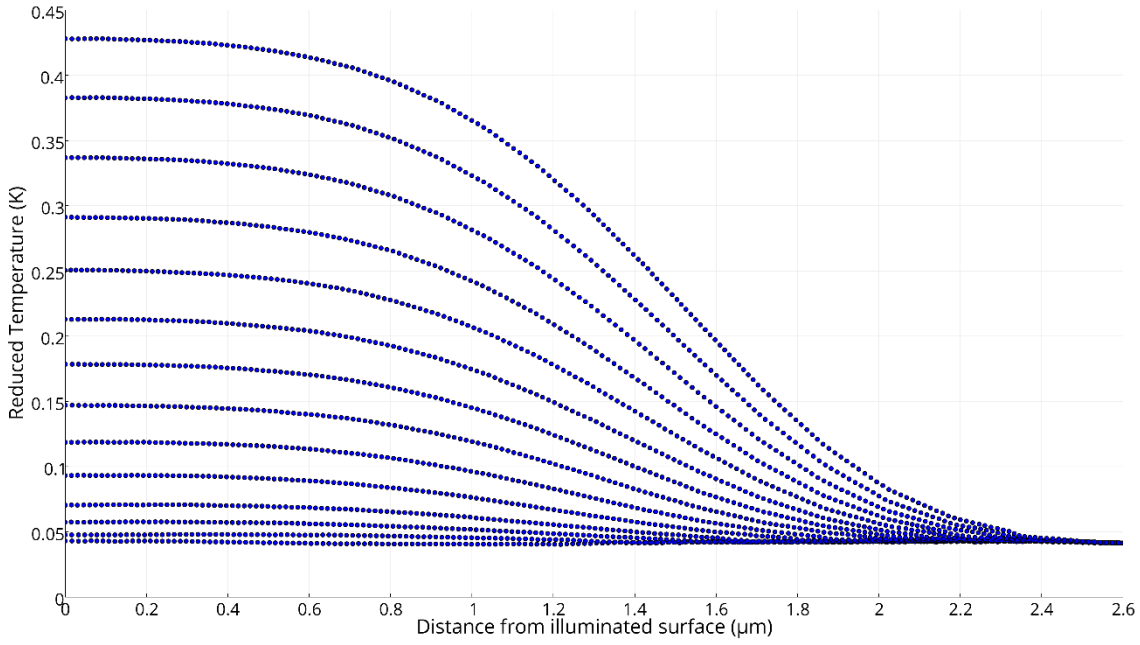

Figure 43: Below boiling point: Electron temperature profile at 0.2 μs time intervals in Al space debris using Kinetic theory when circ function beam irradiance profile is assumed (BBP, Al, Kinetic, Circ, Electron)

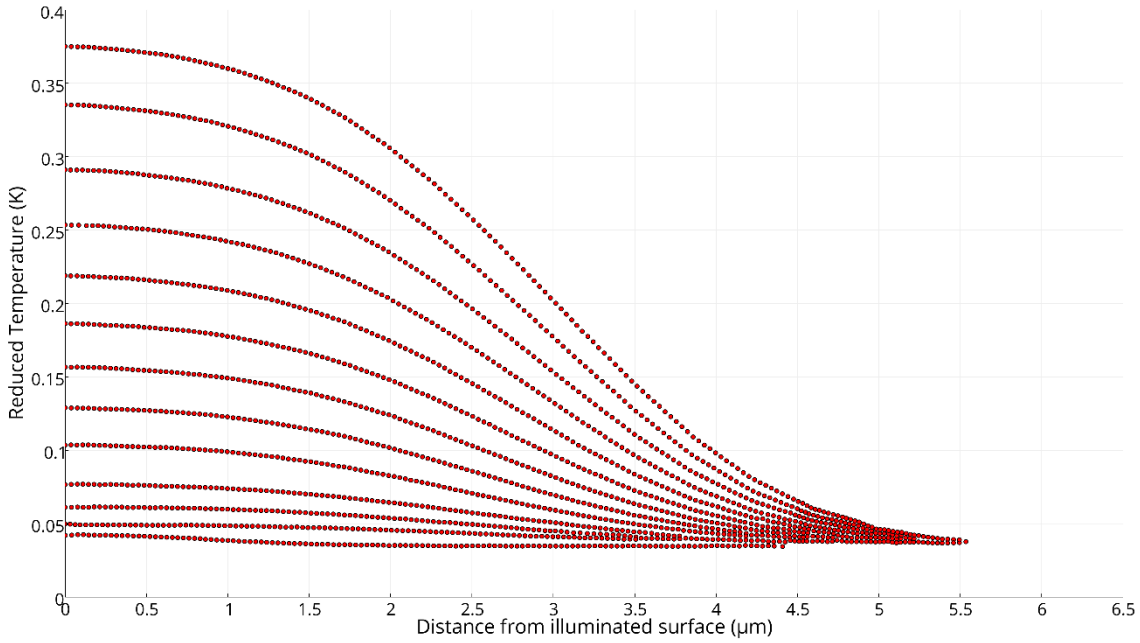

Figure 44: Below boiling point: Electron temperature profile at 0.2 μs time intervals in Cu space debris using Kinetic theory when Gaussian beam is assumed (BBP, Cu, Kinetic, Gaussian, Electron)

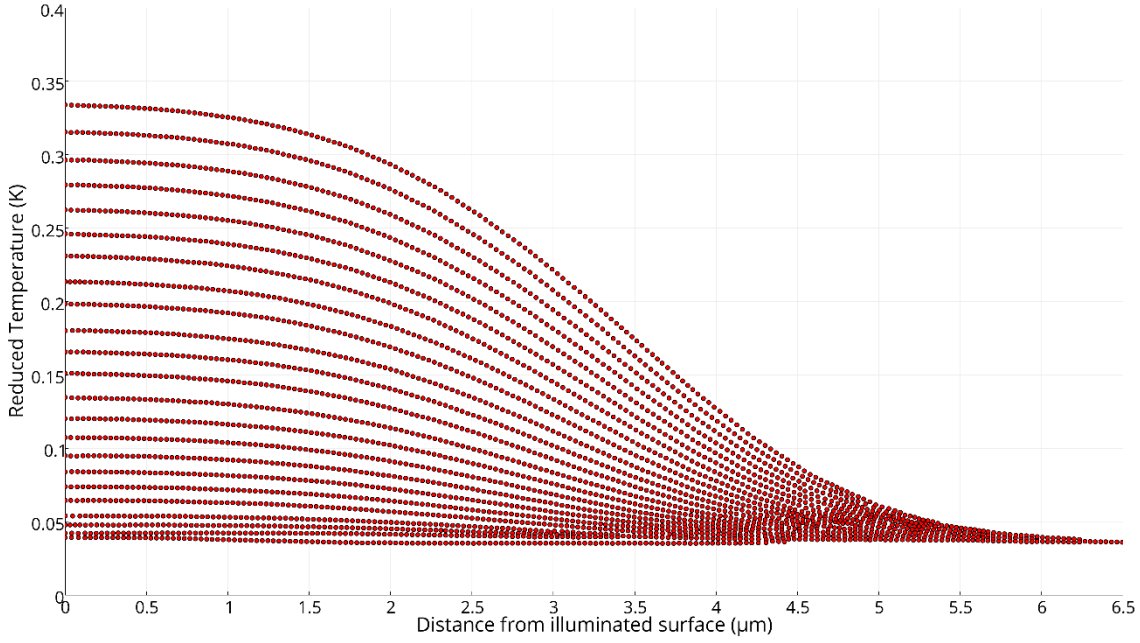

Figure 45: Below boiling point: Electron temperature profile at 0.2 μs time intervals in Cu space debris using Kinetic theory when circ function beam irradiance profile is assumed (BBP, Cu, Kinetic, Circ, Electron)

For simulation, the spatial temperature profile and the penetration distance from the illuminated orbital debris surface are mainly relying on the material type and its physical characteristics and also on the power intensity of the laser beam, which depends on whether a Gaussian beam or circ function beam irradiance profile is assumed. So for the same laser input power, the heating penetration distance from the

illuminated surface of the space debris, due to the interaction with a laser, is a function of the physical characteristics of the wreckage.

Figure 46 to Figure 51 present the spatial temperature profile of the lattice in the same three different space debris materials that are made of nickel (Ni), aluminium (Al) and copper (Cu). Each curve in these figures presents the temperature profile at the same specific time of 0.2 μs time intervals. So as the laser beam illuminating the target material, the time evolves and climbs in a vertical direction, and each curve is a snapshot at every 0.2 μs. Figure 46 and Figure 47 are for nickel space debris, Figure 48 and Figure 49 are for aluminium space debris, and Figure 50 and Figure 51 are for copper space debris.

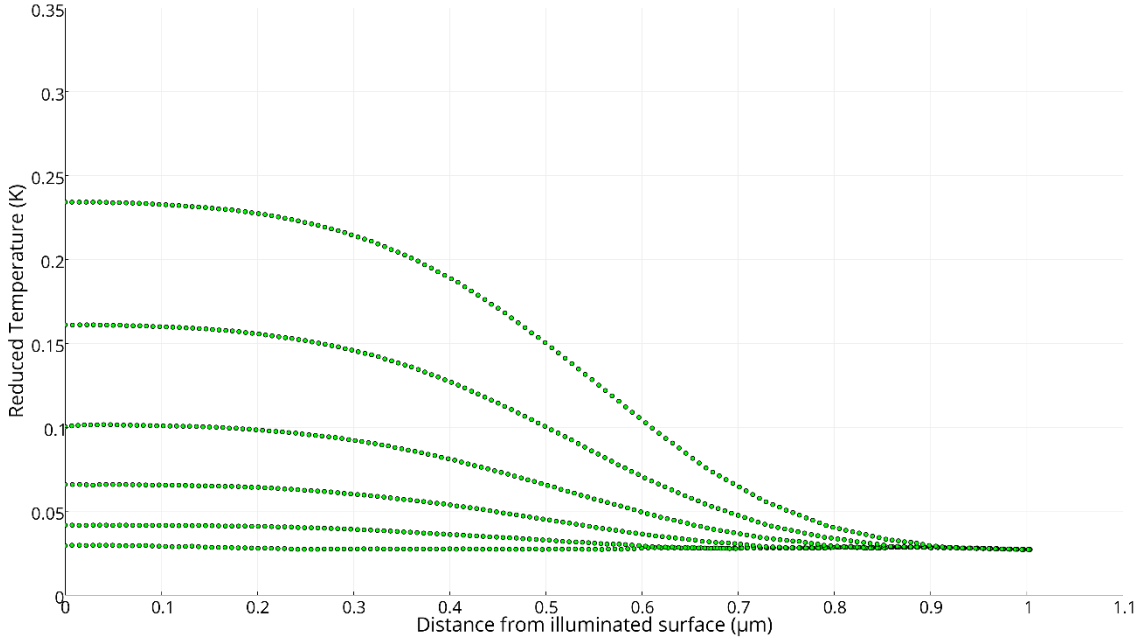

Figure 46: Below boiling point: Lattice temperature profile at 0.2 μs time intervals in Ni target using Kinetic theory when Gaussian beam is assumed (BBP, Ni, Kinetic, Gaussian, Lattice)

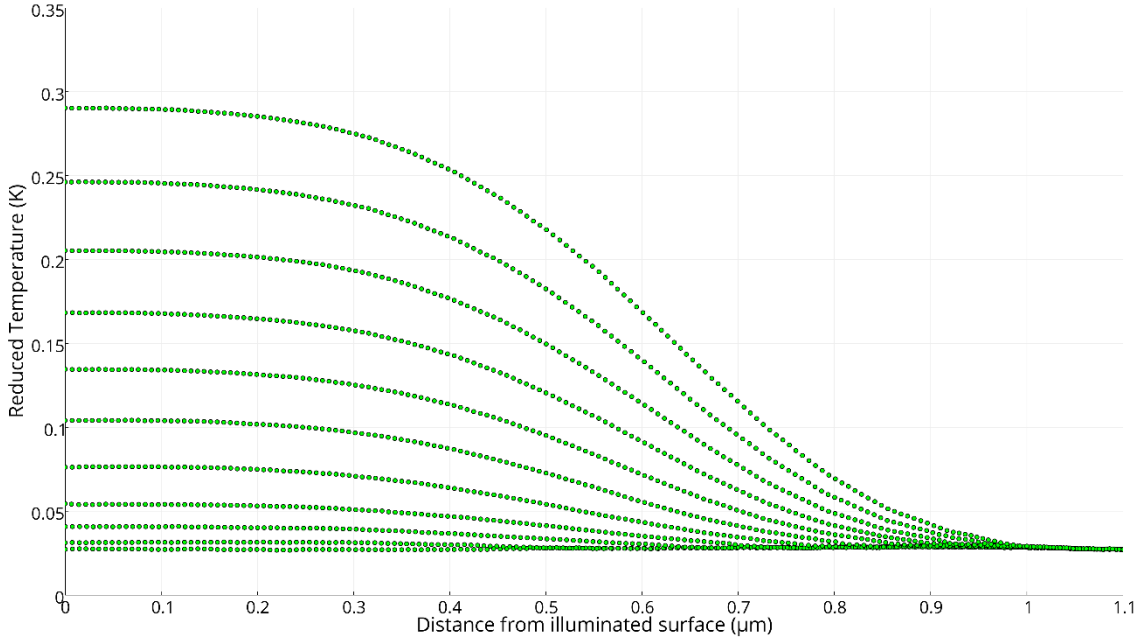

Figure 47: Below boiling point: Lattice temperature profile at 0.2 μs time intervals in Ni target using Kinetic theory when top hat or circ function beam irradiance profile is assumed (BBP, Ni, Kinetic, Circ, Lattice)

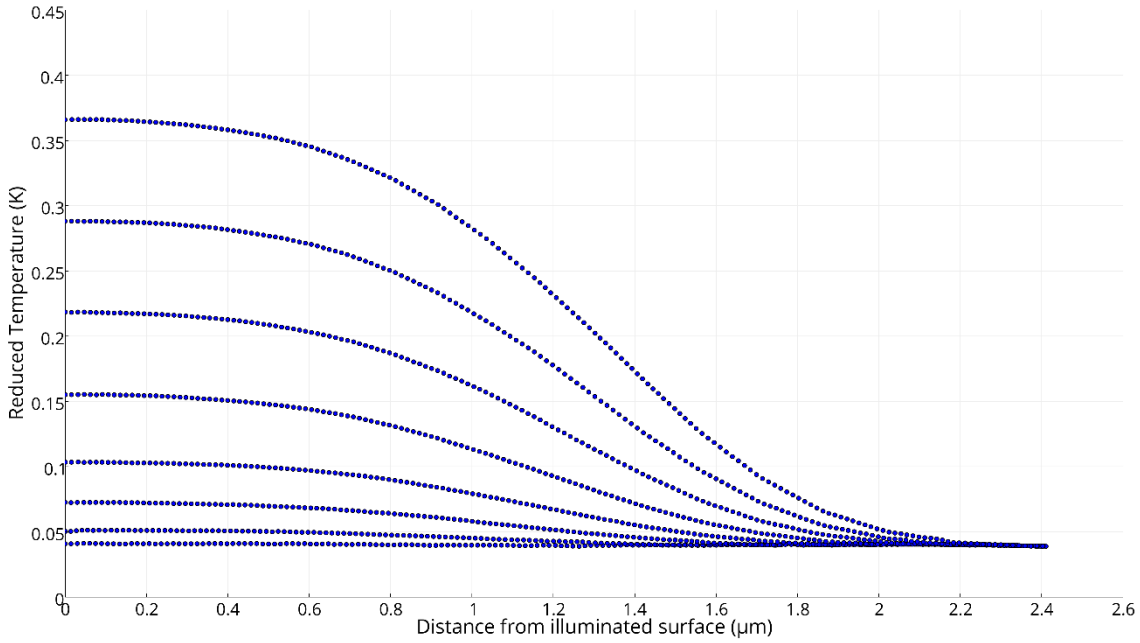

Figure 48: Below boiling point: Lattice temperature profile at 0.2 μs time intervals in Al target using Kinetic theory when Gaussian beam is assumed (BBP, Al, Kinetic, Gaussian, Lattice)

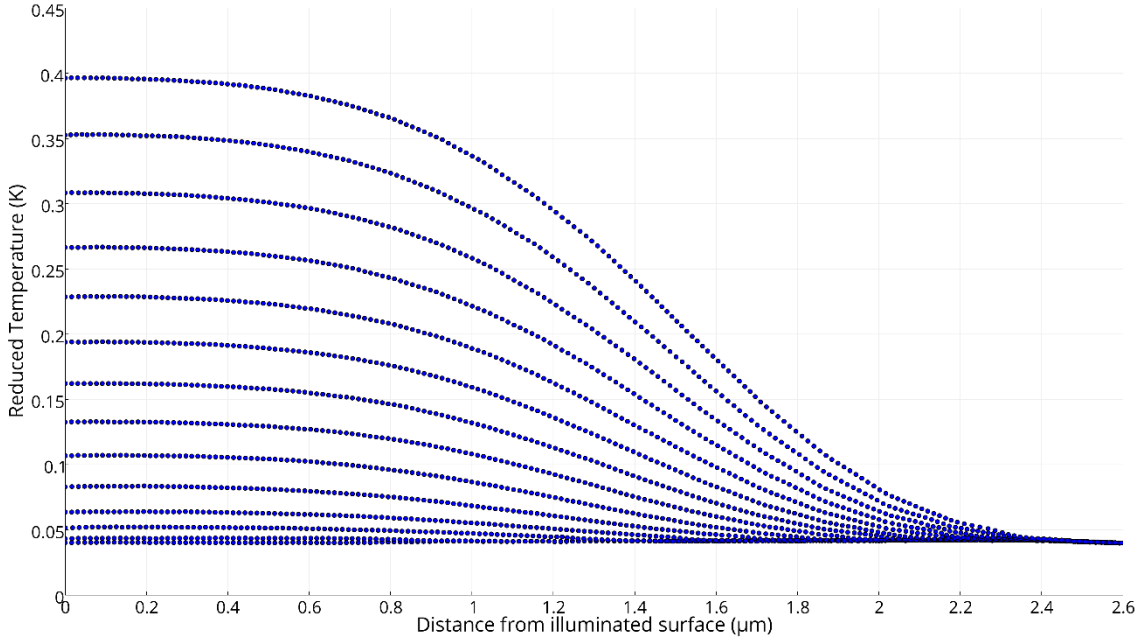

Figure 49: Below boiling point: Lattice temperature profile at 0.2 μs time intervals in Al target using Kinetic theory when top hat or circ function beam irradiance profile is assumed (BBP, Al, Kinetic, Circ, Lattice)

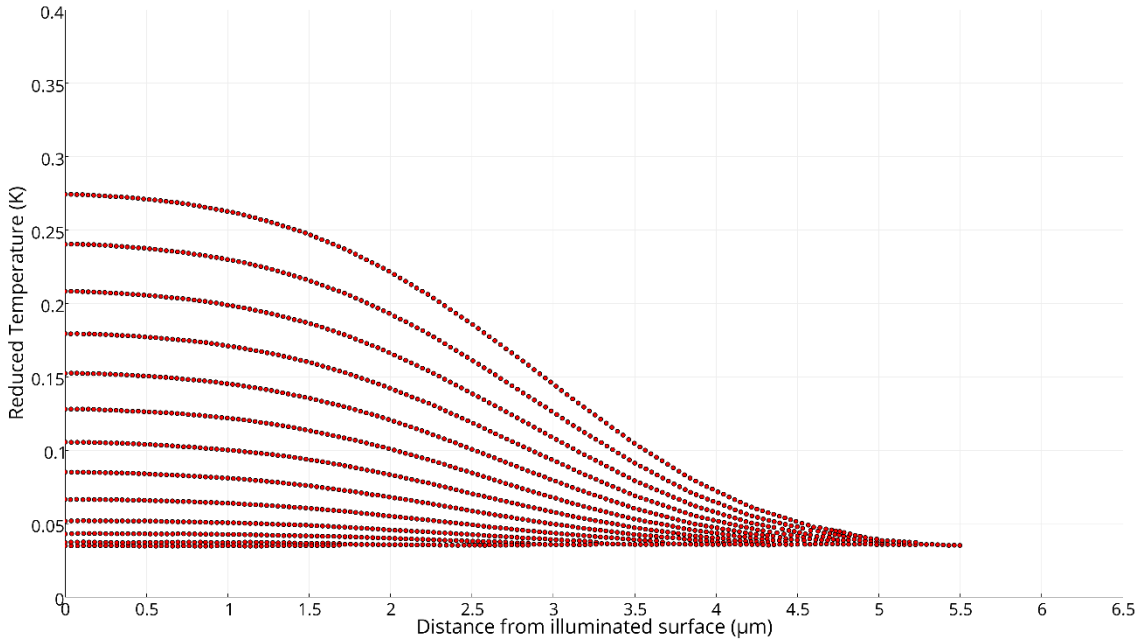

Figure 50: Below boiling point: Lattice temperature profile at 0.2 μs time intervals in Cu target using Kinetic theory when Gaussian beam is assumed (BBP, Cu, Kinetic, Gaussian, Lattice)

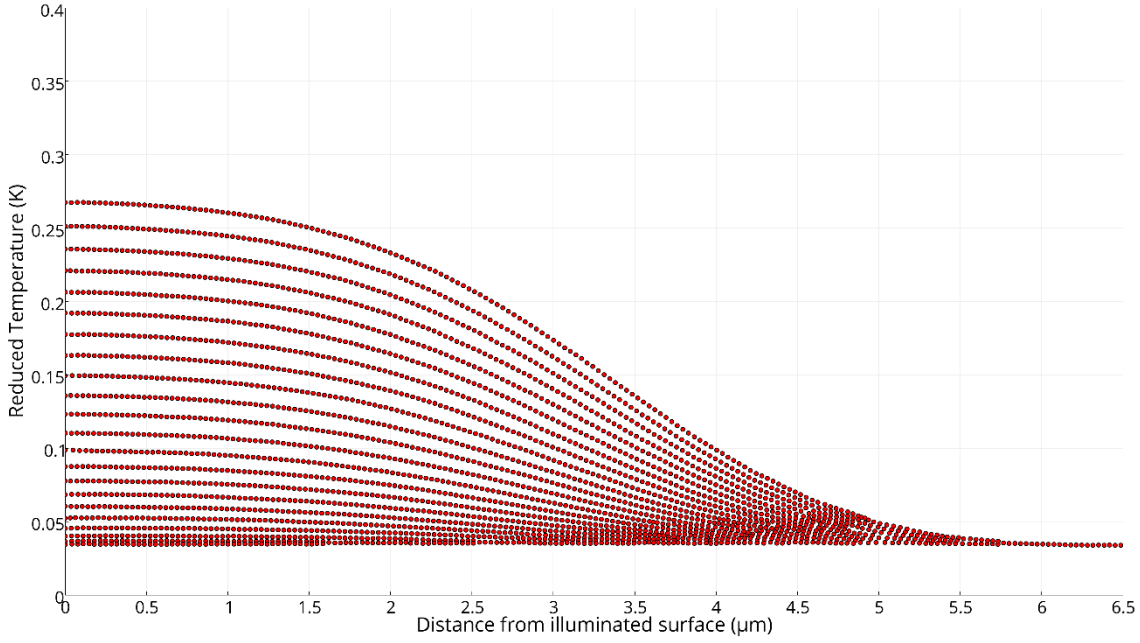

Figure 51: Below boiling point: Lattice temperature profile at 0.2 μs time intervals in Cu target using Kinetic theory when top hat or circ function beam irradiance profile is assumed (BBP, Cu, Kinetic, Circ, Lattice)

In general, the slope of the spatial temperature tangent that is close to the illuminated surface of the target has a very slight negative value. However, as we move away from the illuminated surface towards the depth of the material, this negative slope value falls sharply and then turns back to a minimal negative value, as the material spatial temperature reaches its initial temperature (i.e. the ambient temperature of the material). This behaviour becomes clear as time develops. Table 4 compares the penetration

distance from the illuminated surface for the nickel, aluminium and copper space debris. A reduced temperature of 0.23 K has been chosen as an average reduced temperature (i.e. reference point) to make our comparison as it fits in any of the previous 12 figures above, for both electron and lattice temperature profiles.

Table 4: Penetration distance comparison for nickel, aluminium and copper space debris when Kinetic theory of energy transport is used, below boiling point

Space Debris Material Type	Diffusivity $[m^2/sec]$	Penetration Distance From the Illuminated Surface of Space Debris [μm]		
		When Gaussian Beam Assumed	When Top Hat or Circ Function Beam Irradiance Profile Assumed	Difference
Nickel (Ni) Space Debris	27.2×10^{-6}	0.93	1.04	0.11
Aluminium (Al) Space Debris	90.9×10^{-6}	2.29	2.49	0.21
Copper (Cu) Space Debris	96.1×10^{-6}	5.81	6.05	0.23

From the above table, it is clear that the penetration distance from the illuminated surface of space debris is more significant for high diffusivity debris metals. Also, the penetration distance is greater when a circ function or top hat beam irradiance profile is assumed, compared to the case when a Gaussian beam is assumed.

Using the kinetic theory, Figure 52, Figure 53 and Figure 54 have been produced to present the difference between the electron temperature and the lattice temperature below the boiling point in orbital debris that have surfaces made of nickel, aluminium and copper respectively (the continuous lines in the figures) for both cases: when Gaussian beam is assumed and when top hat (circ function) beam irradiance profile is assumed. The dashed lines in these figures represent the power of the laser beam versus time.

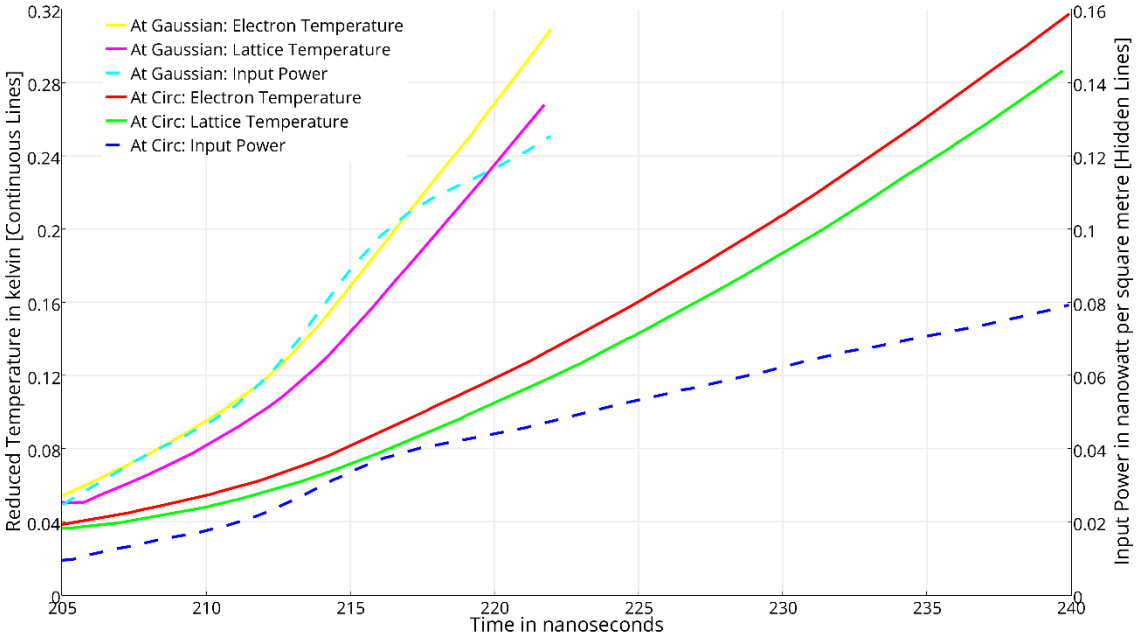

Figure 52: Nickel electron and lattice surface temperatures (continuous lines) below boiling point using kinetic theory. Hidden lines are the laser beam input power as a function of time.

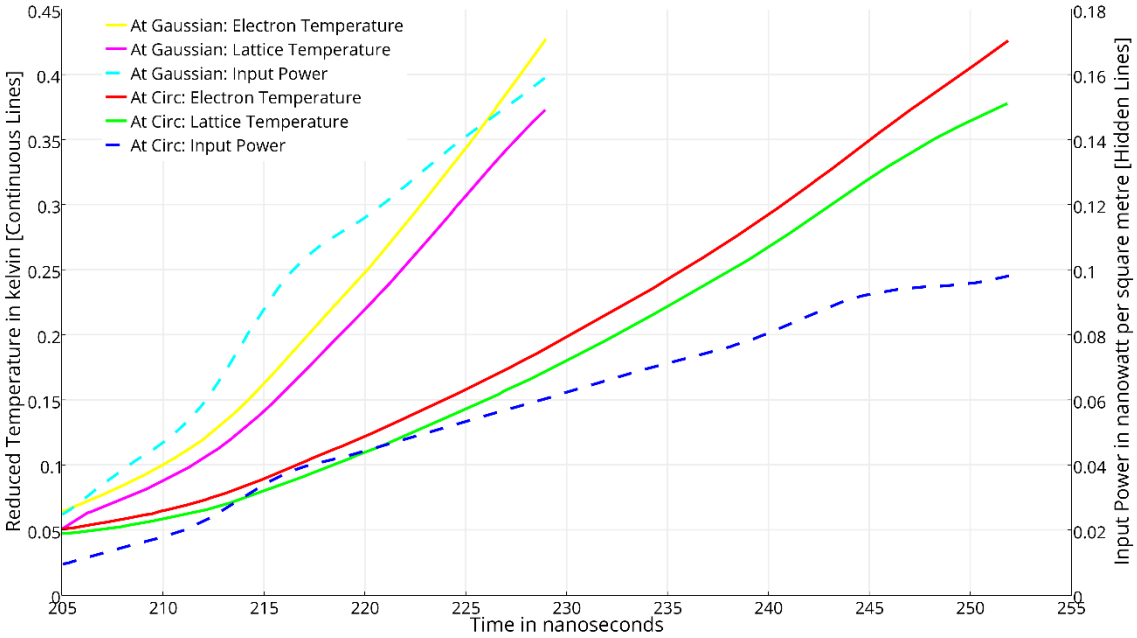

Figure 53: Aluminium electron and lattice surface temperatures (continuous lines) below boiling point using kinetic theory. Hidden lines are the laser beam input power as a function of time.

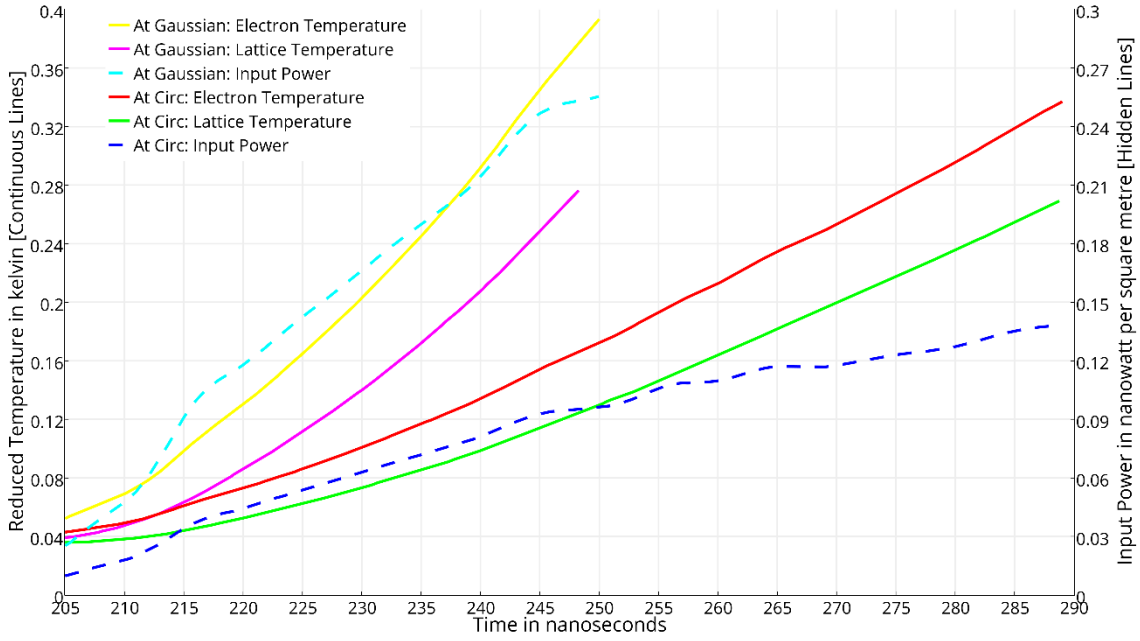

Figure 54: Copper electron and lattice surface temperatures (continuous lines) below boiling point using kinetic theory. Hidden lines are the laser beam input power as a function of time.

As the above three figures show, the variation between electron temperature and lattice temperature is minimum at the beginning of the treatment (i.e. laser-space debris interaction), but as time develops, it becomes larger and larger as the temperature of the space debris surface approaches the boiling point of its material. Also, as the laser-debris interaction time evolves, both the electron surface temperature and the lattice surface temperature of the orbital debris will rise. The rise rate of the debris surface temperature, in this case, is a function of the power delivered by the laser beam, i.e. the input power. Electron and lattice surface temperatures in the nickel space debris increase at a higher rate compared to the aluminium and copper space debris and that is because energy is conveyed away from nickel debris surface at a lower rate in comparison with aluminium and copper debris. The relatively low initial surface reflectivity of orbital debris that is made of nickel leads to transfer most of the delivered energy into increasing the temperature at the debris surface, which results in a higher temperature rise rate for nickel debris comparing to aluminium or copper orbital debris.

The previous three figures also show that it takes almost double the time to reach the same surface temperature level in any of the three space debris materials when the top hat or circ function beam irradiance profile is assumed. This can be assumed as the slowest temperatures rise rate of the space debris surface, unlike the case when the Gaussian beam is assumed, which can be assumed to give the quickest debris surface

temperature rise rate. High rise rate of space debris surface temperature is, in fact, crucial for debris boiling, ablation and deflection.

The electron and the lattice temperature variation at the boiling point and the time taken to reach this point are given in Table 5. Since debris that is made of copper has small valence number, a little figure of electrons participated in the energy transport process and thus there is a significant difference between the electron and the lattice temperatures as the energy of a photon is shared among a smaller number of electrons compared to debris that is made of nickel or aluminium.

Table 5: Time to reach boiling point and the temperature variation of electron and lattice at the boiling point.

Space Debris Materials	Laser Input Energy $[mJ]$	Time to Reach the Boiling Point $[\mu s]$	Temperature Variation Between Electron and Lattice $[K]$
Nickel Space Debris	1.6	1.3	394
Aluminium Space Debris	2.0	1.6	300
Copper Space Debris	8.2	3.1	546

The melting stage has been ignored since the alterations in physical characteristics when a material converts to liquid from solid are little compared to the alteration that happens to the material when it converts to vapour. Consequently, an assumption has been made so that the liquid can be dealt with as a solid and the liquid fluid flow impacts onto the processes of energy transport is disregarded, nevertheless, it is valid as a first estimate.

4.5.2 Kinetic Theory Model: Above Boiling Point (ABP)

A comprehensive explanation of the Kinetic theory model that is extended to contain the evaporation impacts is described in this section. The analysis technique is similar to that in the previous section, Kinetic Theory Model: Below Boiling Point (BBP), exclude for the following two main properties:

- The mirror image method cannot be used directly because the limits are receding

- Due to the space debris material evaporation, there is a mathematical singularity at the illuminated surface of the debris

Solving the problem is a mathematical challenge due to the above two properties, it is simplified by modifying the coordinate systems so that the space debris material moves in the direction of the origin with velocity v_s and this has the impact of maintaining the origin fixed, see Figure 55.

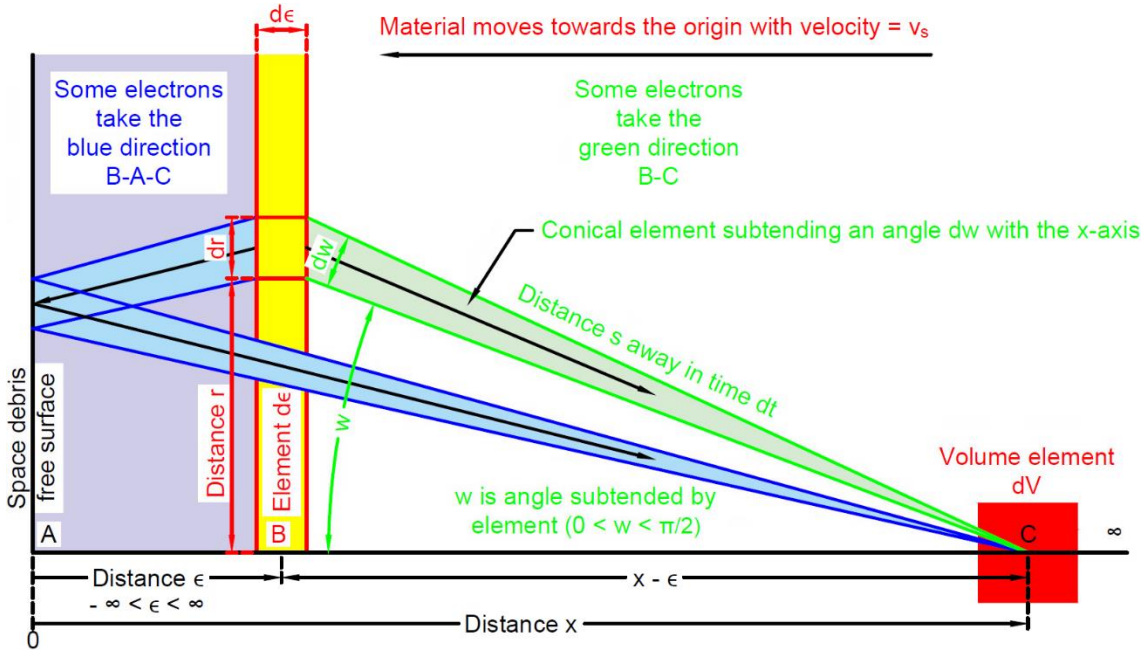

Figure 55: Movement of an electron inside the space debris metal for the top half of the cone: Electrons transport energy from all metal areas of the wreckage and part of this energy is moved to the lattice through collisions with phonons. The debris material is moving towards the origin with velocity v_s and $x = 0$ represents the free surface

A significant amount of energy is transferred away by the ejected space debris material during the target evaporation process, which occurs at a high-power intensity of the laser. The entire structure of the lattice in the impacted area of the debris is destroyed, and some of the wreckage material is vaporised. During the evaporation process, the ejected material from the space debris imparts as a small thrust on the wreckage, which can change its velocity and altitude in Earth orbit and eventually moving it to a lower orbit. The model is established based on the statistical thermodynamics implementation for evaporation utilising the Frenkel [77] assumption with the evaporation rate G in atoms per second as shown below:

$$G = ne^{-\frac{U_0}{kT}}\sqrt{{kT}/{2\pi m}} \qquad \text{Equation 4.43}$$

Where:

$n =$ Number of atoms per unit volume at the surface = Density of atoms (phonon) number $\left[{1}/{m^3}\right]$

$U_0 =$ The energy needed to fully remove 1-atom from the target material = The vaporisation latent heat per atom $[J]$

$k =$ Boltzmann constant $= 1.38064852 \times 10^{-23}\ \left[{J}/{K}\right]$

$T =$ Temperature of phonon (lattice) $[K]$

$m =$ Atom mass $[kg]$

The velocity of space debris surface is evaporating at $v_s\ [{m}/{s}] = G$ when $T = T_s$

$$G = v_s = ne^{-\frac{U_0}{kT_s}}\sqrt{{kT_s}/{2\pi m}} \qquad \text{Equation 4.44}$$

Where:

$T_s =$ Lattice temperature of the surface $[K]$

The challenge is to calculate the energy transported from all electrons in $d\epsilon$ at distance ϵ into dV that is located at distance x. Integrate for ϵ accounts for the contributions from the entire space debris material as the mass material is shifting with velocity v_s. The shifting surface has two impacts on the transport equation that were developed to include the evaporation phase of the debris:

I. Impacts on electron transport: as the wreckage mass material is shifting with velocity v_s and thus the whole bulk move activities include relative velocities and so if an electron is transported with velocity v_1 at the Fermi surface, the relative velocity is shown as following:

$$(v_1 \pm v_s) = v_1\left(1 \pm \frac{v_s}{v_1}\right) \approx v_1 \qquad \text{Equation 4.45}$$

This assumption relies on the electron movement direction; whether it arrives from the left or right of the volume element dV, see Figure 55. The thermal electron velocities are of the order of 10^6 [$^m/_S$] and the velocity of the evaporating surface of the space debris is predicted to not to be more than 10 [$^m/_S$], so $v_1 \gg v_s$. Therefore, for simplification, the impact on the electron transport by the shifting material can be safely ignored and this actually permits not to change the Fermi electron velocity v_1 when we borrow and use any equation from the previous section, for BBP. So, the same electron transport equation can be utilised without the need to make any adjustment or modification.

II. Impact on the energy of the lattice in dV: The lattice energy at distance x, which is initially $E_p(x,t)$, is affected by the convective heat transfer due to shifting material and also by the electron transport. This actually changes the energy equations for both the electron and lattice to:

$$\frac{\partial nE_p(x,t)}{\partial t} - v_s\frac{\partial\left(nE_p(x,t)\right)}{\partial x} = \int_{-\infty}^{\infty}\int_0^{\pi/2}\sin w\,\frac{dw}{2}N'\frac{v_1}{l}\frac{d\epsilon}{l\cos w}e^{-|x-\epsilon|l\cos w} \times f\left[E(\epsilon,\mathrm{t}) + \frac{1}{2}\left(dt - 2\frac{|s|}{v_1}\right)\frac{\partial E(\epsilon,\mathrm{t})}{\partial t} + \frac{I_0[1-R]\delta}{N' v_1\cos w}\left|\int_\epsilon^x e^{-\delta p}dp\right| - E_p(x,t)\right] \qquad \text{Equation 4.46}$$

By adding the evaporation term $\rho L(T_s)v_s$ when $x = 0$, the energy remaining in the electron is:

$$\frac{\partial\left(N'E(x,t)\right)}{\partial t} = dV\int_{-\infty}^{\infty}\int_0^{\pi/2}\sin w\,\frac{dw}{2}N'\frac{v_1}{l}\frac{d\epsilon}{l\cos w}e^{-|x-\epsilon|l\cos w} \times \left[E(\epsilon,\mathrm{t}) + \frac{1}{2}\left(dt - 2\frac{|s|}{v_1}\right)\frac{\partial E(\epsilon,\mathrm{t})}{\partial t} + \frac{I_0[1-R]\delta}{N' v_1\cos w}\left|\int_\epsilon^x e^{-\delta p}dp\right|\right] - \frac{\partial nE_p(x,t)}{\partial t} + v_s\frac{\partial\left(nE_p(x,t)\right)}{\partial x} - \frac{N'v_1E(x,t)}{l} \qquad \text{Equation 4.47}$$

The vaporisation specific latent heat L is reported in [78]:

$$L(T_s) = L_0\left(1 - \left(\frac{T_s}{T_c}\right)^2\right) \qquad \text{Equation 4.48}$$

Where:

L_0 = Vaporisation normal specific latent heat

T_c = Critical temperature of the metal

The next two equations have been obtained by solving the above two equations; and applying similar simplifications that were used in the previous section, for BBP. A comprehensive solution for these equations is given in [79].

$$\rho C_p \frac{dT}{dt} = A_1 f(1-T) \int_{-\infty}^{\infty} KT(t,\epsilon) h(x-\epsilon) d\epsilon + Bf g(x) I_0 + v_s \rho C_p \frac{\partial T}{\partial x} \qquad \text{Equation 4.49}$$

$$\frac{d}{dt}(KT_e) = C_3(1-f+fT) \int_{-\infty}^{\infty} KT_e(t,\epsilon) h(x-\epsilon) d\epsilon - \sigma_1 KT_e + D_1(1-f) g(x) I_0 \qquad \text{Equation 4.50}$$

High-temperature gradients were produced during the process of laser heating. This has been found in the analysis of the laser heating. The temporal and spatial temperature distribution of lattice and electron are predicted for nickel, aluminium and copper space debris materials.

4.6 Results and Discussion

The spatial temperature distribution of electrons at $200\ ns$ time intervals for Ni, Al and Cu space debris are presented in Figure 56 to Figure 61 when the Gaussian beam or circ function beam irradiance profile is assumed. Figure 56 and Figure 57 are for nickel space debris, Figure 58 and Figure 59 are for aluminium space debris, and Figure 60 and Figure 61 are for copper space debris. A significant positive temperature gradient is produced at the surface of the space debris, and that is consistent and in agreement with the thermodynamics laws because energy can only move from a high temperature to low temperature. However, this positive slope is not obvious in these figures due to the limitation of the figures' scale.

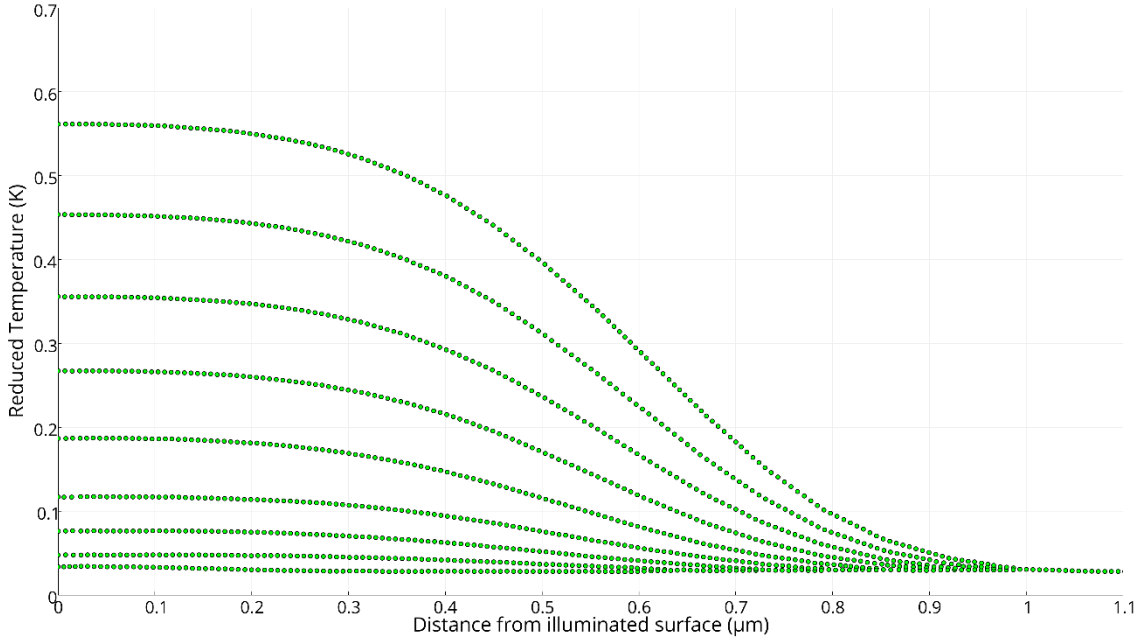

Figure 56: Above boiling point: Electron temperature profile at 0.2 μs time intervals in Ni space debris using Kinetic theory when Gaussian beam is assumed (ABP, Ni, Kinetic, Gaussian, Electron)

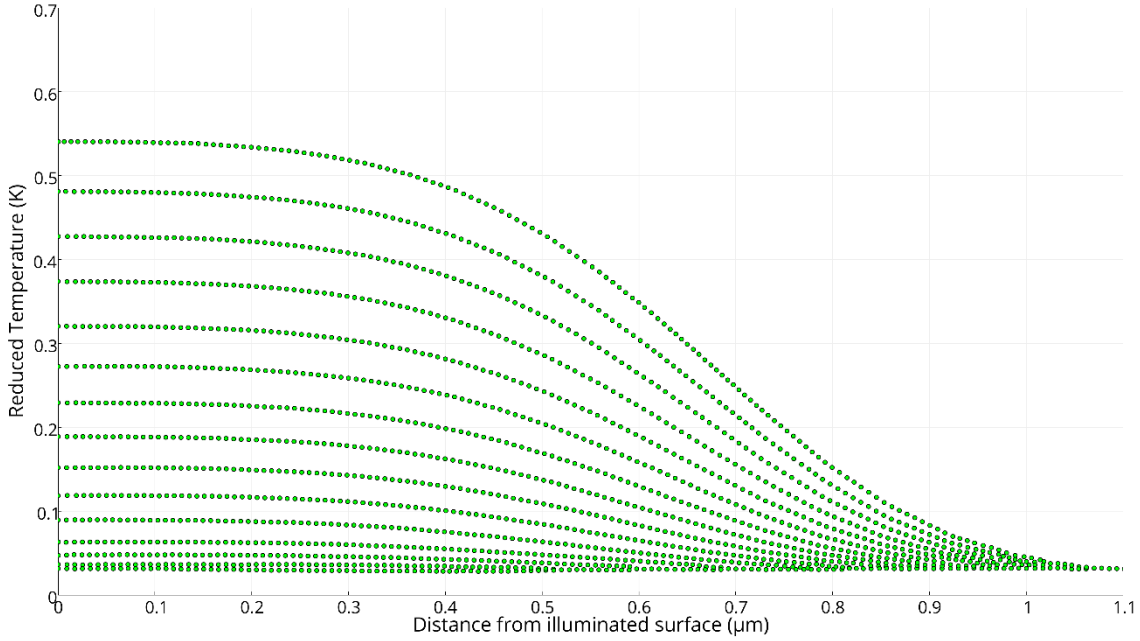

Figure 57: Above boiling point: Electron temperature profile at 0.2 μs time intervals in Ni space debris using Kinetic theory when top hat or circ function beam irradiance profile is assumed (ABP, Ni, Kinetic, Circ, Electron)

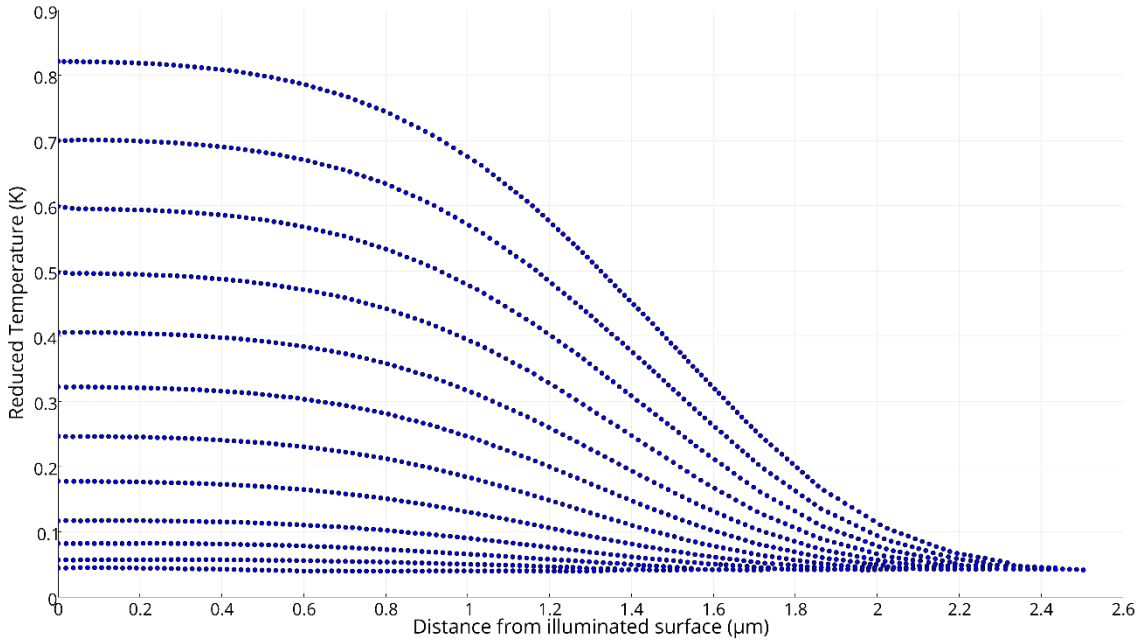

Figure 58: Above boiling point: Electron temperature profile at 0.2 μs time intervals in Al space debris using Kinetic theory when Gaussian beam is assumed (ABP, Al, Kinetic, Gaussian, Electron)

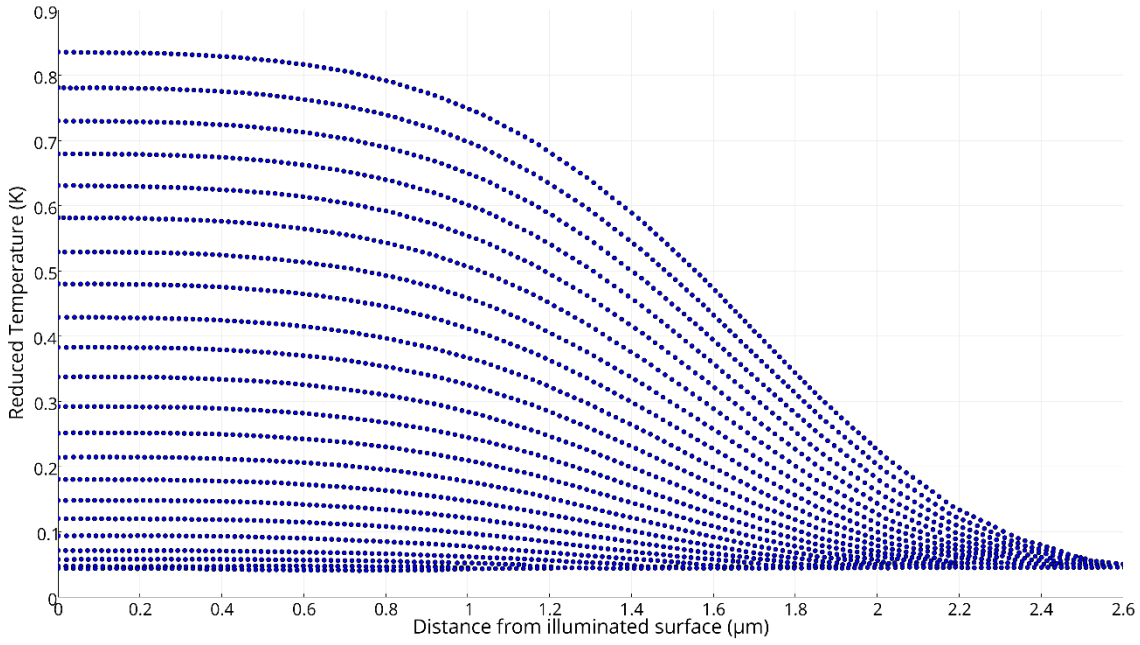

Figure 59: Above boiling point: Electron temperature profile at 0.2 μs time intervals in Al space debris using Kinetic theory when top hat or circ function beam irradiance profile is assumed (ABP, Al, Kinetic, Circ, Electron)

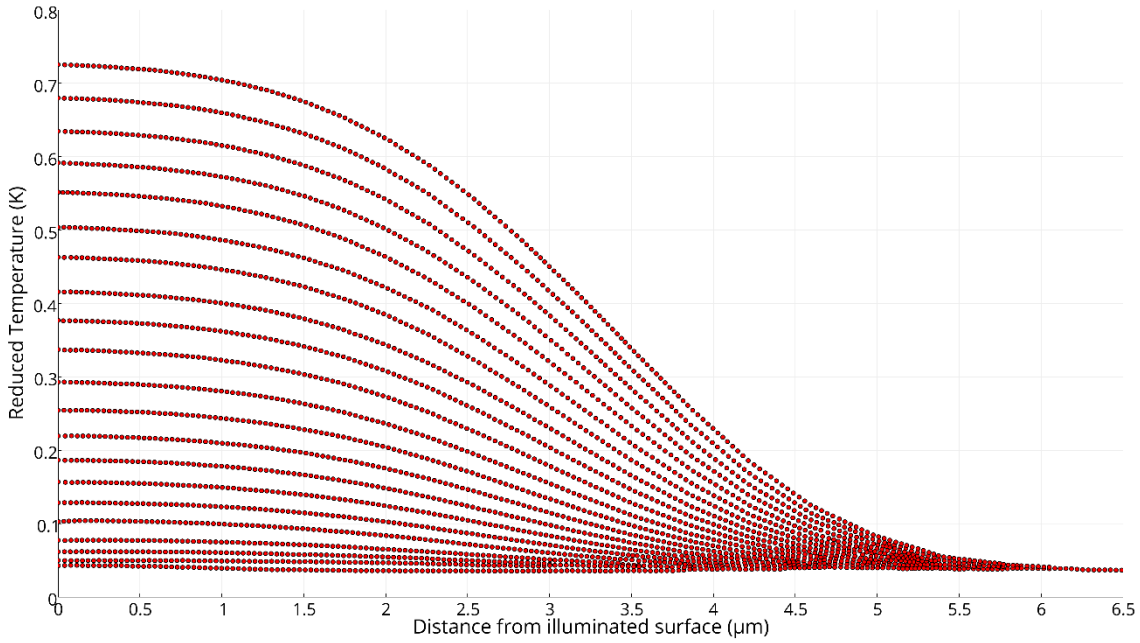

Figure 60: Above boiling point: Electron temperature profile at 0.2 μs time intervals in Cu space debris using Kinetic theory when Gaussian beam is assumed (ABP, Cu, Kinetic, Gaussian, Electron)

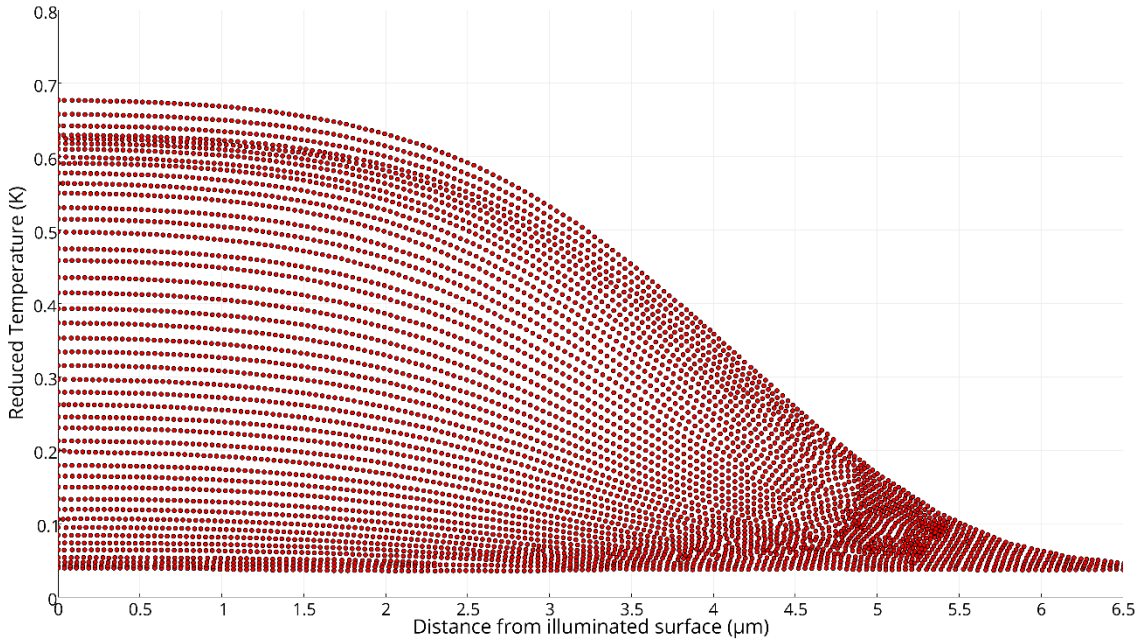

Figure 61: Above boiling point: Electron temperature profile at 0.2 μs time intervals in Cu space debris using Kinetic theory when top hat or circ function beam irradiance profile is assumed (ABP, Cu, Kinetic, Circ, Electron)

For the temperature distribution of lattice in Ni, Al and Cu space debris, Figure 62 to Figure 73 have been produced when the Gaussian beam or circ function beam irradiance profile is assumed. Figure 62 to Figure 65 are for nickel space debris, Figure 66 to Figure 69 are for aluminium space debris, and Figure 70 to Figure 73 are for copper space debris.

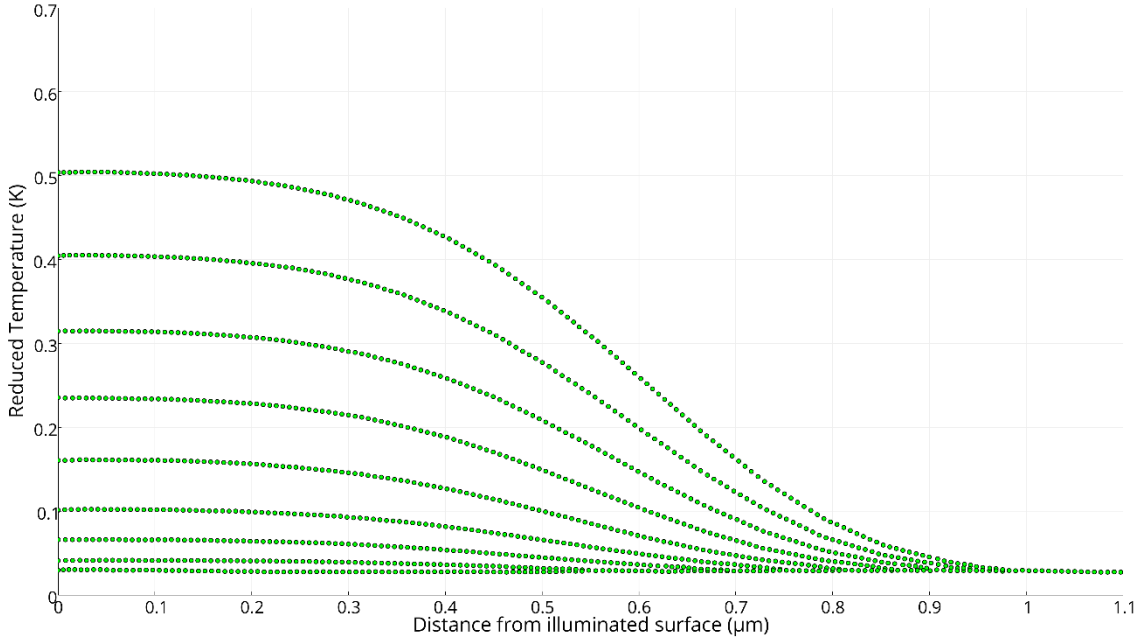

Figure 62: Above boiling point: Lattice temperature profile at 0.2 μs time intervals in Ni space debris using Kinetic theory when Gaussian beam is assumed (ABP, Ni, Kinetic, Gaussian, Lattice)

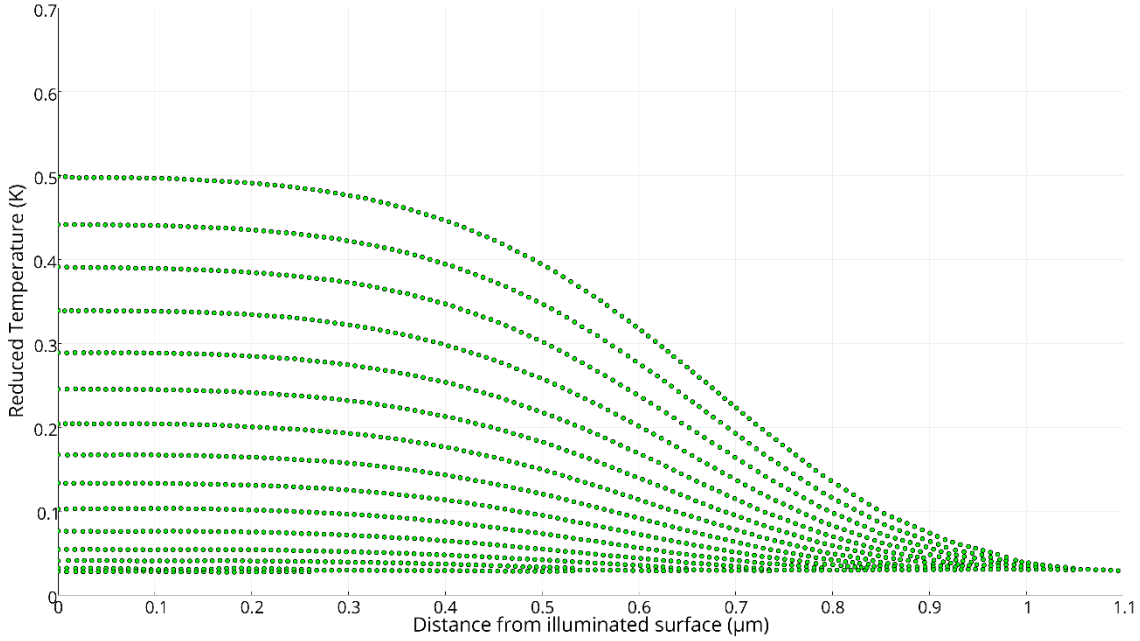

Figure 63: Above boiling point: Lattice temperature profile at 0.2 μs time intervals in Ni space debris using Kinetic theory when top hat or circ function beam irradiance profile is assumed (ABP, Ni, Kinetic, Circ, Lattice)

The positive temperature slope of the lattice that occurs at the surface layer of the Ni space debris is not obvious even if you zoomed in a thin layer underneath the surface of the wreckage due to the limitation of the figures scale; see Figure 64 and Figure 65.

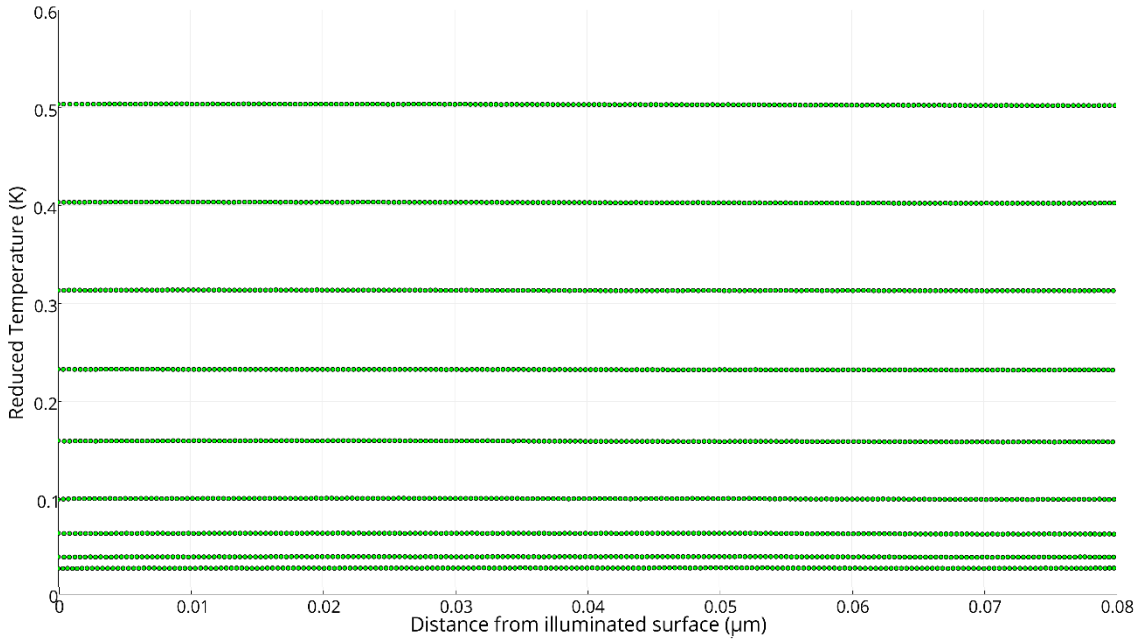

Figure 64: Above boiling point: Zoomed lattice temperature profile at 0.2 μs time intervals in Ni space debris using Kinetic theory when the Gaussian beam is assumed (ABP, Ni, Kinetic, Gaussian, Lattice)

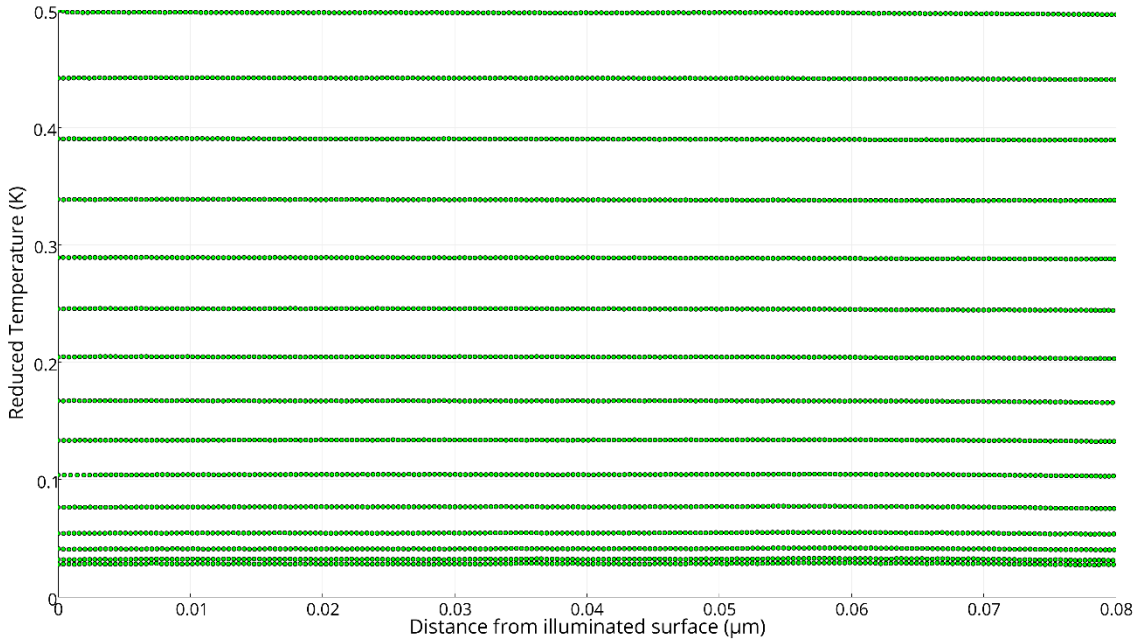

Figure 65: Above boiling point: Zoomed lattice temperature profile near surface at 0.2 μs time intervals in Ni space debris using Kinetic theory when top hat or circ function beam irradiance profile is assumed (ABP, Ni, Kinetic, Circ, Lattice)

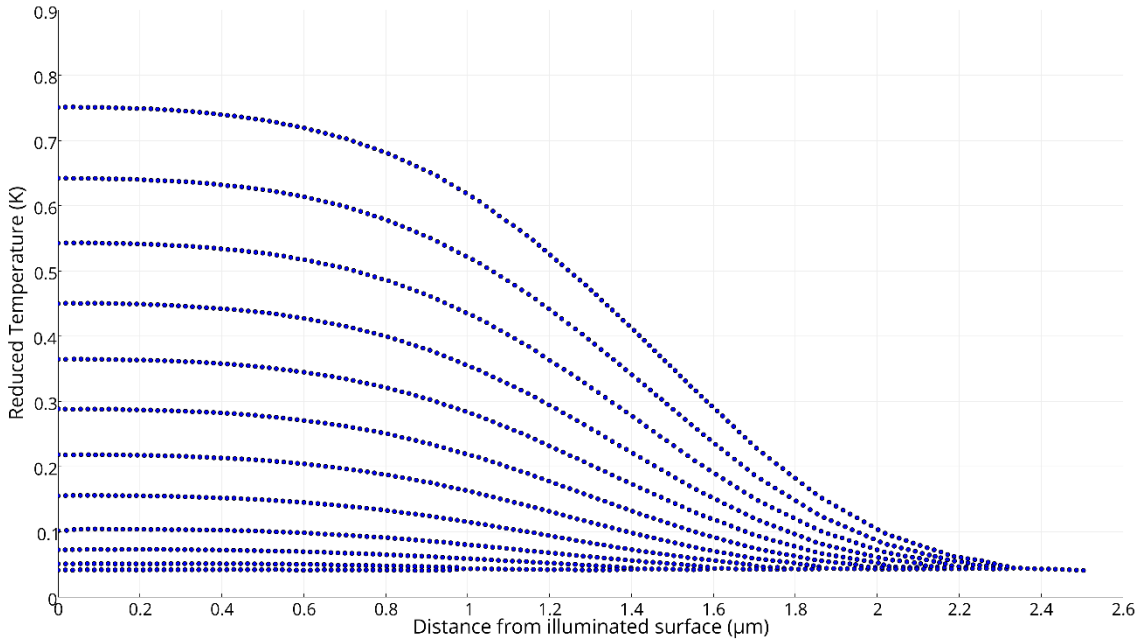

Figure 66: Above boiling point: Lattice temperature profile at 0.2 μs time intervals in Al space debris using Kinetic theory when Gaussian beam is assumed (ABP, Al, Kinetic, Gaussian, Lattice)

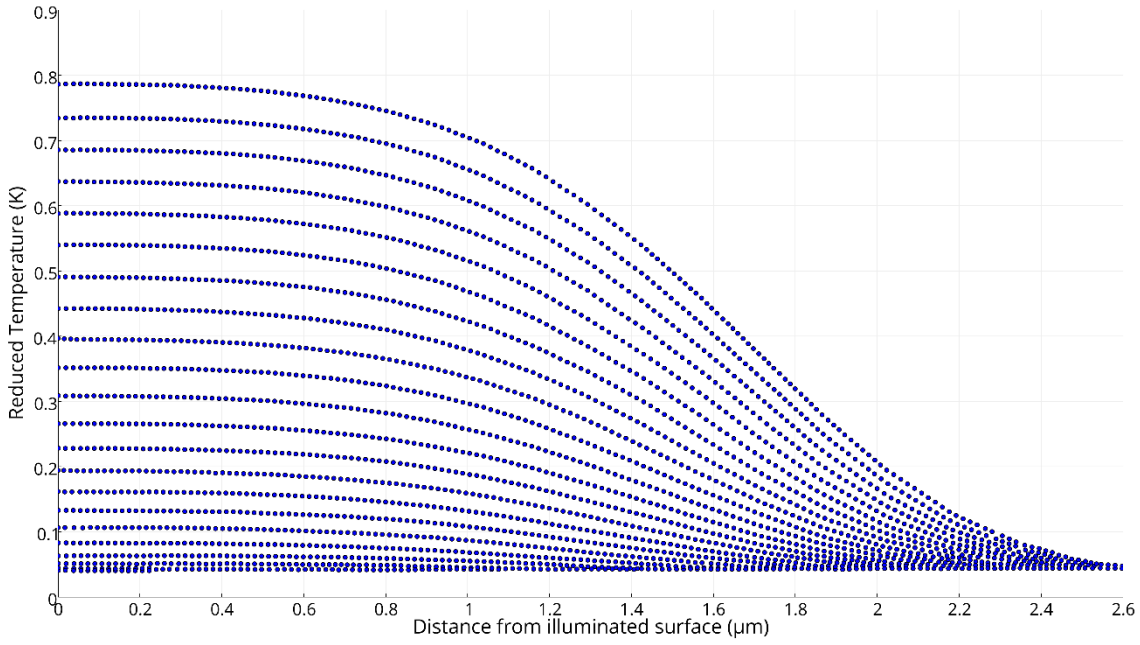

Figure 67: Above boiling point: Lattice temperature profile at 0.2 μs time intervals in Al space debris using Kinetic theory when top hat or circ function beam irradiance profile is assumed (ABP, Al, Kinetic, Circ, Lattice)

In Al space debris, a high positive temperature slope of lattice occurs at the surface layer of the wreckage to a distance of five nm underneath the surface layer of the debris, as shown in Figure 68 and Figure 69.

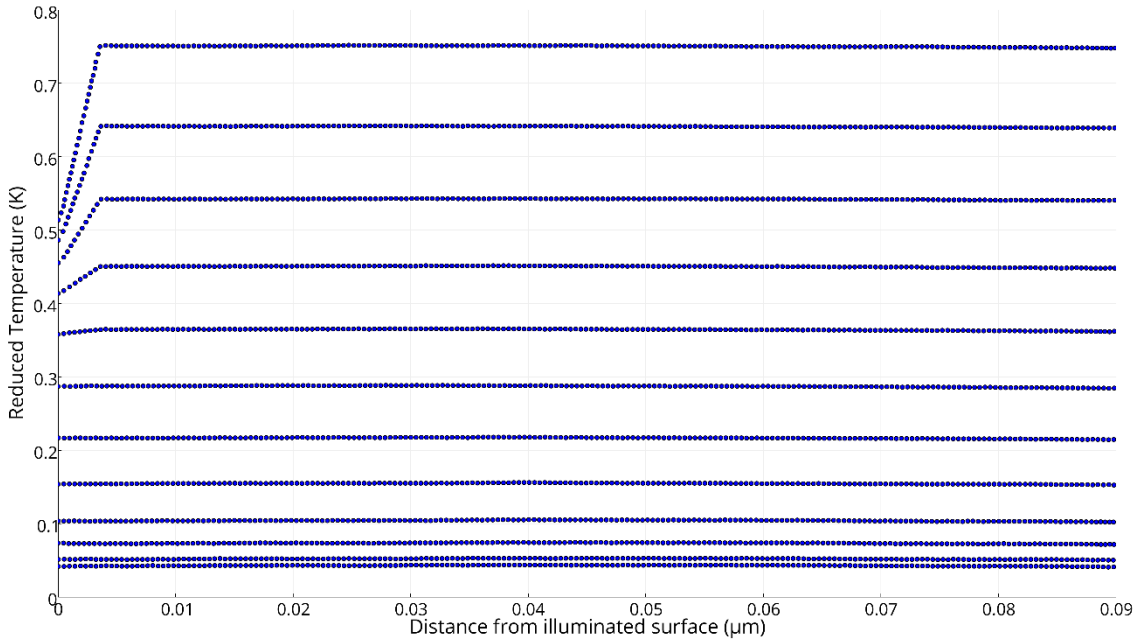

Figure 68: Above boiling point: Zoomed lattice temperature profile at 0.2 μs time intervals in Al space debris using Kinetic theory when Gaussian beam is assumed (ABP, Al, Kinetic, Gaussian, Lattice)

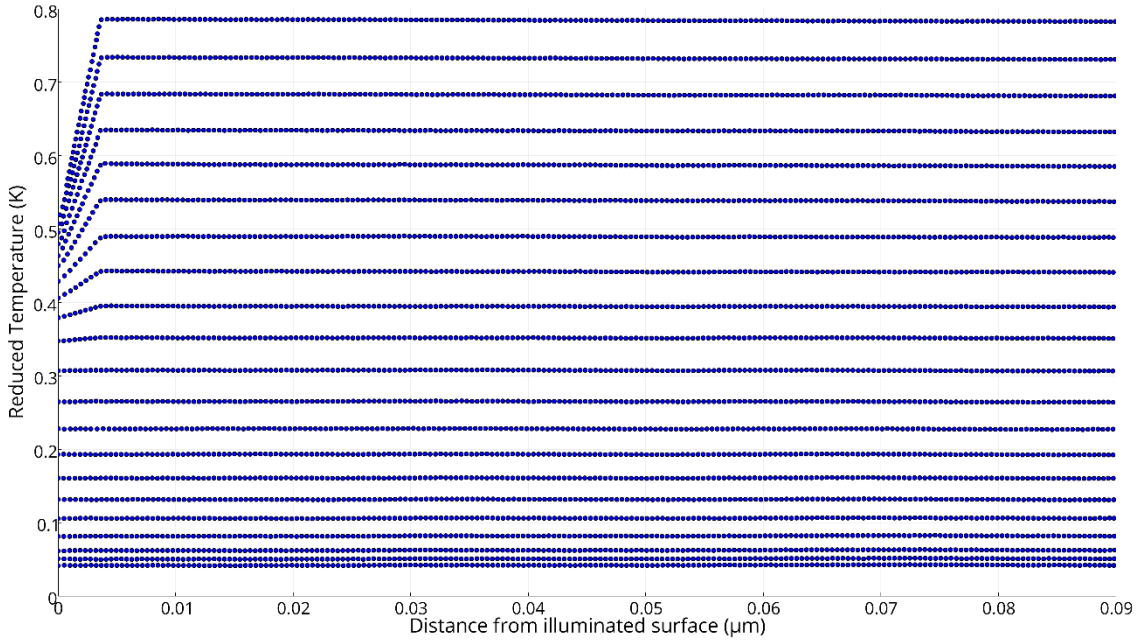

Figure 69: Above boiling point: Zoomed lattice temperature profile at 0.2 μs time intervals in Al space debris using Kinetic theory when top hat or circ function beam irradiance profile is assumed (ABP, Al, Kinetic, Circ, Lattice)

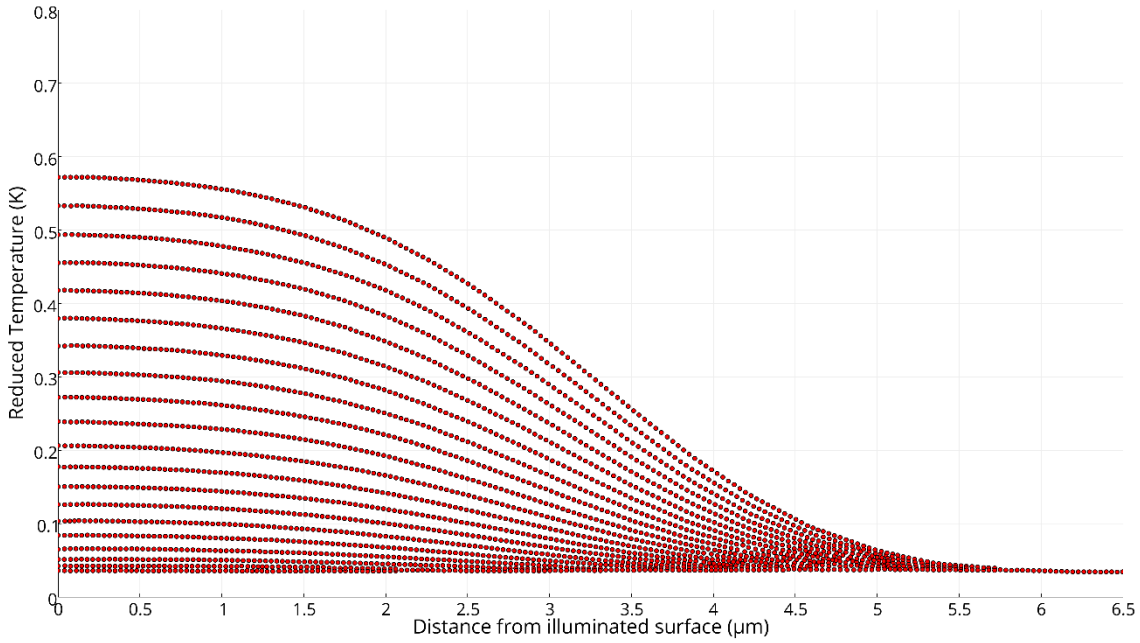

Figure 70: Above boiling point: Lattice temperature profile at 0.2 μs time intervals in Cu space debris using Kinetic theory when Gaussian beam is assumed (ABP, Cu, Kinetic, Gaussian, Lattice)

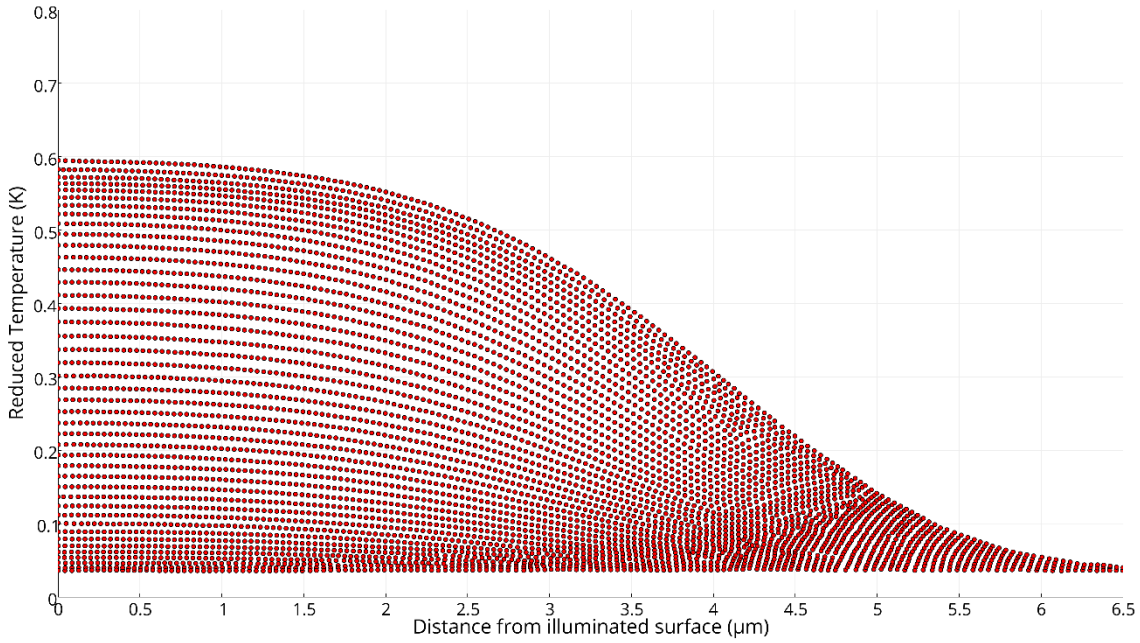

Figure 71: Above boiling point: Lattice temperature profile at 0.2 μs time intervals in Cu space debris using Kinetic theory when top hat or circ function beam irradiance profile is assumed (ABP, Cu, Kinetic, Circ, Lattice)

For Cu orbital debris, this lattice positive temperature slope occurs at a greater distance underneath the surface layer of the wreckage, about 10 nm, see Figure 72 and Figure 73.

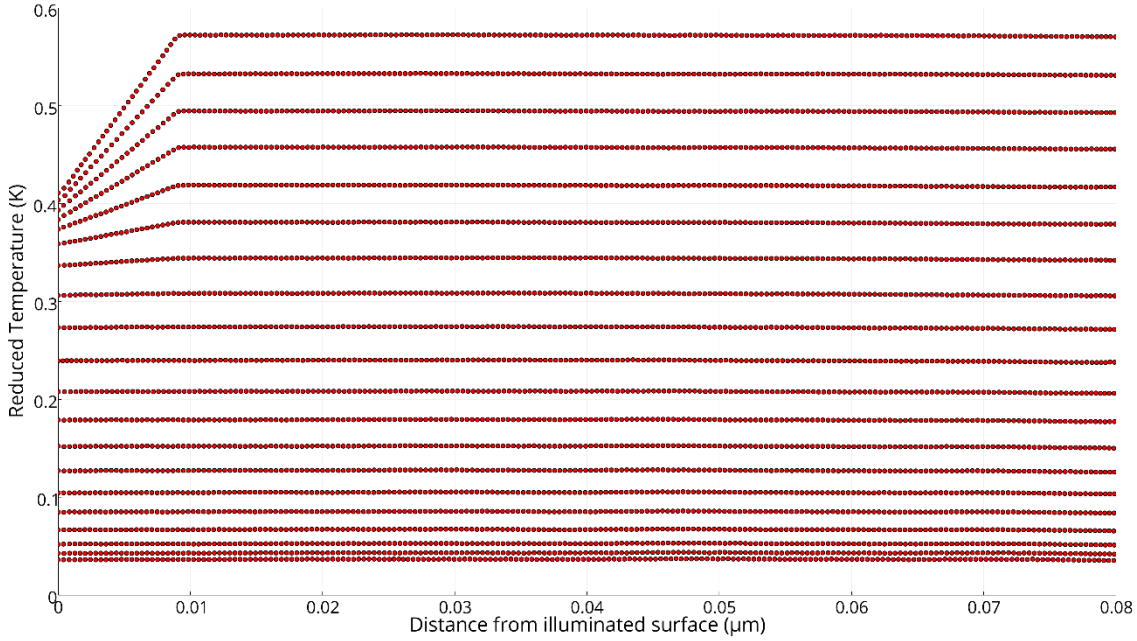

Figure 72: Above boiling point: Zoomed lattice temperature profile at 0.2 μs time intervals in Cu space debris using Kinetic theory when Gaussian beam is assumed (ABP, Cu, Kinetic, Gaussian, Lattice)

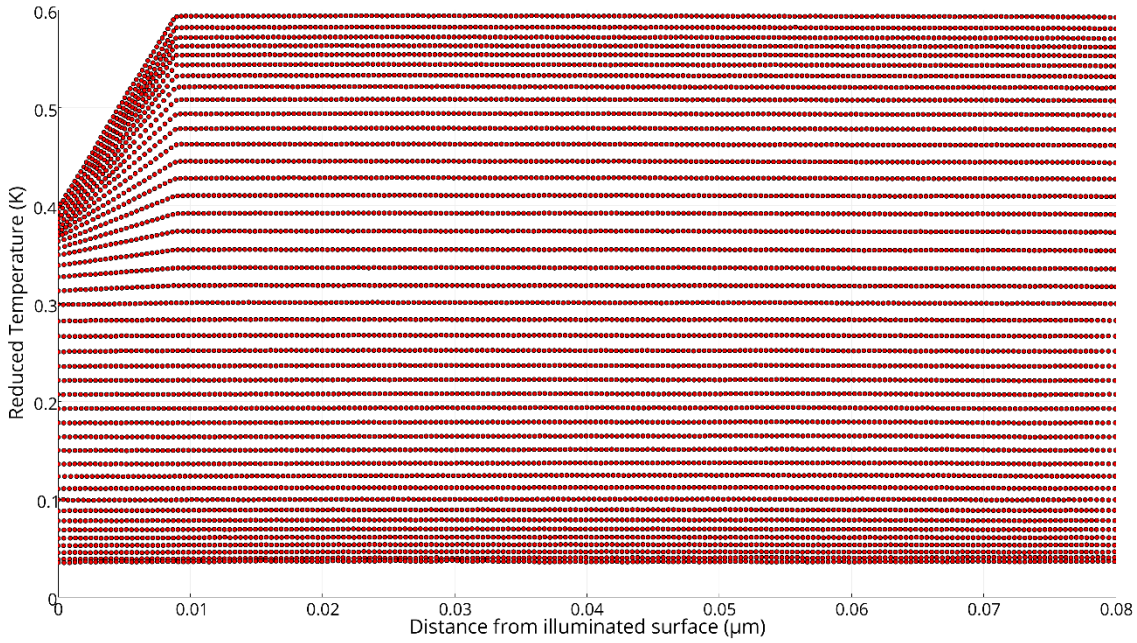

Figure 73: Above boiling point: Zoomed lattice temperature profile at 0.2 μs time intervals in Cu space debris using Kinetic theory when top hat or circ function beam irradiance profile is assumed (ABP, Cu, Kinetic, Circ, Lattice)

The temporal change in laser power and the difference between lattice and electron surface temperature of the debris below and above the boiling points for Ni, Al and Cu space debris are presented in Figure 74, Figure 75 and Figure 76 respectively.

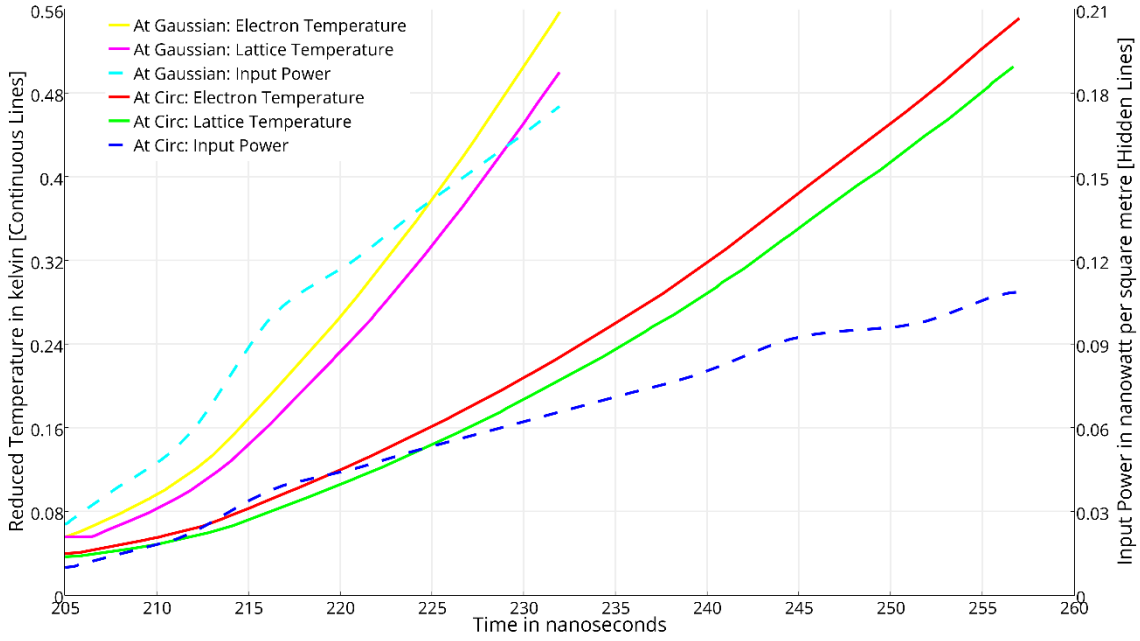

Figure 74: Nickel electron and lattice surface temperatures (continuous lines) below and above boiling point using kinetic theory. Hidden lines are the laser beam input power as a function of time.

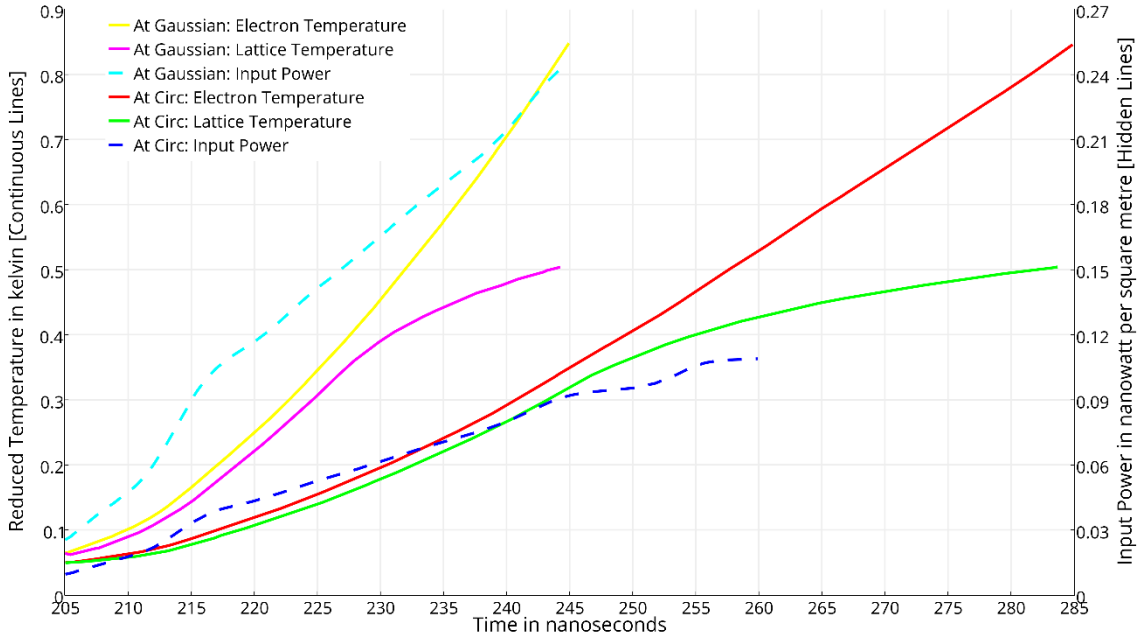

Figure 75: Aluminium electron and lattice surface temperatures (continuous lines) below and above boiling point using kinetic theory. Hidden lines are the laser beam input power as a function of time.

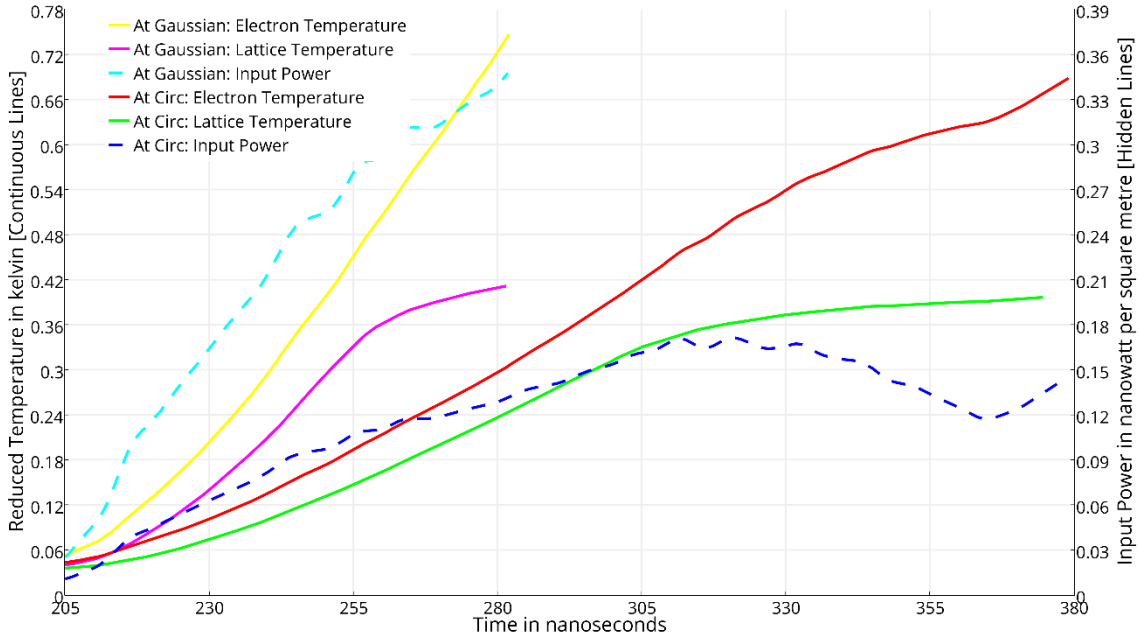

Figure 76: Copper electron and lattice surface temperatures (continuous lines) below and above boiling point using kinetic theory. Hidden lines are the laser beam input power as a function of time.

Figure 74 shows that electron temperature and lattice temperature curves for nickel space junk are rising with little and steady separation between them, even beyond the boiling point of nickel debris that is given in Table 6. This is because nickel has a large number of electrons, 10 electrons, in its outside shells (i.e. outside the filled inner shells) comparing to aluminium that has three electrons or copper which has only one electron in its outside shells. The periodic table in Table 7 has been used to calculate the electronic configuration of Ni, Al and Cu atoms, as shown in Table 8.

Table 6: The boiling point for the selected three space debris targets.

Space Debris Material	Boiling Point $[K]$	T_c = Critical Temperature of the Metal $[K]$	Reduced Temperature at Boiling Point
Nickel Space Debris	3,003	10,800	0.28
Aluminium Space Debris	2,743	7,400	0.37
Copper Space Debris	2,835	8,500	0.33

Nickel has been shown as a transition metal, and the electrons inner structure characterises the transition elements in nickel metal [80]. In fact, the two outside shells in Ni are in charge of chemical reactions. The Fermi level lies close to the lowest part of the d-shell, and the d-shell is not having the whole 10 electrons in nickel. Instead, it has eight electrons [81].

Table 7: Periodic table and its $s-$, $f-$, $d-$, $p-$block

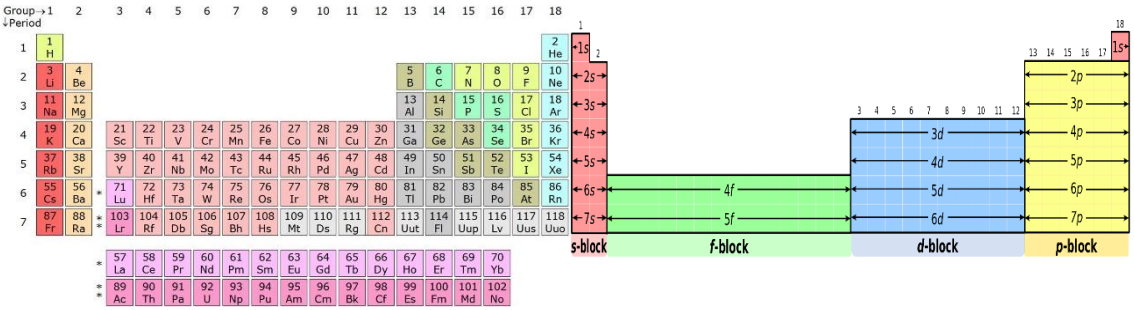

On the other hand, it can be noticed that in Figure 75 and Figure 76 the increase rate of lattice temperature for aluminium and copper debris are slowing down when the boiling point of each debris is reached, comparing to the consistent increase in the electron temperature in these two debris metals. This is because of the lattice energy lost during the evaporation process.

Table 8: Electronic configuration of Ni, Al and Cu atoms

Metal Type	Atomic Number [*electrons*]	Electronic Configuration of the Metal Atom	Number of Electrons in the Outside Shells
Ni	28	$1s^2\ 2s^2\ 2p^6\ 3s^2\ 3p^6\ \mathbf{3d^8}\ \mathbf{4s^2}$	10
Al	13	$1s^2\ 2s^2\ 2p^6\ \mathbf{3s^2\ 3p^1}$	3
Cu	29	$1s^2\ 2s^2\ 2p^6\ 3s^2\ 3p^6\ 3d^{10}\ \mathbf{4s^1}$	1

Note that there are three electrons in the outside shells of Al, but only the $3p^1$ is incomplete unlike Cu, which has only one electron in the outside shell, that is the $4s^1$. Fermi energy level at absolute zero lies close to the lowest part of the $3s^2$ and $3p^1$ shells in aluminium, which is a trivalent metal [82]. For copper, noble metal, the Fermi energy level lies on top of the lowest part of the $4s^1$ shell. This is actually the reason why it is

comparatively not difficult to take out the outside, unbound, electron(s) from Al and Cu atoms compared to electrons in the outside shells of Ni, which are bound forming the ion core. This gives an explanation of the electrons movement phenomena in the outside shells of Al and Cu to higher energy levels and so create a significant divergence between electron temperature and lattice phonon temperature in Al and Cu space debris, unlike in Ni debris.

Chapter 5

Irradiation of Space Debris with Laser Pulses: Fourier Conduction Theory

5 Irradiation of Space Debris with Laser Pulses: Fourier Conduction Theory

5.1 Summary

Comparing with the previous chapter (Chapter 4), which focused on the Kinetic theory of space debris irradiation with laser pulses, this chapter focuses on the Fourier conduction theory, then discusses the results and compares them with the results from the Kinetic theory in order to draw a conclusion. The simulation has been repeated for three different space debris surface materials illuminated with laser pulses. This helped to study the evolution of spatial temperature distribution in the subsurface layers of the space debris.

5.2 Fourier Conduction Theory

This theory is applied to characterise the event of conveying energy where laser radiation photon energy is coupled straight away into the molecular lattice of the space debris material. The model contained evaporation when the surface temperature of the wreckage increased to beyond the boiling point of the debris material. This theory has been utilised by some authors to characterise the series of actions that were happening in the heat transfer when the debris materials were illuminated by a laser beam [83]. The numerical solutions were based on [84], who considered a one-dimensional heat movement towards the depth of the material, which is in this scenario into the depth of the space debris materials. This depth is in the $x-$ direction where the smallest space Δx between two isothermal levels (with ΔT variation between their temperatures) is equal to ten times the mean-free-path between electron and phonon as shown in the following expression:

$$\Delta x = 10l \qquad \text{Equation 5.1}$$

Where:

$x =$ Depth of light penetration

$l =$ Electron-phonon mean free path

The pulsed Nd^{3+} Glass laser output power has been utilised as data in determining the solution of lattice temperatures of the debris material using Kinetic theory. The progress of the lattice temperature profile is assessed in this thesis by employing various assumptions, the Gaussian function assumption and the top hat (circ function) assumption for the intensity distribution of the laser beam.

Fourier theory can give a precise characterisation for the series of actions that are involved in conveying energy, but it demands the following two main assumptions, which are not met. First, the matter is homogeneous, like in the Kinetic model, which is incorrect at an interatomic distance. Second, the heat transported from one side to the other side of a mathematical plane is defined solely by the thermal slope at the plane. Consequently, the following equation can be applied:

$$Q = -KA\frac{dT}{dx} \qquad \text{Equation 5.2}$$

This is actually incorrect for cases when considering higher order temperature gradients that happen in the ranges of the order of $10l$. The conduction Fourier mathematical expression for illuminated space debris materials with laser beam is incorrect because the optical absorption depth, which is $^{1}/_{Absorption\ coefficient\ (\delta)}$, is of the order of $10l$ for almost all debris materials. Generally, the absorption coefficient δ is a function of temperature and wavelength λ. To take sufficient consideration of the absorption process, $\Delta x \ll {}^{2}/_{\delta}$ is needed but this disagrees with the demand that $\Delta x > 10l$. In fact, in order to meet the needs of mathematics and physics Δx should be $\geq 10l$. In differential equation numerical solution for heat conduction, electrons spread in distance $10l$ of the isothermal plane and these electrons provide heat conduction from one side to the other side of the plane [85]. The flow passing x_1 is independent of the flow passing x_2 when $\Delta x > 10l$, the variation explains the gained energy at Δx. Hence:

$$Q = -KA\frac{dT}{dx}\ is\ correct\ if\ \delta \ll {}^{0.5}/_{l} \qquad \text{Equation 5.3}$$

The incident laser radiation at any point that is located at a distance x into a debris material is absorbed and can be estimated using this intensity I equation:

$$I = I_0 e^{-\delta x} \qquad \text{Equation 5.4}$$

Where: $I_0 =$ Incident intensity

The equation validity of the classical Fourier heat conduction in determining generated impacts on an opaque surface after absorbing energy from a high-power laser radiation has been examined in the literature [86]. The author determined the increase in temperature without phase transformation, including time contingent intensity and evaporation impacts. He derived a conclusion that the material surface temperature increases quickly to the vaporisation temperature of the material when a high-power laser pulse hits the material. However, he supposed in his analysis that the temperature of the evaporating surface stays at the boiling temperature of the material. The other thing is that the evaporation temperature of the space debris material does change, as it will rise with recoil pressure, because there is recoil pressure on the wreckage material surface. The profile of the temperature in the volume of the debris material would nearly follow the shape of the laser pulse, which usually takes an irregular shape that falls somewhere between the Gaussian shape and the top hat shape. The Fourier heat conduction is utilised here to define the profile of the temperature in the debris target. The proper one-dimension laser heating expression format of heat conduction is for $s > 0$:

$$\frac{\partial}{\partial t}\left[\rho C_p T\right] - v_s \frac{\partial}{\partial s}\left[\rho C_p T\right] = \frac{\partial}{\partial s}\left[K \frac{\partial T}{\partial s}\right] + \delta I_0 e^{-\delta s} \qquad \text{Equation 5.5}$$

The distribution of spatial temperature should change position as the surface of the debris material is moving, as the interface of vapour-liquid is moving. The one-dimensional moving boundary conditions are illustrated in Figure 77.

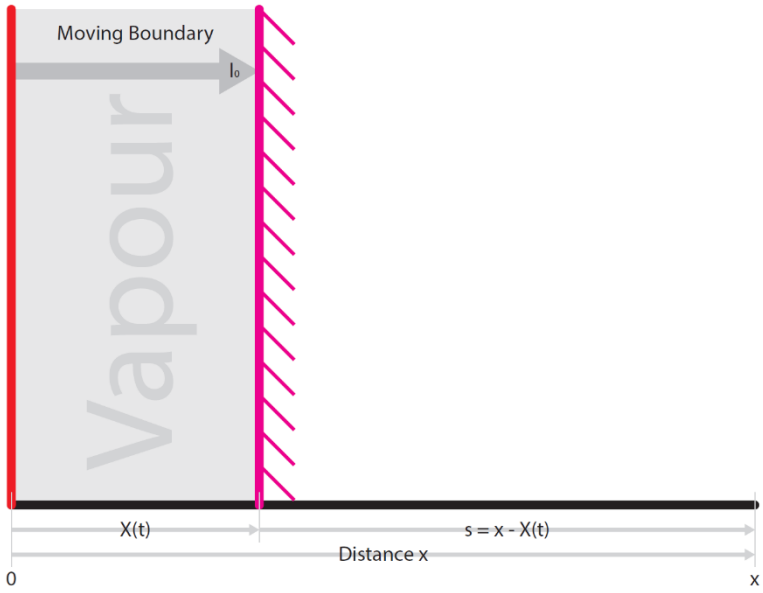

Figure 77: Moving border issue (one-dimensional)

$$K \frac{\partial T}{\partial s}\Big|_{s=0 \; or \; x=X(t)} = 0 \qquad \text{Equation 5.6}$$

Where:

$T(\infty, t) = T_0 =$ Normal specific latent heat of vaporisation

$T(0, s) = T_0 =$ Normal specific latent heat of vaporisation

The related boundary conditions, as well as the initial conditions, were used to solve Equation 5.5. The equilibrium of the energy at the debris surface demands the:

$$Energy\ given\ to\ the\ vaporised\ debris\ material = Energy\ conducted\ from\ the\ solid \qquad \text{Equation 5.7}$$

Therefore, the boundary condition is:

$$\rho L_{T_s} V_s = K \frac{\partial T}{\partial s}\Big|_{s=0} \qquad \text{Equation 5.8}$$

Where:

$L =$ Specific latent heat of vaporisation

L_{T_s} is determined by Riley [87] as:

$$L_{T_s} = L_0 \left[1 - \left[\frac{T_s}{T_c}\right]^2\right] \qquad \text{Equation 5.9}$$

Where:

$T_s =$ Lattice temperature of the surface in Kelvin

$T_c =$ Critical temperature of the metal in Kelvin

More detailed derivation and solution of the expression of Fourier heat conduction is covered by Byabagambi [88].

5.3 Spatial Lattice Temperature

The spatial lattice temperature profile in Ni, Al and Cu space debris using the Fourier theory, when the Gaussian beam was assumed, are presented in Figure 78, Figure 79 and Figure 80, respectively. The spatial distribution was taken every 200 ns, and the physical properties of the debris materials are listed in Table 9. The reduced temperature

is the ratio of the space debris material temperature to the critical temperature of that material.

Table 9: Physical properties of the targeted debris materials

Space Debris Material Type	Critical Temperature of the Space Debris Material (T_c) $[K]$	Absorption Coefficient (δ) $[1/m]$
Nickel (Ni) Space Debris	10,800	68×10^6
Aluminium (Al) Space Debris	7,400	84×10^6
Copper (Cu) Space Debris	8,500	75×10^6

On the other hand, when the top hat or circ function beam irradiance distribution was assumed, Figure 81, Figure 82 and Figure 83 are also produced for Ni, Al and Cu space debris, respectively.

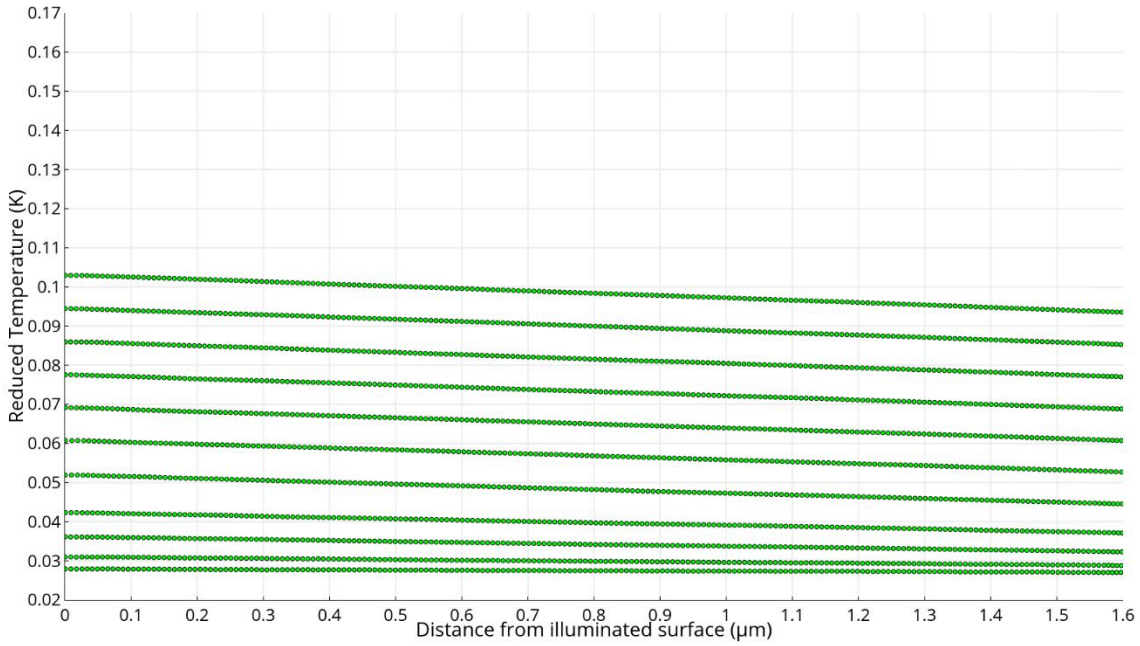

Figure 78: Zoomed lattice temperature profile at 0.2 μs time intervals in Ni space debris using Fourier conduction theory when Gaussian beam is assumed (Ni, Fourier, Gaussian, Lattice)

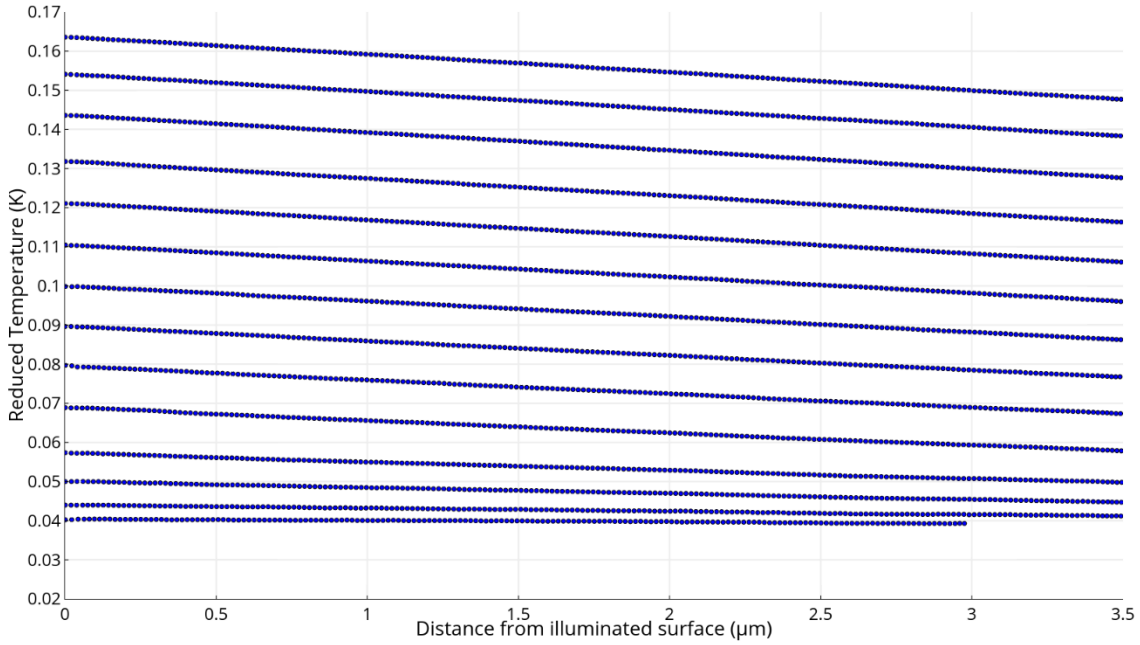

Figure 79: Zoomed lattice temperature profile at 0.2 μs time intervals in Al space debris using Fourier conduction theory when Gaussian beam is assumed (Al, Fourier, Gaussian, Lattice)

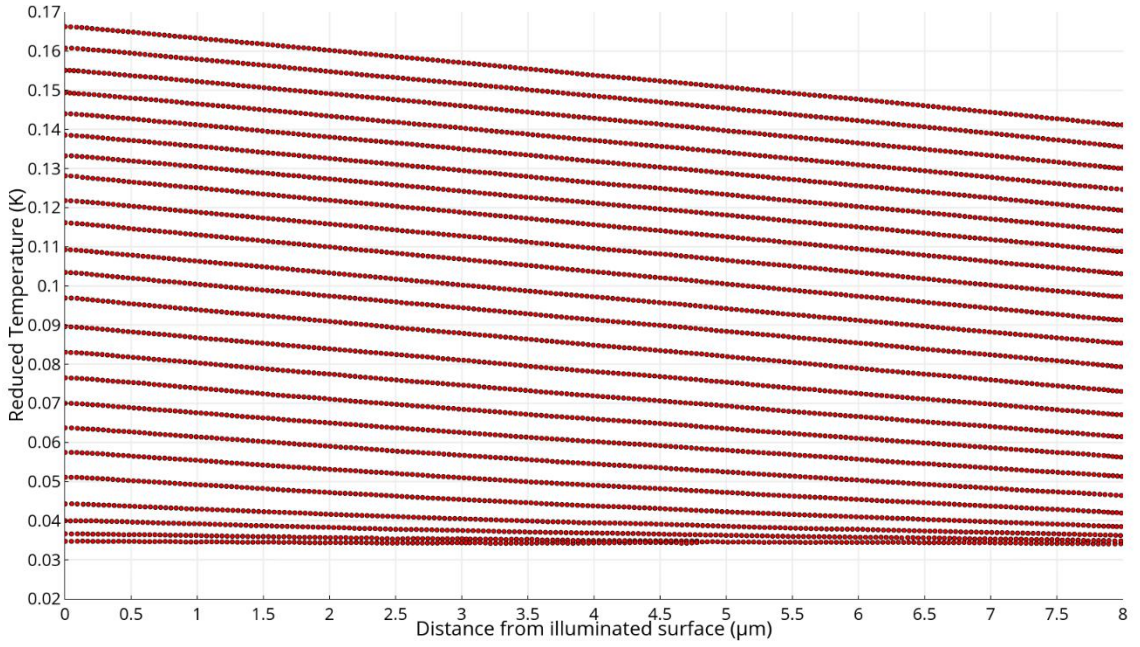

Figure 80: Zoomed lattice temperature profile at 0.2 μs time intervals in Cu space debris using Fourier conduction theory when Gaussian beam is assumed (Cu, Fourier, Gaussian, Lattice)

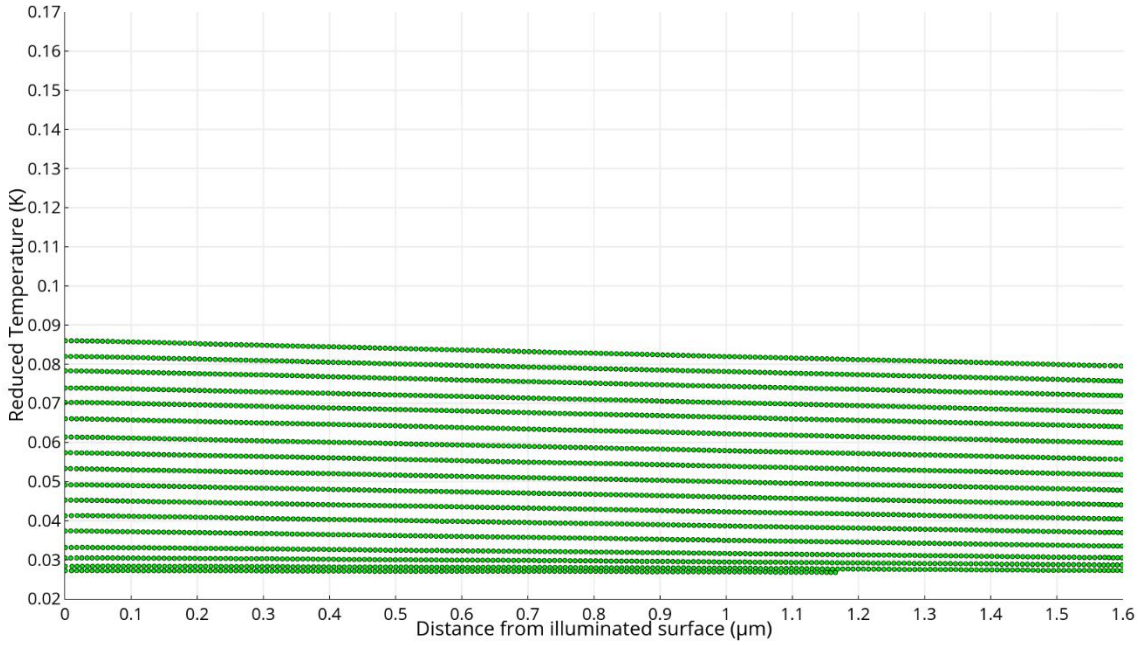

Figure 81: Zoomed lattice temperature profile at 0.2 μs time intervals in Ni space debris using Fourier conduction theory when top hat or circ function beam irradiance profile is assumed (Ni, Fourier, Circ, Lattice)

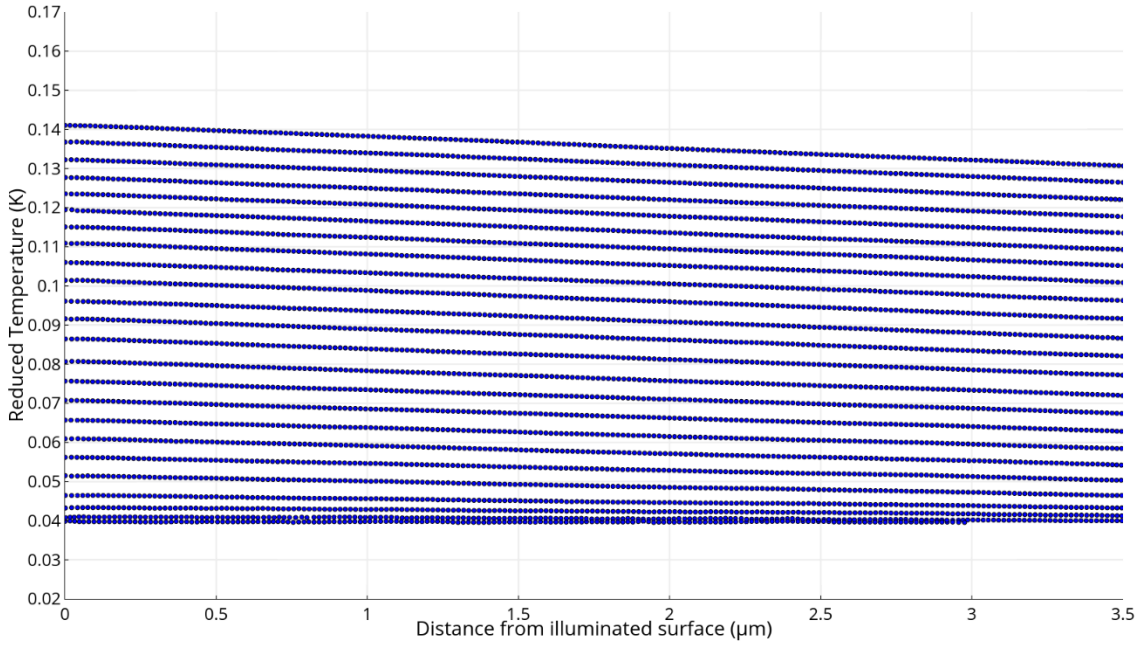

Figure 82: Zoomed lattice temperature profile at 0.2 μs time intervals in Al space debris using Fourier conduction theory when top hat or circ function beam irradiance profile is assumed (Al, Fourier, Circ, Lattice)

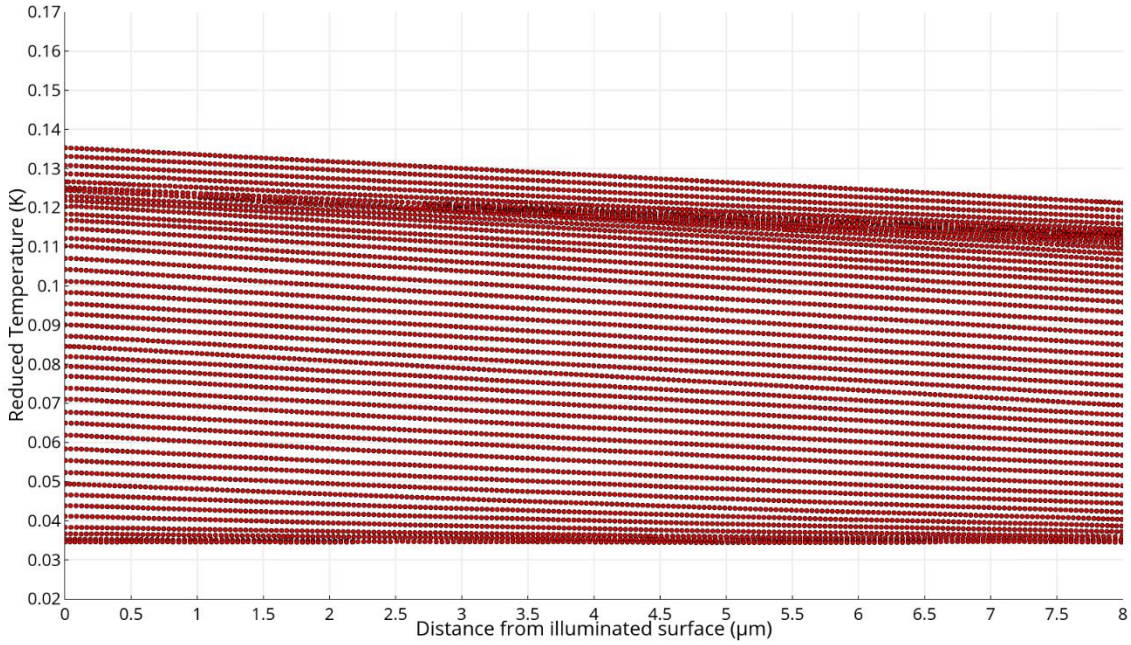

Figure 83: Zoomed lattice temperature profile at 0.2 μs time intervals in Cu space debris using Fourier conduction theory when top hat or circ function beam irradiance profile is assumed (Cu, Fourier, Circ, Lattice)

It is clear that the figures present the lattice temperature profile for each of the three space debris materials at short penetration depth, very close to the illuminated surface. It is also evident that the lattice temperature profiles have slight negative slopes on the surface of the space debris materials, but they have high penetration depths. However, the previous six figures are zoomed in and only focused at short distances from the irradiated space debris surfaces, and that is why the whole penetration depths are not apparent. Therefore, using the Fourier theory, Figure 84, Figure 85 and Figure 86 have been produced to display the complete penetration depths of the spatial lattice temperature profiles in the same Ni, Al and Cu space debris, respectively, when Gaussian beam assumed. Figure 87, Figure 88 and Figure 89 are also produced for the Ni, Al and Cu orbital debris respectively but this time when the top hat or circ function beam irradiance distribution is assumed. The spatial distribution was also taken every 200 ns.

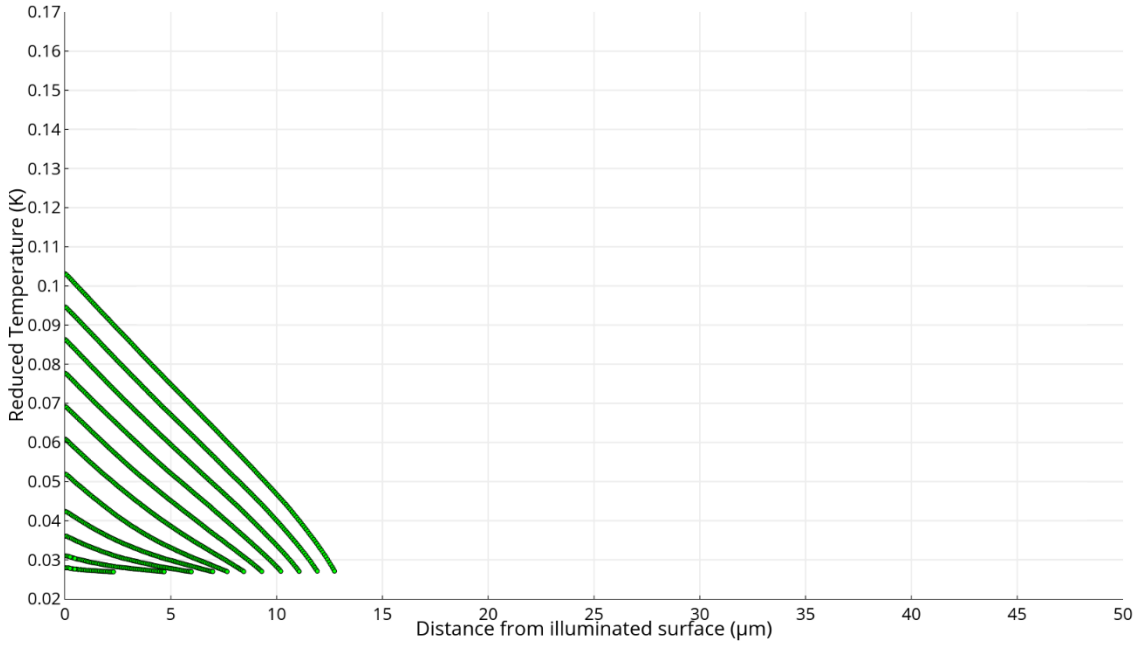

Figure 84: Lattice temperature profile at 0.2 μs time intervals in Ni space debris using Fourier conduction theory when Gaussian beam is assumed (Ni, Fourier, Gaussian, Lattice)

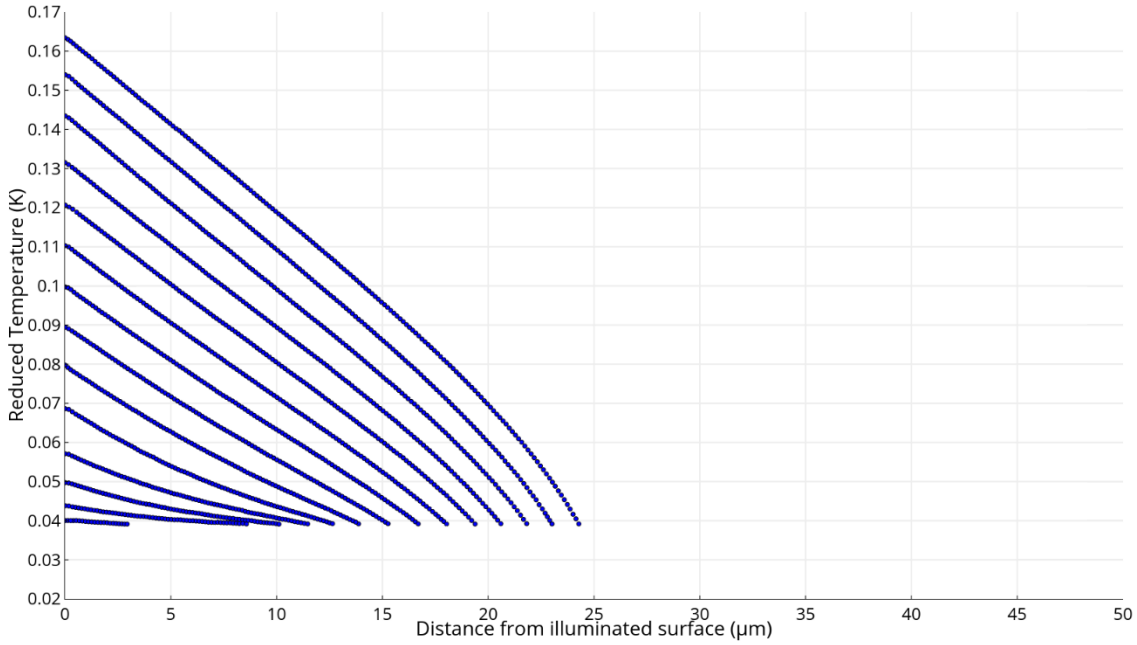

Figure 85: Lattice temperature profile at 0.2 μs time intervals in Al space debris using Fourier conduction theory when Gaussian beam is assumed (Al, Fourier, Gaussian, Lattice)

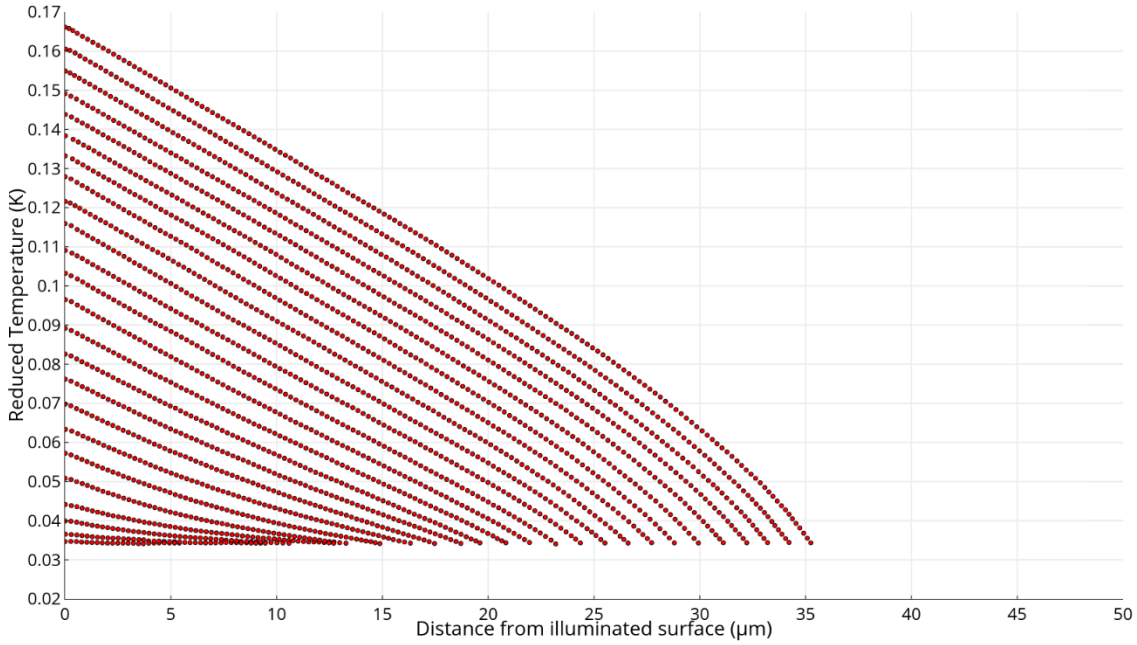

Figure 86: Lattice temperature profile at 0.2 μs time intervals in Cu space debris using Fourier conduction theory when Gaussian beam is assumed (Cu, Fourier, Gaussian, Lattice)

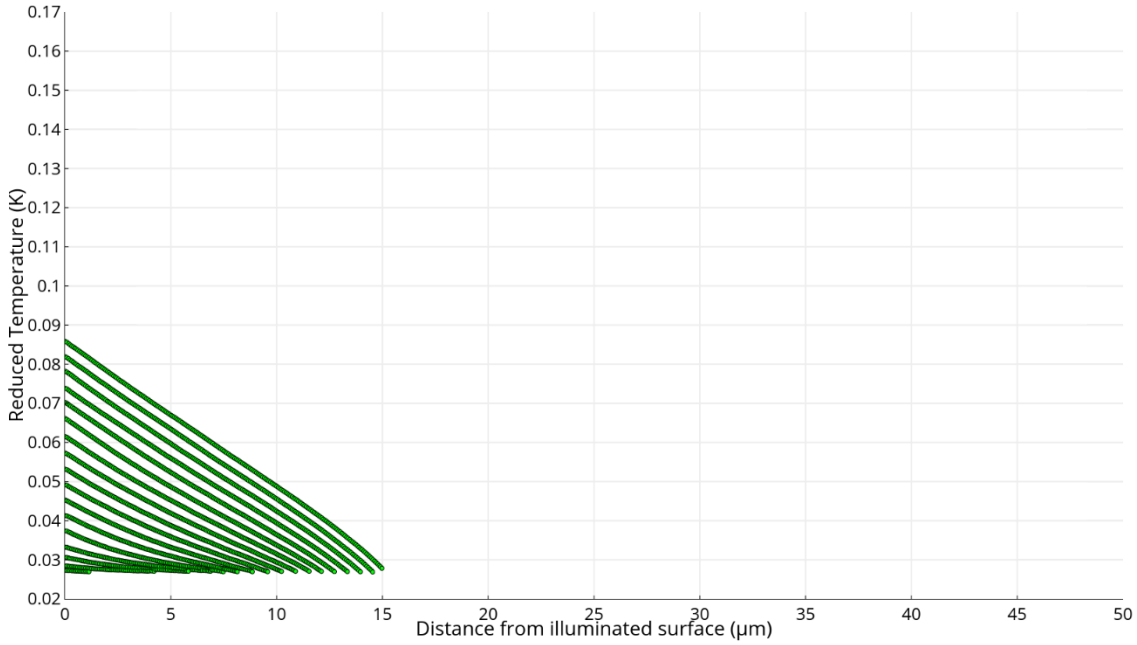

Figure 87: Lattice temperature profile at 0.2 μs time intervals in Ni space debris using Fourier conduction theory when top hat or circ function beam irradiance profile is assumed (Ni, Fourier, Circ, Lattice)

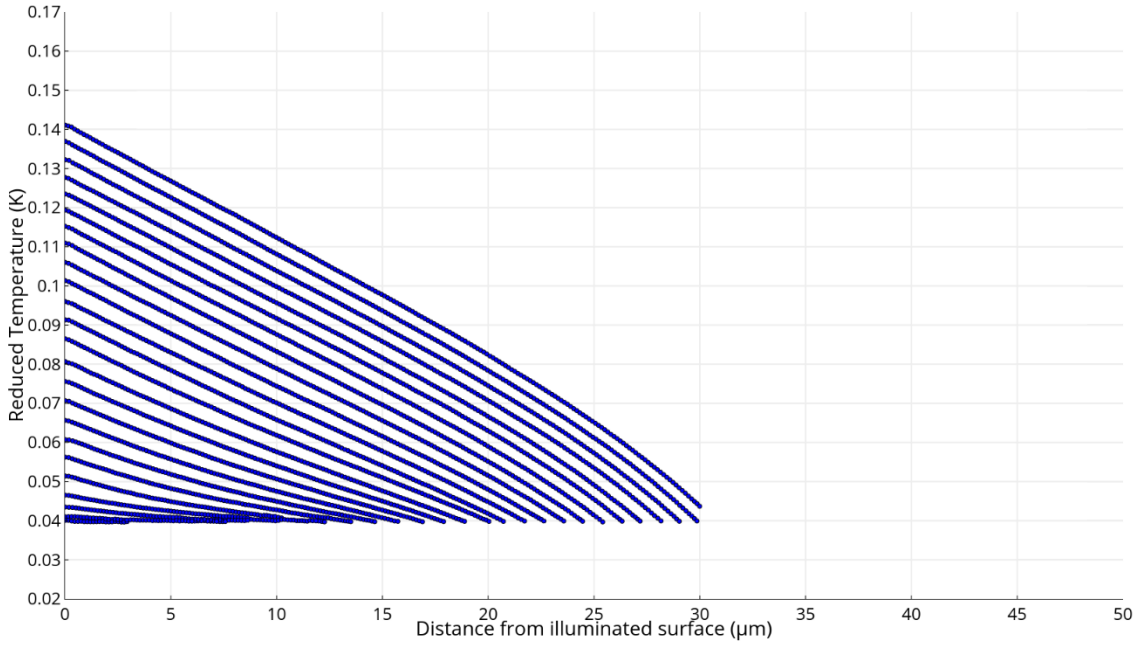

Figure 88: Lattice temperature profile at 0.2 μs time intervals in Al space debris using Fourier conduction theory when top hat or circ function beam irradiance profile is assumed (Al, Fourier, Circ, Lattice)

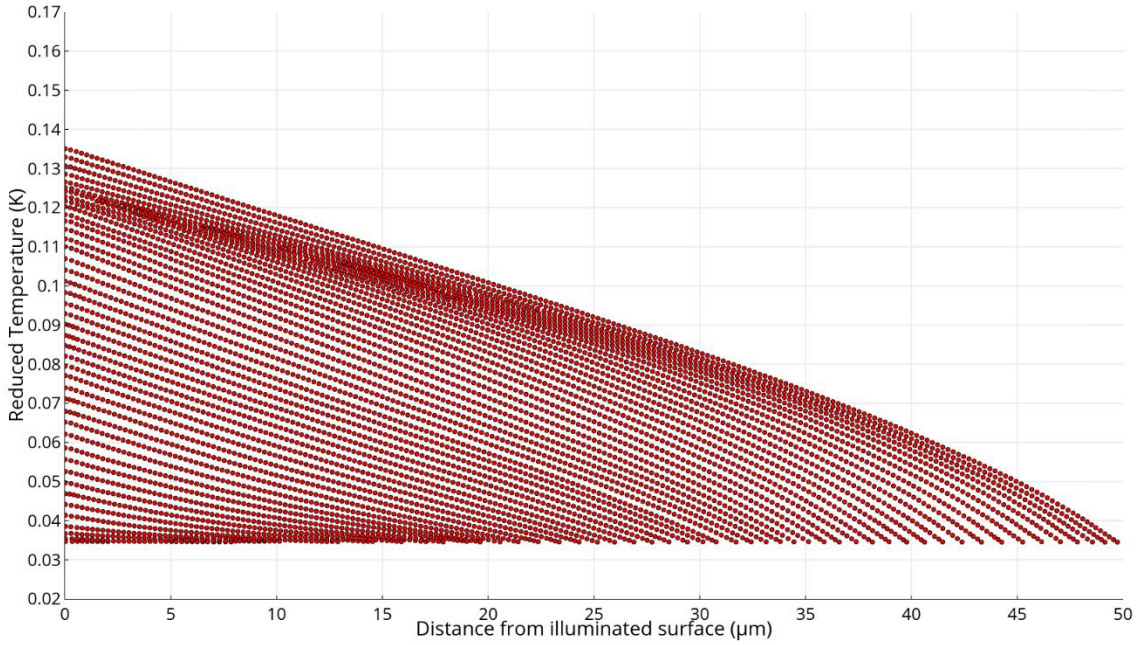

Figure 89: Lattice temperature profile at 0.2 μs time intervals in Cu space debris using Fourier conduction theory when top hat or circ function beam irradiance profile is assumed (Cu, Fourier, Circ, Lattice)

The following two figures, Figure 90 and Figure 91, are produced to provide an in-depth comparison of the lattice temperature profile of the three space debris samples using Fourier conduction theory for both cases, when Gaussian beam assumed and when circ function (top hat) irradiance profile assumed, respectively.

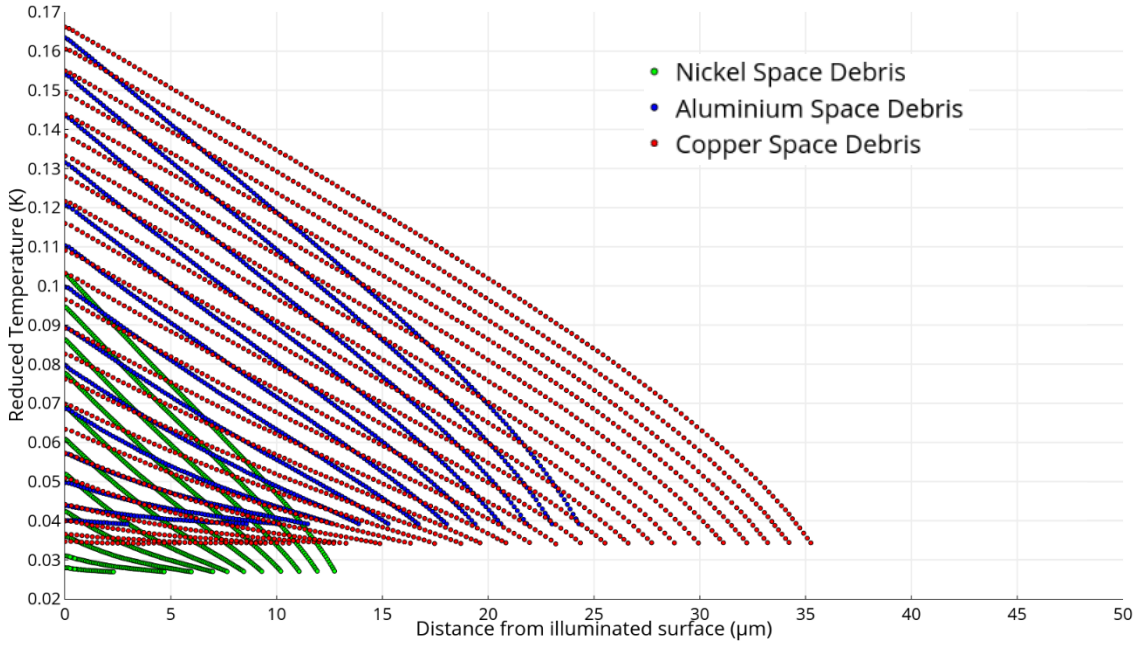

Figure 90: Lattice temperature profile at 0.2 μs time intervals in Ni, Al and Cu space debris using Fourier conduction theory when Gaussian beam is assumed (Fourier, Gaussian, Lattice)

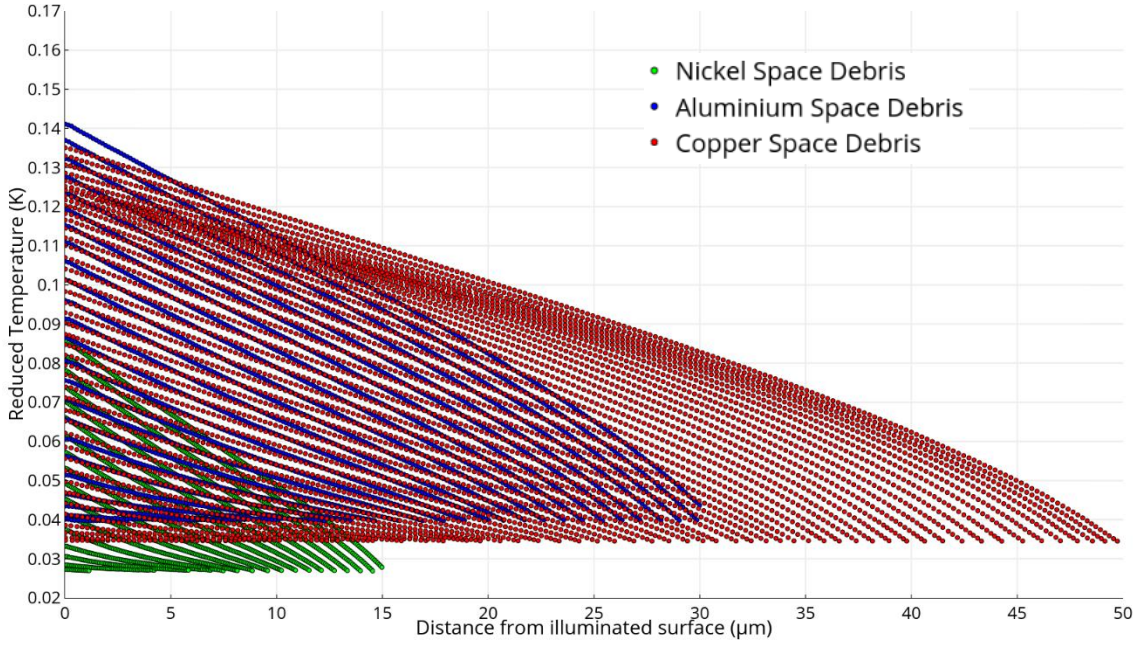

Figure 91: Lattice temperature profile at 0.2 μs time intervals in Ni, Al and Cu space debris using Fourier conduction theory when top hat or circ function beam irradiance profile is assumed (Fourier, Circ, Lattice)

The following table, Table 10, compares the penetration distance from the illuminated surface of the nickel, aluminium and copper space debris. A reduced temperature of 0.08 K has been chosen as a moderately reduced temperature that can be used as a reference point to make our comparison, as it fits in any of the previous figures in this section.

Table 10: Penetration distance comparison for nickel, aluminium and copper space debris when Fourier conduction theory is used

Space Debris Type	Diffusivity $\left[m^2/s\right]$	Penetration Distance From the Illuminated Space Debris Surface [μm]		
		When Gaussian Beam Assumed	When Top Hat or Circ Function Beam Irradiance Profile Assumed	Difference
Nickel Space Debris	27.2×10^{-6}	10.20	13.96	3.76
Aluminium Space Debris	90.9×10^{-6}	13.87	18.88	5.01
Copper Space Debris	96.1×10^{-6}	18.70	25.97	7.27

It is evident, from the above table, that the penetration distance from the illuminated space debris is larger for debris with high diffusivity metals. Furthermore, under the same laser irradiance, the penetration distance is greater by about 37% when the top hat or circ function beam irradiance profile is assumed, compared to the case when Gaussian beam assumed.

5.4 Input Power Profile with Lattice Surface Temperature of Space Debris

The change of the lattice surface temperature with the input power profile in nickel, aluminium and copper space debris at 50 ns time intervals are presented in Figure 92.

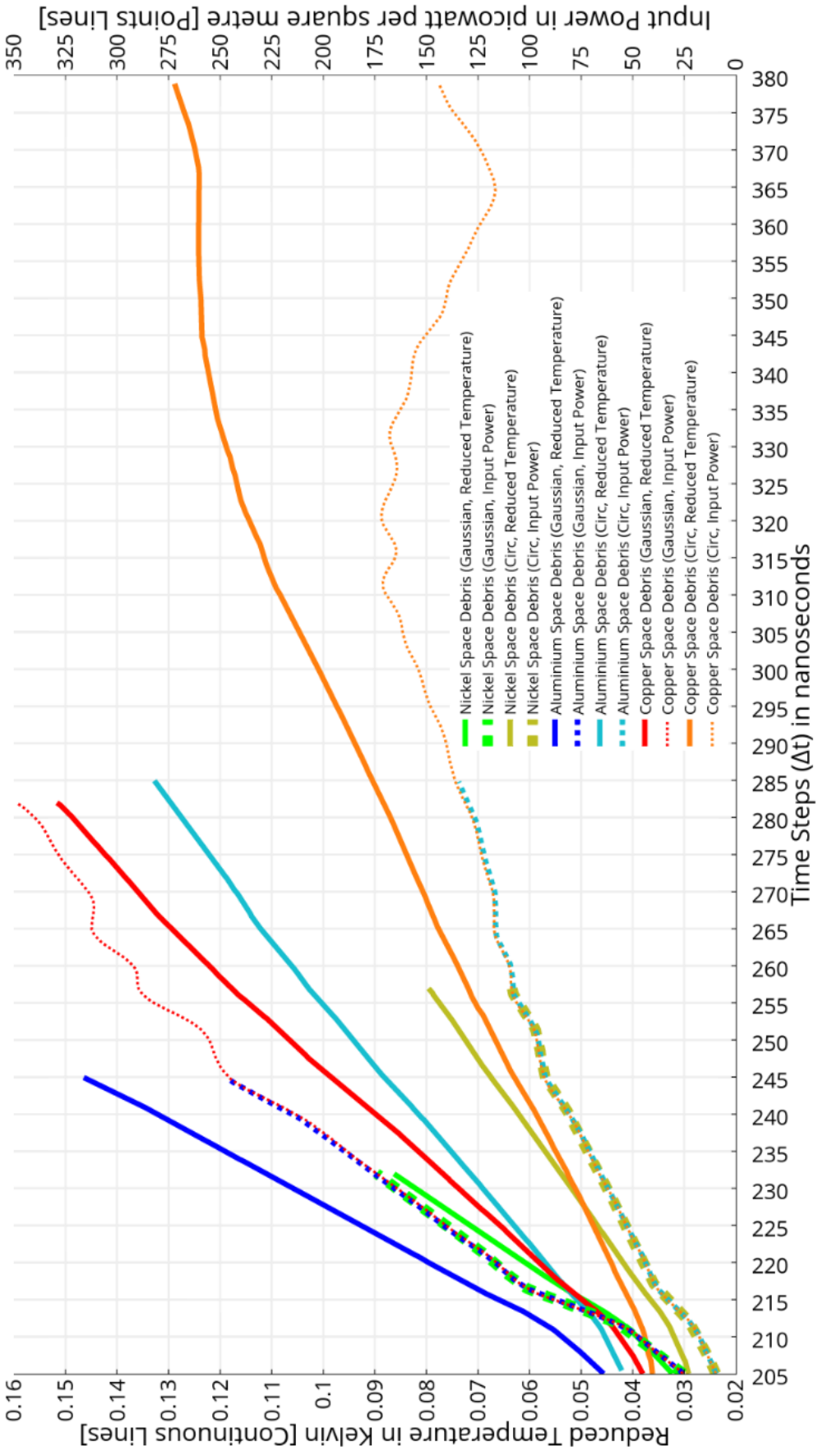

Figure 92: Change of Ni, Al and Cu space debris surface temperatures (continuous lines) using Fourier theory. Points lines are the laser beam input power as a function of time.

The figure showed that the vaporisation of the space debris does not happen because even at large power intensity values of the laser beam, the lattice temperatures are too small. This explains the limitation and inaccuracy of the Fourier theory to simulate the heat conduction mechanism, particularly in the vaporisation phase of the space debris. Therefore, the Fourier equation does not describe the process of heat-transfer that happens when orbital debris is illuminated by short duration plused lasers; it is only valid within precisely defined boundaries.

In the Kinetic theory at an electron temperature of 6000 K, the laser input energy and the required time for the electron to achieve this temperature were studied. Also, the variation in the electron temperature and lattice (phonon) temperature were measured and presented in Table 11. It is clear that Ni space debris will require a shorter time to reach its vaporisation temperature than space debris that is made of Al or Cu because Ni is a transition material and also has small reflectivity, meaning more irradiation will be absorbed inside the Ni space debris.

Table 11: Variation between electron temperature and phonon (lattice) temperature at an electron temperature of 6,000 K using Kinetic theory

Space Debris Type	Laser Input Energy $[mJ]$	Time for Electron to Reach 6,000 K Using Kinetic Theory $[\mu s]$	Difference Between Electron and Phonon (Lattice) Temperatures $[K]$
Ni Space Debris	2.0	1.6	618.745
Al Space Debris	4.3	2.3	2,366.220
Cu Space Debris	12.6	4.1	2,875.240

On the other hand, in Fourier theory, the lattice temperatures were studied for the same values of the laser input energy. The time needed to achieve these lattice temperatures is equal to the time that is required for electrons to achieve 6,000 K when the Kinetic theory was used, this is presented in Table 11 and Table 12.

Table 12: Ni, Al and Cu space debris lattice temperatures using Fourier theory

Space Debris Type	Laser Input Energy $[mJ]$	Lattice Temperature Value Using Fourier Theory $[K]$	Time for Electron to Reach 6,000 K Using Kinetic Theory $[\mu s]$
Ni Space Debris	2.0	1,166.10	1.6
Al Space Debris	4.3	1,273.11	2.3
Cu Space Debris	12.6	1,414.31	4.1

5.5 Fourier Conduction Theory versus Electron Kinetic Theory

For the same time interval and input power, the lattice temperature profiles for nickel, aluminium and copper space debris, with the specification listed in Table 13, have been compared to illustrate the difference between the Fourier conduction theory and the electron Kinetic theory at 2.5 μs. This is depicted in Figure 93.

Table 13: Space debris physical properties

Space Debris Material Type	Absorption Coefficient (δ) $[1/m]$	Electron-Phonon Mean Free Path (l) $[nm]$
Ni Space Debris	68×10^6	5.8
Al Space Debris	84×10^6	14.9
Cu Space Debris	75×10^6	40.0

Based on the results, it is clear that the electron Kinetic theory gives much higher lattice temperature value near the laser-debris illuminated surface compared to the Fourier conduction theory at that instant of time. It also provides larger negative temperature slopes, but less penetration depth means less heat-affected area comparing to the case for Fourier conduction theory. This is similar to the practical conclusion that was obtained by [89].

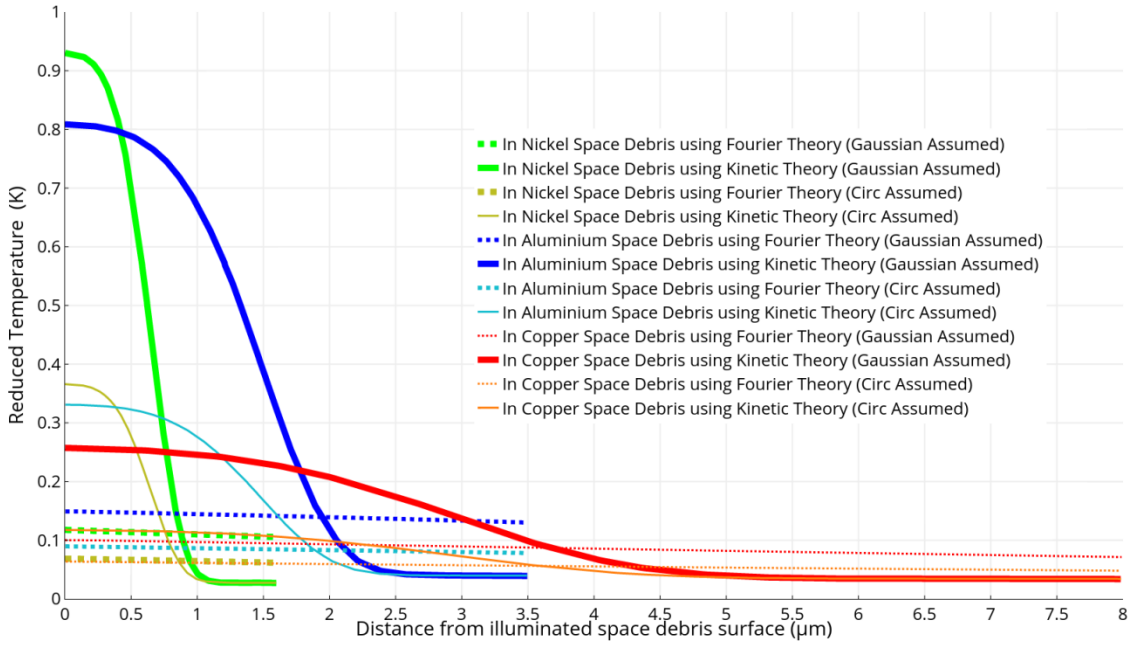

Figure 93: Ni, Al and Cu space debris lattice temperature profiles

Figure 93 also shows that the variation of the lattice temperature between the electron Kinetic theory and the Fourier conduction theory is larger for nickel space debris compared with the change of the lattice temperature for aluminium or copper space debris. Comparing between aluminium and copper space debris, the aluminium debris has a larger variation of the lattice temperature. This significant variation of the lattice temperature in Ni debris is because the electronic configuration of Ni is quite different from Al and Cu space debris. In the wreckage that is made of Ni, the electrons are firmly bound to the core of the ion and less easily pushed into the conduction band. This leads to the fact that the average distance travelled by an electron between collisions with a phonon in Ni space debris is lower compared to the distance travelled in Al or Cu space debris. This means the average free path of an electron-phonon in Ni space debris is shorter than the mean free path of an electron-phonon in Al or Cu space debris. This actually raises the rate of collision between electrons-phonons in Ni debris, and therefore the energy is deposited in a quite narrow layer at the surface of the space junk. Figure 93 also shows that the variation of the lattice temperature between the electron Kinetic theory (Kinetic Theory) and the Fourier conduction theory (Fourier Theory) is smaller by more than a half when the top hat or circ function beam irradiance distribution was assumed, comparing to the case when the Gaussian beam was assumed.

Now the variation between the Fourier conduction theory and the electron Kinetic theory can be summarised in this paragraph. The electrons and lattice phonons in the

Fourier conduction theory are assumed to be in equilibrium and thus the average energy conveyed between electrons and lattice phonons is assumed to be infinite. However, this is not the case particularly for high transient intensities of input power. Unlike the Fourier conduction theory, the electron Kinetic theory permits non-equilibrium between electrons and lattice phonons. This means for large energy gradients, electrons and lattice phonons can have different temperatures. The electron Kinetic theory is valid for non-equilibrium energy transport and for high order temperature gradients. The temperature inclination between two isothermal levels is simply equal to:

$$\frac{\Delta T}{\Delta x} = \frac{T_2 - T_1}{x_2 - x_1} \qquad \text{Equation 5.10}$$

It is assumed to be fixed in the Fourier conduction theory. That is why the classical Fourier heat conduction expression is invalid for non-equilibrium energy transport and at high order of temperature gradients. Lasers produce big and high order of temperature gradients on spatial areas, of the space debris, that are smaller than the absorption depth in the debris. This is incompatible with the presumption of the Fourier conduction theory under these situations. For the electron Kinetic theory, the electrons that are crossing the electromagnetic field absorb the laser energy. Whereas, for the Fourier conduction theory the laser energy is presumed to be immediately absorbed by the space debris material at any distance from the laser-debris illuminated surface. In the electron Kinetic theory, a quicker rate of evaporation is evident due to the predicted higher temperatures gradients and higher temperatures gradient at the surface of the space debris. The electron Kinetic theory predicts a positive temperature inclination at the space debris surface that is illuminated by laser, when vaporisation starts. This also predicts the potential for the superheated or the molten space debris material to appear in the metal of the debris, leading to explosions. For an actual interaction operation, large forces are created that supports the prediction of subsurface nucleation producing an explosive ejection of the orbital debris molten material, which of course can generate thrusts on the debris itself, deflecting it, and changing its orbit. In the electron Kinetic theory, due to the positive gradient of temperature at the orbital debris illuminated surface, a potential blastis predicted when the vaporisation is initiated. This is unclear in the Fourier conduction theory.

5.6 Discussion

Based on the results of Chapter 4 and Chapter 5, the electron Kinetic theory theoretical model characterises the process of heat conduction by laser radiation much better than the theoretical model that is based on the Fourier conduction theory. The developed theoretical model represented the temporal and spatial temperature distribution more precisely in the material of the space debris. The model permits a better understanding of the laser ablation operation on debris in Earth orbit.

In this chapter, the electron Kinetic theory and the classical Fourier conduction theory have been compared with each other. The outcomes show that for the same time interval and input power, the electron Kinetic theory predicts higher temperatures on the space debris surface than Fourier theory. It also predicts sharper temperature gradients, shorter penetration depth in the wreckage and less heat-impacted area of the wreckage, compared to the classical Fourier conduction theory that predicts quite small temperature gradients.

Chapter 6

Theoretical Analysis of Space Debris Propulsion Using Lasers

6 Theoretical Analysis of Space Debris Propulsion Using Lasers

6.1 Summary

Chapter 4 and Chapter 5 studied the physics of the surface temperature profile of orbital debris using the electron Kinetic theory and Fourier conduction theory. This chapter will look into a different aspect of space debris mitigation, that is orbit transfer. Orbit transfer is involved in almost any space mission. This chapter discusses and simulates the utilisation of pulsed laser systems to lower space debris lifetime in Earth orbit through orbit transfer. A theoretical evaluation of the proposed laser deflection technique has been conducted by calculating the impulse of laser radiation on orbital debris with different masses and sizes. The change in orbital velocity, delta-V (Δv), of the space debris after each laser pulse has been simulated in this chapter. The chapter will also investigate and assess the treatment of space debris and the engagement between the laser pulses and different masses of orbital debris. In addition, the average mass fraction and the laser energy that is required to reduce the altitude and the orbital velocity of the space debris has been calculated.

6.2 Characterisation of Space Junk

Space junk are very different in sizes and masses, and they are orbiting the Earth at different altitudes. Thousands-and-millions of junk items are small in size and contained within the LEO band, as discussed in Chapter 1. When two or more bodies collide with each other in space at a hypervelocity close to 14 km/s, there is an immense spectrum of possible outcomes. It ranges from the re-adjustment of shape and size to external surfaces and rotational states. These factors will ultimately influence the overall efficiency and performance margin of any solution to the debris problem.

The outcomes of a collision in space depend mainly on the size of the original two objects, the relative velocity and their materials. They could generate thousands of space debris, as in major collisions. The impact of multiple bodies may cause more cumulative damage than that of the original satellites because even small pieces could still severely affect any operational space system in orbit. The number of debris with a size range bigger than 1 cm in the LEO band is large, and as discussed in Chapter 1, even small debris can cause deadly harm to both manned and unmanned space missions

in orbit and produce more space junk, which renders many useful services challenging to use.

The tracking and interception of multiple space debris at short notice is difficult. The problem is that the length of time small debris stays in, for example, 1000 km altitude orbit before re-entering the atmosphere is of the order of 100 years. Therefore, it is a key objective to reduce the altitude of space debris in order to increase the speed of decay and the re-entry process of the debris, and that is what this chapter will discuss and simulate.

6.3 Laser Ablation Propulsion

Propulsion through laser ablation has been studied in this thesis to model the reduction of orbital debris altitude, which would significantly reduce the lifetime of the debris in orbit. Propulsion and deflection can be generated by creating a low thrust action on small space debris over an extended period of time. This propulsion action can be generated by continuously hitting the debris with laser pulses. That means propulsion by laser ablation could be a potential solution to mitigate space debris, and that is what this thesis is proposing. This thesis developed some novel techniques for the removal of space debris, involving the use of laser ablation propulsion, and simulating the performance achievable by this technique. The previous two chapters study the surface temperature profiles for nickel, aluminium and copper space debris. Here in this chapter, it has been decided to use aluminium (Al) and carbon (C) as space debris targets. Now, the question is what would be the required energy to change a debris from its existing orbit to another lower orbit? The proposed solution uses a repetitively pulsed laser beam with high energy ~ 1,000 J per pulse to target space debris and slow them slightly, i.e. lower their perigee. Aside from the atmospheric drag, lowering the space debris perigee, by the amount necessary, it will cause the debris to re-enter the dense atmosphere where they will burn up. At this point, not enough studies have been done on this process with the use of the laser ablation technique. Thus, substantial research work and development are essential and required to analyse and simulate the validity of this technique. The subsequent sections will evaluate this technique for different masses and space debris materials.

6.4 How Lasers Can Transfer Momentum to Space Debris

Momentum transfer can be induced and accomplished by irradiating the surface of space debris with high-energy pulses of focused laser light. The penetration of the laser

beam into the surface of the space debris has been analysed in previous chapters to understand the super-heating of the exposed material. The absorbed heat from the high-energy laser beam pulses could sublimate the surface of the orbital debris, transforming the illuminated material directly from a solid to a vapour. The ablated material then forms into a plume of ejecta blow-off, which exerts a small and controllable force on the space debris, as shown in Figure 94. That can act as a low thrust controllable deflection engine, which could be powered by every additional laser pulse so that more material will be mobilised for a thicker penetration depth. The laser pulses increase the transfer of momentum that is initially induced by the blast wave.

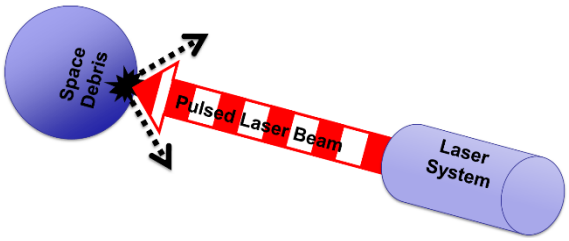

Figure 94: Plume of ejecta produced due to the interaction between laser pulses and an object

This impulsive technique creates ejecta whenever the laser pulse hits the target, and that adds significantly to the total transfer of momentum. This plume of ejecta acts against the orbital debris, providing a small controllable thrust. Over an extended period of time this low thrust propulsion provides a deflection push and can bring space debris from its potentially threatening trajectory to a lower orbit and eventually de-orbit it. This little thrust reduces the orbital velocity of the space debris by Δv and eventually reduces the altitude of the debris and so its lifetime in orbit because any change in the orbital velocity of an object in space will create a new orbital configuration. The difference between the two orbital configurations yields a change in orbital velocity. This lowers the space debris' altitude if and only if the direction of the engine is correctly aligned to the orbital velocity vector of the space debris.

Understanding the velocity, volume and size of the emitted ejecta are exceptionally complex. However, it depends on the structure and composition of the given space debris. Also, the size of the ejecta plume depends on factors including the vaporisation efficiency, the heat capacity and the radiation absorption properties of the target material. So, the engagement action between space junk and a high-power laser will act as a perturbation on the initial orbit of the space junk, and this will vary the junk orbital velocity by Δv. It is safe to say that this technique is still dependent on many factors

such as the size and mass of the space debris, the orbit parameters of the space debris, its shape, its structure and composition, and the energy of the laser beam pulses. It is dependent on the debris centre of mass, the warning time and the laser facility and ability to maintain a continuous interaction with the space debris.

6.5 General Concerns about the Laser Technique

Some spacefaring nations may consider this technique as a threat to their assets in space as targeting objects in space via laser could be considered to be a military application because we know that a laser could be used not only to remove debris but also to attack other things, such as operational space systems. This uncertainty of how other countries or spacefaring nations will react when this technique is used to target space debris can be considered as a disadvantage to this technique. However, this is a common misconception as the energy needed for surveillance and repositioning is orders of magnitude below laser weapons levels. Meanwhile, we believe an international collaboration would be needed in any on-orbit servicing [90] and especially in building or implementing such laser ablation systems, although it is not a simple technology to implement from the political standpoint.

6.6 Design Choices and Challenges

The high-power pulsed laser system could be successfully installed on the ground as a ground-based laser system, or it could be sized, integrated and mounted on-board an artificial satellite, that is specially designed for this mission as a space-based laser system. For the ground-based laser system, the large laser beam with a higher power is possible due to the available power on the ground. Such a system avoids any complex high-power laser system to be attached onboard satellites, and this dramatically reduces the cost of the mission.

On the technical side, to generate sufficient momentum transfer to orbital debris via a laser beam from a ground system, the system would have to be developed to generate focused lasers beams. This requires high-quality optics, from the ground through the atmosphere to reach the targeted debris with enough energy to physically vaporise a tiny debris object. The induced ablation of material from a piece of orbital debris, due to the interaction of the debris with a sufficiently large number of laser pulses, is more than adequate for repositioning and deorbiting small space debris.

For the space-based method to be successful, it may require a constellation of satellites with laser systems integrated onboard the satellite. These will require a substantial and highly efficient onboard power source. These power units are needed to generate laser pulses with enough power to ablate the space debris. Otherwise, they will degrade the performance of the spacecraft and the overall mitigation technique. The legal and political ramifications of launching and operating an in-orbit ablation system in space also need to be addressed. Furthermore, launching new systems into space means adding more to the space debris dilemma. Therefore, the analysis supports the broad diversity and durability of using a ground-based high power laser facility, as shown in Figure 95, rather than launching a new satellite, or probably a constellation of satellites, to mitigate space debris using space-based laser systems. However, a low divergence, high accuracy pointing and high specific impulse laser beam is required to enable the ground-based method and operate at a greater distance from the space debris. This enables the laser beam to reach the space debris in LEO with enough energy to change the orbital velocity of the space debris. Over vast distances, hundreds of km, the laser beam will gradually diverge with distance, and therefore beam divergence cannot be ignored. In fact, even the very tiny dot that we illuminate using a laser to point on board will become hundreds of metres in diameter, depending on the optical quality, by the time it reaches an object in space.

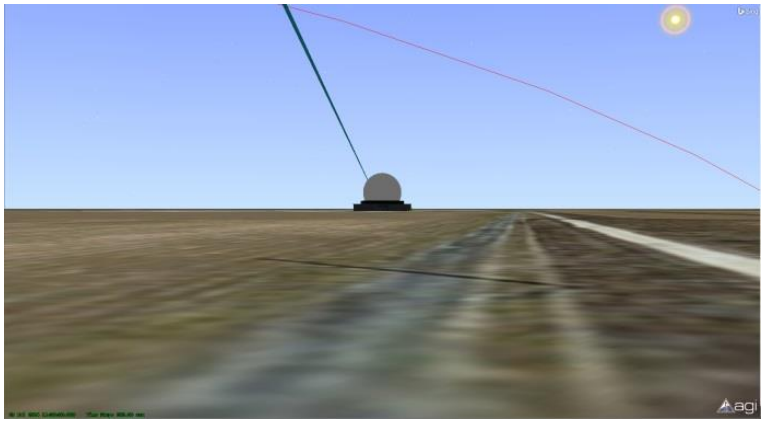

Figure 95: Ground-based laser facility for debris removal

Regardless of the design method, applying any propulsion manoeuvring close to or at the space debris centre of mass is recommended, as the centre of mass defines the stability of the space debris. Otherwise, the momentum transfer and power could be wasted in spinning rather than deflecting the space debris and altering its orbital velocity.

6.7 Dragging and Deorbiting Space Debris

Space debris are distributed around the Earth at different altitudes. The lifetime of an object in space depends mainly on its orbit altitude. In general, the object lifetime in space increases exponentially with its altitude. Therefore, for example, debris in Earth orbits with high altitude may remain in orbit for hundreds of years, possibly more, before they come back and deorbit. Whereas, debris in the lower band of LEO, below 400 km altitude can be of the order of only a couple of years or less than a year before they fall into the atmosphere. Therefore, changing the altitude of an object in space results in a change of its lifetime in orbit. Reducing the lifetime of debris in space will speed up the debris removal rate to an acceptable timescale and this is achieved by lowering the debris orbit to a very low orbit where the drag will be the dominant force to pull the debris down into the atmosphere.

Orbital debris with a long lifetime in space poses a severe threat to any operational satellite. Currently, collision avoidance technique is one of the temporary solutions to prevent collision between an operational satellite and any other object in space, although it uses fuel and thus costs money to manoeuvre a satellite and change its trajectory. However, it is not always feasible to manoeuvre a satellite to avoid or reduce the collision risk with another object in space, and that is why satellites in orbits are a facing damage and collision risk all the time.

Under the criterion of any two standard objects in motion in space, an object in Earth orbit will not deorbit and enter the atmosphere unless perturbed. As we discussed earlier, reducing the orbital velocity of the space debris would be achieved by reducing its altitude, which can be achieved by using high-energy laser pulses because each laser pulse will act as a small thrust engine. Therefore, to force space debris to re-enter the atmosphere, a change in its orbital velocity is required to manoeuvre it into a lower orbit.

The question that we need to answer is what would be the required Δv to lower an object from a circular orbit to a lower orbit. Basically, due to the drag forces objects in space with altitude close to the upper atmosphere level, which is about 100 km, receive perturbations. That drag forces vary the semi-major axis of the orbital object, forcing it to lower its altitude even more and based on the object's size and material, if its altitude is low enough, the object will eventually re-enter the atmosphere. Small debris will

quickly burn up as soon as they re-enter the dense atmosphere, whereas large debris may fall down and hit the Earth surface with impact.

6.8 Required Delta-V (Δv) for Different Operational Conditions

Change in orbital velocity or what is the so-called delta-V is the difference between orbital velocities at two different altitudes or orbit configurations. It is essential to simulate the required Δv to change the altitude of an object in space. This project, mitigating space debris, is looking to lower the altitude of small debris in space.

In orbital mechanics, Hohmann transfer orbit, which is a two-impulse elliptical orbit, can be used to transfer an object in space between two co-planar circular orbits of different altitudes, in the same plane. The transfer itself consists of an elliptical orbit with a perigee of the inner orbit and an apogee of the outer orbit as shown in Figure 96.

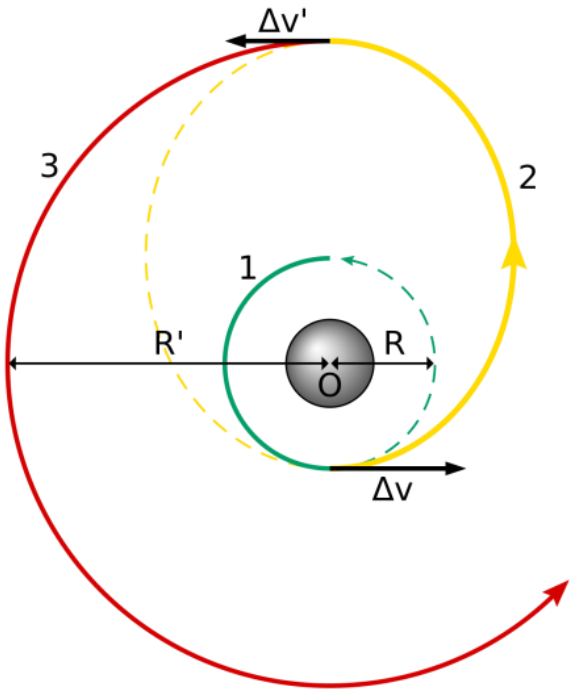

Figure 96: Hohmann Transfer Orbit for Launching a Satellite

Usually, two impulses are required to complete the orbital manoeuvre and perform the Hohmann transfer orbit, one to move an object onto the transfer orbit and a second one to move off that orbit. The arrows direction in the above figure is for launching a satellite into orbit but for deorbiting space debris, which is the case for this project, the arrows must be in the opposite direction. Now, it is essential to know what would be the required Δv to transfer an object from orbit 3 that has a red trajectory to orbit 1, which has a green trajectory? To answer this question, Figure 97 and Figure 98 have been

created using the theory of orbital mechanics and MATLAB codes to represent the required change in orbital velocity Δv for a basic Hohmann transfer to move a space debris between circular orbits, up to 1700 km into a lower orbit, as low as 100 km. At this reduced altitude ~100 km, debris of centimetre size will re-enter the dense atmosphere and burn up.

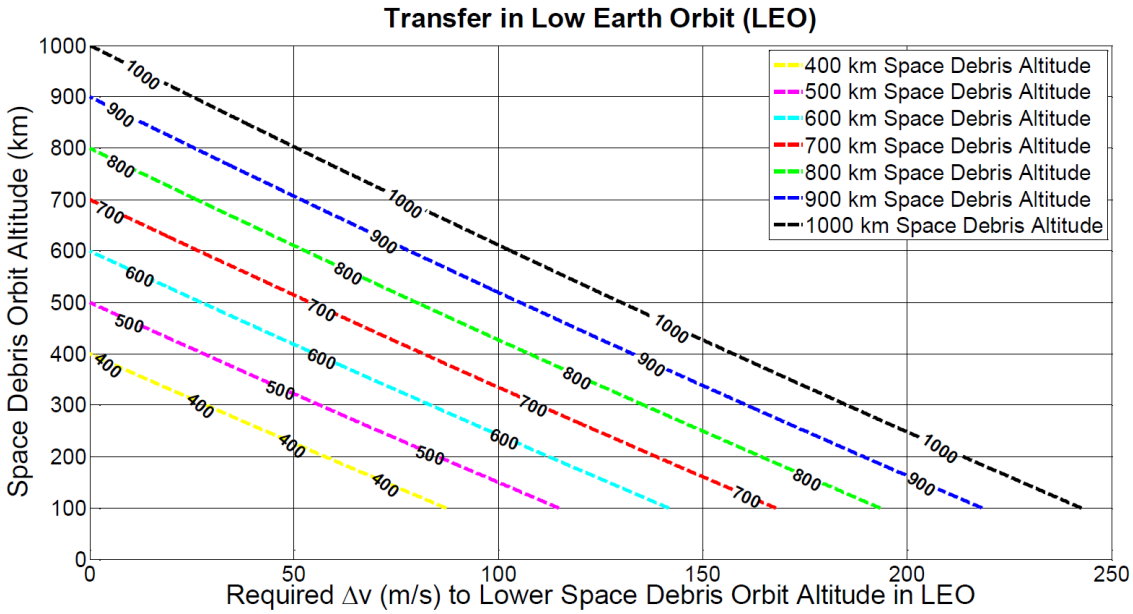

Figure 97: Orbit transfer in LEO (400 km to 1,000 km initial altitude), step size is 100 km

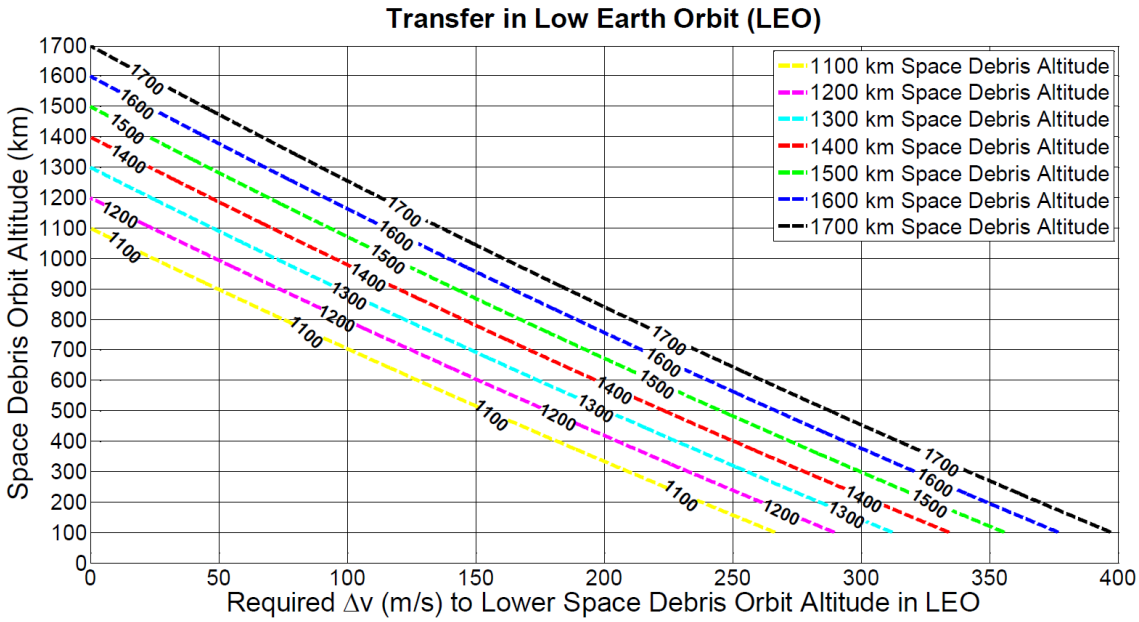

Figure 98: Orbit transfer in LEO (1,100 km to 1,700 km initial altitude), step size is 100 km

The first segment of the Hohmann transfer was implemented as drag will decrease the altitude over time and space debris at 100 km altitude will re-enter the atmosphere. As

the cyan dashed line shows in Figure 98, the change in the altitude of space debris from 1300 km to 100 km requires a Δv of about 310 m/s. Whereas, only a total of 195 m/s Δv is required to change an object orbital altitude from 800 km to 100 km, see the green dashed line in Figure 97. The orbital lifetime of these objects will dramatically reduce as a result of a move to a lower orbital altitude. Therefore, in conclusion, the smaller the change in orbital altitude, the smaller the Δv required to move the object is. Fortunately, due to the presence of drag forces, space debris at low altitudes will re-enter the dense atmosphere and burn up without any active or mechanical form of removal.

6.9 Theoretical Analysis of the Laser Ablation Propulsion

The general principle of the laser ablation technique relies on the utilisation of high energy pulsed laser to ablate the orbital debris in the form of vaporisation. The vapour will be ejected from the debris, and that creates a momentum change similar to the impulse generated by a rocket. This momentum change is usually delivered in the direction of the incoming laser propagation. The main advantage of the propulsion via laser ablation is that there is no physical or mechanical contact between the space debris and the deflection system, especially for the ground-based laser system, and thus there is no need to launch a satellite. However, as discussed before, the laser has to be high in energy to overcome the losses over a significant distance and reach the space debris with enough energy to ablate its material.

Chapter 2 discussed the physical characteristics of space debris and the most commonly used materials in manufacturing satellites; it concluded that human-made debris in space could be a combination of any materials that have been used to build space systems. Therefore, understanding the most common on-orbit debris materials will help the design of the laser beam system and give a more accurate picture of these techniques because, for example, the change in orbital velocity Δv varies a lot between the ejecta created from different space debris. In this chapter, the simulations have been done based on two different materials for the debris. These materials are aluminium and carbon.

It is essential here to express that space debris has to be tracked precisely and accurately so that when the laser beam fires on any debris, it illuminates the debris and does not miss it. That will ensure the momentum change is correctly delivered and induced on the object, moving it to a lower orbit. This momentum change and transfer is a function

of many factors namely the absorption and reflectivity of the debris materials, the wavelength of the laser beam, its output energy, et cetera. The higher the laser energy, the higher the energy absorbed by the debris material and the more the momentum transfer is created. The following equation shows the relationship between the momentum change with the coupling coefficient and the delivered energy.

$$Momentum\ change = \Delta p = c_m E_d \qquad \text{Equation 6.1}$$

Where:

c_m = Coupling coefficient

E_d = Delivered energy

The coupling coefficient c_m depends on the object material. Although, it is mathematically challenging to find the coupling coefficient value, for an ideal case the following values can be assumed for Al and C

Aluminium (Al) : $c_m = 20.0 \times 10^{-6}\ \left[{}^{N.s}/_{J}\right]$

Carbon (C) : $c_m = 13.8 \times 10^{-9}\ \left[{}^{N.s}/_{J}\right]$

The delivered energy E_d is a function of the:

- Laser power at the impact location: which in itself is a function of:
  - Atmospheric attenuation
  - Space loss
  - Optical properties
  - Laser output power
- Absorptivity of the target material
- Reflectivity of the target
- Target area exposed to the laser energy beam

Over the course of the laser ablation process, the delivered energy is almost a fixed value, but the mass of the target is not fixed during this process as the ablated mass is removed from the target at the ablation rate μ. It is very complex to calculate the total ablation rate, but it is approximately equal to:

$$80.0 \times 10^{-9} \left[{}^{kg}/_{J} \right] \quad \text{For Aluminium (Al)}$$

$$12.5 \times 10^{-9} \left[{}^{kg}/_{J} \right] \quad \text{For Carbon (C)}$$

Now, the change in target mass can be represented by the following expression $\Delta m = \mu E_d$. As the laser system generates laser pulses with high energy at a particular frequency, over n number of pulses, the total orbital velocity change can be expressed by the following equation:

$$\Delta v = \sum_{i=1}^{n} \Delta v_i = \sum_{i=1}^{n} \frac{c_m E_d}{m_i} = \sum_{i=1}^{n} \frac{c_m E_d}{m_o - \sum_{j=1}^{i} \mu E_d} \qquad \text{Equation 6.2}$$

For any given deflection method, the more significant the increase in the deflection distance the more efficient the method becomes. It is the increase in the deflection distance that is mainly used to add margin and manoeuvre space debris to avoid any impact and collision events with any nearby operational satellite. From the above equation, the issue now comes down to the output energy of the laser beam. As an example, a laser with $100\ kW$ output power, pulsing for $100\ ns$ every $1\ ms$. This means that the delivered energy $E_d = 1{,}000\ \frac{J}{pulse}$. If we assume that there are no losses between the laser beam and the orbital debris, the total velocity change and the total mass change for a half kilo space debris over thousands of pulses can be calculated and plotted using the previous equation, see Figure 99 and Figure 100.

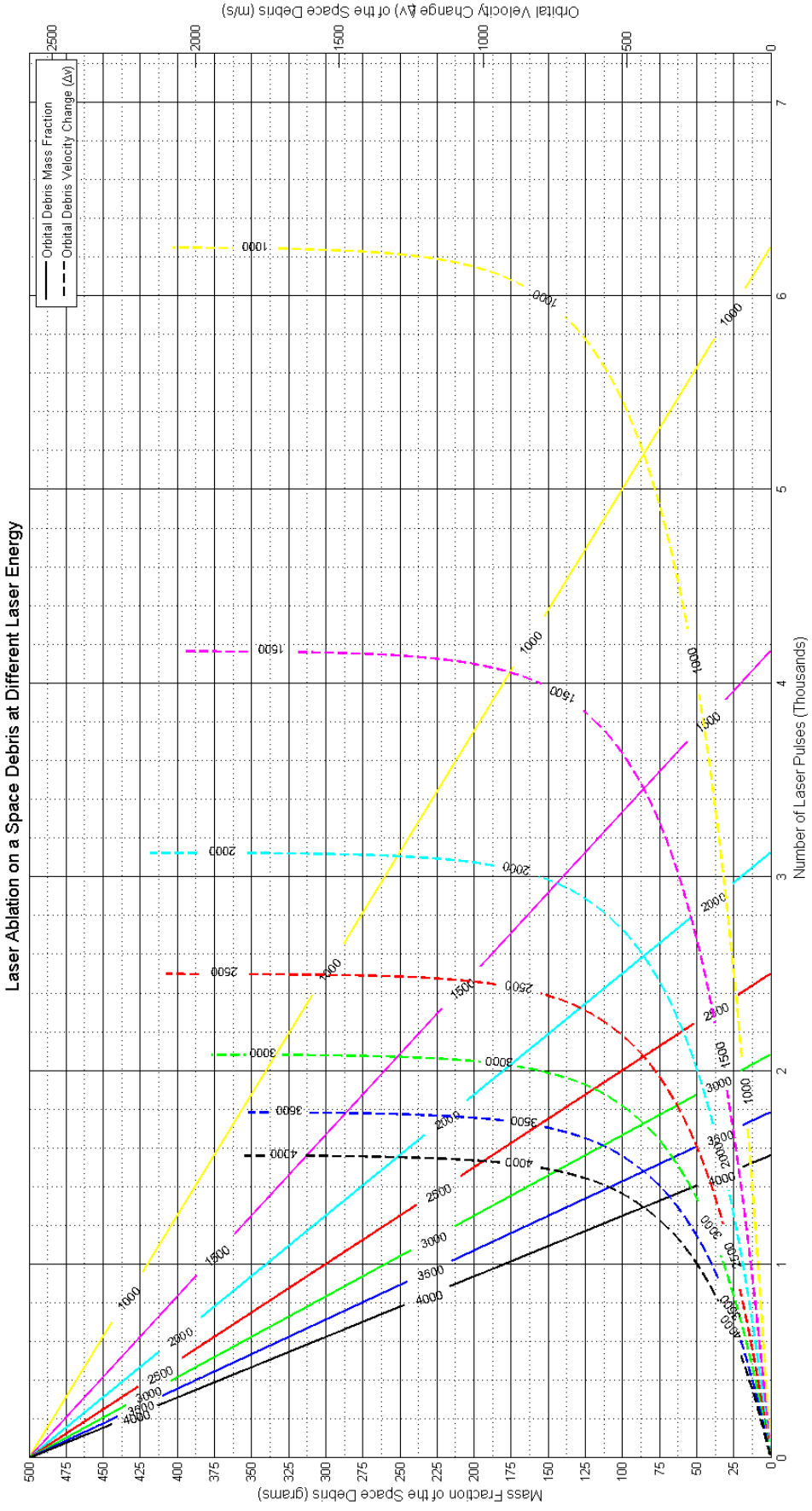

Figure 99: Ablation of 0.5 kg aluminium space debris via laser beam with different energy: from 1,000 J to 4,000 J with step size of 500 J

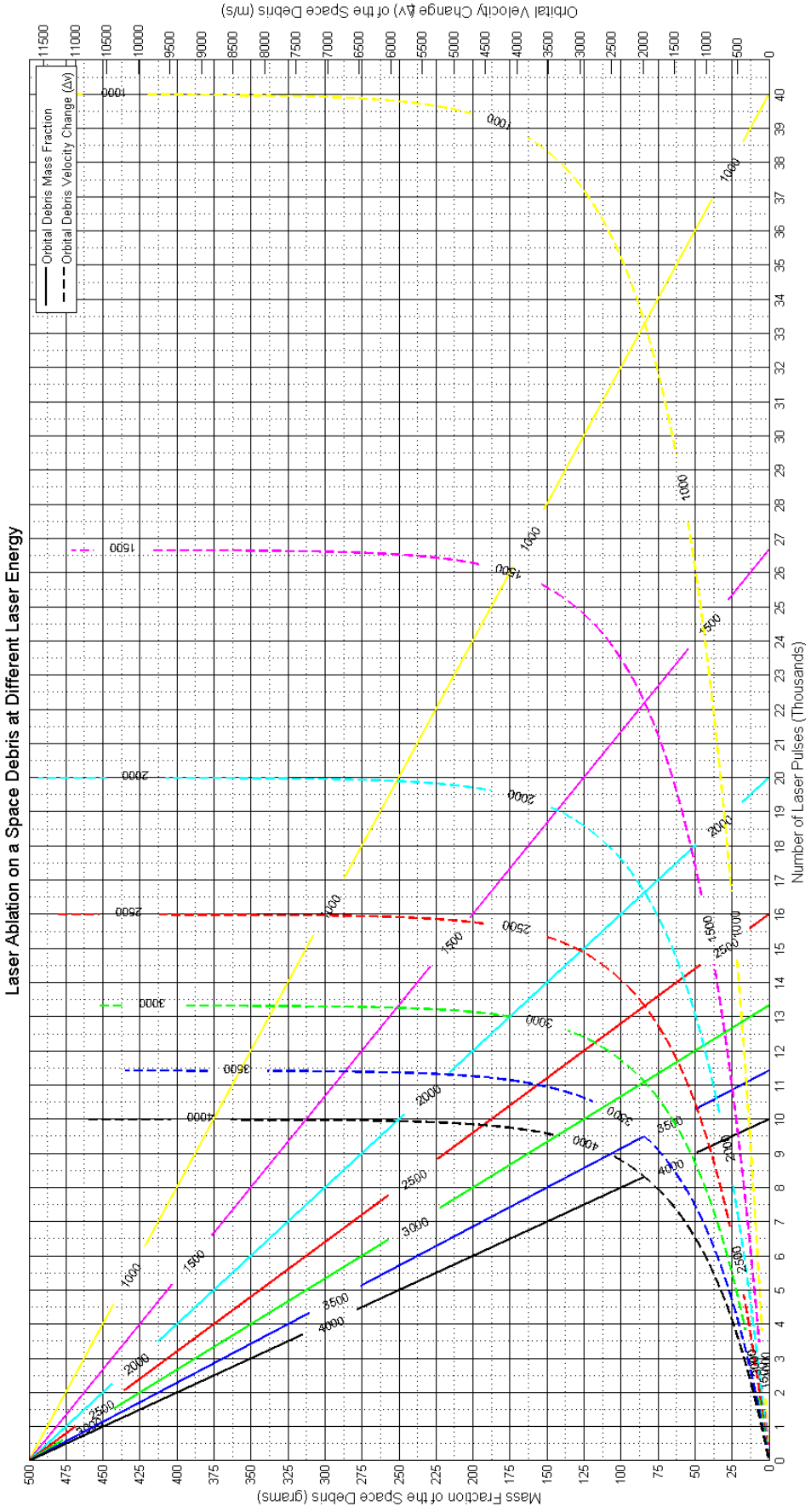

Figure 100: Ablation of 0.5 kg carbon space debris via laser beam with different energy: from 1,000 J to 4,000 J with step size of 500 J

It is tough to find the exact size and mass of a space particle as it depends on many factors like the composition and structure of the satellites that they came from and their orbital velocities at the time of the collision. However, as the debris becomes lighter, the change in its orbital velocity becomes exponentially more substantial.

This proposed mitigation technique could be enhanced even further by increasing the laser pulse energy acting on the space debris. As can be seen from Figure 101 and Figure 102, the more laser energy used per pulse, the more mass fraction the debris loses, and the more momentum transfer generated, which results in a change in the orbital debris velocity.

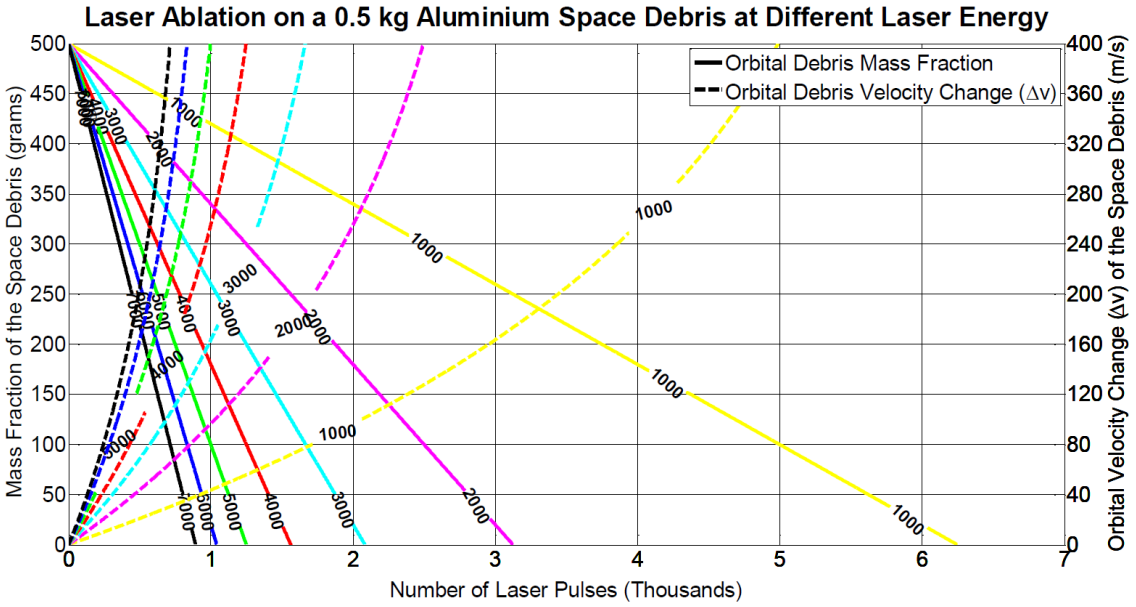

Figure 101: Ablation of 0.5 kg aluminium space debris via laser beam with different energy: from 1,000 J to 7,000 J with a step size of 1,000 J. Over the period of 7,000 laser pulses.

To analyse the above figure, supposing that the laser beam and thus the Δv is applied in the correct direction, the yellow lines in the figure depict that the laser beam with $1{,}000\,\frac{J}{pulse}$ can change the orbital velocity Δv of a $0.5\,kg$ mass of aluminium space debris by $163.5\ {}^{m}/_{s}$ and drop its mass by $240\ g$, which is 48% of its original mass, during the course of about three thousands laser pulses. For an aluminium space debris with $700\ km$ altitude, this $163.5\ {}^{m}/_{s}$ of Δv could push the debris and lower its altitude by $585\ km$, based on the analysis of the red dashed line in Figure 97.

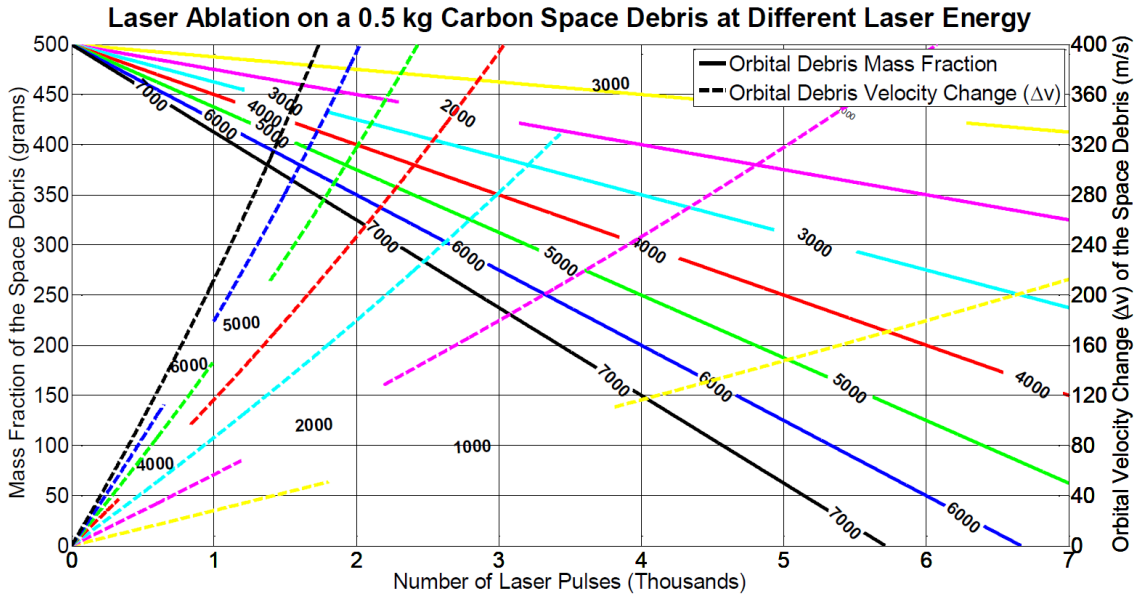

Figure 102: Ablation of 0.5 kg carbon space debris via laser beam with different energy: from 1,000 J to 7,000 J with a step size of 1,000 J. Over the period of 7,000 laser pulses.

This laser system can also change the orbital velocity Δv of a $0.5\ kg$ mass of a carbon orbital debris by $86.07\ {}^{m}/_{s}$ but drop its mass by only $37.5\ g$ over the course of about three thousands laser pulses as shown in the yellow lines of the previous figure. This $86.07\ {}^{m}/_{s}\ \Delta v$ could lower this carbon space debris at an altitude of $400\ km$, which is about the altitude of the ISS (Figure 103) to just above the upper atmosphere altitude of $104\ km$, as shown earlier in the yellow dashed line of Figure 97.

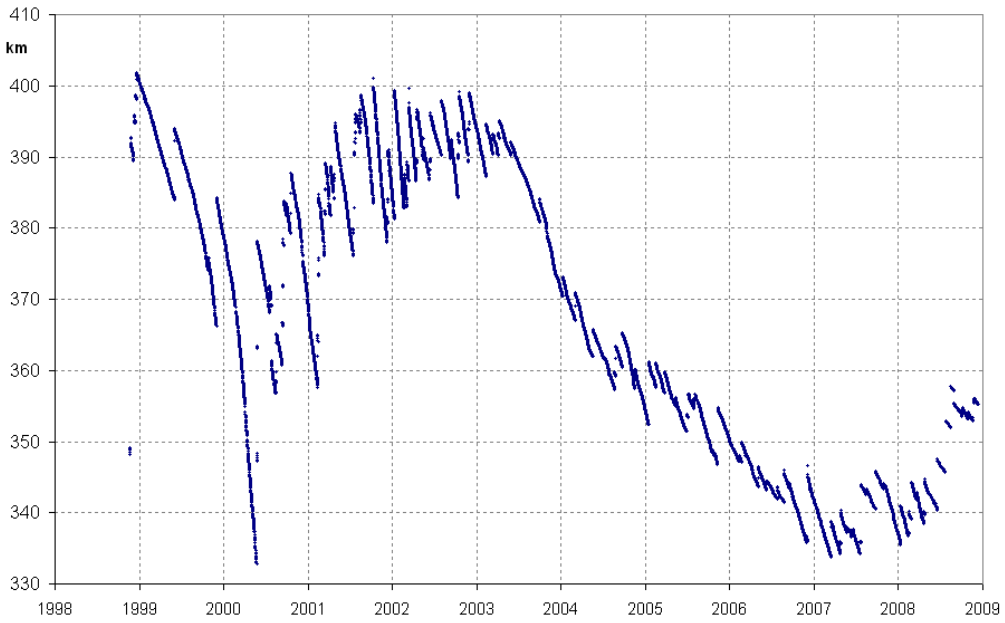

Figure 103: Graph showing the changing altitude of the ISS over the period of 10 years, from November 1998 until January 2009, the discontinuities are where the ISS did a re-boost to raise its altitude.

Figure 101 and Figure 102 also provide a good comparison of the behaviour of the laser system on different space debris, aluminium and carbon, with the same mass of 0.5 kg. The figures present the engagement between the laser beam and the space debris for the first seven thousands laser pulses. Obviously, the more energy the laser pulse has, the more momentum change and the larger the Δv that can be produced from each pulse. More energy means the lower the number of pulses will be required to mitigate the space debris.

Carbon is lighter than aluminium. Therefore, 500 g of a carbon space debris is bigger in size than 500 g of an aluminium space debris. This technique could also be effective for a range of other materials, especially debris that are made of metals.

On the other hand, larger space debris will require more laser pulses or more pulse energy to mitigate them. Figure 104 and Figure 105 show how the same laser system will behave if the space debris were doubled in mass, i.e. one kg. So the same simulations have been done for a 1 kg space debris for both aluminium and carbon to study the behaviour of the laser deflection technique, as shown in the following two figures.

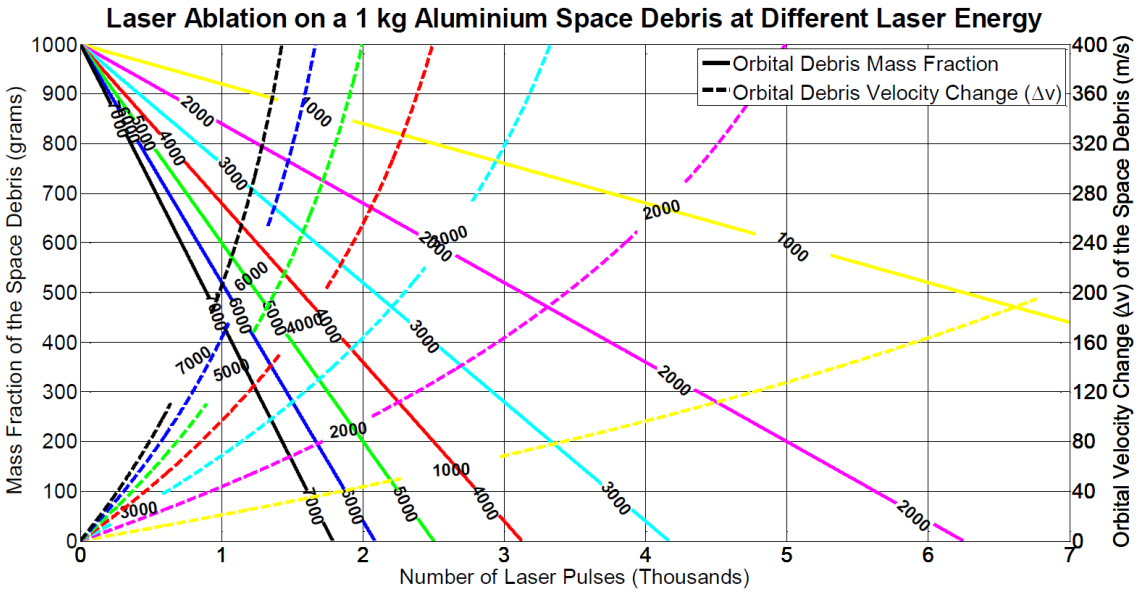

Figure 104: Ablation of 1 kg aluminium space debris via laser beam with different energy: from 1,000 J to 7,000 J with a step size of 1,000 J. Over the period of 7,000 laser pulses.

Over the course of the same three thousands laser pulses, the laser system of 1,000 $\frac{J}{pulse}$ could change the orbital velocity Δv of an aluminium orbital debris with 1 kg mass by 68.61 $^{m}/_{s}$ and drop its mass by 240 g, as shown by the yellow

lines of the above figure. This 68.61 $^{m}/_{s}$ Δv could lower the aluminium space debris at an altitude of 600 km by 248 km; see the cyan dashed line of Figure 97.

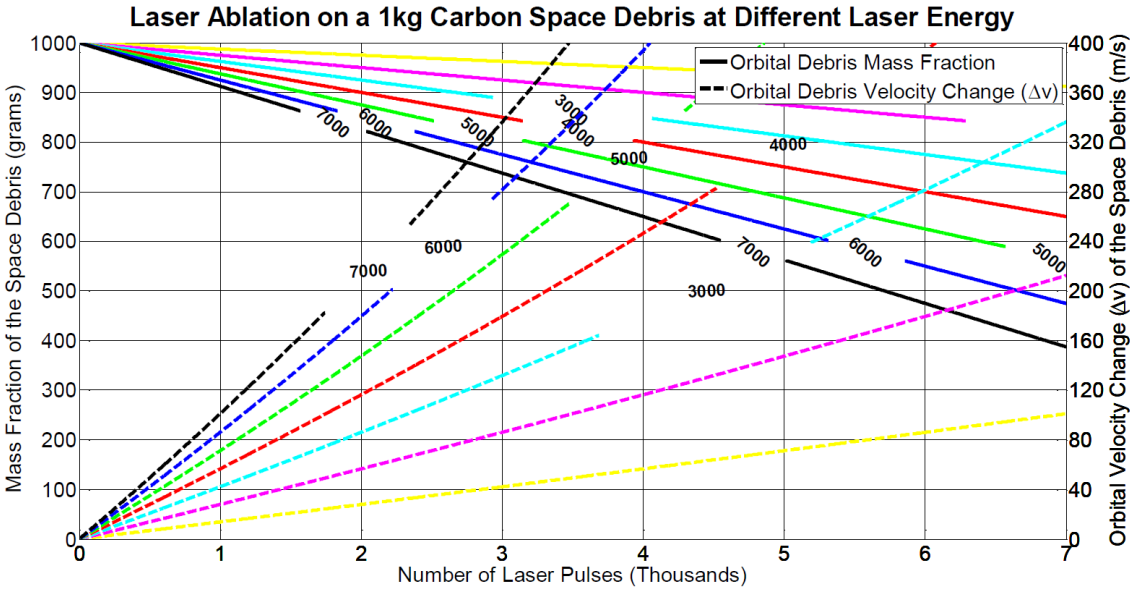

Figure 105: Ablation of 1 kg carbon space debris via laser beam with different energy: from 1,000 J to 7,000 J with a step size of 1,000 J. Over the period of 7,000 laser pulses.

For carbon space debris with one kg mass, the same three thousands laser pulses could change the orbital velocity Δv of the debris by 42.2 $^{m}/_{s}$ but it can only drop its mass by 37.5 g, see the yellow lines of the above figure. This 42.2 $^{m}/_{s}$ Δv could lower the carbon debris at an altitude of 500 km by 150 km; see the pink dashed line of Figure 97. The closer and the higher the energy of the laser pulses are, the higher the change in orbital velocity Δv and the quicker the mitigation action takes effect. This however requires knowledge of the other objects that are close to the targeted space debris.

6.10 Discussion of Results and Conclusion

Giving an external force or low thrust engine to move space debris to a lower altitude orbit where drag will dominate, results in the object losing its altitude and entering the atmosphere where they will burn up. The low thrust force can be produced by focusing a laser beam with high pulse energy onto the space debris. The performance of the laser ablation technique was evaluated in this chapter theoretically, and the simulations in this chapter have shown that the propulsion using laser ablation is possible for mitigating and deflecting space debris, especially small-size debris in LEO. Theoretical and analytical verifications were used to assess the viability of this technique and its performance in inducing a propulsion action. The theoretical results were achieved by ablating different materials of orbital debris, aluminium and carbon, with different

masses of 0.5 kg and 1 kg using a pulsed laser. The simulations covered different laser pulse energy, between 1 kJ to 7 kJ . Results show that a solid-state laser can produce 162 $^{m}/_{s}$ Δv that could lower a 0.5 kg aluminium space debris at an altitude of 700 km by 600 km, causing 48% of its mass to be utilised for the propellant. The simulations in this chapter also showed that the ISS could be saved from a collision with a 0.5 kg carbon orbital debris at an altitude of 400 km. This can be achieved by reducing the debris altitude to around the altitude of the upper atmosphere (100 km) using three thousands laser pulses with 1 $\frac{kJ}{pulse}$. Results for heavier debris like 1 kg showed that the larger Δv is needed in order to lower the altitude of such orbital debris; this can be achieved by using laser systems with higher energy. Otherwise, higher laser pulse energy is necessary.

Chapter 7

Experimental Results Analysis

7 Experimental Results Analysis

7.1 Summary

The experimentally measured data that has been employed here to estimate the temporal temperature difference at the surface of nickel, aluminium and copper space debris when each of them is illuminated by a concentrated Nd^{3+} Glass laser pulse of $1.06\ \mu m$ wavelength was obtained by utilising optical two-colour temperature measurements. This data is compared in this chapter with the results of the Kinetic and Fourier theories for validation.

7.2 Optical Mechanism

The precision of the proposed laser deflection system can be affected by the alignment of the laser system with the space debris and by the temporal and spatial repeatability of the laser output power intensity at the space debris surface from pulse to pulse. The radial surface temperature development has been calculated by [91] who assumed a Gaussian radiation profile for the situation of a nominal diameter with $330\ \frac{GW}{m^2}$ peak power intensity.

Rectifications are necessary to consider that none of the space debris is perfect or an ideal blackbody and to consider that the spatial temperature distribution is Gaussian on at the space debris surface. In this thesis, the distribution of the laser output power was presumed to be mainly a Gaussian beam, but the model validity boundaries are explained by also presuming a top hat or circ function beam irradiance distribution. In the lab, the spectral analysis of the released irradiation from an illuminated surface can be implemented by utilising a grating monochromator. To sample and represent the spectrum at two wavelengths, two optical fibres can be used and placed on the monochromator outlet slit [92]. For the practical measurements, two photodiodes were used to estimate the radiation transported down the two fibres. At the optical fibre, the monochromator bandwidth was $10\ nm$ and the monochromator dispersion was $10.24\ nm$. The optical fibre aperture was $1.6\ mm$ diameter; and the Gaussian distribution radius was $0.35\ mm$ at the e^{-2} point. The overall emissive intensity ratios were calculated for a variety of temperatures up to $6{,}000\ K$ by utilising the Planck expression for three different central wavelengths, which are $662.4\ nm$, $750.0\ nm$ and $950.0\ nm$. Prior to determining the ratio of the emissive power, the measurements

were rectified to consider the various photodiodes responsivities; and the maximum temperature at the illuminated surface was estimated. Since the vaporisation is covered in the new theoretical model, the intensities of the emissive power were determined up to $6{,}000\ K$. Nine sets of measurements were considered to include measurements for nickel, aluminium and copper, as the materials of the space debris that were considered in the theoretical model, at three different central wavelengths, which are $662.4\ nm$, $750.0\ nm$ and $950.0\ nm$. These measurements were recorded with a laser beam focus coincident with the surface of each space debris metal. The emitted radiation of the space debris surface was measured in the lab by a grating monochromator, in the red and near infrared parts of the electromagnetic spectrum at $662.4\ nm$, $750.0\ nm$ and $950.0\ nm$ wavelengths. This part of the electromagnetic spectrum was chosen intentionally because plasma generated at the space debris material was dominated by emission in the infrared part of the spectrum.

The laser output power temporal variation is usually not consistent or does not have a fixed pattern from pulse to pulse therefore, for more precise simulations, it is essential to measure the specific laser shot that is generated in addition to measuring the emitted irradiation from the illuminated space debris surface. Alignment of the optical train is another crucial element that needs to be maintained during the interaction of the laser with the space debris for better results. Therefore, tracking systems are essential to feed the laser system with the space debris coordinates to guide the laser beam before and after each series of shots.

7.3 Measurements of the Laser Output Power

The laser output power temporal variation for nine series of laser firings was used to produce the experimental data. It was notable to see the difference of the temporal variation of the laser output power for nine shots as they are dominated by relaxation oscillations within the laser rod. These relaxation oscillations are hard to suppress but they are governed by arbitrary thermal and mechanical vibrational perturbations from the host material. However, some types of switches can give much more repeatable laser output shots.

The input laser power supply voltage against the laser output energy are presented in Figure 106. The figure shows that the highest energy that can be obtained from the power supply produces $19.78\ J$ per laser pulse and thus this was used for all cases.

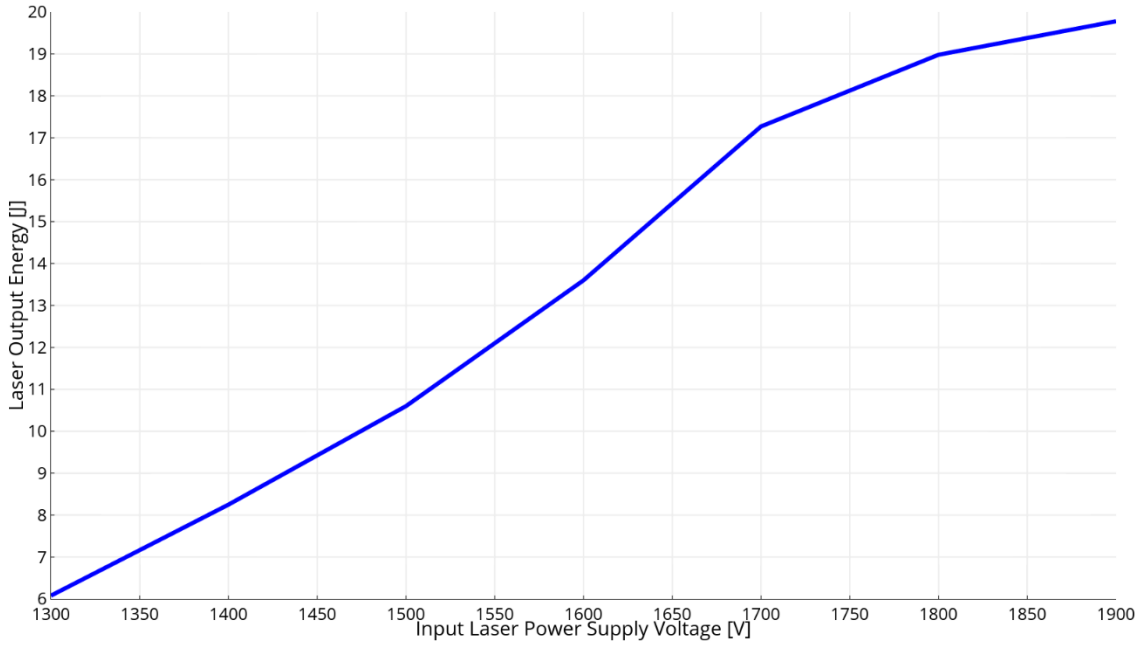

Figure 106: Laser input voltage against the laser output energy.

The 19.78 J value of the laser output energy correlates with the area beneath the curve of the laser output power against time because the curve of the laser output energy E against time is the integration of the laser output power P curve against time, which is in proportion to the temporal difference of the sensor output voltage V. In other words, the laser output energy can be determined by utilising the following expression:

$$E = \int_0^t P dt \qquad \text{Equation 7.1}$$

$$\Rightarrow P = \frac{dE}{dt} = Instantaneous\ laser\ output\ power$$

$$P \propto V$$

$$\Longrightarrow P = HV \qquad \text{Equation 7.2}$$

Where:

H is constant

For numerical integration, Simpson's rule can be used as a numerical approximation of definite integrals. The outcome shows that the constant H is proportional to the energy of the laser output, which is usually known from the calorimetry work. Therefore, the H constant can be estimated by utilising the following equation, after substituting

Equation 7.2 into Equation 7.1. The H value can be utilised to determine the pulse power for the laser as a function of time.

$$E = \int_0^t HVdt \Longrightarrow H = \frac{E}{\int_0^t Vdt} \qquad \text{Equation 7.3}$$

As discussed in Chapter 4, the increase of temperature at the space debris illuminated surface happens in a very short time. In the lab, this needs short time base oscilloscope, which is usually an issue due to the pre-triggering delay length. For the experimental results that are employed in this thesis, the laser system was setup and arranged to generate a pulse of $19.78\,J$. In addition, the emitted radiation from the illuminated surface of the space debris metal was measured with the laser power, at the same time. The voltage was sampled at a period of $0.2\,\mu s$ (i.e. sample rate) and the readings transferred to laser power. Bakewell [93] determined the intensity of the laser power from the distribution of the power at the image plane of lens. The author proposed a Gaussian profile for the distribution of the power intensity at the focal zone of the laser radiation. Some other authors proposed also that the intensity distribution of the power at the waist had a Gaussian profile and determined the maximum value of the Gaussian power intensity. Shayler [94] experimentally measured the real distribution of the power intensity at the focused point. He summarised that the distribution of the power intensity at the laser focal area can be estimated by a Gaussian profile.

For a critical analysis of the space debris surface temperature in this thesis, the distribution of the output radiation for the laser beam has been described by the top hat or circ function, as a worst-case presumption, and also by the Gaussian profile. This is because even when doing all things possible to make sure that the output radiation of the laser beam has a uniform Gaussian distribution of power intensity, horizontal to the optical axis, the Gaussian profile cannot be guaranteed. Therefore, the simulations have been done for both assumptions so that the top hat or circ function beam irradiance assumption produces the bottom limit and the Gaussian beam assumption produces the top limit. These two limits are the performance boundaries, lower bound and upper bound, for the estimated temperature of the space debris illuminated surface.

7.4 Laser Beam Assumptions

The spatial intensity distribution of the laser output power, which is transverse to the optical axis, can be determined as follows:

- Lower bound: For the top hat or circ function beam irradiance distribution assumption

$$P(t) = \pi\omega^2 I(t) \Longrightarrow I(t) = {}^{P(t)}/_{\pi\omega^2} \qquad \text{Equation 7.4}$$

Where:

$P(t) =$ Output power of the laser beam

$I(t) =$ Intensity of the laser beam

$\omega =$ Radius of the laser focused beam

- Upper bound: For Gaussian beam (profile) assumption

$$P(t) = 0.5\pi\omega^2 I(t) \Longrightarrow I(t) = 2\frac{P(t)}{\pi\omega^2} \qquad \text{Equation 7.5}$$

7.5 Determination and Measurement of Emissive Power Ratios and Temporal Change of the Space Debris Surface Temperature

Experimentally measuring the emissive irradiation power against time from a laser-illuminated area of any metal in general, in the lab, can be accomplished by utilising photodiodes, for example using two silicon photodiodes and measuring the outputs of the photodiodes using an oscilloscope with shortest sample periods. The monochromator can be set at the desired central wavelength. Turning off the laser cooling system can help to reduce the photodetector noise [95].

A calibration coefficient can be applied to the measurements of the photodetector $W\lambda_1$ and $W\lambda_2$ for optimal precision of the emissive power ratios. The detected emissive power ratio $R_{Detected}$ was calculated from the following expression:

$$R_{Detected} = \frac{W\lambda_1}{W\lambda_2} = \frac{W(Central\ Wavelength+10.24)}{W(Central\ Wavelength-10.24)} \qquad \text{Equation 7.6}$$

Where: $10.24\ nm$ is the dispersion

Therefore, the determination of the detected emissive power ratio $R_{Detected}$ can be evaluated for $662.4\ nm$, $750.0\ nm$ and $950.0\ nm$ central wavelengths for each of the three-space debris, which are nickel, aluminium and copper debris. Figure 107 presents

the corrected ratios of emissive power against time for nickel, aluminium and copper space debris respectively, at three specified values of the central wavelengths.

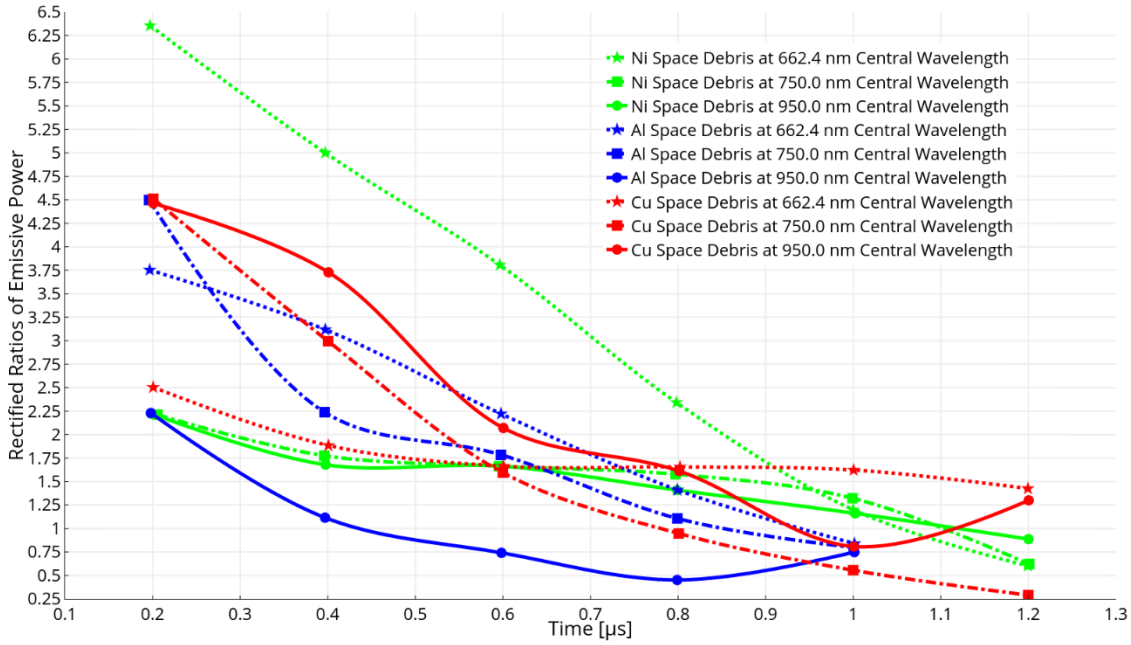

Figure 107: Corrected emissive power ratios against time for nickel, aluminium and copper space debris at 662.4 nm, 750.0 nm and 950.0 nm central wavelengths.

7.6 Implementation of Blackbody Irradiation for the Determination of Space Debris Surface Temperature

Electrons in the space debris absorb the energy of photons when the debris surface is irradiated with the laser beam and thus the energy of electrons rises. Via various energy transfer mechanisms, the space debris temperature rises releasing thermal radiation. The radiant energy travels as electromagnetic waves. The overall emissive power is the overall released irradiation from the debris per unit area and time. It relies on the surface characteristics and temperature of the target in general [96].

By definition, an ideal blackbody absorbs the whole incident irradiation that falls on its surface for all radiant energy wavelengths without reflecting or emitting any energy. Therefore, blackbody can be used as a model, to compare the irradiation characteristics of any space debris. The overall blackbody emissive power relies only on its temperature [97]. It can actually be calculated using Stefan-Boltzmann Law, as shown below:

$$W_B = \sigma T^4 \qquad \text{Equation 7.7}$$

Where:

$$\sigma = Stefan\ Boltzmann\ constant = 5.670367 \times 10^{-8}\ \left[{}^{W}/_{m^2K^4}\right]$$

$$T = Termperature\ of\ the\ surface\ [K]$$

The blackbody emissive power ratios R_{WB} can be determined using the following equation:

$$R_{WB} = \frac{W_{B_1}}{W_{B_2}} \qquad \text{Equation 7.8}$$

Where:

W_{B_1} = Blackbody emissive power ratios across bandwidth $a_1 b_1$

W_{B_2} = Blackbody emissive power ratios across bandwidth $a_2 b_2$

Other irradiation features of a blackbody, with regard heat transport, are its distribution in the spectrum and the change of that distribution with temperature. Planck's Law links the monochromatic emissive power $W_{B\lambda}$ with the wavelength and the temperature, in the equation below. $W_{B\lambda}$ is the energy emitted from the space debris surface throughout a hemispherical angle per unit area in the wavelength interval.

$$W_{B\lambda} = \frac{2\pi h c_0^2}{\lambda^5} \cdot \frac{1}{\frac{c_0 h}{e^{k_B \lambda T}} - 1} = \frac{c_1}{\lambda^5 \left(e^{\frac{c_2}{\lambda T}} - 1\right)} \qquad \text{Equation 7.9}$$

Where:

$$W_{B\lambda} = Monochromatic\ emissive\ power\ at\ wavelength\ \lambda$$

$$h = Planck\ constant = 6.626070040 \times 10^{-34}\ [J.s]$$

$$c_0 = Speed\ of\ light\ in\ the\ medium = 299792458\ [{}^{m}/_{s}]$$

$$k_B = Boltzmann\ constant = 1.38064852 \times 10^{-23}\ \left[{}^{J}/_{K}\right]$$

$$\lambda = Wavelength\ of\ radiation\ [m]$$

$$c_1 = 2\pi h c_0^2 = 0.374177179 \times 10^{-15}\ \left[{}^{W}/_{m^2}\right]$$

$$c_2 = {}^{c_0 h}/_{k_B} = 14.38777354 \times 10^{-3}[m \cdot K]$$

As a result of the intensity distribution of the incident power, normal i.e. Gaussian temperature distribution was assumed. Therefore, the Gaussian expression needs to be used in the previous expression instead of the temperature T term.

$$T = T_0 e^{-ax^2} \qquad \text{Equation 7.10}$$

Where:

a is defined by the ${}^{1}/_{e}$ points

$x =$ Beam radius $= 0.35\ mm$ at $\frac{1}{e^2}$ point

$$T_e = T_{(ax^2=1)} = T_0 e^{-1} = {}^{T_0}/_{e} \qquad \text{Equation 7.11}$$

The temperature needs to be expressed as a function of the Gaussian distribution and also rectified for the impact of the optical systems aperture, which has an area equal to:

$$\int_0^{x_0} 2\pi x dx = Aperture\ area \qquad \text{Equation 7.12}$$

Where:

$x_0 =$Radius of fibre optic $= 0.8\ mm$

The theoretic unrectified temperature of blackbody against the ratios of the emissive power for $662.4\ nm$, $750.0\ nm$ and $950.0\ nm$ central wavelengths λ_c can be calculated by using the Planck expression at the appropriate wavelengths, as shown in the two expressions below. These wavelengths are with $10.24\ nm$ dispersion and $10\ nm$ bandwidth $d\lambda$.

$$W_{B_1} = \int_{a_1}^{b_1} W_{B\lambda} d\lambda = \int_{a_1}^{b_1} \frac{c_1}{\lambda^5 \left(e^{\frac{c_2}{\lambda T}} - 1\right)} d\lambda \qquad \text{Equation 7.13}$$

$$W_{B_2} = \int_{a_2}^{b_2} W_{B\lambda} d\lambda = \int_{a_2}^{b_2} \frac{c_1}{\lambda^5 \left(e^{\frac{c_2}{\lambda T}} - 1\right)} d\lambda \qquad \text{Equation 7.14}$$

The overall emissive power for a blackbody across all irradiation wavelengths per unit area and time is W_B:

$$W_B = \int_0^\infty W_{B\lambda} d\lambda = \sigma T^4 \qquad \text{Equation 7.15}$$

Obviously, for a non-blackbody surface like space debris surface, the emissive power W will be smaller in value comparing with that of the blackbody at a similar temperature. The gross emissive powers released over the aperture of the 2-fibre optics was set by the following expression:

$$W_1 = \int_0^{x_0} 2\pi x \left(\int_{a_1}^{b_1} W_{B\lambda} d\lambda \right) dx = \int_0^{x_0} 2\pi x \left(\int_{\frac{\lambda_c + 10.24}{1000}}^{\frac{\lambda_c + 10.24 + 10}{1000}} W_{B\lambda} d\lambda \right) dx \qquad \text{Equation 7.16}$$

$$W_2 = \int_0^{x_0} 2\pi x \left(\int_{a_2}^{b_2} W_{B\lambda} d\lambda \right) dx = \int_0^{x_0} 2\pi x \left(\int_{\frac{\lambda_c - 10.24}{1000}}^{\frac{\lambda_c - 10.24 + 10}{1000}} W_{B\lambda} d\lambda \right) dx \qquad \text{Equation 7.17}$$

Where:

$10\ nm =$ Bandwidth

$\lambda_c =$ Central wavelength $=$ Wavelength of emitted light detected at the monochromator exit slit centre

For certain temperatures, the temperature corrected blackbody emissive power ratios can be determined by the following ratio:

$$R_{Temperature\ corrected\ blackbody} = \frac{W_1}{W_2} = \frac{\int_0^{x_0} 2\pi x \left(\int_{\frac{\lambda_c + 10.24}{1000}}^{\frac{\lambda_c + 10.24 + 10}{1000}} W_{B\lambda} d\lambda \right) dx}{\int_0^{x_0} 2\pi x \left(\int_{\frac{\lambda_c - 10.24}{1000}}^{\frac{\lambda_c - 10.24 + 10}{1000}} W_{B\lambda} d\lambda \right) dx} \qquad \text{Equation 7.18}$$

Experimental emissive power ratios $R_{Detected}$ were used to assess the temperature of the space debris surface. They fit close to each other however, the difference is more obvious at low temperatures or when the emissive power ratio is bigger than one.

Results show that for any temperature below $3{,}569.33\ K$, the emissive power ratio is higher for lower central wavelengths. For example, at $500\ K$, the emissive power ratios are 1.7329, 2.4999 and 3.3199 for $950.0\ nm$, $750.0\ nm$ and $662.4\ nm$ central wavelengths, respectively.

The uncorrected and corrected emissive power are virtually coincident, especially for large temperature. At temperatures below $950.64\ K$, the ratios of the emissive power, is a function of the uniform temperature of blackbody irradiation and can be obtained by using Equation 7.13 and Equation 7.14, at $950.0\ nm$ central wavelength are slightly higher than the ratios of the emissive power as a function of the corrected temperatures. This is also correct for both $750.0\ nm$ central wavelength at temperatures below $1{,}538.30\ K$ and for $662.4\ nm$ central wavelength at temperatures below $1{,}736.30\ K$.

7.7 Discussion and conclusions

The temperature of the illuminated space debris surface was measured by employing the spectroscopic technique that is discussed in Chapter 4. At equilibrium, the debris surface temperature would be the phonon i.e. lattice temperature. However, the non-equilibrium conditions are usually the dominant conditions.

The measurement signal is mainly influenced by the irradiation from the middle point of the illuminated area of the space debris. This is because the irradiance arriving from the illuminated space debris is proportional to the temperature T^4 in addition to the fact that the illuminated area on the debris has a Gaussian temperature profile. Therefore, the determined temperature of the illuminated space debris via the released irradiation measurement is the centre temperature of the illuminated area of the debris.

The irradiation released from the illuminated area on the space debris is a function of the laser output pulse. It is important to note that the oscillation of the released radiation from the zone on the space debris that experiences irradiation has a frequency of about $125\ kHz$, which is roughly double the frequency of the irradiation or the frequency of the laser pulse. The output of the laser pulse is usually dominated by the relaxation oscillations, which provides the resulted laser beam with intensity increase at a certain frequency. Based on this, it is expected to see small thrusts on the space debris due to the emitted radiation from the illuminated spot on the space debris at a frequency almost twice the frequency of the laser pulse. This is due to the vaporisation that is lasting for a short time and the blasts occurring from the nucleation of space debris sub-surface forcing fast and arbitrary temperature changes, which is based directly on the temperature changes induced by the laser.

Although the real intensity distribution of laser beam is closer to the normal distribution of a Gaussian beam than the top hat or circ function beam, the presumptions of beam profile for both top hat (circ function) beam and Gaussian beam are considered, discussed and analysed in this thesis. This allows presentation of the potential boundaries, minimum and maximum, of the intensity distribution for the laser beam on the space debris and these boundaries can set up the optimistic and pessimistic scenarios for the use of this laser deflection technique for space debris mitigation. Therefore, the pessimistic scenario or the minimum potential boundary for the theoretical simulation are given by the top hat or circ function beam assumption. When a Gaussian beam is assumed, the profile of the laser beam has intensity at the centre of the laser beam that is double the intensity of the top hat or circ function beam irradiance distribution, as simulated in Chapter 3.

7.8 Analysis of Experimental Results

The temperatures of electrons in the nickel, aluminium and copper space debris were estimated by using the Kinetic theory and also by using the Fourier theory. The temperature estimations were based on two beam presumptions, which are Gaussian beam and top hat (circ function) beam. In this section, the theoretical results are compared with experimentally measured values. The temperature change at different central wavelengths of $662.4\,nm$, $750.0\,nm$ and $950.0\,nm$ has been studied and discussed in the following sections for nickel, aluminium and copper metal space debris. The figures in this section demonstrate the temperature temporal development at the centre of the illuminated surface of the space debris.

The output of the laser pulse with respect to time is not identical in any two of the experimental cases, due to the nature of the laser pulses and the limitations of the laser systems. Thus, the integration of the laser output pulse with respect to time was used to assess the proportionality constant that is needed to extract the laser output power from the voltage curve of the laser output pulse.

7.8.1 Results for Nickel Space Debris

I. At central wavelength of 662.4 nm

The following figure, Figure 108, displays the temperature profile versus time for nickel space debris surface with the output power of the laser pulse. The laser output power has also been presented in the figure because it is important to measure the radiation released from the illuminated spot, on the sample space debris, at the same time with the

specific beam pulse producing it due to the fact that the change in the temporal laser output, from shot to shot, is not the same. It can be noticed that after 1 μs of laser-debris interaction the temperature reaches 2000 K, the measured electron temperature starts to rapidly jump to a higher temperature in a very short period of time. This is also true for the theoretical results, when a Gaussian beam is assumed.

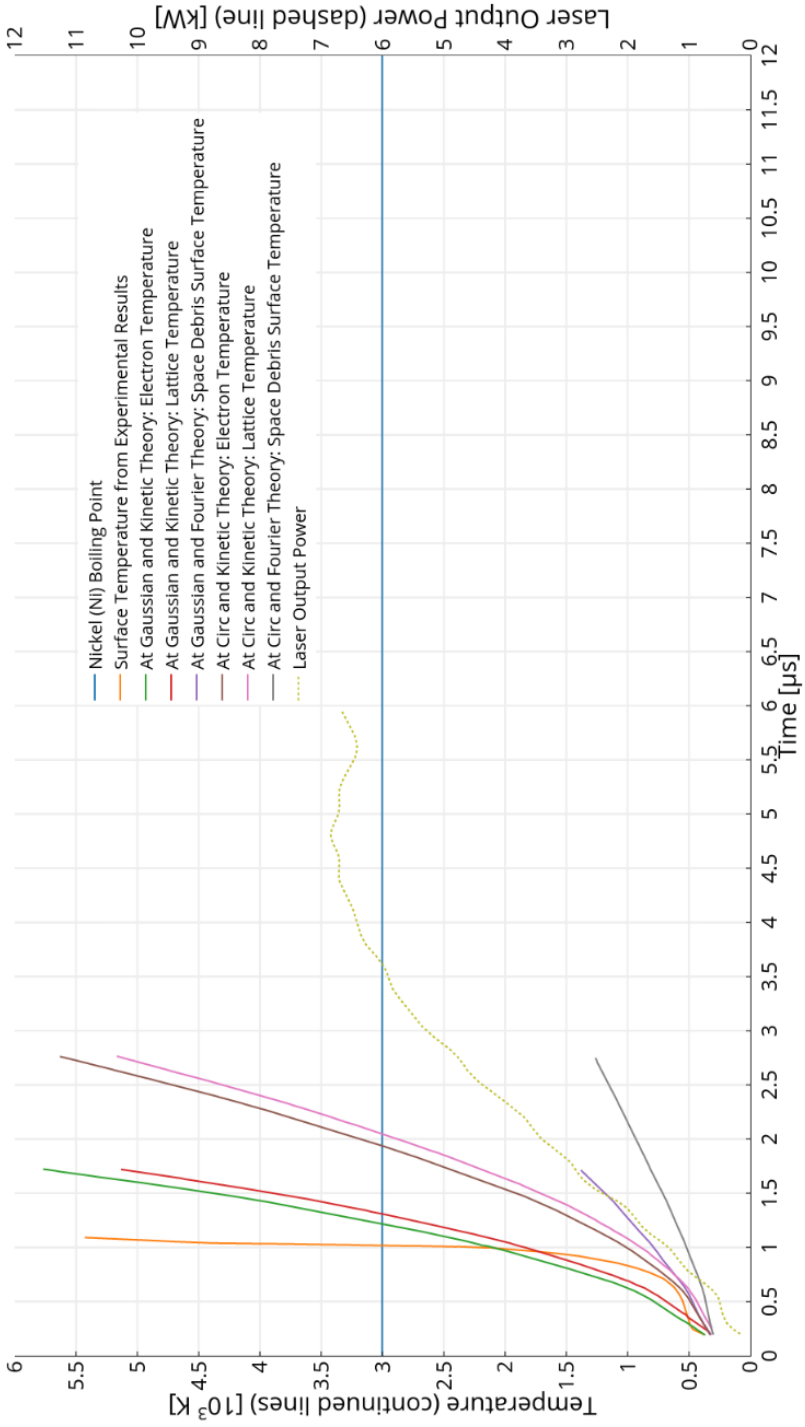

Figure 108: Summarises the nickel (Ni) space debris surface temperature profile with respect to time, using different methods at a central wavelength of 662.4 nm. It also presents the output power of the laser with respect to time.

The figure also demonstrates the temperature temporal development at the centre of the illuminated surface of the nickel space debris. Below 2000 K temperature, the curve of the measured electron temperature falls in the area between two curves of the estimated electron temperature that are produced by assuming Gaussian beam and top hat beam, circ function beam irradiance distribution. It is clear from the figure that for temperatures higher than 2100 K, the curve of the measured electron temperature starts to diverge from the calculated electron temperature curve that is produced using a Gaussian beam, which represents the top boundary of the electron temperature. This divergence is even bigger if we compare the experimental electron temperatures with the calculated ones that are produced using top hat (circ function irradiance distribution) beam.

II. At central wavelength of 750.0 nm

At a central wavelength of 750.0 nm, the nickel space debris surface temperature profile is measured and predicted using a Gaussian beam and circ function (top hat) beam as presented against time in Figure 109. The figure also shows the output power of the laser pulse with respect to time. It can be noticed that just after one μs of debris-laser interaction; the measured electron temperature achieved 2,000 K and started to jump rapidly to a high temperature in a very short time. When a Gaussian beam is assumed, the theoretical results predict a higher increase in both electron and lattice temperatures, compared with the experimental results, however this only happens at temperatures below the boiling point of the nickel space debris material, which is 3003 K.

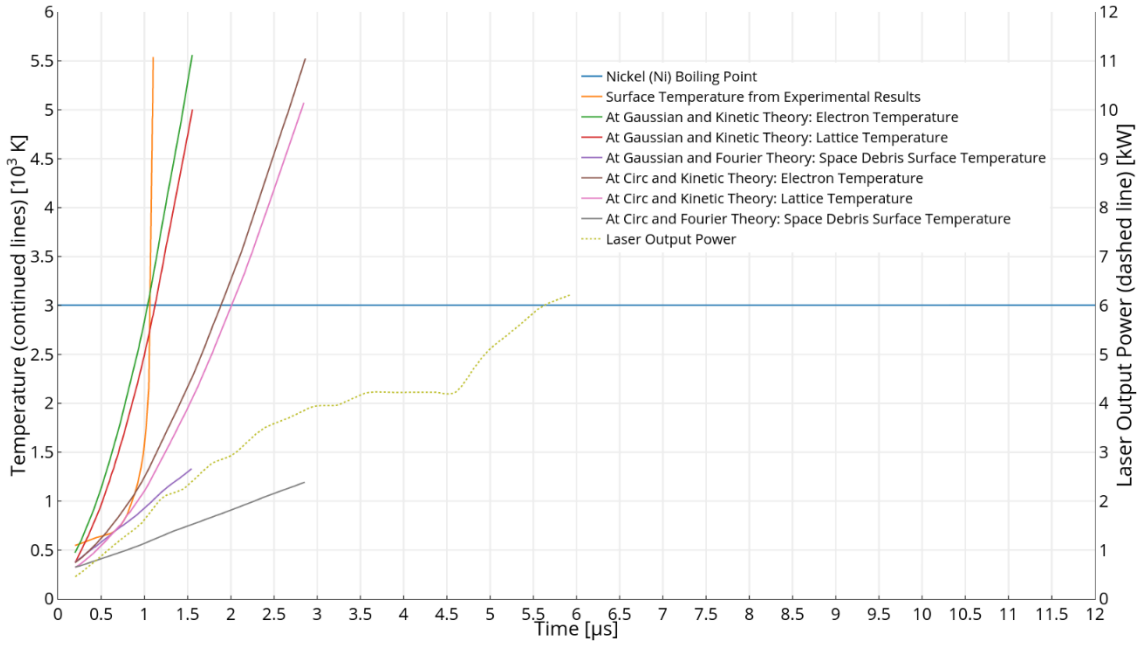

Figure 109: Summarises the nickel (Ni) space debris surface temperature profile with respect to time, using different methods at a central wavelength of 750.0 nm. It also presents the output power of the laser with respect to time.

The above figure actually shows the temporal development of the temperature at the centre of the illuminated surface of the nickel space debris. Below the boiling point temperature of the nickel debris, the curve of the measured electron temperatures falls mainly in the area between two curves of the estimated electron temperatures that are produced by assuming circ function beam irradiance distribution (top hat) and Gaussian beam. It is clear from the figure that for temperatures higher than the boiling temperature of the nickel debris, the curve of the measured electron temperatures starts to diverge from the calculated electron temperatures curve that is produced using Gaussian beam and even more from the one that is produced using top hat (circ function) beam.

III. At central wavelength of 950.0 nm

The surface temperature results for nickel space debris at 950.0 nm central wavelength show similar behaviour of the temperature profiles at 662.4 nm central wavelength except here the measured electron temperatures start to climb rapidly to higher temperature values after 1 μs at a lower temperature of 1200 K, as shown in Figure 110. This is mainly because the measured electron temperature progresses slower at this central wavelength comparing to the case of 662.4 nm central wavelength. The figure shows both the output power of the laser pulse against time as well as displays a

summary of the surface temperature profiles against time of a nickel space debris at 950.0 nm central wavelength.

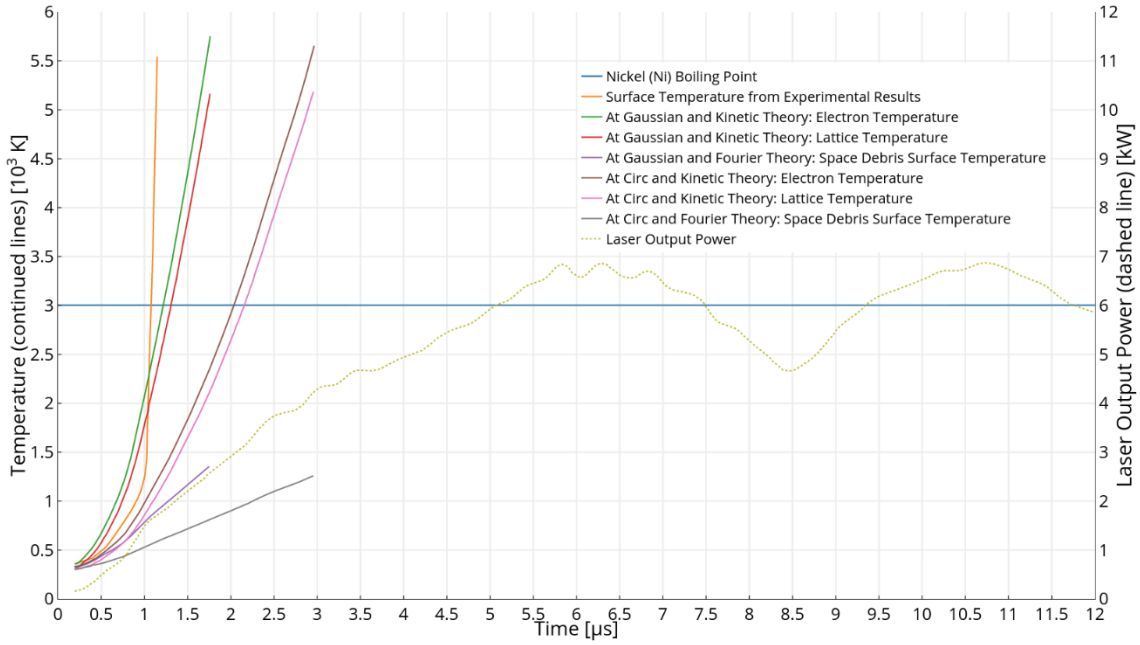

Figure 110: Summarises the nickel (Ni) space debris surface temperature profile with respect to time, using different methods at a central wavelength of 950.0 nm. It also presents the output power of the laser with respect to time.

Below 2200 K, the measured electron temperature falls in the area between the two curves of the estimated electron temperature that are produced by assuming Gaussian beam and top hat beam, circ function beam irradiance distribution. It is clear from the figure that for temperatures higher than 2300 K, the curve of the measured electron temperature starts to diverge from the calculated electron temperature curve that is produced using the Gaussian beam, which represents the top boundary of the electron temperature. This divergence is even bigger if we compare the experimental electron temperatures with the calculated ones that are produced using top hat (circ function irradiance distribution) beam.

In general, at any of the three central wavelengths, the electron and lattice temperature curves for nickel space debris that are predicted using the Kinetic theory are progressing closely to each other especially at low temperatures for both cases, when a Gaussian beam or circ function (top hat) beam is assumed. In fact, the lattice temperature falls beyond the estimated temperature of electron. This is more obvious at high temperatures. On the other hand, the estimated curves of electron temperature using the Fourier theory

show a steady increase in the temperature over a long period, which is not actually describing the measured temperatures, and this becomes more obvious as time evolves.

7.8.2 Results for Aluminium Space Debris

I. At central wavelength of 662.4 nm

The experimentally measured data for the electron temperature of an aluminium surface of space debris at 662.4 nm central wavelength has been compared with the theoretical results, as shown in Figure 111.

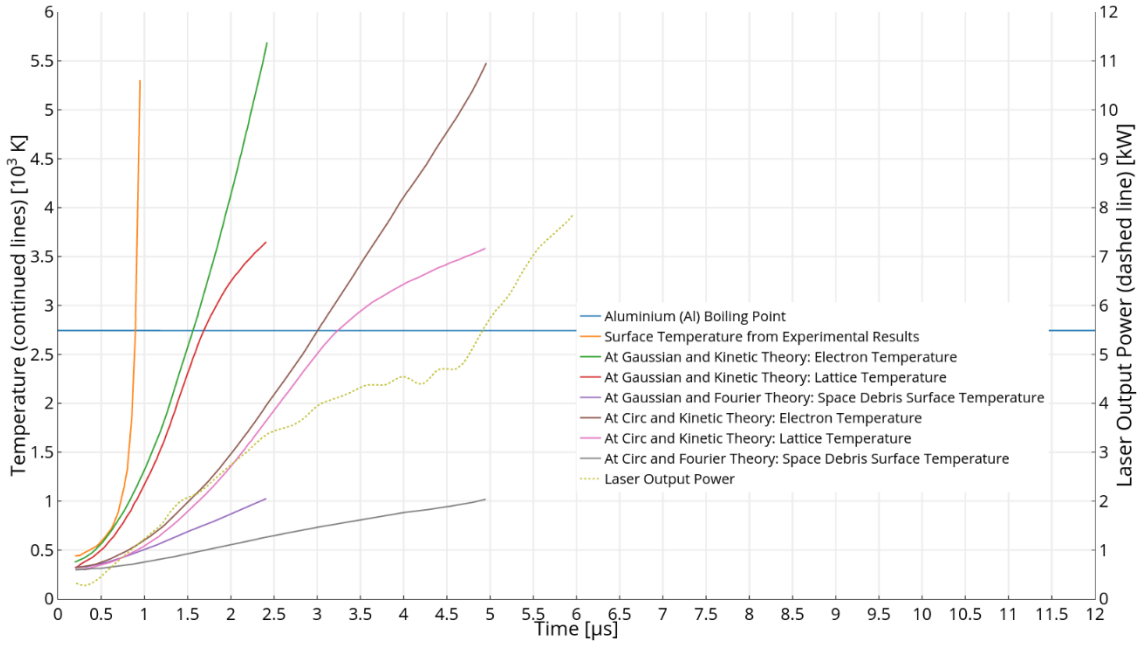

Figure 111: Summarises the aluminium (Al) space debris surface temperature profile with respect to time, using different methods at a central wavelength of 662.4 nm. It also presents the output power of the laser with respect to time.

It can be noticed that during the first 700 ns, the estimated temperature curves using the Gaussian beam provides very good match with the experimental data, up to temperature of 800 K. This means the output laser radiation was very close to a Gaussian beam. However, after this point the experimental data shows very rapid increase in the electron temperature and thus diverges from the estimated data that was produced using a Gaussian beam.

II. At central wavelength of 750.0 nm

At 750.0 nm central wavelength, the Kinetic theory prediction curves using Gaussian beam assumption provide a very close match with the measured temperature curve up to a temperature of 1600 K, after 800 ns of laser-aluminium space debris interaction. After

this point, the curves start to diverge from each other, marking much sharper increase in the experimental data, see Figure 112.

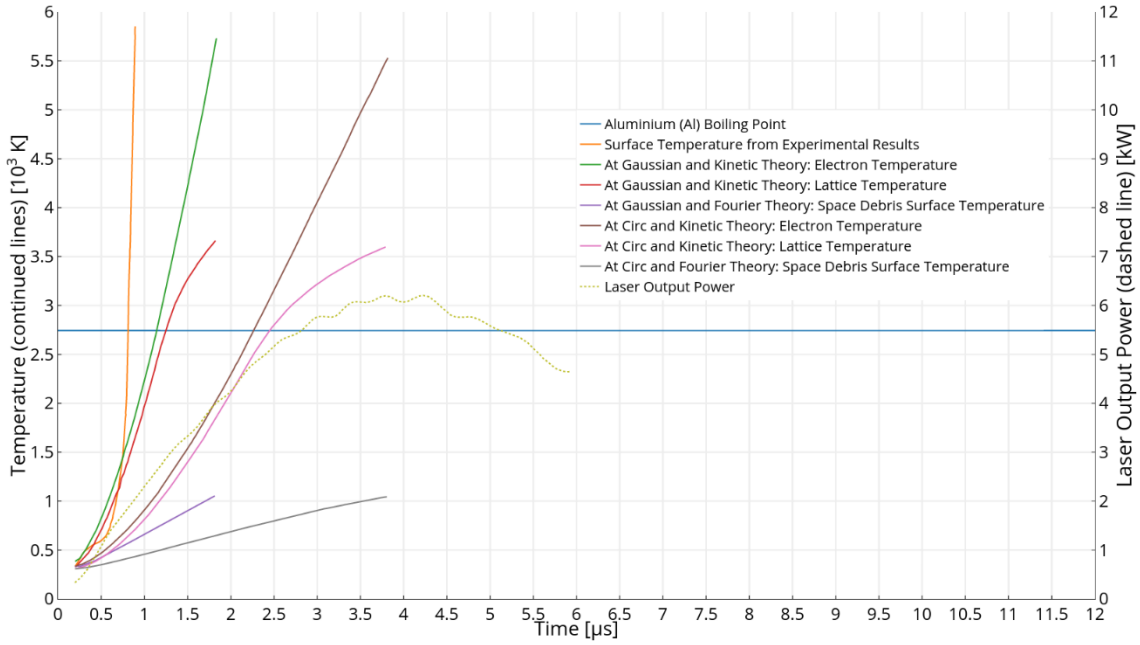

Figure 112: Summarises the aluminium (Al) space debris surface temperature profile with respect to time, using different methods at a central wavelength of 750.0 nm. It also presents the output power of the laser with respect to time.

The temperature profiles at this 750.0 nm central wavelength are quite similar to the ones that were obtained at the 662.4 nm central wavelength.

III. At a central wavelength of 950.0 nm

It is interesting to see the difference between the measured and predicted surface temperature profiles for aluminium space debris at 950.0 nm central wavelength as none of the theoretical predictions gives a close match to the measured temperature profile, see Figure 113.

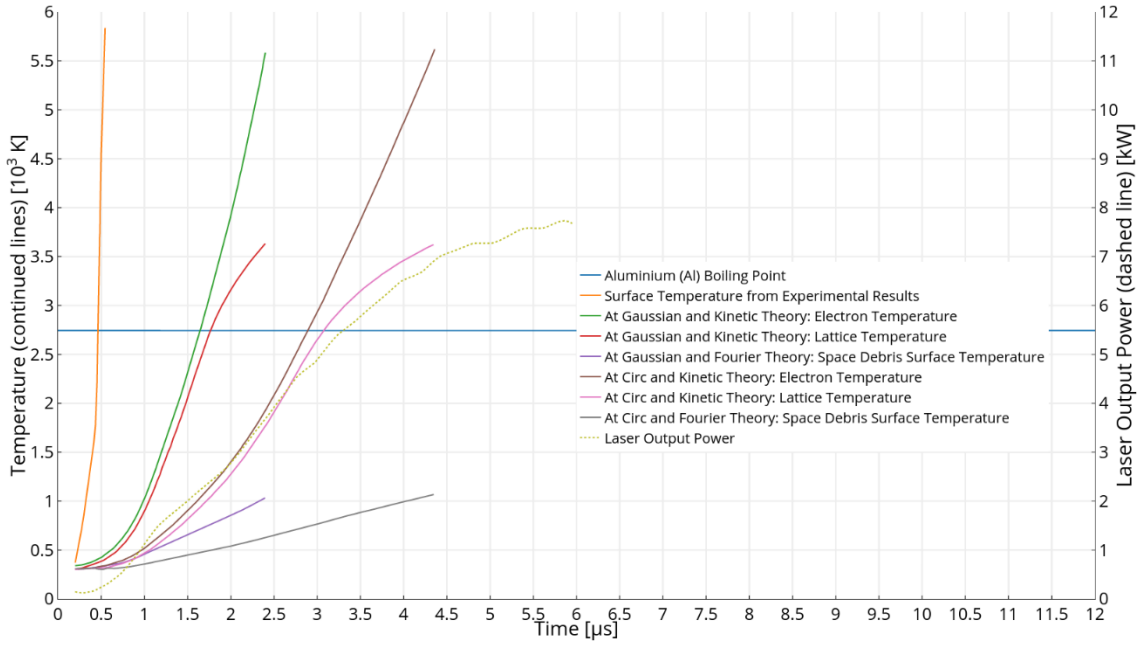

Figure 113: Summarises the aluminium (Al) space debris surface temperature profile with respect to time, using different methods at a central wavelength of 950 nm. It also presents the output power of the laser with respect to time.

The above figure shows that at the beginning of the laser-aluminium space debris interaction, the measured temperature profile started to increase rapidly and within 500 ns, the temperature increase was almost vertical. This measured temperature profile diverges, from the beginning, from any of the theoretical temperature profiles. So at this 950.0 nm central wavelength, the difference between the measured electron temperature values and the estimated values that are obtained using the electron Kinetic theory is clearly large from the start. This indicates the invalidity of the electron Kinetic theory model for this central wavelength, especially for aluminium at temperature higher than the boiling temperature.

In general, at any of the three central wavelengths, the electron and lattice temperature curves for aluminium space debris that are predicted using the Kinetic theory are progressing closely to each other especially at low temperatures for both cases, when Gaussian beam or circ function (top hat) beam presumed. However, this is not like nickel space debris because it is only true for temperatures below the boiling temperature of the aluminium space debris. In fact, the lattice temperature falls beyond the estimated temperature of electron. This is very obvious at high temperatures, above the aluminium boiling temperature. This is mainly because the estimated curve of lattice temperature diverges from the estimated curve of electron temperature. This is correct at the three different wavelengths so the lattice temperature rises slowly as more energy is

lost through the vaporisation process. On the other hand, the estimated curves of electron temperature using the Fourier theory show a steady increase in the temperature over a long period, which is not actually describing the measured temperatures and this becomes more obvious as time evolves. Comparing with targets that are made of nickel material, the theoretical and experimental temperature of the illuminated surface in aluminium space debris increases slowly. This is a very important outcome for the application of space debris deflection using lasers, when the interaction time between the laser beam and the space debris is limited. This means the generated thrust is larger for space debris that are made of nickel than aluminium. This also makes sense as aluminium materials have a higher reflectivity and thermal diffusivity than nickel materials.

7.8.3 Results for Copper Space Debris

I. At central wavelength of 662.4 nm

The following figure, Figure 114, shows the variation of the estimated surface temperature of copper space debris using the Kinetic and Fourier theories as well as the measured temperature of the electrons. It is obvious that the difference between the experimental and theoretical electron temperatures becomes larger as time evolves, especially at temperatures higher than 1100 K where the measured electron temperatures start to increase rapidly in a very short period of time, after a steady increase for about 500 ns.

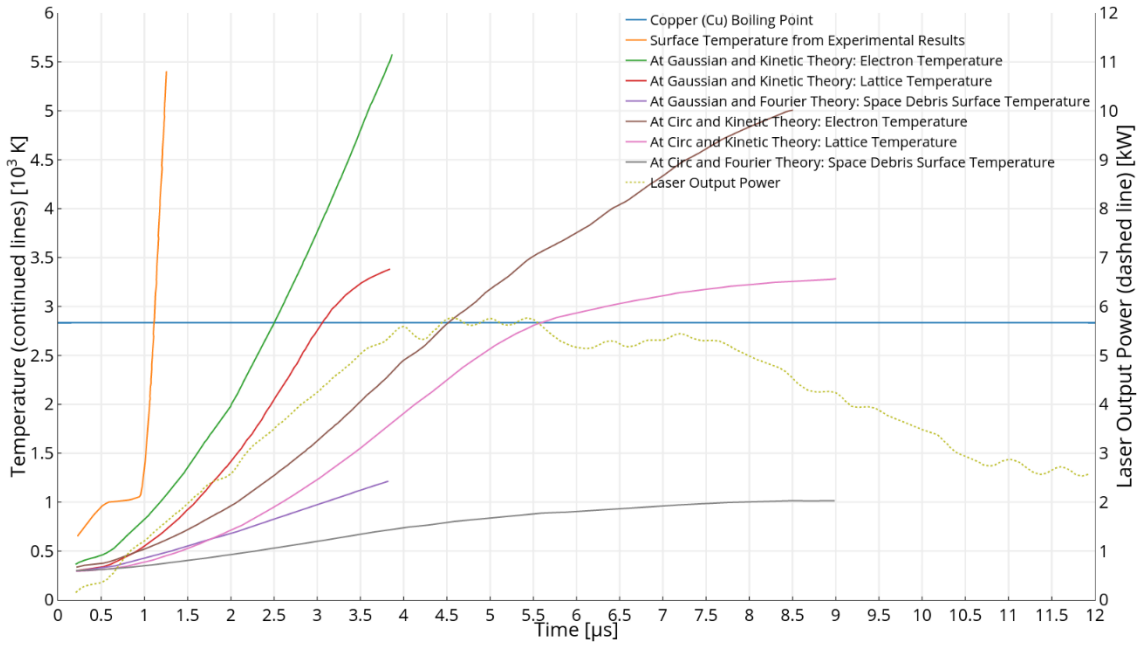

Figure 114: Summarises the copper (Cu) space debris surface temperature profile with respect to time, using different methods at a central wavelength of 662.4 nm. It also presents the output power of the laser with respect to time.

In addition to illustrating the surface temperature profiles of the copper space debris at 662.4 nm central wavelength, this figure also depicts the output power of the laser pulse against time.

II. At central wavelength of 750.0 nm

The results at 750.0 nm central wavelength for a copper space debris surface temperature were not very different from the previous case, at 662.4 nm central wavelength. In fact, the divergence between the measured electron temperature profile and the theoretical profiles starts earlier at this central wavelength, after the interaction of the laser beam with the copper space debris by about 650 ns.

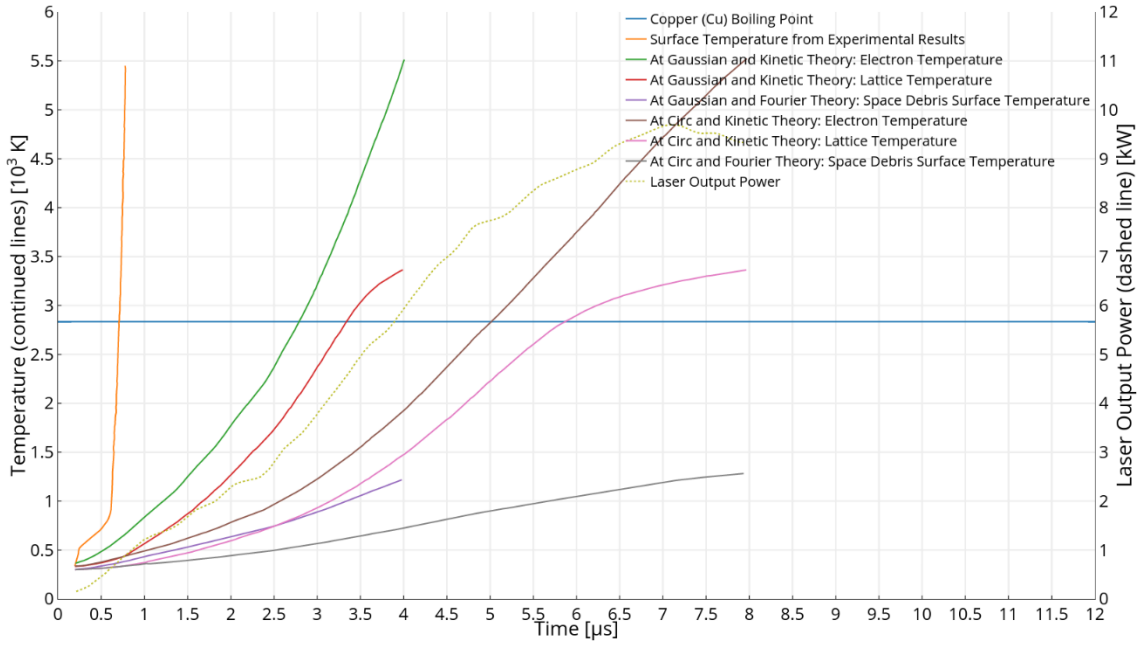

Figure 115: Summarises the copper (Cu) space debris surface temperature profile with respect to time, using different methods at a central wavelength of 750.0 nm. It also presents the output power of the laser with respect to time.

The above figure shows the variation of the estimated temperature of the electrons using the Kinetic and Fourier theories and the measured temperature of the electrons. It is obvious that the difference between the practical and theoretical electron temperatures becomes larger as time evolves, especially at temperatures higher than 900 K when the measured electron temperature increased rapidly within a very short period of time.

III. At central wavelength of 950.0 nm

The estimated electron temperature profiles in copper space debris at 950.0 nm central wavelength using Kinetic theory and Fourier theory are displayed in Figure 116 with the measured electron temperature profile for the copper debris.

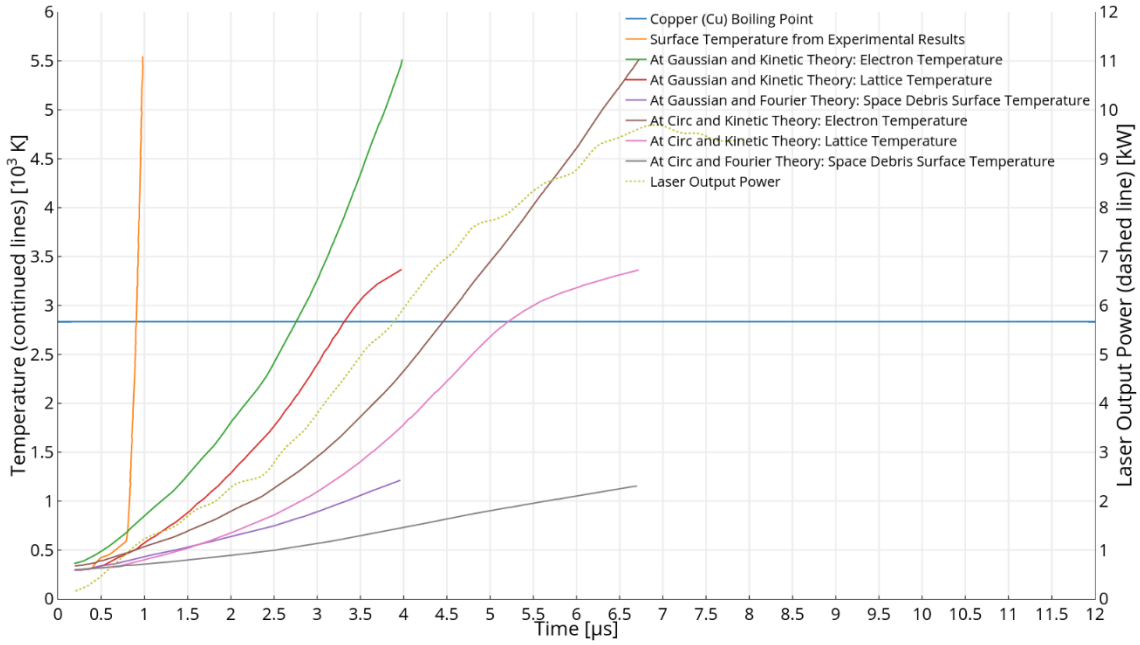

Figure 116: Summarises the copper (Cu) space debris surface temperature profile with respect to time, using different methods at a central wavelength of 950 nm. It also presents the output power of the laser with respect to time.

It is obvious that the difference between the practical and theoretical electron temperatures becomes larger as time evolves, especially at temperatures higher than 600 K where the measured electron temperature increased rapidly within a very short period of time.

In general, at any of the three central wavelengths, the electron and lattice temperature curves for copper space debris that are predicted using the Kinetic theory are progressing not too far from each other especially at low temperatures for both cases, when Gaussian beam or circ function (top hat) beam is assumed. Like aluminium space debris, it is only true for temperatures below the boiling temperature of the copper space debris. In fact, the lattice temperature falls beyond the estimated temperature of the electrons. This is very obvious at high temperatures, above the copper boiling temperature. This is mainly because the estimated curve of lattice temperature diverges from the estimated curve of electron temperature. This is correct at the three different wavelengths so the lattice temperature rises slowly as more energy is lost through the vaporisation process. On the other hand, the estimated curves of electron temperature using the Fourier theory show steady increase in the temperature over a long period, which is not actually describing the measured temperatures and this becomes more obvious as time evolves.

7.8.4 Discussion

Compared to space debris that are made of nickel or aluminium material, the theoretical results showed that the temperature of the illuminated surface in copper space debris increases slowly. This is a very important outcome for the application of space debris deflection using lasers, when the interaction time between the laser beam and the space debris is very limited. This is important because it means that the generated thrust is smaller for space debris that are made of copper than that which are made of aluminium or nickel. The results show that this is true experimentally and theoretically. This also makes sense as copper materials have higher reflectivity and thermal diffusivity than aluminium or nickel materials.

I. Classical Fourier Theory

Due to the assumptions that are considered in this classical theory, the results are small in value compared with both, the values of the Kinetic theory and the measured results. These presumptions assumed phonons and electrons are in equilibrium and also presumed fixed temperature inclination between two isothermal levels that are displaced by Δx.

$$Temperature\ Gradient = \frac{T_2 - T_1}{\Delta x} \qquad \text{Equation 7.19}$$

Where:

$$\Delta x > 10l$$

This classical theory is not correct for situations that are not in thermal equilibrium and for high temperature gradients.

II. Kinetic Theory

Solving the developed model heat flow expressions gives temperature profiles, which were consistent with the mathematical results that are obtained by Byabagambi [98] and validated the reliability of the developed model. Different laser beam pulses were used to obtain the results. The space debris materials heat flow was relying on the heat capacity ρC_p and on how many electrons are in the Fermi surface of the space debris (replacing thermal conductivity 'K'). As a rough guide, the diffusivity $K/\rho C_p$ is relative to the heating rate. So, the heat flow mathematical determination was based on the optical and thermal properties of the space debris materials as well as the laser pulse parameters.

Computer simulations show that a big difference in the thermal characteristics leads to little variation in the temperature profile of the surface temperature of the space debris, this means they are comparatively not sensitive to the space debris thermal characteristics. The phonon temperature is not the same as the electron temperature and that is what the results illustrated. This difference is because of the limited energy transport rate to phonons from electrons. The variation is small at the beginning of the interaction process, between the laser beam and the space debris, but it rises when evaporation takes place. It has been noticed from the results that beyond the boiling temperature the variations between phonon temperature and electron temperature are smaller for nickel material than for aluminium or copper space debris materials. This is mainly due to the optical and thermal properties of the materials and also due to the electronic arrangement of the materials.

7.9 Limitations and Inadequacies

The variation between the theoretically calculated electron temperature, using the Kinetic theory, and the experimental temperature of the electrons is due to some inaccuracies that can be categorised mainly into the following:

7.9.1 Mathematical Model Limitations

The presented mathematical model considers the evaporation phase, but it does not consider the intermediate phase (i.e. the liquid phase) that influences the mass and energy movements due to the complex liquid motion. Therefore, the model becomes progressively inaccurate when the boiling temperature is achieved and that is why the discussion in this chapter was mainly made for temperatures below the boiling temperatures of the space debris materials. The nucleation of the space debris sub-surface produces explosive fluid ejection of the debris material that is unjustified in the mathematical model and remains as a modelling challenge. In addition, the theoretical model is correct at temperatures below 2,000 K above the boiling temperature. This is because at temperatures higher than the critical temperature, the produced plasma absorbs the radiation beam energy.

Furthermore, the Kinetic theory does not consider the impurities or the non-homogeneity of the space debris materials. The theoretical model neither includes the re-irradiated light scattering nor beam light scattering. It also does not contain the energy re-radiation from the illuminated spot on the space debris surface. The model also does not take into account the unpredicted fast temperature increase, which is

results from the decrease in the dissipated energy through the evaporation process. This decrease in the dissipated energy is due to the increase of the boiling temperature, which is the result of the several bars rise in the ambient pressure when the surface of the space debris begins to evaporate. This gives room for further development and future work to consider the impact of this phenomenon.

On the other hand, the theoretical model includes some estimations like space debris metal reflectivity, which is utilised in determining the temperature of the electrons by the Kinetic theory. It is a dimensionless value and a function of wavelength. It describes the ratio of the radiant power that is reflected back from the illuminated spot on the surface of the space debris to the radiant power that is incident on the illuminated zone on the debris. Therefore, space debris materials that have small reflectivity values are easier to deflect than those that have unity reflectivity values. It is experimentally confirmed that the value of reflectivity reduces as the temperature of the illuminated spot rises [99], when the beam pulse power strength grows. So material reflectivity of space debris may drop to half of its ambient reflectivity value as the laser power strength increases.

7.9.2 Measurement Inadequacies

There are always some inadequacies and errors in the measurement mechanism when data is recorded or measured practically. This also applies to the experimental results that are employed in this thesis. For instance, the three target materials that have been tested experimentally were not 100% pure, as they were assumed in the Kinetic theory. Table 14 lists the pureness of the three target materials that were tested.

Table 14: Material Purity of the Space Debris

Space Debris Type	Space Debris Material Purity
Nickel Space Debris	99.8%
Aluminium Space Debris	99.0%
Copper Space Debris	99.9%

At large irradiance values, the practical measurement can be impacted by the nonlinear behaviour of the photodiodes. This can be noticed at large values of irradiation when the vaporisation happens; the gain of the diode begins to be a function of current density.

The transformation to temperature from the ratio of emissive power is subject to some inaccuracies. It is hard to set correction for the Gaussian distribution of temperature at large temperatures when the ratio of emissive power reaches unity.

On the other hand, the H factor is a function of the calorimetry work inaccuracies. A calorimetric method was utilised to standardise the output energy of the laser beam to determine the energy in one neodymium glass laser pulse.

In summary, the list below provides some factors that could affect the practical data that are employed in this thesis:

- Any misalignment or imprecision in the alignment of the laser beam with the targeted space debris
- Photodiodes nonlinear behaviour at large levels of irradiance. Therefore, use of photodiodes with better linearity is recommended.
- Laser beam output pulse repeatability
- Power supply stabilisation for the photodiodes
- Photodiodes quantum efficiency
- Spectral frequency response
- Apparatus noises
- Bandwidth

7.10 Spatial Temperature Distribution

Measuring the spatial temperature distribution into the space debris metal depth is complicated but the measurements of the space debris surface temperature are consistent with the estimated values of the Kinetic theory. It has been decided that since these estimated values are true, the spatial temperature distribution is also true.

7.11 Heating Rate of the Space Debris Surface

The measured and calculated values show that the required time for each of: nickel, aluminium and copper space debris to achieve 5,500 K is varying, see Table 15. This is possibly related to the variation in the reflectivity of the surface of the three space debris materials.

Table 15: Time taken for the space debris materials to achieve 5,500 K

Space Debris Type	Time Taken to Achieve 5,500 K $[\mu s]$	Thermal Diffusivity $\left[cm^2/_s\right]$
Nickel Space Debris	1.6	0.272
Aluminium Space Debris	2.3	0.909
Copper Space Debris	4.1	0.961

The table shows that nickel space debris required a shorter time to reach 5,500 K, compared to copper or aluminium debris. This make sense since nickel material has the smallest diffusivity, comparing to copper or aluminium. In addition, the material reflectivity in both copper and aluminium is higher than the nickel material reflectivity at 1.06 μm wavelength [100].

7.12 Space Debris Material Characteristics Determination

This section mathematically determine a few measurable factors of the thermal properties of the space debris. The optical and thermal characteristics used in the model of Kinetic theory to describe the interchange of energy in the collision action between the lattice and electrons.

7.12.1 f-parameter: The energy loss rate of electrons in elastic collisions with phonons

In general, the wasted energy portion value of an electron in collision elastically with a molecule is provided in the gases Kinetic theory as shown below [101].

$$f = \frac{2m}{M}\left(1 - \frac{\Omega}{W}\right) \qquad \text{Equation 7.20}$$

Where:

$$m = Mass\ of\ electrons = 9.10938356 \times 10^{-31}\ kg$$

$$M = Mass\ of\ molecule\ (lattice\ atom) = Mass\ of\ atom = \frac{Atomic\ weight\ (M_W)}{Avogadro's\ number\ (N_0)} \qquad \text{Equation 7.21}$$

$$N_0 = Avogadro's\ number = 6.022140857 \times 10^{26}\ \left[kg/_{mole}\right]$$

$\Omega = Average\ kinetic\ energy\ of\ molecules\ (lattice\ atoms)$

$W = Average\ kinetic\ energy\ of\ electrons$

Some presumption was used to the previous expression to determine the distribution of surface temperature using the Kinetic theory, for example simplifying the above expression more to compute f by presuming zero kinetic energy for the lattice atoms and thus the expression turns into [102]:

$$f = {}^{2m}/_{M} \qquad \text{Equation 7.22}$$

However, this equation provides an estimated value that is not accurate. In this work, we employed the expression obtained by Cravath [103]. To determine the electrons energy loss rate, the lattice atoms and electrons are presumed to be hard spheres that experience elastic collisions and have a Maxwellian speed distribution similar to the lattice atoms and electron temperatures, as described in the following equation:

$$f(x,t) = \frac{8mM}{3(m+M)^2}\left(1 - \frac{\mathrm{T}(x,t)}{\mathrm{T}_e(x,t)}\right) \qquad \text{Equation 7.23}$$

Where:

$\mathrm{T}(x,t)$ = Temperature of lattice atoms at distance x and time t

$\mathrm{T}_e(x,t)$ = Temperature of electron at distance x and time t

7.12.2 v_1: Electron Speed at Fermi Surface

The average electrons kinetic energy in metal space debris material, even at absolute temperature (zero), is very large compared to that for standard gas molecules, even at thousands of degrees of temperature. This has been presented by utilising the distribution of a Fermi Dirac [104]. At the Fermi surface, the electron speed is determined by using the following equation [105]:

$$v_1 = \sqrt{{}^{2E_F(0)}/_{m}} \qquad \text{Equation 7.24}$$

Where:

$$E_F(0) = Maximum\ electron\ kinetic\ energy\ at\ absolute\ temperature\ (T = 0\ K) = E_F = Fermi\ Energy = \frac{h^2}{8\pi^2 m}(3\pi^2 N)^{2/3}$$ Equation 7.25

Where:

$h = Plank\ constant = 6.626070040 \times 10^{-34}\ J.s$

$$N = Concentration\ conduction\ electrons = \frac{Avogadro\ number\ (N_0)}{Molar\ volume\ (M_Y)} = \frac{N_0}{M_W/\rho}$$ Equation 7.26

Where:

$M_W = Molecular\ weight\ of\ metal$

$\rho = Density\ of\ metal$

7.12.3 l: Average free path of electron

The mean free path between electron-phonons collisions can be determined by the following expression:

$$l = \tau v_1$$ Equation 7.27

Where:

$$\tau = Time\ of\ mean\ collision = \gamma m/Ne^2$$ Equation 7.28

Where:

$\gamma = Electrical\ conductivity$

$e =$ Electronic charge = Eementary electric charge=Electric charge carried by a signle proton=Magnitude of the electric charge carried by a single electron= $1.6021766208 \times 10^{-19}$ C

7.12.4 D: Thermal Diffusivity

This parameter is proportional to the rate of heating. It can be calculated mathematically using the following equation:

$$D = K/\rho C_p$$ Equation 7.29

Where:

$$K = Material\ thermal\ conductivity$$

$$C_p = Material\ specific\ heat$$

$$\rho = Material\ density$$

Based on the results, this thermal diffusivity parameter is important as it calculates how fast the space debris material will take and conduct thermal energy.

7.12.5 Z : Temperature penetration depth

The heat penetration depth with respect to time t (duration of the pulse) can be estimated by using the expression shown below [106].

$$Z = 2\sqrt{Dt} \qquad \text{Equation 7.30}$$

7.13 Ablation of Space Debris Material

The laser beam can ablate some of the space debris surface material once the temperature of the lattice reached the vaporisation temperature. This means some material will leave the surface of the space debris and produce a small thrust, which as discussed before can reduce the altitude of space debris and thus its lifetime in orbit. Since the temperature of the lattice is a function of the power strength of the laser beam, this technique is fundamentally relying on the intensity level of the beam and therefore at high intensity values of beam power, more space debris material mass is ablated and ejected from the surface of the targeted space debris as a vapour. This can actually make a pit in the orbital debris. The results show that for a similar interaction environment, more mass can be ablated from nickel or even aluminium than copper. This means it is quicker and easier to generate effective thrust on an orbital debris that is made of nickel or aluminium than a copper debris. This makes sense as copper has a higher level of thermal reflectivity than nickel or aluminium; this is in addition to the variation in the thermal properties of these three space debris metals. In practise, this means the sparks that are produced at the ablation time from the interaction of the laser beam pulse with a nickel space debris are noticeable and brighter than that with copper or even aluminium debris.

The output of the Nd^{3+} Glass laser has a spiky shape [107], which is a significant feature in deflection and ablation of space debris especially for large peaks that can result in

larger evaporation and ablation. This leads to metal recast on the kerf and splash regions. The top surface of the space debris is largely impacted by the laser beam than the deeper layers of the debris. This is correct for any of the three space debris metals. Apparently, the ablation of the top layer of the illuminated spot on the space debris has a threshold bigger in value comparing to the thresholds of the deeper layers in the debris. This is due to the fact that at the top layer, the plasma generated at threshold takes place outside the space debris and absorbs the power of the incident beam i.e. it protect the debris material. Whereas, at lower or inner layers in the space debris material, the plasma takes place in the debris. This rises the strength of the absorbed power inside the targeted space debris, creating greater ablated mass from the debris by damaging its material [108].

7.14 Outcomes

The estimation of the electron Kinetic theory using top hat (circ function) and Gaussian laser beam presumptions has been compared with the employed experimental results of the electron temperature in nickel, aluminium and copper space debris. The top hat or circ function laser beam presumption provides the bottom boundary (smallest impact level) of the theoretical model whereas the Gaussian laser beam presumption provides the top boundary (highest impact level) of the model.

At temperatures lower than the boiling temperature of the space debris material, the results present sufficient matching with the Kinetic theory. At higher temperatures than the boiling temperature of the space debris material, the results give an improved model comparing it to the Fourier theory. The electron Kinetic theory using the Gaussian laser beam assumption estimates the temperature of the electrons. These temperatures provide sufficient matching with the employed experimental measurements. Little variation is spotted in a few measurements between the employed practical results and the theory results at temperature less than the boiling temperature of the space debris materials. This variation began to be significantly bigger at temperature above the boiling temperature of the space debris metals, where the mathematical model is not valid.

For Fourier theory to gives a precise characterisation of energy transport action, several presumptions were made. However, these assumptions are not valid due to the situations produced from the sharp gradients of energy, which are produced from the

laser radiation. Therefore, the employed experimental data and the results of the Kinetic theory are much higher than that from the classical Fourier theory. This is also because Fourier theory does not consider high order temperature gradients.

Chapter 8

General Summary, Recommendations for Future Work and Conclusions

8 General Summary, Recommendations for Future Work and Conclusions

8.1 General Summary

Debris in space are now sufficiently dense that it is posing a tremendous threat to current space assets and to future space missions particularly in LEO, by runaway collision cascading. The problem of the increasing number of non-operational objects in space is one of the top SSA issues that needs urgent attention and solution. They pose a risk of collision with existing space systems or even with other debris in space and that can generate more debris. The problem is that we have no control on any non-operational objects in space including space debris. The critical density and high probability of impact in the LEO band has now reached the point where collisions between debris are the most dominant debris-generating mechanism; in fact, the number of orbital junk items in this band is increasing exponentially with actual and potential major collision events. Therefore, any feasible solution that could address the space debris problem directly or at least is able to alleviate the orbital debris affects will be of considerable interest to the spacefaring countries, research community in the space field and to the entire world.

This thesis proposes the use of a high-power pulsed laser to ablate space debris and change its trajectory to a lower orbit. Ablating space debris generates a small thrust that can changes its orbital velocity and altitude in orbit. Most of the proposed solutions to the debris dilemma require launching new spacecraft, which without doubt would cost a lot of money, time, and fuel and produce new debris itself in orbit. The outcomes of this thesis have shown that space debris mitigation by laser propulsion is a feasible and a possible method for the contactless propulsion of small space debris in the LEO band. The momentum transfer and the change in orbital velocity Δv are sufficient to change the altitude of the debris. Reducing the altitude of space debris means reducing its lifetime in orbit before it deorbits, re-enters the atmosphere, and burns up. Therefore, this technique is achievable and provides a controllable and contactless method for debris mitigation.

This thesis simulated the required laser beam energy to transfer space debris to lower orbits as well as the amount of mass that needs to be ablated to perform such trajectory transfer. The simulation has been done for different space debris sizes with different masses. Due to the complexity of both the space environment, the interaction process of the laser beam with space debris, and consequently the inevitable approximations, it is expected that the simulation in this work provides some estimates. Also, due to several target material state changes like subsurface nucleation, which leads to expulsion of the melted material, the interaction between the laser beam and the space debris is very complex especially with high energy pulsed beams when vaporisation happens and melted material is removed from the debris.

A list of the most commonly used materials in manufacturing space systems has been created and three materials have been selected to develop a model for the surface temperature profile during the laser-space debris interaction. The selected three materials for the space debris are nickel, aluminium and copper. Analyses and simulations have been done to model the interaction between the laser beam radiation and the surface of the space debris. Energy conveyance in the three-space debris has been inspected and studied theoretically. The developed model provides a valid description and realisation of the interaction technique between the laser beam and the space debris metals as well as the machining processes of the laser beam. Improvements have been made through the validity of the developed model in the Kinetic theory that depicts the technique of energy conveyance in space debris metals. That permits a comprehensive realisation of the operational procedure for the laser.

The interaction process has been studied and the laser ablation model is developed and used to simulate the growth of the spatial temperature distribution by illuminating space debris with different type of laser spot size and power. The viability of this mitigation model and its performance in inducing a melting and boiling action has been studied. The performance of a given space debris in LEO have been simulated in four different scenarios to melt and boil the debris and reduce its size from 10 cm to less than 1 cm in diameter.

The thesis also presented the output power of the radiation beam over the pulse duration in order to simulate the techniques of heat conduction in the space debris from the concentrated radiation. This can be utilised to determine the temperature of the space

debris surface, which relies on the mathematical determination of the power intensity of the radiation at the concentrated zone. Two cases have been considered based on the presumption of the power strength distribution that is extending across the optical line. The two types of distribution were presumed, which are top hat or circ function distribution and symmetrical Gaussian distribution. The top hat or circ function distribution illustrates the minimum level of this ablation technique whereas the uniform Gaussian profile illustrates the maximum level of the technique. Results show that the simulation for the case of Gaussian distribution provides a better description of the temporal and spatial distributions of the surface temperature of the space debris metal. These simulation results validate the estimated values from the developed Kinetic theory model. This developed model contains the vaporisation impacts on the space debris metal, and it permits non-equilibrium among the lattice phonons and the free electrons.

A comparison has been done by utilising Fourier theory. The results for the three different space debris metals show that a model of one-dimensional electron Kinetic theory predicts high values of space debris material temperature and temperature inclinations, compared to the results of the Fourier theory. Although Fourier theory has been utilised in the literature in order to calculate the temperature of materials in general, the results here clarify the inability of Fourier theory in the analysis of heat transfer that happens when pulsed laser beams irradiate metal space debris. Electron temperature, which is the object material temperature, has been computed in this work. Fourier theory and electron Kinetic theory are both simulated theoretically and compared with the employed experimental temperature measurements of electrons at three different central wavelengths. It was noticed that the employed experimental measurements are adequately in agreement with the results of the electron Kinetic theory.

8.2 Recommendations for Future Work

Several recommendations are stated here in this section to enhance the accuracy and reliability of the mathematical model estimations. So, for further enhancements and future work, it is recommended:

- To consider the variation of the pressure in the analysis as pressure measurement is necessary in this situation.

- The proposed model could be enhanced by considering the fact that the pressure of the immediate surroundings of the illuminated spot grows by a number of bars as soon as the vaporisation of the spot begins. This will decrease the vaporisation because it increases the boiling temperature. Therefore, the temperature will increase more quickly than predicted.
- To improve the results of the electron temperature measurement and to determine a correlation between the reflectivity of the space debris and its temperature, a real reflectivity measurement of nickel, aluminium and copper during a laser pulse is necessary at various temperatures.
- To consider the fact that at temperature higher than the critical temperature of the space debris material, plasma is created leading to energy absorption from the radiation of the laser. These components are ignored in the mathematical model simulation to achieve some possible solution
- To measure the ablation speed
- To measure the phonon temperatures
- To measure the spatial temperature allocation
- To do further model enhancement to consider the:
    - Melted stage
    - Impacts of plasma temperature
    - Energy wasted via scattering and beam energy re-radiation

8.3 Conclusions

In conclusion, the outcomes of this thesis describe the possibility for space debris mitigation with lasers. The thesis enhanced the debris mitigation model with lasers, which is based on the energy equilibrium of sublimation. The thesis assessed and simulated the engagement of laser beam pulses with space debris. It simulated the temporal evolution of surface temperature or the surface temperature profile of space debris. It also simulated the laser Gaussian power density distribution and the laser top-hat power density distribution, the two extremes.

Depending on the success of this method, it could become a technique that could be used for future missions of space debris mitigation and deflection because currently space agencies are looking for a novel and realistic techniques that could mitigate space debris in a low cost manner. The harsh environment of space is responsible for causing inaccuracies for many of the proposed removal techniques. That is why the space

community is trying to find a feasible, low risk, practical and economical approach to mitigate debris especially in LEO. The high power pulsed laser (HPPL) technique is a promising technology that can provide practical and economical ways to mitigate the problem of small and even medium size space junk in LEO orbit.

Bibliography and Key References

[1] Walker, J.G., 1977. *Continuous whole-earth coverage by circular-orbit satellite patterns* (No. RAE-TR-77044). ROYAL AIRCRAFT ESTABLISHMENT FARNBOROUGH (UNITED KINGDOM).

[2] Peng, Z. and Kohani, S., 2017. The performance of the constellations satellites based on reliability. *The Journal of Space Safety Engineering*, *4*(2), pp.112-116.

[3] De Weck, O.L., Scialom, U. and Siddiqi, A., 2008. Optimal reconfiguration of satellite constellations with the auction algorithm. *Acta Astronautica*, *62*(2), pp.112-130.

[4] Appel, L., Guelman, M. and Mishne, D., 2014. Optimization of satellite constellation reconfiguration maneuvers. *Acta Astronautica*, *99*, pp.166-174.

[5] Scialom, U., 2003. *Optimization of satellite constellation reconfiguration* (Doctoral dissertation, Massachusetts Institute of Technology).

[6] Pardini, C. and Anselmo, L., 2012. Post-disposal orbital evolution of satellites and upper stages used by the GPS and GLONASS navigation constellations: The long-term impact on the Medium Earth Orbit environment. *Acta Astronautica*, *77*, pp.109-117.

[7] Wood, L., 2012. SaVi: satellite constellation visualization. *arXiv preprint arXiv:1204.3265*.

[8] Milani, A., Farnocchia, D., Dimare, L., Rossi, A. and Bernardi, F., 2012. Innovative observing strategy and orbit determination for Low Earth Orbit space debris. *Planetary and Space Science*, *62*(1), pp.10-22.

[9] Chatwin, C., Young, R. and Birch, P., 2012. Global security.

[10] Ladd, D.N., Walden, C.J. and Trethewey, M.L., 2011. Satellite observations using the Chilbolton radar during the initial ESA'CO-VI'tracking campaign. In *ESA European Space Surveillance Conference 2011*.

[11] Kayal, H., 2009, June. A nano satellite constellation for detection of objects in earth orbit. In *Recent Advances in Space Technologies, 2009. RAST'09. 4th International Conference on* (pp. 95-99). IEEE.

[12] NASA. 2010. *What Is Orbital Debris?*. [ONLINE] Available at: https://go.nasa.gov/2y04w7J. [Accessed 11 September 2017].

[13] the Guardian. 2009. *The objects orbiting the Earth*. [ONLINE] Available at: https://www.theguardian.com/technology/2009/feb/13/space-junk-orbits-earth?CMP=share_btn_tw. [Accessed 11 September 2017].

[14] Johnson, N.L., 2012. A new look at the GEO and near-GEO regimes: Operations, disposals, and debris. *Acta Astronautica*, *80*, pp.82-88.

[15] Johnston, S., Cox, S. and Takeda, K., 2011. Scientific computation and data management using microsoft windows azure. In *Grid and Cloud Database Management* (pp. 169-192). Springer Berlin Heidelberg.

[16] Castor2.ca. 2013. *How Many Satellites?*. [ONLINE] Available at: http://www.castor2.ca/02_Basics/01_How_Many/index.html. [Accessed 11 September 2017].

[17] the Guardian. 2009. *The objects orbiting the Earth*. [ONLINE] Available at: https://www.theguardian.com/technology/2009/feb/13/space-junk-orbits-earth?CMP=share_btn_tw. [Accessed 11 September 2017].

[18] Eoportal.org. 2017. *Orbital Debris - eoPortal Directory - Satellite Missions*. [ONLINE] Available at: https://eoportal.org/web/eoportal/satellite-missions/o/orbital-debris. [Accessed 12 September 2017].

[19] Pardini, C. and Anselmo, L., 2012. Post-disposal orbital evolution of satellites and upper stages used by the GPS and GLONASS navigation constellations: The long-term impact on the Medium Earth Orbit environment. *Acta Astronautica*, *77*, pp.109-117.

[20] Johnson, N.L., 2012. A new look at the GEO and near-GEO regimes: Operations, disposals, and debris. *Acta Astronautica*, *80*, pp.82-88.

[21] Suparco.gov.pk. 2017. *Satellite Orbits*. [ONLINE] Available at: http://suparco.gov.pk/pages/orbit-type.asp. [Accessed 11 September 2017].

[22] Rossi, A., 2008. Resonant dynamics of Medium Earth Orbits: space debris issues. *Celestial Mechanics and Dynamical Astronomy*, *100*(4), pp.267-286.

[23] European Space Agency. 2017. *Mitigating space debris generation*. [ONLINE] Available at: http://www.esa.int/Our_Activities/Operations/Space_Debris/Mitigating_space_debris_generation. [Accessed 11 September 2017].

[24] Forbes.com. 2016. *How Do We Clean Up All That Space Debris?*. [ONLINE] Available at: https://www.forbes.com/sites/jillianscudder/2016/01/06/astroquizzical-space-debris/#6cf21da51a3b. [Accessed 12 September 2017].

[25] Kessler, D.J. and Cour-Palais, B.G., 1978. Collision frequency of artificial satellites: The creation of a debris belt. *Journal of Geophysical Research: Space Physics*, *83*(A6), pp.2637-2646.

[26] Orbitaldebris.jsc.nasa.gov. 2017. *ARES: Orbital Debris Program Office Newsletter*. [ONLINE] Available at: https://orbitaldebris.jsc.nasa.gov/quarterly-news/pdfs/odqnv21i1.pdf. [Accessed 1 October 2017].

[27] Orbitaldebris.jsc.nasa.gov. 2017. *ARES: Orbital Debris Program Office Newsletter*. [ONLINE] Available at: https://orbitaldebris.jsc.nasa.gov/quarterly-news/pdfs/odqnv21i1.pdf. [Accessed 1 October 2017].

[28] Klinkrad, H., 2010. *Space debris*. John Wiley & Sons, Ltd.

[29] Phipps, C.R., Baker, K.L., Libby, S.B., Liedahl, D.A., Olivier, S.S., Pleasance, L.D., Rubenchik, A., Trebes, J.E., George, E.V., Marcovici, B. and Reilly, J.P., 2012. Removing orbital debris with lasers. *Advances in Space Research*, *49*(9), pp.1283-1300.

[30] Eoportal.org. 2017. *Orbital Debris - eoPortal Directory - Satellite Missions*. [ONLINE] Available at: https://eoportal.org/web/eoportal/satellite-missions/o/orbital-debris. [Accessed 12 September 2017].

[31] World of Lasers. 2015. *Properties of Lasers*. [ONLINE] Available at: http://www.worldoflasers.com/laserproperties.htm. [Accessed 11 September 2017].

[32] Adams, C.M. and Hardway, G.A., 1965. Fundamentals of laser beam machining and drilling. *IEEE Transactions on Industry and General Applications*, (2), pp.90-96.

[33] Toller, D.F., 1982. Laser drilling of aero engine components. *NASA STI/Recon Technical Report N*, *84*.

[34] Commons.wikimedia.org. 2012. *File:Commercial laser lines.svg - Wikimedia Commons*. [ONLINE] Available at: https://commons.wikimedia.org/w/index.php?title=File:Commercial_laser_lines.svg&oldid=129842293. [Accessed 12 September 2017].

[35] Commons.wikimedia.org. 2008. *File:Laguerre-gaussian.png - Wikimedia Commons*. [ONLINE] Available at: https://commons.wikimedia.org/w/index.php?title=File:Laguerre-gaussian.png&oldid=158208534. [Accessed 12 September 2017].

[36] Svelto, O. and Hanna, D.C., 1998. *Principles of lasers* (Vol. 4). New York: Plenum press.

[37] Tatnall, A.R., Farrow, J.B., Bandecchi, M. and Francis, C.R., 2011. Spacecraft system engineering. *Spacecraft Systems Engineering, Fourth Edition*, pp.643-678.

[38] Hussein, A., Chatwin, C. and Young, R., 2013. Mitigating space debris in low earth orbit using high power pulsed lasers.

[39] Chun, M.K. and Rose, K., 1970. Interaction of High-Intensity Laser Beams with Metals. *Journal of applied physics*, *41*(2), pp.614-620.

[40] Phipps, C.R., Baker, K.L., Libby, S.B., Liedahl, D.A., Olivier, S.S., Pleasance, L.D., Rubenchik, A., Nikolaev, S., Trebes, J.E., Marcovici, B. and Valley, M.T., 2013. *A Laser Optical System to Remove Low Earth Orbit Space Debris* (No. LLNL-PROC-635293). Lawrence Livermore National Laboratory (LLNL), Livermore, CA.

[41] Rykalin, N.N., Uglov, A., Kokora, A., Cigan, J.M., Mackey, T.S. and O'Keefe, T.J., 1979. Laser machining and welding.

[42] Gagliano, F.P., Lumley, R.M. and Watkins, L.S., 1969. Lasers in industry. *Proceedings of the IEEE*, *57*(2), pp.114-147.

[43] Mason, J., Stupl, J., Marshall, W. and Levit, C., 2011. Orbital debris–debris collision avoidance. *Advances in Space Research*, *48*(10), pp.1643-1655.

[44] Campbell, J.W., 1996. Project ORION: orbital debris removal using ground-based sensors and lasers.

[45] Schall, W.O., 1991. Orbital debris removal by laser radiation. *Acta Astronautica*, *24*, pp.343-351.

[46] Phipps, C. ed., 2007. *Laser ablation and its applications* (Vol. 129). Springer.

[47] Phipps, C.R., Baker, K.L., Libby, S.B., Liedahl, D.A., Olivier, S.S., Pleasance, L.D., Rubenchik, A., Trebes, J.E., George, E.V., Marcovici, B. and Reilly, J.P., 2012. Removing orbital debris with lasers. *Advances in Space Research*, *49*(9), pp.1283-1300.

[48] Phipps, C.R., Albrecht, G., Friedman, H., Gavel, D., George, E.V., Murray, J., Ho, C., Priedhorsky, W., Michaelis, M.M. and Reilly, J.P., 1996. ORION: Clearing near-Earth space debris using a 20-kW, 530-nm, Earth-based, repetitively pulsed laser. *Laser and Particle Beams*, *14*(1), pp.1-44.

[49] Rubenchik, A.M., Barty, C.P.J., Beach, R.J., Erlandson, A.C. and Caird, J.A., 2010, October. Laser systems for orbital debris removal. In *AIP Conference Proceedings* (Vol. 1278, No. 1, pp. 347-353). AIP.

[50] Gibbings, A., Vasile, M., Watson, I., Hopkins, J.M. and Burns, D., 2013. Experimental analysis of laser ablated plumes for asteroid deflection and exploitation. *Acta Astronautica*, *90*(1), pp.85-97.

[51] Hussein, A., Rozenheck, O. and Utrilla, C.M.E., 2016. From detection to deflection: Mitigation techniques for hidden global threats of natural space objects with short warning time. *Acta Astronautica*, *126*, pp.488-496.

[52] Nambiar, S.P., Hussein, A., Silva-Martinez, J., Reinert, J. and Gonzalez, F., 2016, March. Architecture for mitigating short-term warning cosmic threats: READI project. In *Aerospace Conference, 2016 IEEE* (pp. 1-11). IEEE.

[53] Hussein, A., Rozenheck, O. and Utrilla, C.M.E., 2016. From detection to deflection: Mitigation techniques for hidden global threats of natural space objects with short warning time. *Acta Astronautica*, *126*, pp.488-496.

[54] Nambiar, S.P., Hussein, A., Silva-Martinez, J., Reinert, J. and Gonzalez, F., 2016, March. Architecture for mitigating short-term warning cosmic threats: READI project. In *Aerospace Conference, 2016 IEEE* (pp. 1-11). IEEE.

[55] Gourdon, R., Hussein, A., Soni, A., Aliaj, B., Manuel Entrena Utrilla, C., Sisaid, I., Reinert, J., Faull, J., Bettiol, L., Schmidt, N. and Nambiar, S., 2015. The International Space University Space Studies Program 2015 Planetary Defense Project.

[56] Burke, J., Hussein, A., Soni, A., Thangavelu, M., Schmidt, N. and Wilson, T., 2015. Planetary defence: a duty for world defenders.

[57] Uhlig, H.H., 1959. The Theory of the Properties of Metals and Alloys. *Journal of the American Chemical Society*, *81*(14), pp.3808-3808.

[58] Chun, M.K. and Rose, K., 1970. Interaction of High-Intensity Laser Beams with Metals. *Journal of applied physics*, *41*(2), pp.614-620.

[59] Nasa.gov. 2017. *NASA - Micrometeoroids and Orbital Debris (MMOD)*. [ONLINE] Available at: https://www.nasa.gov/centers/wstf/laboratories/hypervelocity/mmod.html. [Accessed 12 September 2017].

[60] Richards, F.A. and Walsh, D., 1969. Time-resolved temperature measurement of a laser-heated surface. *Journal of Physics D: Applied Physics*, *2*(5), p.663.

[61] Bar-Isaac, C., Korn, U., Shtrikman, S. and Treves, D., 1974. Thermal structure of the evaporation front in laser drilling processes. *Applied Physics A: Materials Science & Processing*, *5*(2), pp.121-125.

[62] Alwan, A.A., 1989. *Surface Temperature Transients in Laser Machining of Metals* (Master dissertation, University of Glasgow).

[63] Riley, K., 1974. *Thermodynamics of laser induced interaction processes in solids* (Doctoral dissertation, University of Birmingham).

[64] Rykalin, N.N., Uglov, A., Kokora, A., Cigan, J.M., Mackey, T.S. and O'Keefe, T.J., 1979. Laser machining and welding.

[65] Dugdale, J.S., 2016. *The electrical properties of metals and alloys*. Courier Dover Publications.

[66] Byabagambi, C.A., 1987. *Surface heating in metals irradiated by fast IR laser pulses* (Doctoral dissertation, University of Glasgow).

[67] Harrington, R.E., 1967. Application of the theory of heat conduction to the absorption of blackbody radiation. *Journal of Applied Physics*, *38*(8), pp.3266-3270.

[68] Harrington, R.E., 1968. Thermal conduction near a metal surface exposed to blackbody radiation. *Journal of Applied Physics*, *39*(8), pp.3699-3706.

[69] Riley, K., 1974. *Thermodynamics of laser induced interaction processes in solids* (Doctoral dissertation, University of Birmingham).

[70] Anisimov, S.I., Kapeliovich, B.L. and Perelman, T.L., 1974. Electron emission from metal surfaces exposed to ultrashort laser pulses. *Zh. Eksp. Teor. Fiz*, *66*(2), pp.375-377.

[71] Byabagambi, C.A., 1987. *Surface heating in metals irradiated by fast IR laser pulses* (Doctoral dissertation, University of Glasgow).

[72] Lee, J.F., 1963. *Statistical thermodynamics*. Addison-Wesley Pub. Co..

[73] Physics.uoguelph.ca. 2006. *Index of /~garrettp/teaching/PHY-1070*. [ONLINE] Available at: https://www.physics.uoguelph.ca/~garrettp/teaching/PHY-1070/. [Accessed 19 September 2017].

[74] Kittel, C., 2005. *Introduction to solid state physics*. Wiley.

[75] Ali Omar, M., 1975. Elementary solid state physics. *Addi son-Wesley Pubf ishing Gompony*.

[76] Byabagambi, C.A., 1987. *Surface heating in metals irradiated by fast IR laser pulses* (Doctoral dissertation, University of Glasgow).

[77] Frenkel, A.I., 1945. Kinetic Theory of Liquid. *Uzd, ANSSSR*, p.223.

[78] Riley, K., 1974. *Thermodynamics of laser induced interaction processes in solids* (Doctoral dissertation, University of Birmingham).

[79] Byabagambi, C.A., 1987. *Surface heating in metals irradiated by fast IR laser pulses* (Doctoral dissertation, University of Glasgow).

[80] Mortimer, E.C., 1975. Chemistry: A Conceptual Approach. 3rd.

[81] Dugdale, J.S., 2016. *The electrical properties of metals and alloys*. Courier Dover Publications.

[82] Kittel, C., 1962. Elementary Solid State Physics John Wiley. *New York*, p.169.

[83] Riley, K., 1974. *Thermodynamics of laser induced interaction processes in solids* (Doctoral dissertation, University of Birmingham).

[84] Harrington, R.E., 1967. Application of the theory of heat conduction to the absorption of blackbody radiation. *Journal of Applied Physics*, *38*(8), pp.3266-3270.

[85] Harrington, R.E., 1967. Application of the theory of heat conduction to the absorption of blackbody radiation. *Journal of Applied Physics*, *38*(8), pp.3266-3270.

[86] Ready, J.F., 1965. Effects due to absorption of laser radiation. *Journal of Applied Physics*, *36*(2), pp.462-468.

[87] Riley, K., 1974. *Thermodynamics of laser induced interaction processes in solids* (Doctoral dissertation, University of Birmingham).

[88] Byabagambi, C.A., 1987. *Surface heating in metals irradiated by fast IR laser pulses* (Doctoral dissertation, University of Glasgow).

[89] Alwan, A.A., 1989. *Surface Temperature Transients in Laser Machining of Metals* (Master dissertation, University of Glasgow).

[90] Hacker, J., Losekamm, M., Sardesai, N., Johnson, C., Bell, R., Rey, D., Vigneron, A., Bettiol, L., Brack, D., Braegen, E. and Calder-Potts, G., 2014. On-orbit servicing commercial opportunities with security implications.

[91] Shaylor, P.J., 1976. *Laser drilling phenomenon including beam/vaporized material interactions*.

[92] Alwan, A.A., 1989. *Surface Temperature Transients in Laser Machining of Metals* (Master dissertation, University of Glasgow).

[93] Bakewell, B.A., 1973. *Performance of pulsed laser systems in relation to machining mechanisms* (Doctoral dissertation, Ph. D. Thesis, University of Birmingham, Birmingham).

[94] Shaylor, P.J., 1976. *Laser drilling phenomenon including beam/vaporized material interactions*.

[95] Alwan, A.A., 1989. *Surface Temperature Transients in Laser Machining of Metals* (Master dissertation, University of Glasgow).

[96] Kreith, F., 1962. *Principles of heat transfer*. International Textbook Company.

[97] Mcadams, W.H., 1954. *Heat Transmission: 3d Ed*. McGraw-Hill.

[98] Byabagambi, C.A., 1987. *Surface heating in metals irradiated by fast IR laser pulses* (Doctoral dissertation, University of Glasgow).

[99] Chun, M.K. and Rose, K., 1970. Interaction of High-Intensity Laser Beams with Metals. *Journal of applied physics*, *41*(2), pp.614-620.

[100] Ready, J.F., 1997. *Industrial applications of lasers*. Academic press.

[101] Compton, K.T., 1923. On the motions of electrons in gases. *Physical Review*, *22*(4), p.333.

[102] Harrington, R.E., 1968. Thermal conduction near a metal surface exposed to blackbody radiation. *Journal of Applied Physics*, *39*(8), pp.3699-3706.

[103] Cravath, A.M., 1930. The rate at which ions lose energy in elastic collisions. *Physical Review*, *36*(2), p.248.

[104] Lee, J.F., 1963. *Statistical thermodynamics*. Addison-Wesley Pub. Co..

[105] Kittel, C., 2005. *Introduction to solid state physics*. Wiley.

[106] Ready, J.F., 1997. *Industrial applications of lasers*. Academic press.

[107] Steen, W.M. and Kamalu, J.N., 1983. Laser cutting. *Laser materials processing*, *3*, pp.17-111.

[108] Wood, R.M., 2003. *Laser-induced damage of optical materials*. CRC Press.